Diagnostics for plasma-based electron accelerators

M. C. Downer* and R. Zgadzaj

Department of Physics, University of Texas at Austin, Austin, Texas 78712, USA

A. Debus and U. Schramm

Helmholtz-Zentrum Dresden-Rossendorf, Institute for Radiation Physics, 01328 Dresden, Germany

M. C. Kaluza

Institute of Optics and Quantum Electronics, Friedrich-Schiller-University, 07743 Jena, Germany and Helmholtz Institute Jena, 07743 Jena, Germany

(published 8 August 2018)

Plasma-based accelerators that impart energy gain as high as several GeV to electrons or positrons within a few centimeters have engendered a new class of diagnostic techniques very different from those used in connection with conventional radio-frequency (rf) accelerators. The need for new diagnostics stems from the micrometer scale and transient, dynamic structure of plasma accelerators, which contrasts with the meter scale and static structure of conventional accelerators. Because of this micrometer source size, plasma-accelerated electron bunches can emerge with smaller normalized transverse emittance ($\epsilon_n < 0.1$ mm mrad) and shorter duration ($\tau_b \sim 1$ fs) than bunches from rf linacs. Single-shot diagnostics are reviewed that determine such small ϵ_n and τ_b noninvasively and with high resolution from wide-bandwidth spectral measurement of electromagnetic radiation the electrons emit: ϵ_n from x rays emitted as electrons interact with transverse internal fields of the plasma accelerator or with external optical fields or undulators; τ_b from THz to optical coherent transition radiation emitted upon traversing interfaces. The duration of ~1 fs bunches can also be measured by sampling individual cycles of a copropagating optical pulse or by measuring the associated magnetic field using a transverse probe pulse. Because of their luminal velocity and micrometer size, the evolving structure of plasma accelerators, the key determinant of accelerator performance, is exceptionally challenging to visualize in the laboratory. Here a new generation of laboratory diagnostics is reviewed that yield snapshots, or even movies, of laser- and particle-beam-generated plasma accelerator structures based on their phase modulation or deflection of femtosecond electromagnetic or electron probe pulses. Spatiotemporal resolution limits of these imaging techniques are discussed, along with insight into plasma-based acceleration physics that has emerged from analyzing the images and comparing them to simulated plasma structures.

DOI: 10.1103/RevModPhys.90.035002

CONTENTS

*downer@physics.utexas.edu

I. INTRODUCTION

Energetic electron and positron beams from accelerators probe the fundamental structure of subatomic matter, irradiate cancerous tumors, and produce bright x rays that sterilize food and medical equipment and reveal the structure of molecules essential to life. For decades, radio-frequency (rf) technology has underlain all such accelerators, but is inherently limited to accelerating fields of $\sim$1 MV/cm by the electrical breakdown threshold of metallic structures. Consequently, with rf technology, the next electron-positron collider at the energy frontier (electron energy $E_e \sim$ TeV) will cost over $10 billion, and require construction of tunnels tens of kilometers long (Behnke, 2015). Even GeV-class electron accelerators that underlie the current generation of x-ray lasers and Compton gamma-ray sources at the frontiers of experimental biomedical, materials, and nuclear science typically cost hundreds of millions of dollars and occupy several square kilometers of real estate. These prohibitive costs are forcing a widespread realignment of accelerator research and development toward alternative accelerator technologies that can provide high electron beam quality, energy, and current at dramatically lower cost and size (Ritz, 2014).

Accelerators based on plasmas of subatmospheric electron density ($10^{17} < n_e < 10^{19}$ cm^{-3}) perturbed by ultrashort laser pulses or relativistic charged particle bunches have emerged as a promising pathway toward compact, low-cost electron and positron acceleration. In such accelerators, the electromagnetic (electrostatic) force of the drive laser pulse (particle bunch) expels plasma electrons from within the driver's envelope, creating a positively charged, light-speed accelerating cavity, or "wake," with dimensions of a plasma wavelength $\lambda_p[\mu\text{m}] = (3.3 \times 10^{10})/\sqrt{n_e\ [\text{cm}^{-3}]}$, which is tens of microns for the n_e range cited. Electrostatic fields within these cavities are of the order of $E_z[\text{V/cm}] \approx \sqrt{n_e\ [\text{cm}^{-3}]}$, and thus reach $\sim 10^9$ V/cm for the cited n_e range, thousands of times larger than fields that conventional accelerators can sustain, yet without breakdown concern. This plasma cavity can capture electrons or positrons that are injected into it with mildly relativistic speed along its propagation direction. In some cases, a small independent conventional rf preaccelerator injects the initial particle bunch. A common alternative, unique to electron accelerators, is that the initial driver-plasma interaction creates a mildly relativistic high-energy tail of ambient plasma electrons that self-injects into the cavity. Section II.B discusses a variety of injection strategies and their consequences for beam quality. In all cases, the transient plasma cavity accelerates the captured particles further with GV/cm field strength until either they dephase from it or the drive pulse (bunch) depletes.

Since Tajima and Dawson (1979) first proposed the concept of plasma-based, laser-driven electron acceleration, wakefield acceleration has grown into an international research and development effort encompassing laboratory demonstrations, theoretical modeling, and computer simulations of rapidly increasing sophistication and scope (Esarey, Schroeder, and Leemans, 2009). Within the last few years, two laboratories demonstrated single-stage laser-driven wakefield accelerators (LWFAs) that captured ambient plasma electrons and accelerated them to 2 to 4 GeV energy with few percent energy spread and up to 0.1 nC charge within an acceleration distance of only a few centimeters (Wang *et al.*, 2013; Leemans *et al.*, 2014). Many laboratories have converted LWFAs into femtosecond x-ray sources based on betatron radiation from electrons accelerating within the plasma structure, synchrotron radiation in external undulators, or Thomson backscatter of laser light from accelerated electrons outside the LWFA (Corde *et al.*, 2013), while the pursuit of tabletop x-ray free-electron lasers based on LWFA beams is a forefront research challenge (Gruener *et al.*, 2007; Nakajima, 2008). Dual-stage LWFAs using one (H. T. Kim *et al.*, 2013) or two independent (Steinke *et al.*, 2016) laser drive pulses, a critical step toward multistage LWFAs required for colliders at the energy frontier (Leemans and Esarey, 2009), were also recently demonstrated.

Meanwhile, single-stage plasma accelerators driven by relativistic electron or positron bunches (Chen *et al.*, 1985)—usually simply called plasma wakefield accelerators (PWFAs)—have imparted energy gain of several GeV within an acceleration distance of approximately a meter to independent, externally injected, copropagating electron (Litos *et al.*, 2014) and positron (Corde *et al.*, 2015) witness bunches of 0.1 nC charge while maintaining high beam quality. The possibility of accelerating trailing electrons to twice the energy of the drive electron bunch in a single stage was demonstrated in principle (Blumenfeld *et al.*, 2007), opening the prospect of compact, plasma-based, energy-doubling afterburners for conventional electron accelerators (Lee *et al.*, 2002; Harris, 2016). Computer simulations have shown that PWFAs driven by bunches of relativistic protons can in principle accelerate electrons or positrons to

the energy frontier in one subkilometer stage (Caldwell *et al.*, 2009; Lotov, 2010), a possibility that the Advanced Proton-Driven Plasma Wakefield Accelerator (AWAKE) project at CERN is now beginning to explore in the laboratory (Caldwell *et al.*, 2016; Geschwendtner *et al.*, 2016).

Despite rapid recent progress with LWFAs and PWFAs, concern remains about whether plasma wakefield techniques can be incorporated into practical accelerators useful for high-energy physics or other areas of discovery science, in view of stringent requirements for narrow energy spread, emittance, beam stability and control, and brightness preservation (HEPAP, 2015). This concern brings the subject of this review, diagnostics for plasma-based electron accelerators, to center stage. Diagnostics link the micron-scale structure and femtosecond-scale dynamics of plasma wakes to the key beam properties—bunch duration, transverse emittance, charge, and energy spread—that govern the performance of a collider or light source. They also link observable accelerator properties to theory and computer simulation output. However, diagnostics in widespread use with conventional rf accelerators have, by and large, proven insufficient for characterizing plasma-based electron accelerators.

There are two reasons for this. First, because of the micrometer scale of plasma accelerator structures, plasma-accelerated electron bunches can emerge with shorter duration ($\sigma_s/c \sim 1$ fs) and smaller transverse beam size ($0.1 \lesssim \sigma_r \lesssim 1$ μm) than bunches from meter-scale rf accelerator structures. Thus, beams from plasma-based accelerators can have smaller normalized transverse emittance ($\epsilon_n < 0.1$ mm mrad) than beams from conventional accelerators. Here ϵ_n is the product of a beam's geometric emittance (roughly $\sigma_r\sigma_r'$ at a beam waist, where σ_r' is its angular divergence) and its Lorentz factor γ_e that is conserved in an ideal beam transport system. Small ϵ_n is potentially a key advantage over conventional accelerators, because it enables high luminosity in collider interactions and a wide tuning range in free-electron lasers (FELs). Together with short bunch length σ_z, it is also essential for achieving high peak brightness from Thomson backscatter and FEL light sources. Section II reviews these unique properties of plasma-accelerated electron bunches and the laser-plasma conditions that optimize them, while Sec. III reviews new methods now emerging to measure them with the resolution required to operate practical plasma-based accelerators. Second, plasma accelerator structures, in contrast to fixed, stationary conventional accelerator structures, are evolving and transient as they propagate at luminal velocity, and must be recreated with high fidelity for each bunch. Accelerator performance sensitively depends on details of the plasma structure and dynamics. For example, "bubblelike" electron density cavities created via highly nonlinear interaction of drive pulses and bunches with a plasma yield more monoenergetic beams than sinuosoidal wakes created via linear interactions (Pukhov and Meyer-ter-Vehn, 2002). Moreover, evolution of the bubble structure during propagation governs self-injection of plasma electrons (Kalmykov, Yi, and Shvets, 2009). Accurate single-shot visualization of these plasma structures and their dynamics in the laboratory is essential not only for operating practical plasma accelerators, but for validating individual stages of holistic computer simulation output and for understanding LWFA physics in detail. Section IV reviews the many innovative diagnostic methods that have been and continue to be invented for capturing images of these plasma structures in the act of accelerating electrons and positrons to relativistic energy. This aspect of diagnostics has no counterpart in conventional rf acceleration and is likely to be a continuing source of innovation and discovery. Section V presents our conclusions and our assessment of important future directions in plasma acceleration diagnostics.

II. PROPERTIES OF PLASMA ACCELERATOR STRUCTURES AND BEAMS

A. General properties of plasma electron accelerators

We refer the interested reader to Malka *et al.* (2008), Esarey, Schroeder, and Leemans (2009), Leemans and Esarey (2009), Norreys (2009), Malka (2012), and Hooker (2013) for reviews of the physics and applications of laser-driven plasma-based electron accelerators, and to Muggli and Hogan (2009), Hogan *et al.* (2010), Caldwell *et al.* (2016), and Muggli (2016) for reviews of particle-beam-driven plasma wakefield acceleration. Here we summarize basic features of LWFA and PWFA structures and beams that are needed for the subsequent discussion of diagnostics.

1. Ponderomotive and Coulomb forces

The simplest LWFA consists of a single intense laser pulse focused into a confined gas or preionized underdense plasma. For gas targets, the leading edge of the pulse ionizes the gas, creating plasma. The intense portion of the pulse then creates a light-speed accelerating structure by expelling plasma electrons longitudinally and radially from within its envelope via "ponderomotive" pressure, which is equivalent to the gradient $\vec{\nabla}(\epsilon_0 E_L^2/2)$ of the pulse's cycle-averaged electromagnetic energy density. Here E_L is the local amplitude of the laser electric field in V/m. When each electron's quiver motion in the field E_L is nonrelativistic, the ponderomotive force $\vec{F}_p$ on each electron (mass m_e) is (Kruer, 1988; Esarey, Schroeder, and Leemans, 2009)

$$\vec{F}_p = -m_e c^2 \vec{\nabla}(a^2/2), \tag{1}$$

where $a = eE_L/m_e\omega c$ is the local dimensionless normalized vector potential, equal to the ratio of momentum eE_L/ω that the laser field of frequency ω imparts to an electron in an optical cycle to $m_e c$ as a function of position within the pulse profile. Thus $a \approx 1$ is a soft boundary between nonrelativistic electron undulation and linear laser-plasma interaction at $a < 1$, and relativistic electron motion and nonlinear laser-plasma interaction at $a > 1$. We can relate a to local intensity $I = E_L^2/2Z_0$ of a pulse of wavelength λ by $I(\mathrm{W/m^2}) = (\pi c/2)(4\pi\epsilon_0)(m_e c^2 a/e\lambda)^2$, where $Z_0 = \sqrt{\mu_0/\epsilon_0}$ is the impedance of free space. Thus, from Eq. (1), $\vec{F}_p$ is proportional to the intensity gradient $\vec{\nabla}I$. Identical expressions relate intensity I_0, field amplitude E_{L0}, and laser strength parameter a_0 at the peak of a pulse. Using units $\mathrm{W/cm^2}$ for I_0 and μm for λ, the relationship becomes

$$a_0 = 0.85\sqrt{\lambda^2(\mu\mathrm{m})I_0(10^{18}\ \mathrm{W/cm^2})}. \tag{2}$$

For highly relativistic ($a_0 \gg 1$) pulses, the ponderomotive force can be written $\vec{F}_p = -m_e c^2 \vec{\nabla}\gamma_e$, where $\gamma_e \equiv [1 + (p_e/m_e c)^2]^{1/2} \approx (1 + a^2)^{1/2}$ is the Lorentz factor associated with the electron's quiver motion and p_e is the oscillating electron's momentum. Ions also experience $\vec{F}_p$, but respond much more slowly than electrons. Consequently charge separates, creating longitudinal (accelerating) and transverse (focusing) fields, or wakefields, that can trap and accelerate leptons.

In the PWFA, the Coulomb force of a bunch of density n_b replaces the ponderomotive force (1) as plasma wake driver. For relativistic bunches, the Lorentz-contracted Coulomb electric field is essentially transverse ($\vec{E} \approx E_r \hat{e}_r$), and the bunch's internal space-charge force $en_b E_r$ is reduced by a factor γ_e^{-2} compared to nonrelativistic bunches (Muggli, 2016). Consequently, transverse bunch dynamics over meter-scale path lengths is dominated by emittance and external focusing forces, rather than space charge (Hogan *et al.*, 2003; Muggli *et al.*, 2008b). The boundary between linear (Chen *et al.*, 1985) and nonlinear (Rosenzweig *et al.*, 1991) wake excitation occurs at $n_b \sim n_e$ for PWFA, analogous to $a_0 \sim 1$ for LWFA. Unlike laser drivers, particle-bunch drivers can either "blow out" or "suck in" plasma electrons, depending on whether they are negatively or positively charged. Indeed, PWFA experiments have been (and are being) performed with electron (Blumenfeld *et al.*, 2007; Litos *et al.*, 2014), positron (Blue *et al.*, 2003; Corde *et al.*, 2015), and proton (Caldwell *et al.*, 2016; Geschwendtner *et al.*, 2016) drive bunches.

2. Wake structures

The shape and dynamics of a wake's electron density profile $n_e(r, z, t)$ depend on the duration, focus, and energy (and for PWFAs, charge; for LWFAs, λ) of the drive pulse, and on the density, composition, and preformed structure of the plasma target. As a simple example, a 1D laser pulse of longitudinal duration τ_L (FWHM) less than a plasma period $\tau_p \equiv f_p^{-1} \equiv 2\pi/\omega_p$ and amplitude $a_0 \ll 1$ propagating at group velocity $v_g \approx c$ in a uniform, underdense plasma of unperturbed electron density $\bar{n}_e$ linearly excites a sinuosoidal 1D electron density wake (Tajima and Dawson, 1979)

$$\delta n_e(z, t) = \delta n_{e,0} \sin k_p \zeta. \tag{3a}$$

Here $\delta n_e(z, t) \equiv n_e - \bar{n}_e$ is the local density perturbation of amplitude $\delta n_{e,0}$, $k_p = \omega_p/v_g$ is the plasma wave number, $\omega_p = (\bar{n}_e e^2/\epsilon_0 m_e)^{1/2}$ is the plasma frequency for collective electron density oscillations, $v_{ph,p} = \omega_p/k_p = v_g$ is the plasma wave phase velocity set by v_g, and $\zeta \equiv z - v_g t$. As τ_L varies, $\delta n_{e,0}$ exhibits a broad resonant peak at $\tau_L \sim \tau_p/2$.

In 3D with cylindrical symmetry, a subrelativistic ($a_0 \ll 1$) pulse of duration $\tau_L \lesssim \tau_p/2$, focused to Gaussian transverse profile $a_0 \exp(-r^2/w_0^2)$ of width $w_0 \lesssim \lambda_p$, linearly excites a wake of the form

$$\begin{aligned}\delta n_e(r, z, t) &= \delta n_z(r, z, t) + \delta n_r(r, z, t) \\ &= A e^{-r^2/w_0^2}[1 + f(r)] \sin k_p \zeta\end{aligned} \tag{3b}$$

that can be calculated analytically from cold fluid equations (Gorbunov and Kirsanov, 1987; Esarey *et al.*, 1989). Here A depends on the pump's peak power and its Rayleigh length $z_R = \pi w_0^2/\lambda$, and $f(r) \equiv (\lambda_p^2/\pi\lambda z_R)(1 - r^2/w_0^2)$. The first (second) term in square brackets corresponds to the contribution δn_z (δn_r) arising from the longitudinal (radial) ponderomotive force. Such 2D linear laser wakes were the first to be observed directly in the laboratory with sub-λ_p resolution, using ultrashort laser probe pulses (see Sec. IV.B.2). Researchers took advantage of tight focusing to create $\delta n_r \sim \bar{n}_e$ over $\lesssim$0.1 mm path with subterawatt (sub-TW) lasers (Marquès *et al.*, 1996; Siders, LeBlanc, Fisher *et al.*, 1996), before multi-TW lasers (Backus *et al.*, 1998) became widely available.

With advances in laser technology, excitation of wakes with short ($\tau_L \lesssim \tau_p/2$), mildly relativistic ($a_0 \sim 1$) pulses over multi-mm paths became possible. In this regime, numerical calculations are required to describe wake excitation in 3D, although analytic 1D solutions that exhibit the main physical effects are possible with simplifying assumptions such as a nonevolving driver and a quasistatic plasma structure (Sprangle, Esarey, and Ting, 1990a, 1990b). The wake develops nonsinusoidal features attributable to the relativistic mass increase of the strongly driven plasma electrons. In 1D, the main new features are steepened wave fronts and lengthened wake period (Bulanov, Kirsanov, and Sakharov, 1989; Berezhiani and Murusidze, 1990; Sprangle, Esarey, and Ting, 1990a, 1990b). In 3D, these effects depend on r. A mildly relativistic drive laser pulse that is peaked on axis creates a period-lengthened, steepened wake on axis, but a linear wake off axis. As a result, wave fronts curve, with curvature increasing with distance behind the driver (Sprangle *et al.*, 1992; Decker and Mori, 1994; Bulanov, Pegoraro, and Pukhov, 1995; Andreev, Gorbunov, and Ramazashvili, 1997). Reduction of $\bar{n}_e$ on axis (e.g., by ponderomotive channeling) can further lengthen the on-axis period and accentuate the curvature. Figure 1(a) shows a computer simulation of a wake excited in this regime. Ultimately transverse wave breaking can occur (Bulanov, Vshivkov *et al.*, 1997). Section IV.C describes single-shot diagnostic experiments in which these features of mildly relativistic plasma wakes were first observed in the laboratory (Matlis *et al.*, 2006; Dong *et al.*, 2010a).

As the drive pulse intensifies further to $a_0 \gtrsim 3$, it can evacuate electrons completely from its immediate wake [Fig. 1(b)]. This strongly nonlinear LWFA regime, first discovered in computer simulations (Pukhov and Meyer-ter-Vehn, 2002), leaves behind a nearly spherical bare ion cavity bounded by a thin, dense electron "wall." Figures 1(b)–1(d) show simulations of the self-consistent evolution of the drive laser pulse (red) and trailing ion cavity excited in this strongly nonlinear regime, which researchers began calling the bubble regime (Kostyukov, Pukhov, and Kiselev, 2004). Using 3D simulations, Lu *et al.* (2007) comprehensively documented properties of bubble-regime LWFAs over a wide range of laser-plasma parameters. Because of their special importance for plasma accelerator science in general,

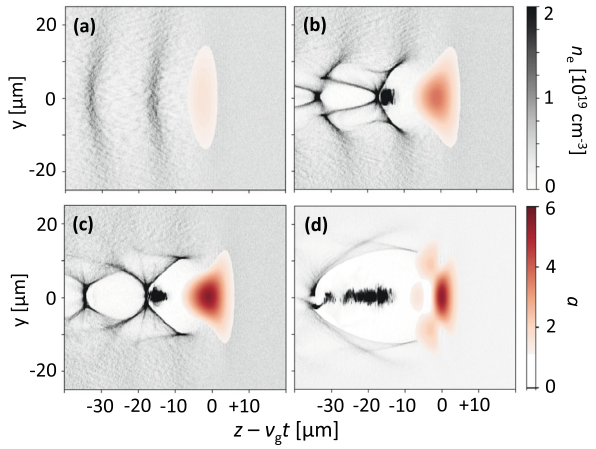

FIG. 1. Particle-in-cell simulation of evolving laser-driven plasma bubble. Gray scale: local electron density n_e; color scale: local strength a of drive laser profile centered at $y = z - v_g t = 0$. Gas jet: He with 1% N, with linear entrance ramp ($0 < z < 0.55$ mm), plateau ($0.55 < z < 2.55$ mm) at $\bar{n}_e = 4.4 \times 10^{18}$ cm^{-3} after ionization, exit ramp ($2.55 < z < 3.1$ mm). Laser pulse: $\lambda = 800$ nm, $\tau_L = 30$ fs, beam waist $w_0 = 19$ μm at $z = 4.1$ mm. (a) $z = 1.72$ mm, $a_0 \approx 1$, mildly nonlinear wake; (b) $z = 2.15$ mm, $a_0 \approx 3$, bubble has formed, ionized inner-shell electrons from N-dopant injected and trapped; (c) $z = 2.37$ mm, $a_0 \approx 6$, bubble evolves, trapped electrons advance; (d) $z = 2.8$ mm, $a_0 \approx 6$, bubble lengthens in down ramp. From R. Pausch.

and diagnostic development, in particular, we review properties of bubble-regime LWFAs separately in Sec. II.C. Section III reviews a new generation of single-shot electron bunch diagnostics developed primarily to meet the challenge of measuring the unusually narrow ($\sigma_r \ll 1$ μm), short ($\sigma_s \sim 1$ μm),"quasimonoenergetic" electron bunches that bubble-regime LWFAs are uniquely capable of producing, often injected from within the plasma [Fig. 1(b)]. Sections IV.C and IV.D review diagnostic experiments that observed the unique structure and strongly nonlinear propagation dynamics of bubble-regime wakes in the laboratory, using ultrashort laser probe pulses.

Electron drive bunches of duration $\tau_b \lesssim \omega_p^{-1}$, width $\sigma_r \lesssim \lambda_p$, because they expel plasma electrons from their envelope, create a hierarchy of plasma wake structures that closely resemble those described for LWFAs. Chen *et al.* (1985) developed the linear theory of the standard PWFA. Predictions of steepened wave fronts and period lengthening in 1D nonlinear theory of PWFA (Rosenzweig, 1987), and of wave front curvature in 2D (Rosenzweig *et al.*, 1991), preceded, but closely parallel, corresponding predictions for LWFA. Section IV.B.1 describes diagnostic experiments in which linear and mildly nonlinear PWFAs were first observed in the laboratory. Rosenzweig *et al.* (1991) also developed the theory of the strongly nonlinear ($n_b > \bar{n}_e$) PWFA regime, usually called the blowout regime in the context of PWFA, which produces wake structures similar to those shown in Figs. 1(b)–1(d). The uniform ion column that an electron driver creates in this regime guides drive and trailing accelerating bunches over many initial beam "beta-function" lengths, analogous to Rayleigh lengths of a laser driver. However, electron (Blumenfeld *et al.*, 2007; Litos *et al.*, 2014) and positron (Corde *et al.*, 2015) drivers produce different wake structures, a distinction that does not arise with LWFAs. Direct observation of these differences, using probing techniques developed for LWFAs (see Secs. IV.C and IV.D) is an important opportunity for future diagnostics research.

3. Accelerating and focusing fields

The wake's electron density change $\delta n_e(r, z, t)$ is the source of its enormous internal accelerating $[\hat{e}_z E_z(r, z, t)]$ and focusing $[\hat{e}_r E_r(r, z, t)]$ fields. In 1D, Poisson's equation $\partial E_z/\partial z = -e\delta n_e(z, t)/\epsilon_0$ yields 1D solutions for the accelerating field $E_z(z, t) = E_0 \cos k_p \zeta$ corresponding to Eq. (3). Since the maximum density perturbation is of the order of $\delta n_e^{(\max)} \approx \bar{n}_e$, the maximum accelerating field is

$$E_0 = m_e \omega_p c/e \tag{4a}$$

$$\approx 0.96\sqrt{\bar{n}_e(\mathrm{cm}^{-3})}\ \mathrm{V/cm}. \tag{4b}$$

Equation (4a) is the so-called cold nonrelativistic wave-breaking field (Dawson, 1959). In the form Eq. (4b), it provides a simple estimate of the maximum accelerating field achievable in a plasma of density $\bar{n}_e$. Drive fields of amplitude $a_0 \gtrsim 1$ are required to reach E_0. For $a_0 \gtrsim 2$, the wake becomes strongly nonlinear [see Figs. 1(b)–1(d)]. 3D computer simulations show that the maximum accelerating field is then (Lu *et al.*, 2007)

$$E_z^{(\max)} \approx E_0\sqrt{a_0}. \tag{4c}$$

Equations (4) can be compared with accelerating fields in conventional rf accelerators, which are currently limited to $\sim 10^6$ V/cm. The plasma accelerator in Fig. 1(c) ($\bar{n}_e = 4.4 \times 10^{18}$ cm^{-3}, $a_0 \approx 6$), in contrast, has maximum accelerating field $E_0\sqrt{a_0} \approx 5 \times 10^9$ V/cm.

In 3D, both accelerating and focusing fields pervade the plasma wake. Figure 2 shows (a) accelerating and (b) focusing

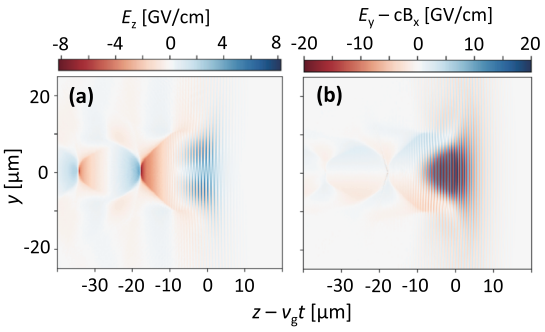

FIG. 2. Internal fields of laser-driven plasma bubble shown in Fig. 1(c) and its driving laser pulse. (a) Accelerating field $E_z(y, \zeta)$, and (b) focusing field. From R. Pausch.

fields inside the wake in Fig. 1(c). In the back half of the positively charged bubble, E_z accelerates electrons forward from their internal injection point near the back wall [see Fig. 1(b)] toward the bubble's center. Simultaneously E_r focuses these electrons toward the propagation axis, maintaining low emittance. The strong E_r of bubbles in longitudinally shaped plasmas can potentially provide emittance-preserving beam transport between LWFA stages, or between an LWFA and conventional accelerator or FEL undulator (Xu *et al.*, 2016).

Field structures in blowout-regime electron-beam-driven PWFAs resemble those in Fig. 2, and those of conventional rf linacs (Rosenzweig *et al.*, 1998). With PWFAs, unlike LWFAs, acceleration of positrons, an essential element for a collider, has been investigated extensively through theory (Lee *et al.*, 2001), simulation, and experiments (Blue *et al.*, 2003; Hogan *et al.*, 2003; Corde *et al.*, 2015) because of the availability of a relativistic positron bunch injector at SLAC's Facility for Advanced Accelerator Experimental Tests (FACET) (Hogan *et al.*, 2010) and its predecessors. E_z accelerates positrons forward from an external injection point just in front of the bubble's center, toward the front of the bubble. Unfortunately, E_r defocuses these positrons away from the propagation axis, causing emittance growth. A possible solution for preserving the emittance is to excite the PWFA in a hollow channel surrounded by an annular plasma (Chiou and Katsouleas, 1998; Schroeder, Whittum, and Wurtele, 1999; Kimura *et al.*, 2011; Gessner *et al.*, 2016). Alternatively, Corde *et al.* (2015) demonstrated that a positron driver can draw a quasistatic reservoir of plasma electrons to the bubble's axis that compensates the defocusing fields. Similar issues will arise when LWFAs accelerate positrons. They highlight the importance of developing laboratory diagnostics of internal fields of plasma lepton accelerators.

Whereas ultrashort optical pulses mostly probe electron density structure of plasma wakes, electron bunches directly probe their internal fields. The experiments of Rosenzweig *et al.* (1988, 1989), detailed in Sec. IV.B.1, used sub-λ_p electron "witness" bunches to probe $E_z(r,z,t)$ and $E_r(r,z,t)$, rather than $\delta n_e(r,z,t)$, of linear and nonlinear PWFAs. Section IV.C.4 details more recent experiments in which few-fs electron witness bunches, derived ironically from a diagnostic bubble-regime LWFA, probed the internal electric fields of a subject bubble-regime LWFA (Zhang *et al.*, 2017). An important exception to the role of optical probes is ultrafast Faraday rotation probes of a plasma wake's internal magnetic fields, created by the current of the accelerating electron bunch and/or by the displacement current of the wake's dynamic electric fields (Kaluza *et al.*, 2010; Buck *et al.*, 2011). Sections III.D.1.c and IV.C.3.a detail these diagnostic experiments.

4. Plasma density range

A reasonable criterion for plasma accelerators to provide significant advantage over conventional rf accelerators is that E_0 be at least 100 times their breakdown field $\sim 10^6$ V/cm. Equation (4b) then dictates a lower limit $\bar{n}_e > 10^{16}$ cm^{-3} on plasma density. In fact, this is about the lowest density at which laser-driven electron acceleration has been reported in the laboratory (Clayton *et al.*, 1993; Amiranoff *et al.*, 1998). Self-injection of plasma electrons into a LWFA becomes inefficient as $\bar{n}_e$ decreases (Froula *et al.*, 2009), and guiding of the drive pulse, either via its own relativistic Kerr effect (Sprangle, Tang, and Esarey, 1987) or via self-formed (Sprangle *et al.*, 1992) or preformed (Durfee, Lynch, and Milchberg, 1995) plasma waveguides, becomes increasingly difficult at low $\bar{n}_e$. Thus the previously cited experiments, and others up to $\bar{n}_e \approx 10^{17}$ cm^{-3} (Amiranoff *et al.*, 1995; Kitagawa *et al.*, 2004), required either external injection or a capillary waveguide. For these reasons most LWFA experiments have used $\bar{n}_e > 3\times 10^{17}$ cm^{-3}.

PWFAs have used density as low as $\bar{n}_e \approx 10^{13}$ cm^{-3} (Rosenzweig *et al.*, 1988, 1989), but then E_0 approaches that of conventional accelerators. Recent PWFAs, however, have used $\bar{n}_e$ from 5×10^{16} cm^{-3} (Litos *et al.*, 2014) to 8×10^{16} cm^{-3} (Corde *et al.*, 2015).

An upper limit on $\bar{n}_e$ for LWFAs comes from the requirement that the plasma be underdense, i.e., $\omega_p < \omega$. When it is not, a laser pulse penetrates only a skin depth ($c/\omega_p \lesssim 10^{-2}$ cm) into the plasma and reflects. When it is, the laser pulse can propagate over distances $0.1 < z < 10$ cm required for its wake to accelerate electrons to $0.1 < E_e < 10$ GeV with gradient $E_0 \sim 10^9$ V/cm. Stated equivalently, $\bar{n}_e$ must be less than the critical plasma density

$$n_{\rm cr} = \frac{\epsilon_0 m_e \omega^2}{e^2} = \frac{1.1\times 10^{21}}{[\lambda(\mu{\rm m})]^2}\ {\rm cm}^{-3}. \tag{5}$$

Thus LWFAs driven by near-infrared ($0.8 < \lambda < 1$ μm) solid-state lasers, the dominant technology for reaching $a_0 \geq 1$ since the 1990s, are limited to $\bar{n}_e < 10^{21}$ cm^{-3}. CO_2 lasers ($\lambda \approx 10$ μm), which drove the earliest LWFAs at $a_0 \ll 1$ in the early 1990s (Clayton *et al.*, 1993), and which, with recent advances in chirped pulse amplification (Polyanskiy, Babzien, and Pogorelsky, 2015), promise to drive future LWFAs at $a_0 \geq 1$ (Pogorelsky and Ben-Zvi, 2014), are limited to driving LWFAs at $\bar{n}_e < 10^{19}$ cm^{-3}.

For particle-bunch drivers there is no counterpart to the critical frequency (5). Nevertheless, for both LWFAs and PWFAs, the pulse (bunch) duration τ_L (τ_b) available at power (bunch density) needed to drive a high-amplitude wake, together with the resonant criterion $\tau_{L,b} \lesssim \omega_p^{-1}$, set a practical upper limit on $\bar{n}_e$. Multi-TW laser pulses at $\lambda \approx 0.8$ μm are currently limited to $\tau_L \gtrsim 10$ fs, limiting a resonant LWFA to $\bar{n}_e \lesssim 3\times 10^{19}$ cm$^{-3} \approx 0.02 n_{\rm cr}$. Chicane compressors can provide nC bunches with $\tau_b \gtrsim 100$ fs, limiting resonant PWFA to $\bar{n}_e \lesssim 3\times 10^{17}$ cm^{-3}. Future multi-TW CO_2 laser pulses ($\lambda \approx 10$ μm) are likely to be limited to $\tau_L \gtrsim 500$ fs (Pogorelsky and Ben-Zvi, 2014), limiting resonant LWFA at this λ to $\bar{n}_e \lesssim 10^{16}$ cm$^{-3} \approx 0.03 n_{\rm cr}$. So-called "self-modulated" (SM) LWFAs and PWFAs, discussed in Sec. II.B, use nonresonant excitation ($\tau_{L,b} \gg \omega_p^{-1}$). Then $\bar{n}_e$ can be higher than the limits stated.

Diagnostics should be versatile enough to probe wake structure over a wide $\bar{n}_e$ range. While many optical probe methods discussed in Secs. IV.C and IV.D were developed to visualize wakes in $\bar{n}_e \sim 10^{19}$ cm^{-3} plasma, diagnostic electron

bunches have probed wakes at $\bar{n}_e \sim 10^{17}$ cm^{-3} (Sec. IV.C.4) or lower (Sec. IV.B.1) density. Section IV.E discusses density scaling of wake diagnostics.

5. Dephasing, pump depletion, and transformer ratio

Within the practical LWFA density range $3\times10^{17} \lesssim \bar{n}_e \lesssim 3\times10^{19}$ cm^{-3} for a $\lambda \sim 0.8$ μm drive pulse, useful acceleration length and achievable single-stage energy gain ΔW_e vary widely. There are two main reasons for this. First, the group velocity $v_g = c(1-\bar{n}_e/n_{\rm cr})^{1/2}$ of the drive pulse (and thus the phase velocity of the plasma accelerating structure) decreases with increasing $\bar{n}_e$, dropping by a fraction $(c-v_g)/c \approx 0.015$ below c at the upper limit $\bar{n}_e/n_{\rm cr} \approx 0.03$ of the LWFA density range. Consequently, a relativistic electron propagating at $\sim c$ in the laboratory frame drifts at velocity $c-v_g$ through the wake's accelerating cavity, which has length of order $\sim\lambda_p/2$. Dephasing between electron and driver limits acceleration time to $\sim\lambda/[2(c-v_g)]$ and acceleration distance in the lab frame to dephasing length $L_d \approx c\lambda_p/[2(c-v_g)]$, or in common laboratory units

$$L_d(\mathrm{cm}) \approx \lambda_p^3/\lambda^2 \approx \frac{3.7}{[\bar{n}_e(10^{18}\ \mathrm{cm}^{-3})]^{3/2}[\lambda(\mu\mathrm{m})]^2}. \quad (6)$$

Thus for $\lambda = 1$ μm and uniform $\bar{n}_e = 0.03n_{\rm cr} = 3\times10^{19}$ cm^{-3}, $L_d \approx 0.02$ cm, limiting electron energy gain to $\Delta W_e = eE_0L_d \approx 100$ MeV and $\Delta W_e \propto (\bar{n}_e)^{-1}$ at other densities. Introduction of a gradual density up ramp $(d\bar{n}_e/dz > 0)$ along the drive pulse propagation path can, in principle, compensate dephasing, since the accelerating cavity then shrinks in proportion to $\lambda_p \propto (\bar{n}_e)^{-1/2}$ as it propagates, keeping the accelerating electron bunch at its rear (Katsouleas, 1986; Bulanov, Vshivkov *et al.*, 1997; Sprangle *et al.*, 2001). However, laser-driven tapered plasmas in the laboratory (Kaganovich *et al.*, 1999; Rittershofer *et al.*, 2010; Abuazoum *et al.*, 2012; M. S. Kim *et al.*, 2013) have not yet accelerated electrons significantly beyond the limit given by Eq. (6).

In contrast, for PWFA, a drive bunch with Lorentz factor γ_b propagates at velocity $v_b = (1-\gamma_b^{-2})^{1/2}c$ independent of $\bar{n}_e$. Thus a highly relativistic driver and its wake propagate vanishingly close to c, e.g., $(c-v_b)/c \approx 10^{-11}$ for 20 GeV $(\gamma_b = 4\times10^5)$ drive bunches used in Litos *et al.* (2014) and Corde *et al.* (2015), effectively eliminating dephasing, an advantage of PWFAs over LWFAs.

Second, depletion of the drive laser pulse energy increases with increasing $\bar{n}_e$. Various laser-plasma instabilities can contribute to depletion, depending on the intensity and duration of the drive pulse. In the strongly nonlinear $(a_0 > 1)$, short pulse $(\omega_p\tau_L < 1)$ regime of greatest interest for electron acceleration, erosion of the leading edge of the drive pulse due to diffraction, scattering, and photon deceleration by the density spike at the leading edge of the plasma wake dominates pump depletion (Decker *et al.*, 1996). 3D simulations in this regime show that pump depletion limits effective acceleration length in the lab frame to $L_{\rm pd} \approx (n_{\rm cr}/\bar{n}_e)c\tau_L$ (Lu *et al.*, 2007), or in common laboratory units

$$L_{\rm pd}(\mathrm{cm}) \approx \frac{0.03\tau(\mathrm{fs})}{\bar{n}_e(10^{18}\ \mathrm{cm}^{-3})[\lambda(\mu\mathrm{m})]^2}. \quad (7)$$

Thus a $\tau_L = 30$ fs, $\lambda = 1$ μm pulse driving a strongly nonlinear wake in plasma of density $\bar{n}_e = 3\times10^{19}$ cm^{-3} depletes within $L_{\rm pd} \approx 0.03$ cm, similar to the dephasing limit for a uniform plasma. Pump depletion fundamentally limits LWFAs. No methods exist to compensate it. Pump depletion and dephasing together limit practical laser-plasma electron accelerators to $\bar{n}_e < 0.03n_{\rm cr}$.

PWFAs are subject to beam-plasma instabilities (Dodd *et al.*, 2002; Deng *et al.*, 2006; Huang *et al.*, 2007). Moreover, maximum energy gain per stage is limited to the product of the drive bunch kinetic energy and a transformer ratio (Ruth *et al.*, 1984), which is equivalent to the pump depletion limit of LWFAs. Thus, for example, a PWFA driven by an electron bunch of energy $E_{\rm drive}$ is limited to accelerating trailing electrons to $\sim 2E_{\rm drive}$. Special shaping of the drive bunch can extend this limit (Chen *et al.*, 1986).

6. Atomic composition of the plasma

In addition to density, atomic composition of the plasma must be chosen carefully. Nearly all LWFA experiments use targets comprised mostly of H_2 or He. This is because field strengths in the range $0.01 < a_0 < 0.1$, realized in the leading edge of relativistic $(a_0 \gtrsim 1)$ drive pulses or in separate preionizing pulses, can field ionize these low-Z atoms completely over a wide footprint. This avoids complicating the wake-forming laser-plasma interaction at $a_0 \sim 1$ with delayed ionization of inner-shell electrons, which occurs at $a_0 \gtrsim 1$ in higher-Z atoms. On the other hand, few-percent admixtures of high-Z gases (e.g., N_2, Ar) into H_2 or He targets can facilitate injection of electrons into a laser-driven wake (McGuffey *et al.*, 2010; Pak *et al.*, 2010), as discussed in Sec. II.C.1.

For PWFAs, lithium is a common choice of target gas (Muggli *et al.*, 1999) because the drive bunch, or a synchronized laser pulse, can ionize it over a multimeter path. Self-ionization can degrade accelerator performance (Deng *et al.*, 2003; O'Connell *et al.*, 2006) so preionization is preferred (Green *et al.*, 2014). As with LWFAs, high-Z admixtures can stimulate injection from within the plasma, known as "Trojan horse" injection (Hidding *et al.*, 2012) in the context of PWFAs.

B. Plasma accelerator configurations

LWFAs (PWFAs) can be excited with one, two, or multiple drive pulses (bunches). Esarey, Schroeder, and Leemans (2009) reviewed the various configurations for LWFAs and Muggli and Hogan (2009), Caldwell *et al.* (2016), and Muggli (2016) reviewed them for PWFAs. Here we summarize configurations important for the ensuing discussion of diagnostics.

1. Standard LWFAs and PWFAs

Section II.A described general properties of simple "standard" LWFAs and PWFAs, driven, respectively, by one laser pulse (see Figs. 1 and 2) or one particle bunch of duration $\tau \lesssim \omega_p^{-1}$. Wake excitation in linear $(a_0 \ll 1, n_b \ll \bar{n}_e)$, weakly

nonlinear ($a_0 \sim 1$, $n_b \sim \bar{n}_e$), or strongly nonlinear ($a_0 \gg 1$, $n_b \gg \bar{n}_e$) regimes results in very different lepton bunch properties.

Most standard LWFA experiments in linear and weakly nonlinear regimes produced no self-injected electrons [an exception was Kitagawa *et al.* (2004)]. Some experiments in this regime accelerated electrons injected from a linac (Amiranoff *et al.*, 1998; Dewa *et al.*, 1998; Bernard *et al.*, 1999).

Standard strongly nonlinear LWFAs can capture, trap, and accelerate electrons from surrounding plasma [see Fig. 1(b)] through various mechanisms. They can produce bunches of a few pC to a few hundred pC charge, few-% energy spread, and kA peak current without external injection. Because of their special importance in motivating beam diagnostic development reviewed in Sec. III, we discuss them separately in Sec. II.C.

Standard PWFAs producing high-quality bunches have so far required externally injected witness bunches whether in linear (Rosenzweig *et al.*, 1988), weakly nonlinear (Rosenzweig *et al.*, 1989), or blowout (Litos *et al.*, 2014; Corde *et al.*, 2015) regimes, although internal injection is an active field of research (Hidding *et al.*, 2012; Wittig *et al.*, 2015). For example, Litos *et al.* (2014) matched the injected electron bunch sufficiently well that 74 pC of injected charge extracted wake energy with up to 30% efficiency while gaining $\Delta E_e > 1$ GeV and maintaining an energy spread as low as 0.7%. Emittance, duration, and energy spread of the accelerated bunches were determined by the external conventional injector rather than the plasma physics of the bubble and were measurable by standard beam diagnostics. Standard PWFAs and linear and mildly nonlinear standard LWFAs have provided the context for many innovations in wake structure diagnostics (see Sec. IV).

2. Self-modulated LWFAs and PWFAs

Starting in 1995, LWFA experiments using "long" ($\tau_L \sim 1$ ps $\gg \omega_p^{-1}$) energetic ($\sim$1 J) laser pulses to drive $\bar{n}_e \sim 10^{19}$ cm^{-3} plasma yielded copious, self-injected, tens-of-MeV electrons with thermal energy distribution (Coverdale *et al.*, 1995; Modena *et al.*, 1995; Nakajima *et al.*, 1995). Strong wake generation and energetic electron production occurred when the peak power P of the drive pulse exceeded the critical power (Andreev, 1992; Antonsen and Mora, 1992; Sprangle *et al.*, 1992)

$$P_c[\mathrm{GW}] = 17(n_{\mathrm{cr}}/\bar{n}_e), \tag{8}$$

for relativistic self-focusing (RSF). RSF, favored at high $\bar{n}_e$, enabled the drive pulse to focus to, and self-guide at (Wagner *et al.*, 1997), higher a_0 inside the plasma than it reached at the plasma entrance. This enabled it to drive self-modulation and forward Raman instabilities efficiently over $\sim$mm paths (Andreev, 1992; Antonsen and Mora, 1992; Sprangle *et al.*, 1992). These instabilities broke up the incident pulse into a train of subpulses of length $c\tau \lesssim \lambda_p$ spaced by λ_p. Simultaneously a wake grew, and Stokes and anti-Stokes sidebands at $\pm n\omega_p$ ($n = 1, 2, 3, \ldots$) appeared on the transmitted drive pulse spectrum, sometimes out to multiple orders, signifying a high-amplitude wake ($E_z \to E_0 \sim$ GV/cm). An extensive literature, summarized by Esarey, Schroeder, and Leemans (2009), developed around such SM wakes. Section IV.A describes time-resolved light-scattering experiments that diagnosed SM-LWFAs under conditions of high (Le Blanc *et al.*, 1996; Gordon *et al.*, 1998) and moderate (Ting *et al.*, 1996) accelerated charge.

SM-LWFA experiments yielded energetic electron beams more simply than standard LWFA experiments, requiring no external injector or waveguide, and generated much higher charge (e.g., $Q \approx 0.5$ nC at $E_e > 1$ MeV) (Wagner *et al.*, 1997). As a result, SM-LWFA dominated LWFA science in the decade following 1995. Breaking of the high-amplitude SM-wave injected plasma electrons indiscriminately throughout the wake, yielding wide energy and angular (e.g., $\sim$8°) (Wagner *et al.*, 1997) spread. High $\bar{n}_e$ restricted L_d to $\sim$0.1 cm [see Eq. (6)], and thus energy gain to $eE_0L_d \lesssim 100$ MeV. These electron bunch properties posed no special challenges for, and stimulated no significant advances in, beam diagnostics.

The self-modulation beam-plasma instability (Bret, Gremillet, and Dieckmann, 2010) has emerged as a key first step in reshaping $\tau_b \sim 300$ ps, TeV proton bunches from the CERN Super Proton Synchrotron (SPS) or Large Hadron Collider (LHC) into λ_p-spaced multibunch trains that can excite high-gradient ($E_0 \gtrsim 10^8$ V/cm, $\bar{n}_e \gtrsim 10^{16}$ cm^{-3}) plasma wakes efficiently (Caldwell and Lotov, 2011). Compressing CERN proton bunches to single $\tau_b \sim 300$ fs bunches needed to drive high-gradient wakes resonantly would be prohibitively expensive using conventional techniques. Effective seeding of the instability is needed to create a stable bunch train and to avoid parasitic instabilities. Initial experiments in the AWAKE project (Caldwell *et al.*, 2016; Geschwendtner *et al.*, 2016) are using an ionization front created by a short laser pulse that copropagates in the front part of the proton drive bunch. Single-shot wake diagnostics (Secs. IV.C and IV.D) scaled to the appropriate $\bar{n}_e$ (Sec. IV.E) can potentially play a key role in evaluating these seeding strategies.

3. Multipulse LWFAs and PWFAs

LWFAs can be driven by two or more laser pulses. In the plasma beat-wave accelerator (PBWA), two long pulses of frequencies ω_1 and ω_2 resonantly excite a plasma wave when $\Delta\omega \equiv \omega_1 - \omega_2 \approx \omega_p$. The first laser-driven plasma electron accelerators (Kitagawa *et al.*, 1992; Clayton *et al.*, 1993; Amiranoff *et al.*, 1995) utilized PBWA and provided the context for extensive plasma wave diagnostic development based on collective Thomson scattering (Clayton *et al.*, 1985). Section IV.A discusses later applications of these techniques to SM-LWFA. See Clayton (2009) and Esarey, Schroeder, and Leemans (2009) for reviews of PBWAs.

Related to PBWAs and SM-LWFAs is excitation of LWFAs with optimized trains of short ($\tau < \omega_p^{-1}$) pulses, i.e., multiple-pulse (MP) LWFAs (Umstadter, Esarey, and Kim, 1994; Umstadter *et al.*, 1995; Hooker *et al.*, 2014). Esarey, Schroeder, and Leemans (2009) and Hooker *et al.* (2014) cited earlier theoretical work. In a simple MP-LWFA, m identical pulses of energy $\mathcal{E}$, field strength $a_0 \ll 1$ separated

by λ_p each adds coherently to the wake, ultimately generating a wake equivalent to that generated by a single identically shaped pulse of energy $m\mathcal{E}$. Nevertheless, the weaker pulses can potentially be generated by lasers capable of higher wall-plug efficiency and repetition rate than lasers that generate single Joule-class pulses. The flexibility to tailor interpulse spacing, or shape and amplitude of individual pulses, offers additional potential advantages. In the nonlinear regime ($a_0 \gtrsim 1$), an optimized pulse train can excite a stronger wake than the equivalent-energy single pulse (Umstadter, Esarey, and Kim, 1994; Umstadter *et al.*, 1995). In addition, an appropriately timed trailing pulse can remove the wake behind the primary accelerating bucket, recover its energy by blue-shifting, and avoid unnecessary plasma heating (Hooker *et al.*, 2014). Recently Cowley *et al.* (2017) reported the first MP-LWFA experiments, using diagnostic techniques described in Sec. IV.C.

PWFAs can benefit similarly from excitation via optimized particle-bunch trains. Section IV.B.1 reviews diagnostic experiments on the multibunch PWFA (Kallos *et al.*, 2008; Muggli *et al.*, 2008a).

C. Electron beams from strongly nonlinear LWFAs

Three reports of bubble regime LWFAs that produced relativistic electron bunches with $\Delta E_e/E_e$ ranging from ~0.02 (Geddes *et al.*, 2004; Mangles *et al.*, 2004) to 0.24 (Faure *et al.*, 2004) transformed laser-plasma accelerator science in 2004. Reported charge within the quasimonoenergetic peak ranged from 22 pC (Mangles *et al.*, 2004) to > 100 pC (Faure *et al.*, 2004; Geddes *et al.*, 2004). The transformation was so complete that today most LWFAs operate in the bubble regime.

The peaked electron energy distributions highlighted in these reports originated from a unique process that, although highly nonlinear, injected electrons precisely into a small fraction of the bubble's $\sim\lambda_p^3$ volume. Simulations (Pukhov and Meyer-ter-Vehn, 2002) showed that, as a bubble formed, an electron density spike built up at its rear [see Fig. 1(b)] and eventually broke, injecting electrons. Since these electrons were localized in space and time [see the black dot at the back of the bubble in Fig. 1(b)], they experienced nearly the same field and thus accelerated with small energy spread.

This injection mechanism had two corollaries beyond the question of energy spread. First, the small injection volume could lead to unusually small normalized transverse emittance ϵ_n, as discussed in Sec. II.C.2. Second, the small injection volume could also lead to unusually short bunch duration τ_b, as discussed in Sec. II.C.3. In 2004, researchers could only speculate about the values of ϵ_n and τ_b. Simulations provided only rough guidance, and methods for measuring them did not exist. Section III reviews new diagnostic methods that emerged in the past decade specifically to address the challenge that bubble-regime LWFAs first posed in 2004. Table I summarizes reported bunch properties that these methods determined, with references to appropriate sections of Sec. III. The properties of beams accelerated in PWFAs, on the other hand, are, to a large extent, governed by the conventional accelerator that injected them. Thus PWFA beam diagnostics are closer to those used widely at conventional accelerators. We refer interested readers to Li and Hogan (2011) and Green *et al.* (2017) for an overview of beam diagnostics at the FACET project.

TABLE I. Properties of electron bunches from strongly nonlinear LWFAs determined by diagnostic methods reviewed in Sec. III. The best reported values (boldface type) are not achieved simultaneously. Q = charge within $\Delta E_e/E_e$, E_e = electron energy gain, $\Delta E_e/E_e$ = fractional energy spread, ε_n = normalized transverse emittance, and τ_b = bunch duration.

Bunch property	Typical range	Sections
Q (nC)	0.01–**0.5**[a]	II.C.1, III.B.1
E_e (GeV)	0.01–**4**[b]	III.B.2
$\Delta E_e/E_e$ (FWHM)	**0.01**[c]–1	II.C.1, III.B.2–III.B.4
ε_n (mm mrad)	~**0.1**[d]–1	II.C.2, III.C
τ_b (fs)	~**1.6**[e]–10	II.C.3, III.D

[a] $E_e \approx 0.3$ GeV, $\Delta E_e/E_e \approx 0.15$ (Couperus *et al.*, 2017).
[b] $Q \approx 0.006$ nC, $\Delta E_e/E_e \approx 0.06$ (Leemans *et al.*, 2014).
[c] $Q \approx 0.01$ nC, $E_e \approx 0.2$ GeV (Rechatin *et al.*, 2009); $Q \sim 0.02$ nC, $E_e \approx 0.06$ GeV (Gallacher *et al.*, 2009); $0.01 < Q < 0.08$ nC, $0.2 < E_e < 0.6$ GeV (Wang *et al.*, 2016).
[d] $Q \sim 0.001$ nC, $E_e \approx 0.4$ GeV (Plateau *et al.*, 2012).
[e] $Q \approx 0.015$ nC, $E_e \approx 0.085$ GeV (Lundh *et al.*, 2011).

1. Charge and energy spread

The 2004 results were based on measurements with standard magnet spectrometers and charged particle sensors, instruments that had not previously been used to measure few-MeV-wide spectral peaks from LWFAs, nor to evaluate charge within these peaks. Unlike conventional accelerators, LWFAs produced copious poorly characterized low-energy electrons and background radiation. Moreover, their beams fluctuated in pointing from shot to shot and diverged in a few-mrad angle cone. Questions about the accuracy of absolute values of Q and $\Delta E_e/E_e$ reported under these conditions in early bubble-regime LWFA papers emerged (Glinec *et al.*, 2006). Section III.B details how researchers met the diagnostic challenges that bubble-regime LWFAs posed for absolute charge and energy measurements.

Efforts to improve upon the tens-to-hundreds pC charge, quasimonoenergetic energy spread, and shot-to-shot fluctuations of self-injected LWFA beams by microcontrolling the injection process are a highlight of post-2004 research. FELs and colliders demand bunches with < 1% energy spread, nC charge, and high reproducibility. Faure (2017) reviewed several "controlled injection" schemes applied to bubble-regime LWFAs. The right-hand column of Fig. 3 depicts them schematically, while the main panels summarize results of 21 studies. For consistency, $\Delta E_e^{(\mathrm{FWHM})}$ values in Fig. 3 represent raw electron spectrometer output, without corrections for instrument resolution. Thus, in some cases, a plotted value exceeds the value reported in the corresponding publication, after such corrections were applied. With this uniform criterion we can compare the relative effectiveness of different injection methods for producing high Q and/or small $\Delta E_e/E_e$ objectively.

Experiments that relied on self-injection [gold data points in Figs. 3(a) and 3(b)] yielded the most widely varying (a) $\Delta E_e/E_e$ and (b) Q results. The former include some of

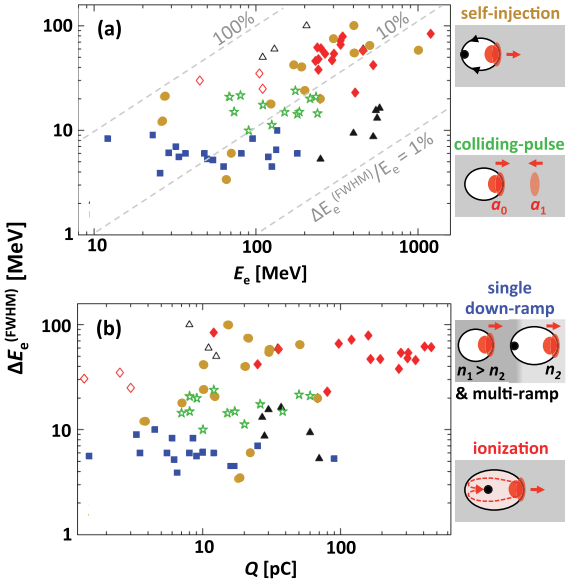

FIG. 3. Measured energy spread $\Delta E_e^{(\mathrm{FWHM})}$ of quasimonoenergetic peaks of electrons from bubble-regime LWFAs vs (a) peak energy E_e and (b) charge Q within the peak, from 21 experiments using electron injection methods depicted schematically in the right-hand column: self-injection, filled gold circles (Faure *et al.*, 2004; Mangles *et al.*, 2004; Leemans *et al.*, 2006; Osterhoff *et al.*, 2008; Gallacher *et al.*, 2009; Kneip *et al.*, 2009; H. T. Kim *et al.*, 2013; Wang *et al.*, 2013; Li *et al.*, 2017); colliding pulses, green stars (Faure *et al.*, 2006; Rechatin *et al.*, 2009); single shock-induced density ramp, filled blue squares (Schmid *et al.*, 2010; Buck *et al.*, 2013; Khrennikov *et al.*, 2015; Swanson *et al.*, 2017); tailored multiramp, open black (Gonsalves *et al.*, 2011) and filled black (Wang *et al.*, 2016) triangles; ionization-induced, open red (McGuffey *et al.*, 2010; Pak *et al.*, 2010) and filled red (Pollock *et al.*, 2011; Mirzaie *et al.*, 2015; Couperus *et al.*, 2017) diamonds. Plotted $\Delta E_e^{(\mathrm{FWHM})}$ are not corrected for instrumental broadening.

the widest (50–100 MeV) and one of the narrowest (3 MeV) reported $\Delta E_e^{(\mathrm{FWHM})}$ values. After deconvolving instrument broadening, Gallacher *et al.* (2009) reported $\Delta E_e^{(\mathrm{FWHM})}/E_e \approx 0.01$ for the last result [plotted at $E_e = 65$ MeV in Fig. 3(a)], a milestone in LWFA research. The wide variation of $\Delta E_e^{(\mathrm{FWHM})}$ shows the sensitivity of self-injection to different experimental conditions and the difficulty of controlling it. Reported Q varied from a few pC to ~50 pC [Fig. 3(b)].

Faure *et al.* (2006), based on theory by Esarey *et al.* (1997), controlled injection with a second pulse (amplitude $0.1a_0 \lesssim a_1 \lesssim 0.4a_0$) that collided with the LWFA drive pulse (a_0) of similar wavelength λ (see Fig. 3, right column, second schematic). The resulting interference introduced a ponderomotive force wave of period λ, amplitude proportional to $2a_0a_1/\lambda_0$, and near-zero phase velocity. When positioned near the back of the bubble, this wave could induce injection with spatial precision $\sim\lambda$ into a LWFA operating below its self-injection threshold (Faure *et al.*, 2006), or control phase-space volume for trapping within a self-injected bubble, thus controlling accelerated charge and its energy spread (Rechatin *et al.*, 2009). Adjusting delay between the pulses controlled the collision point location within the jet and thus acceleration length. Adjustment of a_1 fine-tuned Q and ΔE_e. Experiments using colliding-pulse injection (green data points in Fig. 3) have consistently yielded $\Delta E_e^{(\mathrm{FWHM})}$ between 10 and 25 MeV, showing improved control compared to self-injection. E_e and Q tuning ranges 60–200 MeV and 6–60 pC, respectively, have been achieved. After deconvolving instrument response, Rechatin *et al.* (2009) reported $\Delta E_e^{(\mathrm{FWHM})}/E_e \approx 0.01$, also a milestone. Use of two or more injection pulses may yield further improvements (Esarey *et al.*, 1997).

Another group of experiments (blue and black data points in Fig. 3) controlled injection by sculpting the plasma's longitudinal density profile $\bar{n}_e(z)$. A density down ramp $\partial\bar{n}_e/\partial z < 0$ along a wake's propagation direction decreases its phase velocity, encouraging injection (Bulanov *et al.*, 1998; Suk *et al.*, 2001). Down-ramp injection can occur below the self-injection threshold, enabling better control. Geddes *et al.* (2008) demonstrated longitudinal momentum spread as small as 0.17 MeV/c for < 1 MeV electrons emerging from a LWFA generated in a down ramp of length $> \lambda_p$. Later Schmid *et al.* (2010) and Buck *et al.* (2013) introduced a more abrupt down ramp of scale length $< \lambda_p$ (Fig. 3, right column, third schematic) by inserting a knife edge into a supersonic gas flow to create a local shock front. This simple approach has proven robust, enabling consistent output of bunches with $\Delta E_e^{(\mathrm{FWHM})} < 10$ MeV as E_e tuned up to ~200 MeV [blue points in Fig. 3(a)]. Most results yielded $Q < 30$ pC [blue points in Fig. 3(b)], although $Q \approx 90$ pC was achieved with more laser energy.

The success and simplicity of down ramps prompted researchers to tailor more sophisticated density distributions to improve flexibility (Guillaume *et al.*, 2015). Using one laser pulse, Gonsalves *et al.* (2011) and Wang *et al.* (2016) drove tandem, differently sloped ramps, each performing a separate function: injection, rephasing, or beam focusing. Recent work with this approach yielded more energetic (250–500 MeV) and higher Q (30–70 pC) bunches than single down ramps, while maintaining $\Delta E_e^{(\mathrm{FWHM})} \sim 10$ MeV (solid black triangles in Fig. 3). After deconvolving instrument resolution, Wang *et al.* (2016) reported $\Delta E_e^{(\mathrm{FWHM})}/E_e < 0.01$, the smallest yet reported for LWFAs.

For controlled injection of $Q > 100$ pC bunches, researchers have driven bubble-regime LWFAs in H_2 or He carrier gas doped with higher-Z gas (e.g., N_2). The leading edge of the drive pulse fully ionizes the carrier (e.g., He I, II form at $a_0 \approx 0.03$, 0.1, respectively) (Augst *et al.*, 1991) and outer shell electrons of the dopant. From these electrons, the main part of the drive pulse ($a_0 > 1$) forms the bubble and ionizes K-shell electrons of the dopant inside the bubble. The bubble's internal fields can then trap and accelerate these electrons (see Fig. 3, right column, fourth schematic), even below the self-injection threshold. Early "ionization-injected" LWFAs yielded 45–250 MeV electrons [open red diamonds in Fig. 3(a)] with < 10 pC charge [open red diamonds in Fig. 3(b)], and energy spread from ~30 MeV (McGuffey *et al.*, 2010; Pak *et al.*, 2010) to ~300 MeV (Clayton *et al.*, 2010). Subsequently, Liu *et al.* (2011) and Pollock *et al.* (2011) reduced energy spread by confining dopant gas to a short initial stage, followed by a longer acceleration stage

without dopant. Mirzaie *et al.* (2015) achieved a similar goal by focusing 100 TW pulses into uniformly doped gas in an unmatched geometry. Subsequent coevolution of laser pulse and bubble self-truncated ionization injection, yielding accelerated bunches with $Q \sim 10(50)$ pC, $E_e > 1$ GeV (< 1 GeV), and $\Delta E_e^{(\mathrm{FWHM})} < 100$ MeV. Couperus *et al.* (2017) accelerated $Q \sim 0.5$ nC bunches to $E_e \sim 300$ MeV, $\Delta E_e \sim 45$ MeV, exploiting beam loading to improve beam quality. Solid red diamonds in Fig. 3 show a selection of these later results.

Two broad conclusions emerge from this brief overview of controlled LWFA injection. First, controlled injection has improved consistency of LWFA output, compared to self-injection. Each method generates bunches within a narrower ΔE_e range than self-injection, although methods differ from each other: e.g., colliding-pulse and down-ramp methods yield $\Delta E_e < 10$ MeV over wide E_e and Q ranges, while ionization injection yields $\Delta E_e \sim 50$ MeV with higher charge. Second, a few milestone results (Gallacher *et al.*, 2009; Rechatin *et al.*, 2009; Wang *et al.*, 2016) notwithstanding, the goal of producing $\Delta E_e/E_e \ll 0.01$ has proven difficult to realize consistently with single-stage LWFAs. Although research continues, and although $\Delta E_e/E_e$ may improve in multistage LWFAs, emphasis in the design (Huang, Ding, and Schroeder, 2012) and diagnosis (Lin *et al.*, 2012) of FELs has shifted from *overall* ΔE_e to *correlated* energy spread of longitudinal slices within a bunch profile, which can be smaller than ΔE_e. Sections III.B.4 and III.D.1.a discuss how the plasma accelerator community has met the diagnostic challenge of measuring slice energy spread of LWFA electron bunches.

2. Transverse emittance

Electron bunches that emerge from bubble-regime plasma accelerators have potentially outstanding properties for compact light sources and colliders: ultrasmall transverse ($\sigma_r \sim 0.3$ μm) and longitudinal ($\sigma_s \sim 1$ μm) size, which when combined with moderate charge ($Q \sim 0.3$ nC), could yield "condensed matter" charge density ($Q/e\sigma_r^2\sigma_s \sim 2\times 10^{22}$ cm^{-3}) and 100 kA peak currents. Here r (s) denotes transverse (longitudinal) beam coordinates. To be useful, however, LWFA bunches must be transported to the usage point without losing these outstanding properties. Conventional particle transport lines consisting of magnetic solenoids and quadrupoles were designed for beams with not only larger source size ($\sigma_r \sim 1$ mm, dictated by cathode size), but smaller divergence $\sigma_r' \ll 1$ mrad and energy spread $\Delta E_e/E_e = \Delta\gamma_e/\gamma_e < 10^{-3}$ than LWFA bunches, for which $\sigma_r' \gtrsim 1$ mrad and $\Delta\gamma_e/\gamma_e \gtrsim 10^{-2}$ are typical. The different σ_r' and $\Delta\gamma_e/\gamma_e$ originate from contrasting conditions under which LWFA and conventional bunches are "born" (Antici *et al.*, 2012). LWFA bunches form within focusing and accelerating fields of magnitude E_0 [see Eq. (4a)], which impart initial momenta $p_r(0) \sim p_s(0) \sim eE_0/\omega_p \sim m_e c \sim$ MeV$/c$ and uncorrelated energy spread ~MeV to the bunch electrons. Subsequent acceleration of a bunch to ~GeV energy over distance L yields $\sigma_r' \sim p_r(0)/p_s(L) \sim 10^{-3}$ rad at the accelerator exit as observed. Correlated energy spread also grows, due to the nonuniform accelerating field. In contrast, electrons emerge from conventional cathodes with momenta $p_r \sim p_s \sim$ eV$/c$. In ideal uniform extraction fields, subsequent acceleration of a collimated bunch to MeV$/c$ would yield $\sigma_r' \sim 10^{-3}$ mrad and $\Delta\gamma_e/\gamma_e \sim 10^{-6}$. Because of their larger σ_r', $\Delta\gamma_e/\gamma_e$, and initial energy, LWFA beams are poorly matched to conventional particle transport systems (Antici *et al.*, 2012). Innovative capture and transport methods are therefore needed to realize LWFA applications (Dornmair, Floettmann, and Maier, 2015; van Tilborg *et al.*, 2015; Steinke *et al.*, 2016; Xu *et al.*, 2016).

Here we focus on diagnostic challenges of *measuring* LWFA beam transport properties. Large σ_r' and $\Delta\gamma_e/\gamma_e$ render many conventional diagnostics unsuitable for LWFA beams (Cianchi *et al.*, 2013). Sections III.C.2 and III.C.3 describe new diagnostics researchers have developed in response to this challenge. Emittance ε is the area of transverse phase space (units mm mrad) occupied by a beam of particles, each with spatial and angular coordinates x and $x' = dx/ds = p_x/p_s = p_x/\beta\gamma_e m_e c$. Some express ε as the area of an ellipse in phase space, using units π mm mrad. Here we omit the factor π. Under conditions of the Liouville theorem, ε is motion invariant, like the wavelength of a laser beam in an optical transport system. Geometric rms emittance of a relativistic ($\beta \approx 1$) beam is defined by

$$\varepsilon^2 = \langle x^2\rangle\langle x'^2\rangle - \langle xx'\rangle^2, \tag{9}$$

where $\langle\,\rangle$ is an average over the particle ensemble. For a beam of given ε, local spread in particle position and trajectory slope is described by Twiss or Courant-Snyder beam envelope parameters (Lee, 2004)

$$\beta_T = \frac{\langle x^2\rangle}{\varepsilon}, \qquad \gamma_T = \frac{\langle x'^2\rangle}{\varepsilon}, \qquad \alpha_T = -\frac{\langle xx'\rangle}{\varepsilon}. \tag{10}$$

Beta function $\beta_T(s)$ describes the rate at which local beam size $\sigma_x(s) = \sqrt{\langle x^2(s)\rangle} = \sqrt{\beta_T(s)\varepsilon}$ changes along s in free space, analogous to the Rayleigh range of a laser beam. γ_T describes local divergence. α_T is the correlation between x and x'; $\alpha_T = 0$ at a beam waist.

Analysis of a collimated ($\alpha_T = 0$) electron bunch, which "matched" propagation in a fully blown out plasma channel can produce, illustrates use of Eqs. (10), and estimates $\sigma_x(L)$ of a bunch emerging from a strongly nonlinear LWFA. Transverse forces within the bubble confine the matched (subscript m) bunch to constant radius $\sigma_{x,m} = \sqrt{\beta_{T,m}\varepsilon}$, leading to beta function (Krall and Joyce, 1995; Reiser, 2008)

$$\beta_{T,m} = \frac{1}{k_\beta} = \frac{\sqrt{2\gamma_e}}{k_p} \tag{11a}$$

$$\approx 7\times 10^6\sqrt{\gamma_e/n_e[\mathrm{cm}^{-3}]}\ \mathrm{mm}, \tag{11b}$$

where k_β (k_p) denote betatron (plasma) wave numbers. From Eq. (11b), $\beta_{T,m} < 1$ mm for LWFAs, in contrast to > 1 m for confined conventional beams. Figure 4(a) shows matched $\sigma_{x,m} \sim 0.2$ μm and $\sigma_{x,m}' = \sigma_{x,m}/\beta_{T,m}$ for $\gamma_e = 500$ under conditions similar to those in which Weingartner *et al.* (2012) measured $\varepsilon = 0.5\times 10^{-9}$ m rad.

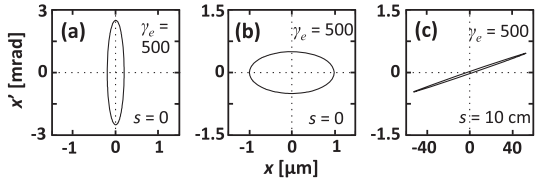

FIG. 4. Emittance evolution of LWFA beams for conditions similar to those of Weingartner *et al.* (2012). Calculated phase-space ellipses (a) at LWFA exit ($s = 0$) after matched propagation in LWFA, acceleration to $\gamma_e = 500$, and passage through steep plasma boundary that preserved phase-space ellipse; (b) the same, except after adiabatic emittance-preserving ($\varepsilon_n = 0.25$ mm mrad) transition at the plasma edge; (c) bunch from (b) after 10 cm of ideal propagation ($\sigma_{\gamma_e} = 0$).

Normalized emittance ε_n facilitates description of beams with relative energy spread $\sigma_{\gamma_e}^2 = (\langle\gamma_e^2\rangle - \langle\gamma_e\rangle^2)/\langle\gamma_e\rangle^2$ and enables a meaningful comparison of beams with different γ_e. Assuming $\beta = 1$, negligible space charge (Gruener *et al.*, 2007), and negligible correlation between transverse coordinates and energy, ε_n is

$$\varepsilon_n^2 = \langle x^2\rangle\langle\gamma_e^2 x'^2\rangle - \langle x\gamma_e x'\rangle^2. \tag{12a}$$

Antici *et al.* (2012) pointed out that for LWFA beams with large σ_r' and $\Delta\gamma_e/\gamma_e$, it is more meaningful to express Eq. (12a) in terms of $\sigma_{\gamma_e}^2$. It then becomes

$$\varepsilon_n^2 = \langle\gamma_e\rangle^2(\sigma_{\gamma_e}^2\sigma_x^2\sigma_x'^2 + \varepsilon^2) \tag{12b}$$

$$\approx\langle\gamma_e\rangle^2(\sigma_{\gamma_e}^2\sigma_x'^4 s^2 + \varepsilon^2), \tag{12c}$$

where Eq. (12c) holds far from the accelerator (large s), where $\sigma_x(s) \approx \sigma_x' s$. In Eq. (12b), the second term in parentheses is just Eq. (9). For beams with small σ_{γ_e} and σ_x', the first term is negligible, leaving the simple relationship $\varepsilon_n = \langle\gamma_e\rangle\varepsilon$ between ε_n and ε. For LWFA beams, on the other hand, the first term in Eq. (12b) dominates. This contribution is not motion invariant, but grows as the bunch propagates [see Eq. (12c)]. Thus in contrast to monoenergetic beams, for which ε_n is conserved, $\varepsilon_n(s)$ grows for LWFA beams (Cianchi *et al.*, 2013). In principle one could refocus the bunch, i.e., decrease s again in Eq. (12c), and reverse ε_n growth. However, conventional optics cannot refocus to the small $\beta_T(s \approx 0)$ typical of bunches exiting a LWFA. If the energy spread is strongly correlated, "slice" emittance at longitudinal position ζ within a bunch will grow via Eq. (12c) at a slower rate determined by local slice energy spread (Sec. III.B.4). These issues complicate measurement and interpretation of ε_n downstream of a LWFA.

An electron bunch's outcoupling from a LWFA influences its downstream propagation. Figure 4(a) shows the phase-space profile of a beam that exited the LWFA nonadiabatically through a steep density gradient, preserving its shape. In contrast, the profile in Fig. 4(b) results from exiting the LWFA adiabatically, with focusing strength changing slowly within a betatron wavelength. This conserves ε_n and rotates the ellipse to favor smaller σ_x' (Sears, Buck *et al.*, 2010; Weingartner *et al.*, 2012; Floettmann, 2014). Consequently this beam diverges more slowly. Figure 4(c) shows this beam's ellipse after 10 cm ideal ($\sigma_{\gamma_e} = 0$) free-space propagation, illustrating rapid conversion of angular spread into correlated divergence, necessitating careful matching of downstream acceleration stages (Dornmair, Floettmann, and Maier, 2015; Xu *et al.*, 2016). Nonzero σ_{γ_e} accelerates beam divergence in both cases.

3. Bunch duration

Bunch duration τ_b determines peak current, a critical parameter for LWFA-based FELs and colliders. No single prediction of the duration of bunches emerging from strongly nonlinear LWFAs exists. Different laser-plasma conditions can yield different τ_b, τ_b can change with propagation, and numerical instabilities can arise when simulating electron dynamics that vary strongly over ultrasmall space and time scales (Lehe *et al.*, 2013). Nevertheless, a few simulation studies have addressed the question of bunch duration near the exit of a nonlinear LWFA. Continuous injection into a continuously evolving bubble can lead to τ_b as long as half a plasma period (Kalmykov *et al.*, 2012). At the opposite extreme, F. Li *et al.* (2013) predicted that a broad ($w_0 \sim 20\lambda$), intense ($a_0 \sim 6$) laser pulse passing from a density up ramp to a density plateau can inject an electron sheet as short as tens of attoseconds into a subsequent wake. In between these extremes, simulations of colliding-pulse (Schroeder *et al.*, 1999; Fubiani *et al.*, 2004), down-ramp (Fubiani *et al.*, 2006), and ionization-induced (Li *et al.*, 2016) injection have predicted τ_b to be a small fraction of a plasma period, generally $1 \lesssim \tau_b \lesssim 5$ fs for the specified conditions. Section III.D reviews new diagnostic methods that researchers have developed over the past decade to measure τ_b in this range.

III. DIAGNOSTICS OF PLASMA-ACCELERATED ELECTRON BUNCHES

Unconventional methods have become necessary to diagnose the few-fs duration, initially sub-μm radius, kA-peak-current, mrad-divergence, few-percent energy spread LWFA electron bunches described in Sec. II.C, both within the accelerator and in the downstream world of applications. As an added challenge, when rapid feedback is needed, repetition rate is low, or shot-to-shot fluctuations are significant, single-shot diagnosis is essential.

This section reviews new beam diagnostics that have emerged to meet these challenges. Electromagnetic radiation from THz to γ rays that electron bunches emit both within the accelerator and at downstream instruments is central to many of these diagnostics. Thus, Sec. III.A reviews the theory of radiation from plasma-accelerated electrons. Therein we summarize short-wavelength Thomson, undulator (Sec. III.A.2), and betatron (Sec. III.A.3) radiation briefly for completeness, but refer the interested reader to Corde *et al.* (2013) for a more in-depth summary. On the other hand, we describe the theory of longer-wavelength transition radiation (TR) at greater length (Sec. III.A.4), because TR diffraction and spectroscopy are emerging as primary beam diagnostics for plasma accelerators. Moreover, other reviews of TR in this context are lacking. Subsequent sections review experimental

procedure and results for diagnosing bunch charge and energy distribution (Sec. III.B), transverse emittance (Sec. III.C), and bunch length (Sec. III.D).

Clayton (2009) reviewed the state of beam diagnostics for plasma-based accelerators approximately a decade ago. Here we emphasize developments since then. Li and Hogan (2011) and Green *et al.* (2017) reviewed the comprehensive suite of *e*-beam diagnostics used in PWFA experiments at FACET. Thus we do not review them here. We review plasma structure diagnostics at FACET in Sec. IV.D.3.

A. Radiation from plasma-accelerated electrons

Relativistic electrons that oscillate transversely emit forward Doppler-upshifted radiation into a relativistically contracted solid angle cone (width $\sim 1/\gamma_e$) in the laboratory frame (Esarey, Ride, and Sprangle, 1993; Ride, Esarey, and Baine, 1995; Corde *et al.*, 2013). Insertion devices with alternating magnetic dipoles (undulators or wigglers), counterpropagating electromagnetic radiation (Thomson backscatter), or focusing plasma wakefields (betatron radiation) provide the fields needed to stimulate such radiation.

1. Synchrotron radiation

The description of radiation from plasma-accelerated electrons begins naturally with synchrotron radiation (SR), which provides a foundation for describing all other classical radiation effects based on electron trajectories. Classical radiation is emitted when charges accelerate. The total power P that one relativistic electron of normalized velocity $\vec{\beta}$ [Lorentz factor $\gamma_e = (1-\beta^2)^{-1/2}$] radiates is given by the Lorentz-invariant Larmor formula

$$P = \frac{e^2 c}{6\pi\varepsilon_0}\left[\left(\frac{d(\gamma_e\vec{\beta})}{d\tau}\right)^2 - \frac{1}{c^2}\left(\frac{d\gamma_e}{d\tau}\right)^2\right], \tag{13}$$

where τ denotes Lorentz-invariant proper time. For a charge moving with constant β in a circle of radius ρ, as in a synchrotron, Eq. (13) becomes

$$P = \frac{e^2 c\gamma_e^2}{6\pi\varepsilon_0}\left(\frac{d(\gamma_e\vec{\beta})}{dt}\right)^2 = \frac{e^2 c\gamma_e^4}{6\pi\varepsilon_0\rho^2}. \tag{14}$$

Equation (14) displays the strong γ_e^4 electron energy scaling of SR explicitly. Any centripetal force yields an effective instantaneous radius ρ. For example, $\rho = m_e c\beta\gamma_e/eB$ in a constant magnetic field of magnitude B.

The far-field spectral intensity that one electron with acceleration $\dot{\vec{\beta}}$ radiates into solid angle $d\Omega$ in direction $\vec{n}$ is (Jackson, 1999)

$$\frac{d^2 I}{d\omega d\Omega} = \frac{e^2}{16\pi^3\varepsilon_0 c}\left\|\int_{-\infty}^{+\infty} f(\vec{n},\vec{\beta})e^{\imath\omega[t-\vec{n}\cdot\vec{r}(t)/c]}dt\right\|^2, \tag{15}$$

where $f(\vec{n},\vec{\beta}) \equiv \vec{n}\times[(\vec{n}-\vec{\beta})\times\dot{\vec{\beta}}]/(1-\vec{\beta}\cdot\vec{n})^2$. The far-field approximation is valid for interaction volumes with dimensions much smaller than the distance to the observer. Integrating Eq. (15) over all angles and one revolution yields spectral power

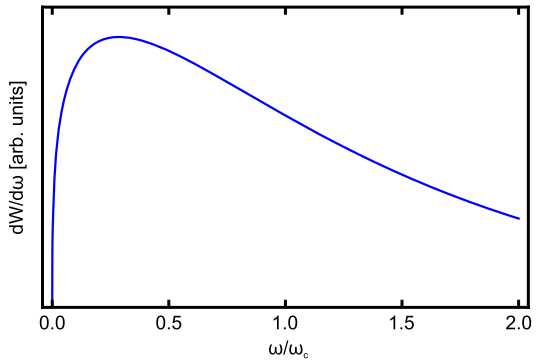

FIG. 5. Spectral power of synchrotron radiation (SR), given by Eq. (16).

$$\frac{dW_{\rm SR}}{d\omega} = \sqrt{3}\frac{e^2}{4\pi\varepsilon_0 c}\gamma_e\frac{\omega}{\omega_c}\int_{\omega/\omega_c}^{+\infty} d\xi K_{5/3}(\xi), \tag{16}$$

plotted in Fig. 5. K_ν is a modified Bessel function of the second kind, and

$$\omega_c = 3c\gamma_e^3/2\rho \tag{17}$$

is the *critical frequency*. Intuitively, ω_c is related to the reciprocal of the duration $\Delta t = 2/\omega_c$ of a single ultrashort "lighthouse" burst of radiation, with corresponding broadband spectrum (Fig. 5), that a fixed distant observer in the orbital plane sees from the circulating electron. Formally, ω_c is the median frequency of SR spectral intensity that this observer sees, i.e., half the total energy is emitted above, half below ω_c (Jackson, 1999; Onuki and Elleaume, 2002; Clarke, 2004). The angular energy distribution observed at angle θ from the particle's orbital plane is

$$\frac{dW_{\rm SR}}{d\Omega} = \frac{7e^2}{96\pi\varepsilon_0 c}\frac{\omega_c\gamma_e^2}{(1+\gamma_e^2\theta^2)^{5/2}}\left(1+\frac{5}{7}\frac{\gamma_e^2\theta^2}{1+\gamma_e^2\theta^2}\right). \tag{18}$$

Each electron emits light in a directional $1/\gamma_e$ angle cone centered on its instantaneous velocity, polarized predominantly in the plane of its orbit (power ratio $P_\parallel/P_\perp = 7$). Relativistic electrons generally emit x rays. Since the 0.1–1 μm dimension of plasma-accelerated electron *bunches* exceeds an x-ray wavelength, x-ray SR from such bunches is spatially and temporally incoherent.

2. Undulator and Thomson backscatter radiation

From Eq. (15), $f(\vec{n},\vec{\beta})$ (and thus $d^2I/d\omega d\Omega$) is maximized when the denominator $(1-\vec{\beta}\cdot\vec{n})^2$ is minimized, i.e., when $\beta\approx 1$ and $\vec{\beta}\|\vec{n}$, and when the numerator $(\vec{n}-\vec{\beta})\times\dot{\vec{\beta}}$ is maximized, i.e., when $\dot{\vec{\beta}}\perp\vec{n}$. These two conditions are realized for an observer along the axis of a wiggler or undulator, in which periodic external fields perturb relativistic ($\beta\approx 1$) electrons propagating toward the observer ($\beta\|\vec{n}$) transversely ($\dot{\vec{\beta}}\perp\vec{n}$). Onuki and Elleaume (2002)+ and Clarke (2004) reviewed the principles behind, and characteristics of, wiggler

and undulator radiation. Here we summarize the main points required for subsequent discussion.

When electrons pass through N_u periods of alternating magnetic fields (strength B_0, period λ_u), they bend into a sinusoidal trajectory with maximum deflection angle $\phi_e = K/\gamma_e$, where

$$K = e\lambda_u B_0/(2\pi m_e c) \approx 0.93\lambda_u[\mathrm{cm}]B_0[\mathrm{T}] \tag{19}$$

is the normalized undulator parameter. K is the ratio of the deflection angle ϕ_e to the emission cone angle γ_e^{-1}, and distinguishes wiggler ($K > 1$) from undulator ($K < 1$) modes. Here we focus on the latter, for which emission cones of consecutive oscillations of one electron overlap, and thus superpose coherently.

Locally, a portion of this electron's trajectory within one undulator period can be approximated by a portion of a circle of radius ρ. Equations (14)–(18) and Fig. 5 then describe the properties of this single radiation burst. Repetition over N_u periods sends to a distant observer a train of Doppler-shifted bursts separated by time $\Delta t_u(\lambda_u, \theta, \beta)$ determined by the Lorentz-contracted λ_u, the observer's angle θ from the electron beam axis, and β. These bursts interfere in the frequency domain, modulating the broadband SR spectrum (Fig. 5) at spectral period $\omega_u = 2\pi/\Delta t_u$, provided $\omega_u < \omega_c$. When the latter condition is realized (generally for $K \to 1$), the observer sees radiation at a fundamental frequency $\omega_u(\lambda_u, \theta, \beta)$ and its harmonics $n\omega_u$ $(n = 1, 2, 3, \ldots)$, each with bandwidth $\Delta\omega_u/\omega_u = 1/N_u$, as in Fig. 6(c). This is analogous to the train of high-order harmonics observed from atoms excited near the ionization threshold by a multicycle laser pulse (Protopapas, Keitel, and Knight, 1997). When $\omega_u > \omega_c$ (generally for $K \ll 1$), the observer sees only a single spectral peak at $\omega_u(\lambda_u, \theta, \beta)$, as in Fig. 6(a). The detected frequencies are (Onuki and Elleaume, 2002; Clarke, 2004; Corde *et al.*, 2013)

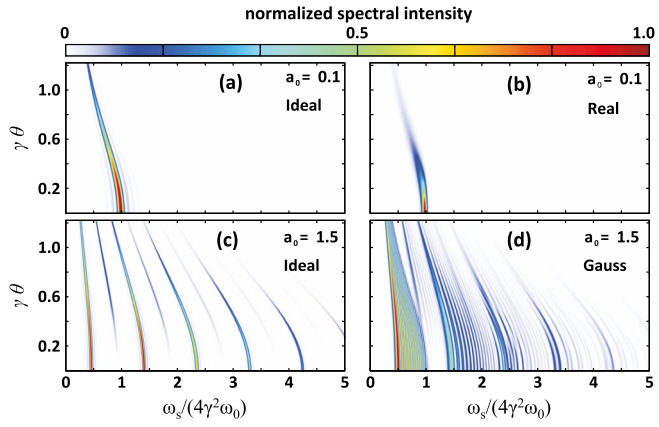

FIG. 6. Calculated Thomson scatter spectra for head-on electron-photon collision vs observation angle $\gamma\theta$ in the bending plane. Top row: Plane-wave excitation at $a_0 = 0.1$ for (a) monoenergetic and (b) realistic electron energy distribution, showing emission of $n = 1$ peak. Bottom row: Excitation of monoenergetic electrons at $a_0 = 1.5$ for (c) plane wave and (d) temporally Gaussian pulse, showing emission of several harmonics. The color scale is normalized to the maximum value for each plot. Adapted from Debus *et al.*, 2009.

$$\omega_{\mathrm{sc}} = \frac{2\gamma_e^2}{1 + K^2/2 + \gamma_e^2\theta^2} n\omega_u, \tag{20}$$

where the term $K^2/2$ takes into account the reduction of longitudinal electron velocity caused by transverse quiver motion. The frequency upshift (20) is the combined result of Lorentz contraction of λ_u seen by the electron and Doppler shift of the electron's oscillation frequency viewed in the lab frame. Emission from an electron bunch of dimensions greater than a radiated wavelength is incoherent, although pinhole spatial filtering, when possible, can recover spatial coherence (Attwood *et al.*, 1999).

In the past decade, researchers have studied undulator radiation from LWFA electrons at visible (Schlenvoigt *et al.*, 2008; Gallacher *et al.*, 2009), UV (Lambert *et al.*, 2012), and XUV (Fuchs *et al.*, 2009; Shaw *et al.*, 2012; Anania *et al.*, 2014) wavelengths. Compact, short-period undulators custom designed for LWFAs have emerged (Eichner *et al.*, 2007). This radiation underlies single-shot, nonintercepting diagnostics of LWFA bunch energy and energy spread (Sec. III.B.3) and transverse emittance (Sec. III.C.3). Moreover, these results are widely viewed as first steps toward a LWFA-driven x-ray FEL (XFEL) (Gruener *et al.*, 2007; Nakajima, 2008). Achieving gain, however, will require beams with ε_n and slice energy spread that challenge current LWFA capabilities (Maier *et al.*, 2012; Seggebrock *et al.*, 2013). This highlights the need for improved diagnostics and control of these quantities.

The oscillating electric field of a linearly polarized laser field (frequency ω_0, field strength a_0) that "collides" with electrons can serve as an optical undulator of period $\lambda_u \sim 1$ μm. Undulator radiation from one electron, now known as Thomson backscatter, is emitted at frequencies (Brown and Kibble, 1964; Bardsley, Penetrante, and Mittleman, 1989; Esarey, Ride, and Sprangle, 1993)

$$\omega_{\mathrm{sc}} = \frac{2\gamma_e^2(1 - \cos\varphi_{\mathrm{coll}})}{1 + a_0^2/2 + \gamma_e^2\theta^2} n\omega_0, \tag{21}$$

equivalent to Eq. (20), with a_0 playing the role of K, and ω_0 the role of ω_u. Here φ_{coll} is the collision angle. For head-on collisions ($\varphi_{\mathrm{coll}} = 180°$), exact backscatter ($\theta = 0$), and $a_0 \ll 1$, Eq. (21) reduces to $\omega_{\mathrm{sc}} \approx 4\gamma_e^2\omega_0$. Thus Thomson backscatter of near-infrared ($\hbar\omega_0 \approx 1$ eV) light from $\gamma_e \gtrsim 500$ electrons, a range available from LWFAs, provides tunable, directional MeV photons. For $\varphi_{\mathrm{coll}} = 180°$, Eq. (21) differs from Eq. (20) by a factor of 2, since two Doppler shifts are involved instead of one. Figure 6 shows calculated θ-dependent Thomson spectra for $\varphi_{\mathrm{coll}} = 180°$ that illustrate Eq. (21) for various cases. Figures 6(a) and 6(c) show spectra for idealized plane-wave scatter from monoenergetic electrons at (a) $a_0 \ll 1$ or (c) $a_0 \sim 1$. The plane wave is analogous to a long magnetic undulator with (a) $K \ll 1$ or (c) $K \sim 1$ with many identical units that enforce constant oscillation amplitude, yielding narrow (a) single or (c) multiple harmonics. Figure 6(b) shows the slightly broadened spectra for plane-wave Thomson scatter (at $a_0 < 1$) from polyenergetic electrons. Figure 6(d) shows drastic redshift and smearing of the multiharmonic spectrum for a few-cycle spatially and

temporally Gaussian pulse ($a_0 \sim 1$) scattering from monoenergetic electrons (Debus *et al.*, 2009).

The upper limit of total photon yield from linear ($a_0 \ll 1$, thus $n = 1$) Thomson scatter is (Esarey, Ride, and Sprangle, 1993)

$$N_{\rm sc} = 2\pi\alpha_f N_u N_e a_0^2 (\Delta\omega_{\rm sc}/\omega_{\rm sc}), \tag{22}$$

where $\alpha_f = 1/137$ is the fine-structure constant, N_u is the number of laser oscillations, and N_e is the number of electrons in the overlap region. The actual yield can be much smaller for nonideal beams and laser pulses (Debus *et al.*, 2009; Rykovanov *et al.*, 2014). Hartemann *et al.* (2005) calculated that peak brightness of Thomson backscatter of a laser pulse ($N_{h\nu}$ overlapping photons) colliding head on with an electron bunch of normalized emittance ε_n, duration τ_b scales as $\gamma_e^2 N_e N_{h\nu}/\varepsilon_n^2 \tau_b$. The small ε_n, τ_b bunches available from LWFAs are thus advantageous for high Thomson backscatter yield. Explicit calculations (Hartemann *et al.*, 2007) for backscatter of a laser pulse (21 fs, $\hbar\omega_0 = 1.5$ eV, $a_0 \approx 0.3$) from a LWFA electron bunch ($N_e \approx 3 \times 10^9$, $\gamma_e = 340$, $\varepsilon_n \approx 4$ mm mrad) predicted $\sim 10^7$ Thomson photons at $\hbar\omega_{\rm sc} = 0.7$ MeV, comparable to the limit (22) for these conditions. Debus, Bussmann *et al.* (2010) suggested that Thomson yields $N_{\rm sc} \sim 10^{10}$ are achievable with a similar LWFA using a laser pulse with tilted front in a side-scatter geometry, which enables a longer laser-electron interaction length (i.e., higher N_u) than a head-on, backscatter geometry.

In the past decade, starting with Schwoerer *et al.* (2006), researchers have developed many LWFA-based Thomson x-ray sources, most using the near-head-on, backscatter geometry. Umstadter (2015) reviewed developments through 2015. Developments since 2015 include linear ($a_0 < 1$) backscatter from GeV electrons, resulting in γ-ray photons up to $\hbar\omega_{\rm sc} \approx 85$ MeV (Shaw *et al.*, 2017), and nonlinear ($a_0 > 1$) backscatter from sub-GeV electrons, resulting in high-energy tails up to ~20 MeV (Yan *et al.*, 2017). As with undulator radiation, Thomson backscatter underlies diagnostics of LWFA bunch energy and energy spread (Sec. III.B.3) and transverse emittance (Sec. III.C.3).

3. Betatron radiation

Esarey *et al.* (2002), Wang *et al.* (2002), and Kostyukov, Kiselev, and Pukhov (2003) predicted that electrons accelerating in plasma wakes would emit betatron radiation when they undulate transversely in response to the wake's radial field E_r [see Fig. 7(a)]. The ion cavity can act as either an undulator or wiggler, depending on how far from the axis electrons are injected. Soon thereafter, Rousse *et al.* (2004) observed betatron radiation in the laboratory. Since then betatron radiation has become a versatile ultrashort broadband x-ray source (Ta Phuoc *et al.*, 2006; Albert *et al.*, 2008, 2013; Kneip *et al.*, 2008, 2010; Schnell *et al.*, 2013) as well as an important electron diagnostic (see Sec. III.C.2). Corde *et al.* (2013) reviewed betatron (and other x-ray) radiation from plasma accelerators comprehensively and introduced its basic physics based on original work by Esarey *et al.* (2002), Kostyukov, Kiselev, and Pukhov (2003), and Thomas (2010).

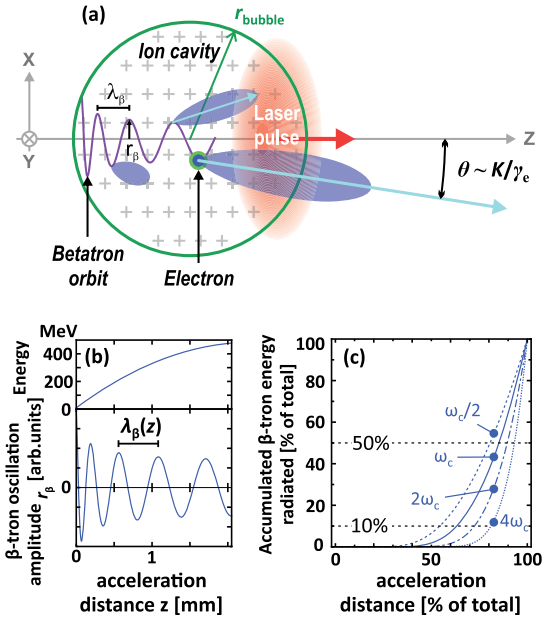

FIG. 7. Properties of betatron motion and radiation. (a) Schematic of betatron radiation from relativistic electrons oscillating in the electron-depleted LWFA cavity with uniform ion background. (b) Electron acceleration (top) and typical electron trajectory (bottom) within an LWFA cavity. As the electron accelerates, the betatron wavelength λ_β increases, and the betatron oscillation amplitude r_β decreases. (c) Percentage of accumulated spectral energy radiated for selected frequencies with respect to the acceleration length, assuming linear acceleration and uniformly distributed turning points.

Here we focus on properties of betatron radiation required for diagnostics.

As for wigglers, one can assign betatron oscillations a period $\lambda_\beta = 2\pi/k_\beta \simeq 2\pi\sqrt{2\gamma_e}/k_p = \lambda_p\sqrt{2\gamma_e}$, where γ_e is averaged over an oscillation and k_p (λ_p) is the plasma wave number (wavelength). Thus, for example, in an accelerator producing $\gamma_e = 200$ electrons in $\bar{n}_e = 10^{19}$ cm^{-3} plasma ($\lambda_p = 10$ μm), we get $\lambda_\beta \approx 200$ μm. We can also assign oscillation amplitude r_β, which injection dynamics determine. The product of γ_e, k_β, and r_β defines the dimensionless plasma wiggler parameter

$$K = \gamma_e k_\beta r_\beta = 1.33 \times 10^{-10}\sqrt{\gamma_e n_e[{\rm cm}^{-3}]}\, r_\beta[\mu{\rm m}]. \tag{23}$$

For the $\gamma_e = 200$, $\lambda_p = 10$ μm accelerator with $r_\beta = 1$ μm, we get $K = 2\pi$. Oscillations with $K \gg 1$ and constant γ_e radiate a quasicontinuous broadband spectrum (Esarey *et al.*, 2002)

$$\frac{dW_\beta}{d\omega} \simeq 2N_\beta \frac{dW_{\rm SR}}{d\omega}, \tag{24}$$

$$\frac{dW_\beta}{d\Omega} \simeq 2N_\beta \frac{dW_{\rm SR}}{d\Omega} \tag{25}$$

as for SR [see Eqs. (16) and (18)], where N_β is the number of oscillation periods. For betatron radiation, θ in Eq. (18) is the angle between the mean electron direction and $\vec{n}$. Half the

energy is radiated below (or above) the critical frequency, which can now be expressed in terms of K:

$$\omega_c = 3K\gamma_e^2(2\pi c/\lambda_\beta). \tag{26}$$

For the above example, $\hbar\omega_c \approx 4.7$ keV. From Eq. (25) and Fig. 7, betatron radiation is emitted within a cone of half-angle $\theta_{1/2} = K/\gamma_e$ ($= \pi/100$ for the above example).

Electron energy loss per unit distance is

$$W_\beta^{(\mathrm{loss})} = \frac{e^2}{48\pi\varepsilon_0}\gamma_e^2 k_p^4 r_\beta^2 \simeq 1.5\times 10^{-45}(\gamma_e n_e[\mathrm{cm}^{-3}] r_\beta[\mu m])^2 \ \frac{\mathrm{MeV}}{\mathrm{cm}}. \tag{27}$$

$W_\beta^{(\mathrm{loss})} \approx 0.006$ MeV/cm for the example of $\gamma_e = 200$, $n_e = 10^{19}$ cm^{-3}. Thus one electron emits on average

$$\langle N_{\omega_c}\rangle = \frac{2\pi}{9}\frac{e^2}{\hbar c(4\pi\varepsilon_0)} N_\beta K \simeq 5.6\times 10^{-3} N_\beta K \tag{28}$$

photons of mean energy $\hbar\omega_c$ over N_β oscillation periods. For our example, each electron emits $\langle N_{\omega_c}\rangle/N_\beta \approx 10^{-3}$ photons per oscillation. Thus a 100 pC bunch emits $\sim 10^7$ photons per oscillation.

Betatron radiation *differs* from wiggler radiation in that radiating electrons simultaneously *accelerate* longitudinally. Thus γ_e increases along the acceleration path, which implies $\lambda_\beta \propto \gamma_e^{1/2}$ [see Fig. 7(b)]. Moreover, it can be shown (Corde *et al.*, 2013) that $r_\beta \propto \gamma_e^{-1/4}$ [see again Fig. 7(b)], implying $K \propto \gamma_e^{1/4}$ [via Eq. (23)], and $\omega_c \propto \gamma_e^{7/4}$ [via Eq. (26)]. Because of these scalings, the conceptually simple spectrum consisting of a fundamental frequency ω_c and discrete harmonics of order $N_c \simeq 3K^2/4$ (Corde *et al.*, 2013) smears into a broad continuum. In addition, betatron power increases nonlinearly with γ_e [see Eqs. (18) and (25)]. Thus most radiation, especially frequencies beyond ω_c, is emitted at the highest γ_e, near the end of the accelerator [see Fig. 7(c)]. The source can be further localized longitudinally for electron bunches undergoing collective, high K oscillation, for which radiation is generated mostly at extrema of the electron trajectory [see Fig. 7(a)]. If N_β is small, most betatron radiation can be generated at the final extremum, within the time scale of an electron bunch duration.

Variations in K and γ_e during acceleration also render betatron radiation of even a single electron temporally incoherent. Betatron radiation from electron bunches is both temporally and spatially incoherent. This is because a typical critical energy $\hbar\omega_c \approx 10$ keV corresponds to $\lambda \approx 1.24$ Å, much smaller than the spatial extent of a μm-scale LWFA electron bunch. Nevertheless, Shah *et al.* (2006) and Kneip *et al.* (2010) observed interference fringes in the shadow of an atomically sharp knife edge inserted into a bright betatron beam at distance l from the source. The knife edge selected radiation from a small angle range $\theta \ll K/\gamma_e$. The limiting condition $L_{\mathrm{trans}}\Delta k = 1$ then yielded a transverse coherence length $L_{\mathrm{trans}} \approx \lambda l/4\pi\sigma_r$. Such transverse coherence properties provide one diagnostic of σ_r via betatron radiation. The betatron spectrum provides another (see Sec. III.C.2). A simpler measurement of the penumbra of a mask (Schnell *et al.*, 2013) can set an upper limit on σ_r. Litos and Corde (2012) proposed that observations of the profile and spectrum of betatron radiation emitted by a PWFA drive bunch could diagnose its proximity to matched beam propagation.

4. Transition radiation

Transition radiation is emitted when a relativistic electron passes suddenly from one medium into another with a different refractive index (Ginzburg and Frank, 1946; Frank, 1966; Ter-Mikaelian, 1972; Ginzburg and Tsytovich, 1979). Within a material, the transiting electron repels surrounding electrons, exciting time-varying radial currents [in metals, Fig. 8(a)] or polarization waves (in dielectrics) that radiate. However, in the bulk, as long as the phase velocity of the radiation differs from the velocity of the relativistic electron, i.e., there is no Čerenkov radiation, various contributions to the radiation field interfere destructively on volume average. For every plane wave excited at one position there is another with opposite phase. Bulk absorption can also suppress residual radiation when cancellation is incomplete. However, an interface or free surface breaks volume symmetry, enabling net radiation. Moreover, net radiation into vacuum is not absorbed. In contrast to synchrotron, Compton, and betatron radiation, here the *medium*, rather than the relativistic electron, radiates.

Several researchers have derived rigorous expressions for TR from Maxwell's macroscopic equations (Pafomov, 1971; Ter-Mikaelian, 1972; Schroeder *et al.*, 2004; Sütterlin *et al.*, 2007). Here one applies Maxwell's interface conditions $\vec{n}_{12}\times(\vec{E}_2 - \vec{E}_1) = 0$ and $(\vec{D}_2 - \vec{D}_1)\cdot\vec{n}_{12} = \rho_s$ to the Coulomb field of a relativistic electron passing though an interface of given geometry, then identifies the radiating part of the field. Alternatively, the image charge (or "annihilation radiation") picture [see Fig. 8(b)] describes TR microscopically and intuitively (Ter-Mikaelian, 1972; Carron, 2000; Bolotovskii and Serov, 2009). As a relativistic electron propagating inside a conductor reaches the surface at time

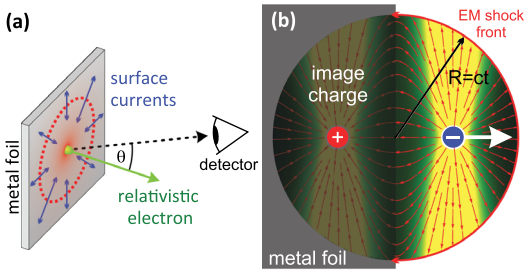

FIG. 8. Transition radiation (TR). (a) Relativistic electron bunch passing through metal foil induces transient surface currents that radiate radially polarized light. (b) Electric field lines (thin red arrows) emanating from relativistic electron (blue circle enclosing the "−" sign) emerging from the conductor, and converging upon its image charge (red circle enclosing the "+" sign) inside the conductor. The electron's previously shielded field expands at c as it emerges from the conductor. The electromagnetic shock front (solid red arc) that terminates this expanding field, and bends field lines back to the surface, is the source of TR.

$t = 0$, its previously shielded Coulomb field expands into vacuum at the speed of light, and combines with the field of its image charge receding into the metal. At time t, this field vanishes beyond an expanding sphere of radius ct centered where the electron emerges from the metal. Since electric field lines terminate only at charges, field lines at this electromagnetic shock front bend back to the conductor surface. This shock front, which for an ideal conductor with an infinite planar surface is infinitesimally thin, is the source of broadband TR.

a. TR from one electron

The angular (Ω) distribution of TR spectral power $dW_e/d\omega$ from a single electron (e) transiting the steplike surface of an ideal, semi-infinite conductor at normal incidence provides a foundation for describing many basic observable characteristics of TR. It is given by the Ginzburg-Frank formula (Ter-Mikaelian, 1972; Schroeder *et al.*, 2004)

$$\frac{d^2W_e}{d\omega d\Omega} = \frac{r_e m_e c}{\pi^2}\frac{\beta^2 \sin^2\theta}{(1-\beta^2\cos^2\theta)^2}, \tag{29}$$

where $r_e = e^2/(4\pi\varepsilon_0 m_e c^2)$ is the classical electron radius and θ is the angle between the observation direction and the electron propagation direction [see Fig. 8(a)]. The spectral power distribution (29) vanishes on axis ($\theta = 0$), and for highly relativistic ($\gamma_e \gg 1$) electrons, peaks at $\theta \simeq 1/\gamma_e$, and falls off rapidly at larger θ [see Fig. 9(a)]. The angular width of this cone is thus a signature of electron energy. The power distribution is axially symmetric, and the TR field is linearly polarized within a plane defined by the electron trajectory and the observation direction. Thus the entire TR beam can be described as radially polarized, consistent with it vanishing on axis. A lens centered on the electron propagation axis focuses the TR cone to a radially polarized, "donut"-shaped intensity profile [see Fig. 9(b)] with FWHM $\simeq \sqrt{2}\lambda$ (Artru, Chehab *et al.*, 1998; Castellano and Verzilov, 1998). Integrating Eq. (29) over Ω for $\gamma_e \gg 1$ yields single-electron TR spectral power

$$\frac{dW_e}{d\omega} = (2r_e m_e c/\pi)\ln(\gamma_e), \tag{30}$$

which depends only weakly on γ_e. A relativistic electron generates backward (reflected) and forward (transmitted) TR cones, respectively, upon entering and exiting a foil [see Fig. 9(c)].

Equations (29) and (30) are frequency independent, a consequence of the assumption of a semi-infinite, perfectly conducting planar foil. In reality, radiator size and conductivity $\sigma(\omega)$ are finite, and $\sigma(\omega)$ and foil relative permittivity $\varepsilon(\omega)$ depend on frequency. These factors lead to a frequency-dependent TR power spectrum, including low- and high-frequency cutoffs. The effect of finite radiator size stems from the expansion of the electron's relativistic Coulomb field envelope at angle $\sim 1/\gamma_e$ in the plane perpendicular to its propagation direction [see Fig. 9(d)]. As a result, the passing electron perturbs metal electrons at distance ρ from its path over longitudinally extent $\sim\rho/\gamma_e$, which in turn determines the TR wavelength. Thus TR of wavelength λ originates at characteristic distance $\sim\lambda\gamma_e$ from the electron's path. A small radiator thus emits less energy at long wavelengths and diffracts these wavelengths more. Both effects combine to create a low-frequency cutoff of the TR spectrum. Conversely, the critical cut-off frequency $\omega_{\rm crit} = \gamma_e\omega_p$ of the foil sets a *high*-frequency limit on TR. Above $\omega_{\rm crit}$, both metals and dielectrics become transparent. Consequently the discontinuity in index of refraction that underlies TR disappears, and the spectral power $dW_{\rm TR}/d\omega$ drops as rapidly as ω^{-4} (Dolgoshein, 1993). For Al, $\hbar\omega_p = 32.8$ eV. Generally, $\omega_{\rm crit}$ lies in the extreme ultraviolet (EUV) to soft x-ray range for solid foils. Schroeder *et al.* (2004), however, observed much lower $\omega_{\rm crit}$ for low-energy electrons passing through an underdense plasma-vacuum interface.

Practical e-beam diagnostics often use foils that are tilted, thin, or rough, introducing additional TR characteristics beyond Eqs. (29) and (30). A foil with surface normal oriented *obliquely* to the electron's path generates a backward TR cone centered on the specular "backreflected" direction [see Fig. 10(a)]. The forward "transmitted" TR cone is still centered

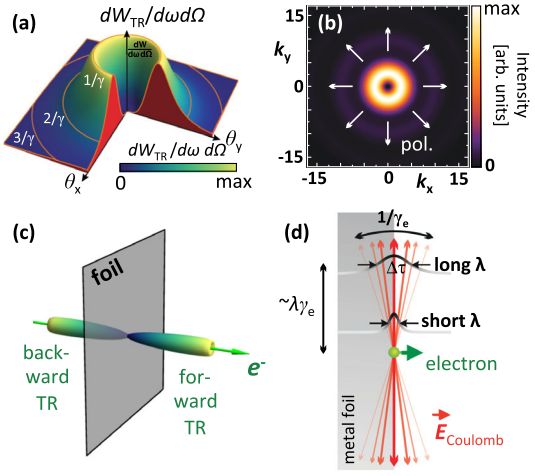

FIG. 9. Properties of TR for relativistic electron incident normally on foil. Angular distribution of power: (a) far from the source; (b) imaged to focus, for arbitrary wavelength λ, $k_{x,y}$ in units of λ^{-1}, white arrows show radial polarization; (c) backward (left) and forward (right) TR emission. (d) Envelope of Lorentz-contracted Coulomb field (fan of near-vertical red arrows) expands laterally at angle $\sim 1/\gamma$, creating an electromagnetic disturbance of longitudinal extent λ at transverse distance $\sim\lambda\gamma$. Thus shorter TR wavelengths are emitted closer to the electron.

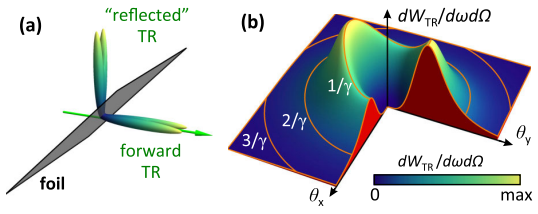

FIG. 10. Angular distribution of TR power for relativistic electrons incident at 45° on foil: (a) "reflected" and forward TR cones, and (b) far-field distribution of one cone, showing a break in azimuthal symmetry.

around the electron propagation direction. Rotational symmetry of both cones is broken [see Fig. 10(b)]. In addition, a TR radiator must be thicker than the *formation length* $L_f = \beta c/\omega|1-\beta\sqrt{\varepsilon}\cos\theta|$ (Ter-Mikaelian, 1972; Dolgoshein, 1993; Carron, 2000) over which TR (observed at angle θ from the electron's trajectory) accumulates. Physically, this is the distance over which the Coulomb field of the relativistic electron and the emitted TR drift by one wavelength from one another. TR is greatly diminished for media thinner than L_f. In a transparent medium, such as underdense plasma, L_f can be ~100 μm. In metals, $\varepsilon \simeq i\sigma/\varepsilon_0\omega$ is imaginary, and L_f reduces to $\simeq\delta/\sqrt{2}\cos\theta$, where the skin depth $\delta = \sqrt{2/\omega\mu_0\sigma}$ is typically in the nm range. Thus silver-coated Kapton foils can be a good flat TR source.

A related quantity is the *vacuum formation length* $L_{f,0}$, which defines a coherence length over which TR fields from two or more spatially separated sources interfere. For example, when forward TR from one foil reflects from a second tilted foil, separated by distance $L_{\rm sep} < L_{f,0}$, in which the same e bunch generates backreflected TR, the two TR *fields* (not intensities) add coherently. Diagnostics based on the Wartski interferometer (Wartski *et al.*, 1975; Fiorito and Rule, 1994; Fiorito *et al.*, 2006) and TR radiators using multiple interfaces (Artru, Yodh, and Mennessier, 1975; Dolgoshein, 1993) exploit this effect experimentally. It can also impact the resolution of imaged TR (Artru, Castellano *et al.*, 1998; Artru, Chehab *et al.*, 1998). In the frequency domain this can lead to intensity modulations, whose frequency width $\Delta\omega = \omega_2 - \omega_1$ is defined by $L_{\rm sep}$. For some natural number l, $L_{\rm sep} = lL_{f,0}(\omega_1)$ for the lower frequency and $(l+1)L_{f,0}(\omega_2)$ for the higher frequency. As a numerical example, $L_{f,0} = \gamma_e^2 c/\omega$ for $\varepsilon = 1$ and $\theta = 0$ and equals ~1 cm for TR of wavelength $\lambda \approx 1$ μm generated by 100 MeV electrons. Generally $L_{f,0}$ greatly exceeds the rms *height* ($\sigma_{\rm rms}$) of surface roughness features. Nevertheless roughness can impact TR significantly if surface variations exceed λ within a characteristic disc of radius $\gamma_e\lambda$. In this case, various, sometimes conflicting, effects of roughness on TR have been reported: increased flux due to increased surface area; decreased flux due to transverse shielding, which can also lead to depolarization and disappearance of the central intensity minimum; and a speckled intensity pattern (Arutyunyan *et al.*, 1979; Baghiyan, 2001, 2004; Reiche and Rosenzweig, 2001). Roughness affects forward and backward TR in the same way.

b. TR from electron bunches

TR is a useful diagnostic to the extent that it can reveal internal structure of relativistic electron *bunches* containing N_e electrons. To describe TR from a bunch, one must superpose the TR fields of the individual electrons. At wavelengths λ much longer than longitudinal (σ_z) and transverse (σ_r) bunch dimensions, these fields differ negligibly in phase, and add coherently. The spectral energy

$$\frac{d^2W_{\rm CTR}}{d\omega d\Omega} = N_e^2\frac{d^2W_{\rm e}}{d\omega d\Omega} \tag{31a}$$

of such *coherent* transition radiation (CTR) scales with N_e^2. On the other side, at wavelengths much smaller than the bunch dimensions, the TR fields of different electrons differ by $\geq 2\pi$ in phase, and thus add incoherently. The spectral energy

$$\frac{d^2W_{\rm ITR}}{d\omega d\Omega} = N_e\cdot\frac{d^2W_{\rm e}}{d\omega d\Omega} \tag{31b}$$

of such *incoherent* transition radiation (ITR) scales linearly with N_e. Longitudinal and transverse coherence influence TR in different ways. For $\lambda \gg \sigma_z$, forward TR is fully coherent, and thus $\sim N_e\times$ stronger than for $\lambda \ll \sigma_z$. The result is a high-frequency cutoff in the bunch TR spectrum that has no counterpart in single-electron TR theory. Similarly, the bunch radius σ_r governs transverse coherence. Transverse coherence is maintained for $\sigma_r \ll \gamma_e\lambda$ for a collimated bunch, or $\sigma_r \ll \lambda/\Delta\psi$ for a bunch with divergence $\Delta\psi \ll 1$. For this reason CTR foils often are placed close to LWFAs, before their beams diverge to larger radii.

Microbunching or complex longitudinal bunch profiles complicate the CTR spectrum. A train of two or more bunches separated by delay $\Delta t > \sigma_z/c$ create a corresponding train of TR bursts. The power spectrum of the train is intensity modulated with period $2\pi/c\Delta t$ in the frequency domain. The spectrum of a complex microbunched format with multiple Δt contains multiple modulation periods and is not easily distinguished from a single bunch with complex internal structure.

The total energy loss $W_{\rm tot}$ of an electron bunch to CTR can be estimated by integrating Eq. (30) over all frequencies and multiplying by N_e^2. For an electron incident normally on a TR foil, and for $W_{\rm tot}$ much less than total bunch kinetic energy $N_e(\gamma-1)m_ec^2$, the result is (Schroeder *et al.*, 2004)

$$W_{\rm tot} \simeq (4r_em_ec^2)N_e^2\ln(\gamma_e)/\lambda_{\rm min} \tag{32a}$$

$$\simeq 3.6\times10^{-2}(Q[{\rm nC}])^2\ln(\gamma_e)/\lambda_{\rm min}[\mu{\rm m}], \tag{32b}$$

where Q denotes bunch charge. This energy loss criterion determines limits on maximum Q, radiated bandwidth, and time resolution for diagnostics based on CTR.

Weak ITR at short λ is useful for calibrating degree of coherence at longer λ, and for testing detector dynamic range. Collimated ITR from small sources can reveal spatial bunch characteristics through statistical analysis of intensity noise in its spectrum (Sannibale *et al.*, 2009).

The ideal conductor approximation usually suffices for modeling TR from realistic electron bunches quantitatively (Schroeder *et al.*, 2004; van Tilborg *et al.*, 2004; Casalbuoni *et al.*, 2005, 2008; Casalbuoni, Schmidt, and Schmuser, 2005). The most general expression for TR from a bunch of N_e electrons transiting an infinitely wide ideal conductor surface is an integral over individual electron contributions:

$$\frac{d^2W_{\rm OTR}}{d\omega d\Omega} = \frac{e^2N_e}{(4\pi\varepsilon_0)\pi^2c}\left\{\left[\int d^3\vec{p}\,g(\mathcal{E}_\parallel^2+\mathcal{E}_\perp^2)\right]_{\rm ITR} + N_e'\left[\left|\int d^3\vec{p}\,g\mathcal{E}_\parallel F\right|^2+\left|\int d^3\vec{p}\,g\mathcal{E}_\perp F\right|^2\right]_{\rm CTR}\right\}, \tag{33a}$$

where $g \equiv g(\vec{p})$ is the electron momentum distribution, $N_e' \equiv N_e - 1$, normalized TR field amplitudes are

$$\mathcal{E}_{\parallel} = \left(\frac{u\cos\psi[u\sin\psi\cos\phi - (1+u^2)^{1/2}\sin\theta]}{\mathcal{N}(\theta,u,\psi,\phi)} \right), \quad (33b)$$

$$\mathcal{E}_{\perp} = \left(\frac{u^2\cos\psi\sin\psi\sin\phi\cos\theta}{\mathcal{N}(\theta,u,\psi,\phi)} \right) \quad (33c)$$

with denominator

$$\mathcal{N}(\theta,u,\psi,\phi) = [(1+u^2)^{1/2} - u\sin\psi\cos\phi\sin\theta]^2 - u^2\cos^2\psi\cos^2\theta, \quad (33d)$$

where $u = p/mc = \gamma_e\beta$ is normalized momentum, and the form factor is

$$F = \frac{1}{g(\vec{p})}\int d^2\vec{r}_{\perp} e^{-i\vec{k}_{\perp}\cdot\vec{r}_{\perp}} \times \int dz e^{-iz(\omega-\vec{k}_{\perp}\cdot\vec{v}_{\perp})/v_z} h(\vec{r},\vec{p}), \quad (33e)$$

where v_z is the electron velocity projected along z. Quantities with subscript "||" are oriented along the normal $\vec{z}$ to the foil surface; "⊥" quantities lie in this surface (x-y plane). Polar angle ψ and azimuthal angle ϕ denote electron directions with respect to $\vec{z}$. Without loss of generality, the observation angle θ with respect to $\vec{z}$ lies in the x-z plane. The 6D frequency distribution $h(\vec{r},\vec{p})$, with corresponding $g(\vec{p})$, describes electron phase space. Both h and g are normalized to yield unity when integrated over all of their respective coordinates.

From the general equations (33), one can generate simpler, approximate expressions useful for analyzing many experiments. As one example, when transverse electron momentum is negligible ($\psi \ll 1$), electrons are highly relativistic ($\gamma_e \gg 1$), and electron position $\vec{r}$ and momentum $\vec{p}$ are uncorrelated, one can write $h(\vec{r},\vec{p}) = \rho(\vec{r})g(\vec{p})$. The form factor (33e) then simplifies to

$$F(\omega,\theta) = \int d\vec{r}\rho(\vec{r})e^{-i\vec{k}\cdot\vec{r}}, \quad (34)$$

i.e., the Fourier transform of the normalized 3D bunch charge distribution $\rho(\vec{r})$. This is the quantity of interest in most beam characterization experiments. If additionally the bunch is cylindrically symmetric (ϕ independent) and incident normally ($\langle\psi\rangle = 0$) on a TR foil, Eqs. (33) simplify to (Schroeder *et al.*, 2004)

$$\frac{d^2W_{\mathrm{TR}}}{d\omega d\Omega} = \left\langle \frac{d^2W_e}{d\omega d\Omega} \right\rangle [N_e + N_e^2|F(\omega,\theta)|^2], \quad (35)$$

where $\langle d^2W_e/d\omega d\Omega\rangle$ is the weighted average of Eq. (29) over the bunch's separately measured electron energy distribution, and equals Eq. (29) for a monoenergetic bunch. For fully coherent (incoherent) TR, $F = 1$ ($F = 0$) and Eq. (35) reduces to Eq. (31a) [Eq. (31b)]. If additionally the transverse and longitudinal bunch charge distributions are uncorrelated, we can write $\rho = \rho_{\perp}(\vec{r}_{\perp})\rho_{\parallel}(z)$ and $F = F_{\perp}(\vec{k}_{\perp})F_{\parallel}(k_z)$ (Schroeder *et al.*, 2004; van Tilborg *et al.*, 2004). For a Gaussian bunch with $h(\vec{r},\vec{p}) = g(\vec{p})[(2\pi)^{3/2}\sigma_r^2\sigma_z]^{-1}\exp(-r_{\perp}^2/2\sigma_r^2)\exp(-z^2/2\sigma_z^2)$,

$$F_{\perp} = e^{-(1/2)(\omega/c)^2\sigma_r^2\sin^2\theta}, \quad (36a)$$

$$F_{\parallel} \simeq e^{-(1/2)(\omega\sigma_z/v)^2}. \quad (36b)$$

If $F_{\perp}$ is characterized independently, then CTR spectral intensity measured over a wide bandwidth directly yields $|F_{\parallel}(\omega,\theta)|^2$ via Eq. (35). This is the basis of frequency-domain measurements of ultrashort bunch length (Heigoldt *et al.*, 2015). However, the longitudinal bunch profile $\rho_{\parallel}$ does not follow directly from $|F_{\parallel}(\omega,\theta)|$ via Eq. (34) because phase information is lacking. Additional information and assumptions are needed to extract $\rho_{\parallel}$ (Bajlekov *et al.*, 2013; Bakkali Taheri *et al.*, 2016).

As a second example, Eqs. (33) can be adapted to evaluate TR from a radiator with lateral structure, or finite lateral extent, instead of an infinite foil. This example underlies several important diagnostic applications. These include evaluation of TR in the *far field*, which is defined by observation distances that are large with respect to a *finite* source size. A far-field description is essential, in turn, for modeling focused TR [see Fig. 9(b)] from electron bunches (Artru, Chehab *et al.*, 1998; Castellano and Verzilov, 1998), which diagnoses the bunch's lateral density profile, and for modeling time-domain TR, which diagnoses bunch duration (van Tilborg *et al.*, 2004). This example is also relevant for TR from an electron bunch passing through a hole of characteristic size $\sim\gamma_e\lambda$ in a foil, a configuration that avoids electron scattering within the foil, while sensitively diagnosing variations in electron bunch pointing and transverse structure (Fiorito, 2001), and for modeling TR generated as electrons exit a μm-scale plasma channel or wakefield structure (van Tilborg *et al.*, 2004). When the radiator is transversely confined or structured, *diffraction* of TR comes into play. When diffraction is significant, (C)TR is then often called *(coherent) diffraction radiation*, or (C)DR (Bolotovski and Voskresenski, 1966; Pafomov, 1971; Ter-Mikaelian, 1972; Karlovets and Potylitsyn, 2008). A circular disk radiator of radius ρ_0 is an important special case, for which Eq. (33a) becomes (Schroeder *et al.*, 2004)

$$\frac{d^2W_{\mathrm{CDR}}}{d\omega d\Omega} = \frac{e^2}{\pi^2 c(4\pi\varepsilon_0)}N_e(N_e-1)\sin^2\theta \times \left| \int du g_{\parallel}(u)F(\theta,u)\frac{u(1+u^2)^{1/2}}{1+u^2\sin^2\theta}D(\rho_0,u,\theta) \right|^2, \quad (37a)$$

where we suppressed the dependence of F and D on $k = \omega/c$ for brevity, and $D(\rho_0,u,\theta)$ is a *diffraction factor*

$$D(\rho,u,\theta) = D(b,u\sin\theta) = 1 - J_0(bu\sin\theta)\left[bK_1(b) + \frac{b^2}{2}K_0(b)\right] - \frac{b^2}{2}K_0(b)J_2(bu\sin\theta), \quad (37b)$$

where $b \equiv k\rho_0/u$, and J_{ν} (K_{ν}) are ordinary (modified) Bessel functions. Diffraction is important for long-wavelength TR,

specifically when $\gamma_e\lambda \gtrsim \rho_0$ (or equivalently $b \lesssim 2\pi/\beta$). In the opposite limit, $D(\rho_0, u, \theta)$ is close to unity for all θ within the TR radiation cone. $d^2W_{\mathrm{CDR}}/d\omega d\Omega$ for an electron bunch passing through a circular *hole* of radius ρ_0 can be derived from Eq. (37) using Babinet's principle (Jackson, 1999). Other important analytic CDR results for different D include the donut-shaped intensity distribution

$$I(k,\rho) = \frac{e^2k^2c}{8\pi^2\varepsilon_0 v^2}\left|\int_0^1 d\zeta \frac{\zeta^2}{\zeta^2 + (\beta\gamma)^{-2}} J_1(k\rho\zeta)\right|^2 \qquad (38)$$

of CTR and CDR imaged from a foil surface to a detector [Fig. 9(b)], and the CTR field observed at distance R from a foil of dimensions $\ll R$ (van Tilborg *et al.*, 2004)

$$\vec{E}(\vec{x},t) = -\frac{eN}{\pi R(4\pi\varepsilon_0)}\vec{e}_\perp \int dk \langle \mathcal{E}(\theta,u) D(\omega,u,\theta,\rho) \times F(\omega,u,\theta)\rangle_u e^{-ik(ct-R)}, \qquad (39)$$

which is the basis of time-domain measurements of the electron bunch duration. For more complex CTR and CDR sources, the general integral (33) can often be solved numerically (Shkvarunets and Fiorito, 2008).

B. Bunch charge and energy measurement

Single-shot measurements of total charge $Q = N_e e$ of each N_e-electron bunch, and of the distribution $dQ/dE_e = edN_e/dE_e$ of charge with electron energy E_e, are among the most important beam diagnostics required for any accelerator. The event rate at a collider interaction point or the brightness of undulator radiation depends directly on Q, while narrow energy spread is essential for exciting meaningful particle collisions or for driving an FEL. Plasma electron acceleration science has adopted some standard charge and energy spectrum diagnostics from conventional accelerators. Yet unique properties of plasma-accelerated bunches have necessitated redesign or recalibration of these standard instruments. Section III.B.1 reviews redesigned integrating current transformers (ICTs) that measure absolute Q noninvasively in a noisy environment and cross-calibrated scintillating screens and imaging plates that measure spatially resolved electron charge at the sub-pC/mm^2 level in one shot. Section III.B.2 reviews magnet spectrometer designs that accommodate unique electron energy distributions and pointing fluctuations typical of plasma-accelerated beams. Remaining sections review emerging diagnostics with origins inside the plasma accelerator community: nonintercepting E_e and dN_e/dE_e diagnostics based on undulator radiation spectroscopy (Sec. III.B.3), and diagnostics of correlated slice energy spread based on CTR imaging and optical or plasma-wave microdeflectors (Sec. III.B.4).

Figure 11 schematically overviews a LWFA beam diagnostic system. Noninvasive ICTs are placed early in the diagnostic chain. Absorbing spatially resolved charge detectors at the magnetic spectrometer's focal plane comprise the end of the beam line. Beam dumping and radiation protection are also needed. Charge detectors are shown in the context of betatron x-ray, TR, and undulator radiation diagnostics.

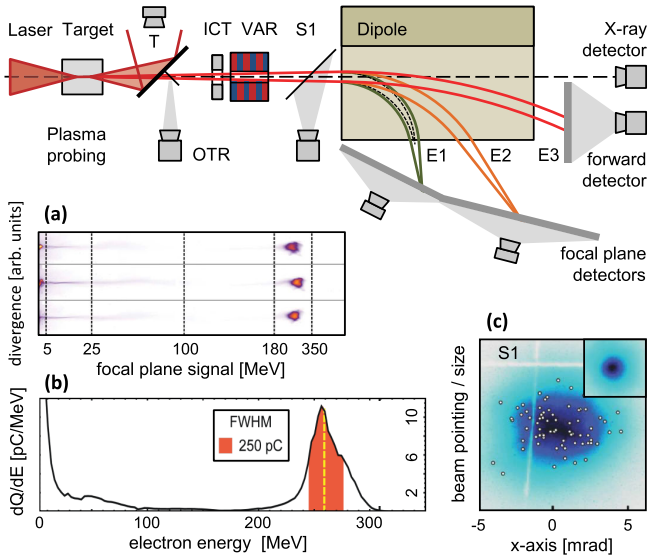

FIG. 11. (Top) Schematic LWFA beam diagnostic setup and sample results. After decoupling from copropagating laser light, wakefield accelerated electron bunches pass through radiating (OTR) or scintillating foils to monitor beam profile and pointing (S1), integrating current transformer (ICT) for charge analysis, optional undulator (VAR) and focusing magnets, and a dispersive dipole magnet for energy analysis, before terminating at spectrometer focal plane detectors. X rays emitted by the electron bunch are measured behind the magnet, which bends electrons away from the x-ray detector. (Bottom) Electron spectrometer data including (a) raw data for three consecutive pulses from focal plane detectors, and (b) energy spectrum from the Draco 150 TW laser at Helmholtz-Zentrum Dresden-Rossendorf (HZDR); (c) beam pointing and profile (inset) data recorded with Lanex screen, from ATLAS at the Max-Planck Institute for Quantum Optics (MPQ). Top, adapted from Schramm *et al.*, 2017. Bottom, adapted from (a) Schramm *et al.*, 2017, (b) Couperus *et al.*, 2017, and (c) Osterhoff *et al.*, 2008.

1. Total and spatially resolved charge measurement

Faraday cups are a classic method to measure total Q, but intercept the beam, and can become unacceptably bulky when they must capture GeV electrons with large stopping distances. Nevertheless, they have been tested for low-MeV LWFAs (Hidding *et al.*, 2007). Nuclear activation provided invasive, cumulative total Q measurements in early LWFA experiments (Leemans *et al.*, 2001; Reed *et al.*, 2007). However, ICTs, which measure integrated current $\int I(t)dt$ that a bunch induces in a coil upon passing through it, have become the instrument of choice for measuring total Q from plasma-based accelerators, because they are compact, *noninvasive*, single shot, and energy independent over a wide range (Unser, 1989; Bergoz *et al.*, 1991). The constant of proportionality between Q and $\int I(t)dt$ depends on the ICT's geometry and electrical characteristics and must be calibrated. ICTs were used to report Q in many early bubble-regime LWFA experiments (see Sec. II.C.1).

The major problem that LWFAs posed for ICTs was strong background radiation that unavoidably accompanied LWFA electron bunches and contaminated ICT signals. The charge of interest from LWFAs is usually contained within a primary

quasimonoenergetic peak [see, e.g., the ∼270 MeV peak in Figs. 11(a) and 11(b)]. Often, however, lower-energy electrons [see the $\lesssim$5 MeV feature in Figs. 11(a) and 11(b)] and uncharacterized additional electrons below the spectrometer's detection edge outnumber electrons in the main high-energy group. Unless shielded, ICTs are sensitive to all of these electrons and thus can overestimate Q of the energetic peak. LWFAs are also prolific sources of electromagnetic pulses (EMPs), e.g., from electronic devices that drive high-power lasers, supersonic gas jets, or high-voltage capillary discharges, or from the laser-plasma interaction itself. An ICT, or its connecting cables, can pick up prompt EMPs from these sources that obscure the electron signal. Interaction of the drive laser or accelerated bunch with gas cell, alignment apertures, or the ICT itself can create prompt secondary particles or x rays that also distort the signal. The first calibrations of ICTs against EMP-insensitive detectors [scintillating screens (Glinec *et al.*, 2006) or imaging plates (Hidding *et al.*, 2007)] that were independently calibrated at rf accelerators showed that in noisy LWFA environments, ICTs overestimated Q by factors ranging from 3 to 4 times (Hidding *et al.*, 2007) to $>$ 10 times (Glinec *et al.*, 2006). This called into question Q values reported in previous LWFA experiments.

Nakamura *et al.* (2011) investigated the reasons for these discrepancies by cross calibrating an ICT with a scintillating screen (Kodak Lanex) and a nuclear activation measurement (Leemans *et al.*, 2001). ICT and Lanex were first cross calibrated using electrons of energy up to 1.5 GeV from an rf accelerator. Then all three detectors were cross calibrated at a LWFA outputting electrons over the same energy range. In the LWFA environment, special care was taken to shield the ICT from EMPs, secondary radiation, and $<$ 1 MeV electrons. All three diagnostics agreed within $\pm 8\%$ for $Q \gtrsim 5$ pC bunches, showing that ICTs could measure Q from LWFAs accurately with proper shielding. Further research showed that residual EMPs within a narrow frequency bandwidth were the primary limit on ICT sensitivity for $Q < 5$ pC. Frequency filtering of the ICT's signal processing electronics improved sensitivity to the sub-pC level, while improving noise immunity and retaining excellent cross calibration with other detectors (Nakamura *et al.*, 2016). The filtered ICT was marketed, an example of commercial product development spurred by plasma accelerator diagnostics research.

Spatially resolved absolute charge measurement underlies beam profile monitors and magnetic spectrometers. Plasma accelerator researchers have used a variety of detectors to resolve accelerated electrons spatially, including cloud chambers and surface barrier detectors (Clayton *et al.*, 1994), scintillators with photomultipliers (Umstadter *et al.*, 1996), scintillating fibers (Gahn *et al.*, 2000), radiochromic film (Giulietti *et al.*, 2002; Galimberti *et al.*, 2005), imaging plates (IPs) (Mangles *et al.*, 2004; Wang *et al.*, 2013), and scintillating screens with cameras. Scintillating screens and IPs have become the most popular choices because they combine wide area detection, high spatial resolution, insensitivity to EMPs, wide dynamic range, reusability, and low cost with sensitivity good enough to detect spatially dispersed few-pC electron bunches in one shot. Nevertheless, the sensitivity of these detectors to x-ray radiation has to be considered in designing detector assemblies.

The working principle and readout concept of scintillating screens and IPs differ considerably from each other. Scintillating screens are based on prompt cathodoluminescence, i.e., rapid conversion of deposited electron (or x-ray) energy into light. Transparent rare-earth oxysulfide host crystals (e.g., Gd_2O_2S) doped with luminescing rare-earth ions (e.g., Tb^{3+}) were developed as medical x-ray phosphors in the 1970s (Wickersheim, Alves, and Buchanan, 1970). As a powder embedded in a urethane binder, they comprise the active layer of Kodak "Lanex" screens, used widely at conventional and plasma-based electron accelerators (Buck *et al.*, 2010). The high density (7.44 g/cm^3) and high average Z of Gd_2O_2S favor strong electron energy deposition (∼0.1 MeV per incident 1 MeV $\lesssim E_e \lesssim$ 1 GeV electron) (Glinec *et al.*, 2006) via impact excitation. This, combined with high (∼16%) (Glinec *et al.*, 2006) intrinsic conversion efficiency of deposited electron energy to excited states of Tb^{3+}, and then to light emission (typically green), results in high electron detection sensitivity. For example, Buck *et al.* (2010) reported a lower detection limit of ∼0.5 pC in a spot with 11 mm FWHM (i.e., ∼10 fC/mm^2) for $E_e = 40$ MeV, $\tau_b = 2$ ps electron bunches incident on KODAK Biomax MS screens. However, this limit depends on the type of scintillator and the optical detection system and may also depend on E_e and τ_b. The efficiency of the imaging system and camera can be calibrated absolutely using reference light sources in the plane of the screen (Buck *et al.*, 2010; Nakamura *et al.*, 2011; Kurz *et al.*, 2018). Light emission increases linearly with charge density over 3 to 4 orders of magnitude, with saturation setting in typically at 10–100 pC/mm^2 (Buck *et al.*, 2010). Saturation corrections, however, extend their usable range to many 100 pC/mm^2. The short (∼1 ms) luminescence lifetime is well suited to high-repetition-rate electron sources. Recently, the consortium responsible for the scintillating screen calibration of Buck *et al.* (2010) updated the work under improved conditions and will soon report revised calibrations (Kurz *et al.*, 2018). They also identified signs of permanent aging at accumulated charge densities of only a few 10 nC/mm^2, which may necessitate frequent replacement or scrolling of screens that monitor ∼100 pC bunches at a high repetition rate.

IPs, also developed for medical radiography (Miyahara *et al.*, 1986; Amemiya and Miyahara, 1988), are based on photostimulated luminescence (PSL) (Iwabuchi *et al.*, 1994). Incoming electrons, positrons, x rays, or ions deposit energy in fine Eu^{2+}-doped phosphor crystals (e.g., BaFBr), embedded in flexible plastic, by converting Eu^{2+} ions to Eu^{3+}. Color centers in the host crystal trap the freed electrons, storing the deposited energy and "exposing" the plate. Sequential visible (typically $\lambda = 0.632$ μm) irradiation of 50–200 μm "pixels" (defined by the focused light, not by material boundaries) in a calibrated off-line scanner (manufactured by Fujifilm) releases the trapped electrons. These recombine with Eu^{3+} ions to form excited Eu^{2+} ions, which luminesce (typically $\lambda_{PSL} = 0.39$ μm) with intensity proportional to the deposited energy. A photomultiplier tube detects the PSL. Exposed IPs fade over several hours (Tanaka *et al.*,

2005; Zeil *et al.*, 2010), are erasable by exposure to intense light, and reusable almost indefinitely. IP sensitivity to relativistic electrons is high and nearly energy independent. For example, Tanaka *et al.* (2005) reported detection of 10^3 electrons with $E_e > 80$ MeV within a ~100 μm pixel—i.e., $\sim 10^{-2}$ pC/mm^2. However, detection limits vary depending on the noise floor from coexposure to x rays, cosmic rays, and other background radiation. IPs provide a large dynamic range ($> 10^5$)—(Zeil *et al.*, 2010) report no observable saturation effects—but multiple, time-consuming, scans are required to read highly exposed plates. IPs are insensitive to EMPs (Tanaka *et al.*, 2005; Zeil *et al.*, 2010). The measured signal in a well-tested (Tanaka *et al.*, 2005; Hidding *et al.*, 2007; Zeil *et al.*, 2010) range is absolute and universal. Since exposed IPs must be scanned off-line, they are best suited for low-repetition-rate systems or for cross calibration of scintillating screens.

A decade ago, measurements of total Q from LWFAs were plagued with order-of-magnitude uncertainties (Glinec *et al.*, 2006), while convenient spatially resolved charge detectors, despite decades of use as slowly integrating medical x-ray detectors, remained uncalibrated as single-shot detectors of intense, sub-ps, relativistic electron bunches. The plasma accelerator community has now transformed this situation. Shielded, filtered ICTs that measure sub-pC, absolute Q accurately in noisy LWFA environments are now commercially available. Scintillating screens and IPs are now extensively cross calibrated at conventional ($\tau_b \sim$ few ps) and LWF ($\tau_b \sim$ few fs) electron accelerators for matching bunch structure and energy. Ongoing research is examining the response of these detectors to high *average* charge flux (Kurz *et al.*, 2018), and the dependence of sensitivity, saturation, and linearity on τ_b in the sub-ps range.

2. MeV and GeV magnetic spectrometers

The dipole magnet spectrometer (Brown, 1975) is the workhorse for single-shot measurement of electron energy spectra in both conventional (Brown, 1975) and plasma-based (Glinec *et al.*, 2006; Nakamura *et al.*, 2008; Sears, Cuevas *et al.*, 2010) accelerators. Plasma-based electron accelerators, however, pose two special challenges. First, their electrons usually span a wide energy range (as much as low-MeV to multi-GeV). Even in quasimonoenergetic plasma accelerators, low-energy electrons usually accompany the main high-energy peak [see Figs. 11(a) and 11(b)]. Accurate, simultaneous measurement of both is essential to diagnosing accelerator performance. In contrast, conventional accelerator beams usually need to be characterized accurately only over a narrow energy band. Second, plasma accelerators usually launch electrons over a few-mrad range of angles into the magnetic spectrometer, due to betatron oscillations or to pointing fluctuations of the driver. While a well-designed spectrometer can bring angularly dispersed low-MeV electrons of a given E_e to a common focus at the detector, this is often not feasible with GeV electrons. Special measures are therefore needed to characterize GeV electron trajectories through a spectrometer to avoid errors in evaluating dN_e/dE_e. In contrast, electron beams in conventional accelerators usually enter the spectrometer highly collimated.

Magnetic spectrometers for plasma accelerators can cover MeV to multi-GeV energies in one setup, albeit with varying resolution. The bending radius ρ of a relativistic electron in homogeneous magnetic field B

$$\rho = \frac{m_e c \beta \gamma_e}{eB} \approx 1.7 \times 10^{-3} \frac{\gamma_e}{B[\mathrm{T}]} \text{ m} \tag{40}$$

defines the scale of the spectrometer, e.g., $\rho \approx 1$ m for $\gamma_e = 600$ with a practical upper limit $B \sim 1$ T.

Figure 11 schematically illustrates the trajectories of electrons at three representative energies $E_1 < E_2 < E_3$ through a uniformly magnetized rectangular area, which is usually limited by available space and by magnet weight and cost. At energy E_1, circular trajectories bounding the envelope of an incoming beam cross just outside the magnetic field, at deflection angle $\theta_{\mathrm{def}} \approx 90°$. Shifts in the object plane toward the magnet entrance (equivalent to a divergent incoming beam) simply shift the image plane. Resolution is thus limited only by the negligible source size in the object plane or by aberrations in the focusing field (Nakamura *et al.*, 2008; Sears, Cuevas *et al.*, 2010). Electrons of somewhat higher energy E_2 exit the magnetic field at an oblique angle. The image plane shifts significantly, often necessitating a separate detector as shown in Fig. 11. In addition, the influence of fringe fields becomes energy dependent. Nevertheless, relative energy resolution $\Delta E_e/E_e$ on the percent level is usually possible without additional magnet design modifications (Savran *et al.*, 2010), as shown in Fig. 12(a). Mapping of the field distribution (including fringe fields) and numerical analysis of beam trajectories is needed to define image plane and resolution precisely.

For energy E_3, reached when ρ equals roughly twice the magnet length, focal plane detection must be abandoned in the near forward direction. This regime includes the critical quasimonoenergetic peak of many plasma-based electron

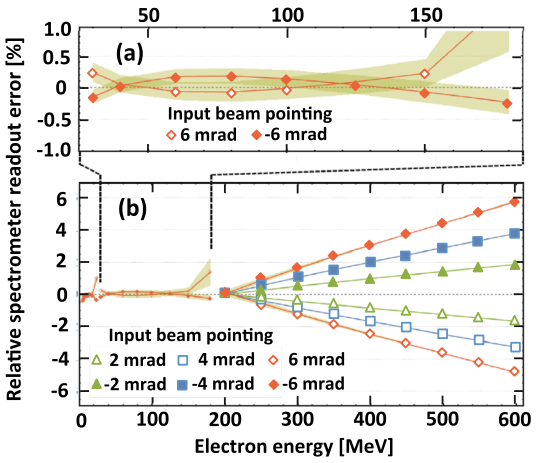

FIG. 12. Energy read-out error of the dipole magnetic spectrometer for various electron entrance angles (−6 to 6 mrad) and energies ($0 < E_e < 600$ MeV): (a) low electron energy, detector in the focal plane of the magnet (corresponding to $E_{1,2}$ in Fig. 11), and (b) high electron energy, detector in the forward direction before the focal plane (corresponding to E_3 in Fig. 11). Adapted from Schramm *et al.*, 2017.

accelerators. Declining spectrometer dispersion $d\theta_{\rm def}/dE_e$ at high E_e by itself tends to decrease energy resolution in this regime. With loss of focal plane detection, uncompensated beam divergence further compromises resolution. The detection point of an electron becomes sensitive to the beam pointing jitter, as shown in Fig. 12(b), impairing energy *calibration*. Special measures are then needed to ensure an accurate energy measurement. If space is available, additional beam optics can recover focal plane detection (Weingartner *et al.*, 2011; Litos *et al.*, 2014). Alternatively, hard apertures can collimate the beam at the expense of charge. Reference grids, transmission beam pointing monitors (Cha *et al.*, 2012), or feedback from secondary radiation (Shaw *et al.*, 2017) can monitor beam pointing, allowing shot-to-shot correction for jitter. Pollock *et al.* (2009) and Clayton *et al.* (2010) introduced a correction scheme with two tandem scintillating screens. By correlating common electron spectral features on each screen, they deduced the complete electron trajectory through the spectrometer, including launch angle. For greater precision, Wang *et al.* (2013) employed two tandem grids of 125 μm tungsten wires to cast sharply defined shadows on dispersed electron signals recorded on one IP. Analysis enabled measurement of E_e up to 2 GeV, and associated launch angles, with only $\pm 5\%$ uncertainty at the 2σ level using a 1.1 T magnetic field within a 4×4 cm central plateau. This is a low-cost solution for accurately calibrating dN_e/dE_e up to low-GeV energy. Alternatively, much larger magnets can be used—e.g., a circular 1.25 T field of 40 cm diameter was used to characterize 4 GeV LWFA electrons (Nakamura *et al.*, 2008; Leemans *et al.*, 2014).

Dipole magnet spectrometers have accurately characterized plasma-accelerated electrons from low-MeV to multi-GeV energies (Blumenfeld *et al.*, 2007; Leemans *et al.*, 2014; Litos *et al.*, 2014), resolving peaks as narrow as $\Delta E_e/E_e \approx 0.01$ (Rechatin *et al.*, 2009). With the highest-performing plasma accelerators currently producing bunches with a few percent energy spread, the field has not yet challenged magnetic spectrometer technology to achieve higher energy resolution. With scintillating screens, read-out sensitivities of 0.1 pC/MeV can be achieved. Scintillating fibers (Sears, Cuevas *et al.*, 2010) enable higher sensitivity at greater cost and with digitized energy resolution. Since beam propagation remains undisturbed in the nonbending plane, the spectrometer's detector simultaneously measures beam divergence.

3. Spectroscopy of on-axis undulator radiation

A nonintercepting alternative to magnet spectrometers is spectroscopy of forward-directed light that relativistic electron bunches emit on passing through an undulator or Thomson backscatter light field (see Sec. III.A.2). For diagnostics, low values of undulator parameter K [Eq. (19)] or field strength a_0 [Eq. (2)] are preferred to avoid perturbing the electron bunch or complicating the spectrum of emitted radiation (see Fig. 6). Such a noninvasive approach is essential for monitoring E_e, ΔE_e, angular divergence, and other beam characteristics in early stages of a multistage plasma accelerator (Steinke *et al.*, 2016). It is especially valuable for characterizing few-GeV electrons, a range in which dipole electron spectrometers have difficulty providing image plane diagnostics (see Sec. III.B.2) and require large expensive magnets.

Measurement of maximum frequency $\omega_{\rm sc}^{(\max)} \propto [\gamma_e^{(\max)}]^2$ of light emitted on axis directly determines the maximum electron Lorentz factor $\gamma_e^{(\max)}$, which in quasimonoenergetic plasma accelerators corresponds to the primary spectral peak of interest. The lower right portion of Fig. 13 summarizes results of correlated measurements of Lorentz factors of single-stage LWFA electrons in the range $100 < \gamma_e^{(\max)} < 400$ (made with magnetic spectrometers) and of the photon energy of undulator radiation from visible (1.8 eV) (Schlenvoigt *et al.*, 2008; Gallacher *et al.*, 2009) to EUV (83 eV) (Fuchs *et al.*, 2009; Anania *et al.*, 2014) that the electrons generated in undulators of periods $0.5 < \lambda_u \leq 2.0$ cm. The measurements agreed well with the relation $\hbar\omega_{\rm sc} = 2\gamma_e^2\hbar\omega_u$ (solid orange, red, magenta lines), from Eq. (20) for $K < 1$, $\theta \to 0$. In this photon energy range, and probably up to $\hbar\omega_{\rm sc} \sim$ few keV (corresponding to $E_e \sim$ few GeV), optical to soft x-ray spectrometers can measure $\hbar\omega_{\rm sc}$ at least as accurately as magnetic spectrometers can measure γ_e. The emergence of miniature, short-period undulators designed specifically for LWFAs (Eichner *et al.*, 2007) will help to make the noninvasive $\gamma_e^{(\max)}$ measurement compact and cost effective.

The upper left portion of Fig. 13 summarizes corresponding results for Thomson backscatter of $\lambda = 0.8$ μm light from LWFA photons of similar $\gamma_e^{(\max)}$ range. Since $\omega_0 \gg \omega_u$, photon energies now range from 60 keV to 1 MeV (Powers *et al.*, 2014; Khrennikov *et al.*, 2015; Tsai *et al.*, 2015; Golovin *et al.*, 2016), and agree well with the relation $\hbar\omega_{\rm sc} = 4\gamma_e^2\hbar\omega_0$ (solid blue, black lines), from Eq. (21) for $a_0 < 1$, $\theta \to 0$, and $\varphi_{\rm coll} = 180°$. Experiments with 1–2 GeV ($2000 < \gamma_e < 4000$) electrons (not shown) extended the range to $\hbar\omega_{\rm sc} \sim 80$ MeV (Shaw *et al.*, 2017). In this photon energy range, the challenge shifts to accurate spectroscopy of such

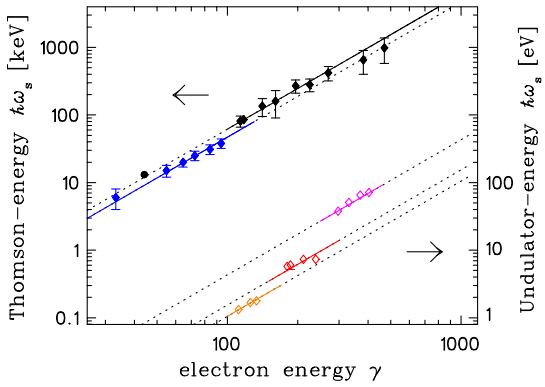

FIG. 13. Photon energies of undulator and Thomson backscatter radiation from LWFA electrons. Lower right, from low to high $\hbar\omega_s$: radiation (open diamonds) from undulators of period $\lambda_u =$ 20 mm (orange, $1 < \hbar\omega_s < 2$ eV) (Schlenvoigt *et al.*, 2008); 15 mm (red, $5 < \hbar\omega_s < 8$ eV) (Anania *et al.*, 2014); 5 mm (magenta, $40 < \hbar\omega_s < 70$ eV) (Fuchs *et al.*, 2009). Upper left: Thomson backscatter radiation (filled diamonds) generated by ultrashort $\lambda_0 = 0.8$ μm laser pulses of field strength $a_0 \sim 0.8$ (blue, $6 < \hbar\omega_s < 40$ keV) (Khrennikov *et al.*, 2015); 0.3 (black, $80 < \hbar\omega_s < 1000$ keV) (Powers *et al.*, 2014). Note the redshift of higher a_0 data. Black circle: data from Fig. 16 for comparison.

hard x rays (Gahn *et al.*, 1998; Günther *et al.*, 2011; Sarri *et al.*, 2014; Horst *et al.*, 2015; Golovin *et al.*, 2016). If adequate resolution can be achieved, the possibility of realizing Thomson backscatter from low-MeV (Ta Phuoc *et al.*, 2012) to multi-GeV (Shaw *et al.*, 2017) electrons simply by inserting a plasma mirror (foil) after the plasma to backreflect the spent drive laser pulse (see Sec. III.A.2) offers an exceptionally low-cost electron energy diagnostic.

In addition to $\gamma_e^{(\max)}$, the spectroscopy of undulator or Thomson radiation can also diagnose *spread* $\Delta\gamma_e$ of a peaked electron energy distribution if additional beam parameters are known (Brown and Hartemann, 2004; Chouffani *et al.*, 2006; Schlenvoigt *et al.*, 2008; Jochmann *et al.*, 2013; Golovin *et al.*, 2016; Krämer *et al.*, 2018), see Sec. III.C. Relative on-axis photon energy spread (for $K \ll 1$, $a_0 \ll 1$) is determined not only by relative electron energy spread $\Delta\gamma_e/\gamma_e$, but by electron angular spread σ_r', laser bandwidth $\Delta\omega_0$ (for Thomson backscatter only), number of periods N_u, and solid angle $\Omega_{\rm det}$ covered by the on-axis detector:

$$\left(\frac{\Delta\omega_{\rm sc}}{\omega_{\rm sc}}\right)^2 = \left(\frac{2\Delta\gamma_e}{\gamma_e}\right)^2 + (\gamma_e^2\sigma_r'^2)^2 + \left(\frac{2\Delta\omega_0}{\omega_0}\right)^2 + \left(\frac{1}{N_u}\right)^2 + (\gamma_e^2\Delta\Omega_{\rm det}^2)^2. \quad (41)$$

Electron beam optics can reduce divergence (Becker *et al.*, 2009; Fuchs *et al.*, 2009; Anania *et al.*, 2014), but then chromatic selectivity distorts the spectrum.

Absolute E_e and $\Delta E_e/E_e$ of LWFA beams of energies ($60 < E_e < 120$ MeV) and divergences ($1 < \sigma_r' < 3.5$ mrad) have been resolved with undulator radiation ($N_u \sim 50$) ranging from near-IR (Gallacher *et al.*, 2009) to vacuum ultraviolet (Anania *et al.*, 2014). After deconvolving the σ_r' contribution, Gallacher *et al.* (2009) obtained $\Delta\gamma_e/\gamma_e$ as small as ~0.01, in agreement with independent magnet spectrometer measurements, equivalent to the smallest LWFA energy spread observed with a magnetic spectrometer alone (Rechatin *et al.*, 2009). When magnetic quadrupoles precollimated the LWFA beam, $\Delta\gamma_e$ of the selected main peak became the dominant contribution to $\Delta\omega_{\rm sc}$. However, discrepancies between $\Delta\gamma_e$ determined from undulator and magnetic spectrometer were observed (Anania *et al.*, 2014). Extension of such measurements to GeV electrons will be a priority for future research.

4. Slice energy spread

More than a decade after the first demonstrations of quasimonoenergetic plasma accelerators, electron bunches with overall energy spread $\Delta E_e/E_e$ below 0.01 have not been observed. Yet $\Delta E_e/E_e \sim 10^{-3}$ and kA peak current are vital for short-wavelength conventional (Röhrs *et al.*, 2009; Behrens *et al.*, 2014) and LWFA-driven (Gruener *et al.*, 2007) FELs. $\Delta E_e/E_e$ of high-quality plasma-accelerated bunches can, however, be dominated by *correlated* spread. This means that $\Delta E_e/E_e$ is the sum of spreads of longitudinal slices of the bunch, each of which is individually much lower than $\Delta E_e/E_e$. Relative slice energy spread 10^{-3} could enable FEL gain with plasma accelerators (Huang and Kim, 2007). Bunch decompression reduces energy spread over the slice at the expense of decreasing the peak current (Seggebrock *et al.*, 2013). Dispersively matched transverse gradient undulators could then operate with different energy slices (Huang, Ding, and Schroeder, 2012) simultaneously. Diagnosis of slice energy spread is thus a key component of current plasma accelerator research.

Lin *et al.* (2012)) deduced slice properties of LWFA bunches *indirectly* by imaging visible CTR several meters downstream from an LWFA. If $\Delta E_e/E_e \sim 0.05$ were present throughout the bunch's longitudinal profile, sub-μm density and momentum modulations, a prerequisite for nonzero form factor F [Eq. (34)] and thus for generating *coherent* TR at visible wavelengths [Eq. (35)], would disappear within a few centimeters of propagation (Glinec *et al.*, 2007; Lundh *et al.*, 2011). Lin *et al.* (2012) created such modulations by generating wakes in sufficiently dense ($\bar{n}_e > 10^{19}$ cm^{-3}) plasma such that the trailing edge of the drive laser pulse modulated the accelerating bunch. Yet several meters downstream of the LWFA, they observed two clear signatures of CTR: (1) intensity up to 10^3 times stronger than calculated from Eq. (35) with $F = 0$; (2) imaged TR spatial profiles containing "hot spots" much smaller than the overall beam profile. Persistence of coherent features over such long propagation lengths required $\Delta E_e/E_e|_{\rm slice} \lesssim 0.005$, well below the total energy spread.

A method for measuring $\Delta E/E|_{\rm slice}$ *directly* in the time domain was developed for FEL drivers and FACET (Dolgashev *et al.*, 2014): an *X*-band (typically 11.4 or 12 GHz) rf transverse deflection cavity streaks the bunch, and energy-resolved monitoring of the streaked transverse profile recovers longitudinally distributed dN_e/dE_e. A slice resolution of 70 fs was demonstrated at SLAC for the 20 GeV FACET beam, and better resolution can be reached for the Linac Coherent Light Source (LCLS) operating conditions because the beam has lower emittance. However, rf cavities cannot resolve $\Delta E/E|_{\rm slice}$ of a few-fs LWFA bunches. New approaches employing light fields (C. Zhang *et al.*, 2016) or plasma wakefields (Dornmair *et al.*, 2016) as transverse deflectors are now emerging. Since these methods are closely connected with bunch duration measurement, we discuss them in Sec. III.D.1.a.

C. Transverse emittance measurement

Early measurements of transverse emittance of LWFA electron bunches adopted mask and focus-scan techniques developed for conventional accelerator beams (Sec. III.C.1). But resolution and E_e range limits motivated development of new methods based on betatron x-ray spectroscopy (Sec. III.C.2) and undulator and transition radiation (Sec. III.C.3).

1. Conventional mask and focus-scan methods

a. Masks

Techniques using beam-intercepting masks (subscript m) with 1D (2D) arrays of slits (pinholes), i.e., "pepper pots," were designed to characterize emittance of low-MeV, space-charge-dominated electron beams (Lejeune and Aubert, 1980; Mostacci *et al.*, 2008), although Delerue (2011) and Thomas, Delerue, and Bartolini (2013) recently extended

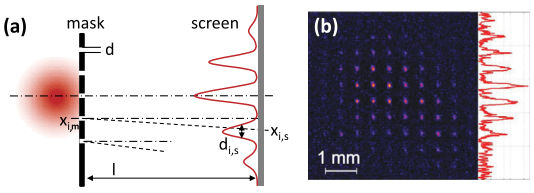

FIG. 14. Pepper-pot measurement of beam emittance. (a) Opaque mask with slits or holes transmits diverging beamlets across the beam profile. Thin downstream Ce:YAG screen at distance l detects expanded beamlet profiles (width $d_{i,s}$, location $x_{i,s}$) with typically $\lesssim 10$ μm resolution. (b) Screen image of 125 MeV LWFA beam 30 cm downstream of the source, yielding $\varepsilon_n \sim 2.2 \pm 0.7$ mm mrad (resolution ~ 1.2 mm mrad), divergence ~ 3 mrad. (b) From Brunetti *et al.*, 2010.

their use to rf-accelerated GeV electrons. Figure 14(a) shows a schematic 1D geometry. A beam impinges at centroid position $\bar{x}$ with average x momentum $\bar{x'}$ on an array of slits, each of width d, centered at $x_{i,m}$. The ith slit transmits a beamlet of well-defined origin and low enough charge en_i that it becomes "emittance dominated,"i.e., positions x_j and transverse momenta x'_j of electrons passing through the slit ($j = 1, 2, \ldots, n_i$), rather than Coulomb repulsion, dominate beamlet propagation. A screen (subscript s) at distance l, often thin cerium-doped yttrium aluminum garnet (Ce:YAG) to avoid grain-size resolution limits of Lanex, records the centroid position $x_{i,s}$ [yielding average x momentum $x'_i = (x_{i,s} - x_{i,m})/l$], spatial profile (diameter $d_{i,s}$), and (if linear in response) relative electron number n_i of each expanded beamlet. As long as each beamlet's angular spread $\Delta x'_i$ is not too large, the averages $\langle x^2 \rangle_i$, $\langle x'^2 \rangle_i$, and $\langle xx' \rangle_i$ that contribute to its x emittance ε_i [see Eq. (9)] are related straightforwardly to observed beamlet (n_i, $x_{i,m}$, x'_i, $d_{i,s}$) and whole beam ($\bar{x}$, $\bar{x'}$) quantities. A sum of ε_i over slits then yields emittance ε of the subset of incident electrons that passed through the slits, assuming negligible space charge. Zhang (1996) derived complete expressions for ε_i and ε. Generalization to 2D [Fig. 14(b)] is straightforward. With sufficient charge, the pepper-pot technique can measure ε in one shot. Analogous pinhole or lenslet arrays characterize transverse phase structure of optical beams (Platt and Shack, 2001).

Cianchi *et al.* (2013) pointed out limits of the pepper-pot method for resolving ε of LWFA beams, which is dominated by divergence rather than space charge. While for typical injector beams, the ratio of divergence to initial beam size is ~ 1 mrad/mm, for LWFA beams it is $\sim 10^3$ mrad/mm [e.g., $\sigma_r(0) \approx 1$ μm, $\sigma'_r \approx 1$ mrad]. Because of their relatively strong divergence, the phase-space profile of LWFA beams flattens after a few cm of free-space propagation, with x' strongly correlated with x [see Fig. 4(c)]. Consequently, a slit at $x = x_i$ sees a very small uncorrelated spread $\Delta x'_i = (d_{s,i} - dx_{s,i}/x_i)/l$ of x' values and has difficulty resolving it above the uninformative geometric slit projection $d(x_{i,s}/x_i)/l$. Narrowing the slit width d to compensate scatters the beam. Thus pepper pots tend to undersample transverse phase space of LWFA beams.

Nevertheless, pepper-pot measurements placed first-generation upper limits on LWFA beam emittance before other measurements existed. Experiments for quasimonoenergetic, $\sigma'_r \sim$ few-mrad LWFA beams in the energy range 15 to 200 MeV with scanning pinhole (Fritzler *et al.*, 2004), scanning slit (Sears, Buck *et al.*, 2010), and pepper-pot masks (Brunetti *et al.*, 2010; Manahan *et al.*, 2014) yielded upper-limit ε_n estimates between 1 and 3 mm mrad with $\sim 30\%$ relative errors. These results were based on estimated upper-limit initial beam size $\sigma_r(0) \sim \lambda_p \sim 10$ μm. However, Cianchi *et al.* (2013) later showed that for $\sigma_r(0) \sim 1$ μm [see Figs. 4(a) and 14(b)], the phase-space ellipse of a $\sigma'_r \sim$ few-mrad beam flattens so quickly that pepper pots with realistic pinhole diameters (tens of μm) cannot resolve their emittance. Indeed betatron x-ray spectroscopy shows $\sigma_r < 1$ μm (see Sec. III.C.2). On the other hand, mask techniques remain useful for characterizing LWFA beams transmitted through emittance-increasing optics (Manahan *et al.*, 2014) or for evaluating transport conditions between acceleration stages (Dornmair, Floettmann, and Maier, 2015; Xu *et al.*, 2016).

b. Focus Scans

Conventionally, ε of non-space-charge-dominated beams is often characterized by measuring their transverse profile after focusing optics, e.g., at a fixed location while changing focusing strength (quadrupole scan) or at multiple locations with fixed optics (multiscreen measurements) (Rees and Rivkin, 1984; Minty and Zimmermann, 2013). To recover three Twiss parameters [Eq. (10)], at least three measurements, usually over multiple shots, are needed. Mostacci *et al.* (2012) reviewed this technique and analyzed new measurement uncertainties that come into play for LWFA and other beams with greater than or similar to a few percent energy spread [see Fig. 3(a)], compared to $\sim 0.1\%$ for conventional focus-scan measurements, and with large σ_r (due to strong divergence) at the first quadrupole in a sequence. The resulting chromatic effects cannot only introduce systematic errors into measurement of ε, but can degrade ε of the beam under test. The severity of these effects depends on the specific quadrupole configuration and on incident beam properties. For example, to characterize a beam with $E_e \sim 150$ MeV, $\Delta E_e/E_e \sim 0.01$, and $\varepsilon_n \sim 1$ mm mrad using a single quadrupole requires sub-mm spot size to avoid strong emittance dilution (Cianchi *et al.*, 2013).

Weingartner *et al.* (2012) turned energy spread into a diagnostic advantage by inserting an energy-dispersing magnetic dipole between a fixed high-gradient quadrupole doublet (Becker *et al.*, 2009) and a Ce:YAG screen located 10 cm and ~ 2 m, respectively, after a ~ 250 MeV LWFA. Screen luminescence displayed *energy-resolved* beam size as quadrupole position scanned over multiple shots, avoiding chromatic errors in determining ε. Alternatively, this configuration enabled a rare *single-shot* focus-scan measurement by exploiting the quadrupole focal length's dependence on E_e. Thus the beam's natural energy spread mapped onto an equivalent focus scan at the detector without the need for moving or adjusting the field strength of the quadrupole. Both multishot and single-shot measurements yielded $\varepsilon_n = 0.2$ mm mrad with 5%–10% uncertainty, well below the upper limits set

by pepper-pot measurements. Active lensing in plasma discharge cavities provides a complementary means for performing focus scans close to the plasma accelerator, ensuring small spot size (van Tilborg *et al.*, 2015). Recently Barber *et al.* (2017) applied an energy-resolved focus scan to determine the influence of the injection scheme on beam emittance. Results showed that shock-induced down-ramp injection yielded a factor of 2 lower normalized emittance ($\varepsilon_n \sim 1$ mm mrad) than ionization injection at equal charge densities ($dQ/dE \sim 2$ pC/MeV).

2. Betatron x-ray spectroscopy

In contrast to conventional beam-intercepting emittance diagnostics outside the accelerator, betatron spectroscopy (see Sec. III.A.3) emerged as a noninvasive, albeit indirect, alternative for diagnosing ε_n within, and near the end of the accelerator where most betatron radiation is emitted [see Fig. 7(c)]. Measured quantities are electron spectrum dQ/dE_e [Fig. 11(b)], betatron x-ray spectrum $dW_\beta^{(\mathrm{meas})}/d\omega$ (Fig. 15), and $\bar{n}_e$. A simple analysis fits $dW_\beta^{(\mathrm{meas})}/d\omega$ to a calculated single-electron betatron power spectrum $dW_\beta/d\omega$ [see Eqs. (16) and (24) and the green curve in Fig. 15], and extracts the critical frequency ω_c [Eq. (26)], typically ~10 keV for LWFAs producing few-hundred-MeV electrons. Then using $\omega_c \propto \gamma_e^3 k_\beta^2 r_\beta \propto \gamma_e^2 \omega_p^2 r_\beta$ [from Eqs. (23) and (26)], one obtains the betatron oscillation amplitude r_β of a single electron, using γ_e and ω_p from the quasimonoenergetic peak of dQ/dE_e and the $\bar{n}_e$ measurement, respectively. The extracted r_β can be interpreted as an ensemble average amplitude $\bar{r}_\beta$, then equated with Plateau *et al.* (2012) or related with help from auxiliary measurements to Schnell *et al.* (2012), intra-LWFA bunch radius σ_r. Combining σ_r with measured beam divergence $\sigma_r'^{(\mathrm{meas})}$ outside the accelerator, e.g., from the width of the electron spectrometer signal orthogonal to the dispersion plane, yields the estimate

$$\varepsilon_n \approx \gamma_e \sigma_r \sigma_r'^{(\mathrm{meas})} \tag{42}$$

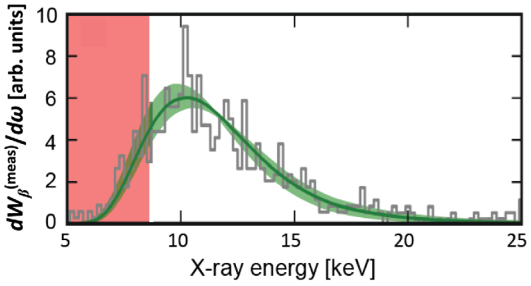

FIG. 15. Measured betatron radiation spectrum $dW_\beta^{(\mathrm{meas})}/d\omega$ (solid black histogram) used to determine beam radius σ_r inside LWFA that produced a peaked electron energy spectrum similar to the one shown in Fig. 11(b). Solid green curve: calculated spectrum $dW_\beta/d\omega$, assuming $\sigma_r \lesssim r_\beta = 0.8$ μm. Shaded green area: variation in $dW_\beta/d\omega$ for 25% variation in σ_r. Red-shaded area (5–8 keV): low-energy regime with reduced detection efficiency and measurement quality. Experimental conditions matched those of Köhler *et al.* (2016) and Couperus *et al.* (2017).

for the uncorrelated component of normalized emittance [i.e., the first term on the right-hand side of Eq. (12a)]. However, Eq. (42) neglects correlations between x and x' [the second term on the right-hand side of Eq. (12a)]. Moreover, $\sigma_r'^{(\mathrm{meas})}$ can misrepresent $\langle \gamma_e^2 x'^2 \rangle$ inside the LWFA if the plasma-vacuum boundary reshapes the beam's phase-space ellipse [see Figs. 4(a) and 4(b)], thereby altering its downstream divergence (Sears, Buck *et al.*, 2010; Weingartner *et al.*, 2012).

Plateau *et al.* (2012), Schnell *et al.* (2012), and Köhler *et al.* (2016) used this simple analysis method to estimate ε_n from quasimonoenergetic LWFAs under a variety of conditions. They measured $dW_\beta^{(\mathrm{meas})}/d\omega$ in a single shot using a shielded, backilluminated x-ray charge-coupled device (CCD) camera operating in photon-counting mode, i.e., each pixel absorbed on average less than one x-ray photon. The charge deposited in an illuminated pixel determined the photon's energy. The x-ray spectrum consisted of a histogram of all illuminated pixels (Fig. 15). Plateau *et al.* (2012) found r_β as low as 0.1 μm for a 0.4 pC, $\gamma_e = 920$ bunch, in agreement with the matched beam radius $\sigma_r = \sqrt{2\gamma_e}\sigma_r'/k_p$ inferred from downstream divergence measurements and plasma conditions. Use of Eq. (42) yielded $\varepsilon_n \sim 0.1$ mm mrad. Schnell *et al.* (2012) observed monotonically decreasing r_β (4 to 0.4 μm) as γ_e increased (50 to 250), a consequence of the relativistic electron mass increase. Köhler *et al.* (2016) integrated the evolving x-ray spectrum of the accelerating electron bunch in fitting $dW_\beta^{(\mathrm{meas})}/d\omega$, thereby determining r_β with unprecedented resolution (Fig. 15). These researchers cross-checked extracted r_β values, typically with lower resolution, by independently analyzing x-ray shadows of sharp edges or wires. For a $\gamma_e = 160$ bunch for which betatron spectroscopy yielded $r_\beta = 0.9 \pm 0.3$ μm, Schnell *et al.* (2012) found x-ray source size $\sigma_x = 1.8 \pm 0.3$ μm from x-ray shadowgraphy, and inferred $\sigma_r = 1.6 \pm 0.3$ μm by modeling radiation from a Gaussian bunch. Kneip *et al.* (2012) used x-ray shadowgraphy alone to estimate σ_r, but observed no γ_e dependence.

Curcio *et al.* (2017) used the same single-shot experimental method to obtain $dW_\beta^{(\mathrm{meas})}/d\omega$, but introduced a more sophisticated analysis that included ensemble averages $\langle x^2 \rangle$, $\langle \gamma_e^2 x'^2 \rangle$, and $\langle x\gamma_e x' \rangle^2$ from the outset in calculating $dW_\beta/d\omega$, instead of single-electron theory. They assumed bunches were radially symmetric and did not interact with the tail of the drive pulse. Accordingly, they confined analysis to shots that produced radially symmetric betatron x-ray profiles, and to conditions for which bubble radius significantly exceeded drive pulse length. With these simplifications, they solved the inverse problem to recover a complete intra-LWFA radial beam profile $P(r)$, instead of just an average σ_r, and a complete distribution $\Theta(\theta_d)$ of transverse angles $\theta_d = dr/dz$, including correlations $r(\theta_d)$. This enabled determination of $\varepsilon_n = 0.6 \pm 0.1$ mm mrad for a $\gamma_e = 640 \pm 6$ beam, including correlations $\langle x\gamma_e x' \rangle^2$, solely from $dW_\beta^{(\mathrm{meas})}/d\omega$ and dQ/dE_e measurements, without invoking $\sigma_r'^{(\mathrm{meas})}$. Nevertheless, calculated σ_r' agreed with $\sigma_r'^{(\mathrm{meas})}$ for the conditions investigated. On the other hand, estimating emittance

of the same beam from Eq. (42), using $\sigma_r'^{(\mathrm{meas})}$, yielded $\varepsilon_n = 1.5 \pm 0.3$ mm mrad, demonstrating that correlations contribute significantly to ε_n inside a plasma bubble.

Accelerating electrons with nonplanar trajectories, angular momentum, can generate radially asymmetric betatron x-ray intensity profiles (Ta Phuoc *et al.*, 2006). Although a linearly polarized drive laser pulse imparts no net angular momentum to its wake, if it has a radially asymmetric spatial profile, it creates a plasma bubble with asymmetric focusing forces $F_x \neq F_y$. Accelerating electrons and their heavier plasma cavity can then acquire equal and opposite, cyclically evolving angular momenta, while total angular momentum remains constant. Thaury *et al.* (2013) observed such periodic cycling of betatron x-ray asymmetry by controlling acceleration length with colliding-pulse injection (see Sec. II.C.1). Since angular momentum over and above emittance influences downstream beam propagation, its accurate single-shot diagnosis is essential. Additionally, observation of a nonuniformly polarized betatron x-ray profile signifies a preferred oscillation direction, which can arise from bunch interaction with the rear of the drive laser pulse (Mangles *et al.*, 2006; Németh *et al.*, 2008; Cipiccia *et al.*, 2011; Curcio *et al.*, 2015).

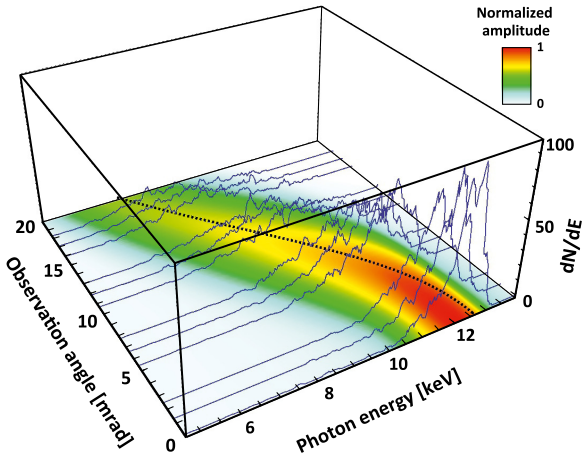

FIG. 16. Thomson-backscattering spectra dN/dE vs observation angle θ. Electron beam: $E_e = 22.5$ MeV, $\Delta E_e/E_e \approx 0.0025$, $\tau_b \approx 4$ ps, and $Q = 77$ pC linac bunches; laser: $\lambda = 800$ nm, $\Delta\lambda \approx 20$ nm, and $a_0 \approx 0.05$. Black solid curves: experimental data; dotted curve: Eq. (21); linear color scale: numerical model of $dN(\theta)/dE$ with blue minimum, red maximum. From Jochmann *et al.*, 2013.

3. Undulator and transition radiation diagnostics

Radiation that electron beams emit outside an accelerator, e.g., undulator or Thomson scatter (Sec. III.A.2) or TR (Sec. III.A.4), can also characterize their emittance indirectly. Leemans *et al.* (1996), (Chouffani *et al.* (2006), Jochmann *et al.* (2013), and Krämer *et al.* (2018) developed basic principles for diagnosing beam divergence $\sigma'_{x,y}$ using 90° and 180° Thomson scattering. These studies used tens-of-MeV electron bunches of negligible energy spread ($\Delta\gamma_e/\gamma_e \lesssim 0.003$) from conventional linacs. In the 90° geometry, a ~100 fs laser pulse scattered from a longitudinal slice of a 10–15 ps bunch, selected by changing bunch-laser delay. The energy-integrated transverse Thomson x-ray intensity profile was measured on a phosphor screen, then fit to a single-electron angular power distribution $dW_{\mathrm{sc}}/d\Omega$ integrated over a Gaussian distribution of electron propagation angles to extract $\sigma'_{x,y}$. The 180° geometry integrated over bunch length, but θ-dependent Thomson-scatter spectra, given by Eq. (21) with $\varphi_{\mathrm{coll}} = 180°$ for *one* electron, were measured with high spectral or angular resolution using either Si(Li) and *p*-type/intrinsic/*n*-type (PIN) semiconductor photodiode detectors (Chouffani *et al.*, 2006) or a pixelated x-ray CCD (Jochmann *et al.*, 2013) similar to those used in betatron x-ray spectroscopy (see Sec. III.C.2). Figure 16 shows typical results from Jochmann *et al.* (2013). The peak of the x-ray photon energy distribution $dN(\theta)/dE$ (red swath) closely tracked Eq. (21) (black dotted curve), except for a ~5% redshift near $\theta = 0$, attributable to the fraction of the diverging electron ensemble that deviated from $\varphi_{\mathrm{coll}} = 180°$. The width and asymmetry of $dN(\theta)/dE$ (black solid curves) changed dramatically with increasing observation angle θ. Numerical fits to these distinctive features enabled extraction of electron angular distribution with unprecedented accuracy.

The accuracy of these measurements relied on small relative energy spread $\Delta\gamma_e/\gamma_e$, just as undulator-based measurements of $\Delta\gamma_e/\gamma_e$ relied conversely on small angular spread (see Sec. III.B.3). Small detector angle (Ω_{det}) and small laser ($\Delta\omega_0$) or undulator (N_u^{-1}) bandwidths were also essential. Equation (41) summarized the trade-offs (Krämer *et al.*, 2018). The principal new challenge that LWFA beams presented for undulator and Thomson-based emittance characterization was their comparatively large $\Delta\gamma_e/\gamma_e$ (see Sec. II.C.1, Fig. 3). Fuchs *et al.* (2009) chromatically focused an LWFA beam into an undulator, thereby selecting a narrow energy band. However, the measurement is then destructive. As a noninvasive alternative, Golovin *et al.* (2016) obtained single-shot, θ-resolved spectra equivalent to Fig. 16 by Thomson scattering a 40 fs ($\Delta\omega_0/\omega_0 \sim 0.03$) laser pulse at $\varphi_{\mathrm{coll}} = 170°$ from a ~60 MeV LWFA beam with $\Delta\gamma_e/\gamma_e \sim 0.1$. Under these conditions $\Delta\gamma_e$, σ'_r, and $\Delta\omega_0$ all contributed to the observed spectral width. They then simulated Thomson scatter using a beam of variable γ_e, $\Delta\gamma_e$, and σ'_r to achieve the best global fit to the θ-dependent spectrum. The fit correctly recovered independently measured γ_e and $\Delta\gamma_e$, and output the beam's local σ'_r at the collision point. The latter was observed approximately to double as the beam propagated from the LWFA exit to a point 40 cm downstream, a signature of emittance growth due to space charge.

In addition to σ'_r, a measurement of σ_r is needed to estimate ε_n via Eq. (42). Golovin *et al.* (2016), similar to Kneip *et al.* (2012), Schnell *et al.* (2012), and Köhler *et al.* (2016) earlier (see Sec. III.C.2), used x-ray knife-edge shadowing, which has difficulty resolving $\sigma_r \lesssim 1$ μm beams expected near a LWFA exit. A potential minimally invasive alternative is TR imaged from a thin foil surface to a detector. For $\sigma_r \gg 1$ μm beams, this image is simply a replica of the transverse beam profile. For $\sigma_r \lesssim 1$ μm beams, TR images formed from visible light no longer directly resolve this profile. On the other hand, the imaged profile transforms to the annular point spread function of a single electron [Fig. 9(b), Eq. (38)]. Properties of the central minimum, which has been observed from extremely low ε_n conventional beams (Karataev *et al.*, 2011), can potentially

diagnose σ_r in this range. Bourgeois *et al.* (2012) recovered transverse LWFA beam profiles from CTR images using an iterative algorithm. Near an LWFA exit, a second upstream foil is needed to deflect the intense drive laser pulse.

D. Bunch length measurement

Conventional radio-frequency electron accelerators based on photocathodes illuminated with short laser pulses generally produce electron bunches as short as a few picoseconds, limited by energy spread, and peak currents up to ~100 A. The advent of compact XUV and x-ray free-electron lasers drove the development of magnetic chicane compressors capable of reducing these durations to ~100 fs, while increasing peak current to > 1 kA (Dohlus, Limberg, and Emma, 2005). Such sources have provided drive and injected bunches for recent electron-beam-driven PWFA experiments (Litos *et al.*, 2014; Corde *et al.*, 2015). Time-domain diagnostic methods such as transverse deflection structures (TDSs) (Behrens *et al.*, 2012) and electro-optic (EO) methods (Berden *et al.*, 2007) are well suited, and widely used, for characterizing bunch durations in this range. LWFAs operating in the bubble regime, on the other hand, are capable of producing electron bunches of only a few femtoseconds duration. Measurement of such short bunch durations, and their internal profiles, is one of the greatest new, ongoing diagnostic challenges that plasma electron accelerators have posed. Some researchers have addressed this challenge with creative extensions of time-domain TDS (C. Zhang *et al.*, 2016) and EO (van Tilborg *et al.*, 2006; Debus *et al.*, 2010) methods. Buck *et al.* (2011) introduced a time-domain magneto-optic (MO) method to resolve LWFA bunch durations in the few-fs range (Secs. III.D.1.c and IV.C.3). Most recently, frequency-domain, wide-bandwidth optical TR (OTR) methods have successfully characterized few-fs bunch profiles (Lundh *et al.*, 2013; Heigoldt *et al.*, 2015). Preliminary CDR (Castellano *et al.*, 2001; Fiorito, 2001) and Smith-Purcell radiation (Andrews *et al.*, 2014a) results also appear promising.

1. Time-domain methods

Purely electronic time-domain bunch characterization methods, such as integrating current transformers (Nakamura *et al.*, 2016), resolve bunch duration at best down to the nanosecond level. TDS and EO methods, on the other hand, provide sub-ps characterization.

a. Transverse deflecting structures

A TDS, analogous to a streak camera, imparts a rapidly time-varying transverse momentum kick to an electron bunch that deflects electrons at different longitudinal positions within a bunch to different transverse locations on a downstream detector. Microwave transverse deflecting cavities have resolved longitudinal features of bunches from conventional rf accelerators down to the hundreds of fs scale (Röhrs *et al.*, 2009; Ding *et al.*, 2011; Xiang *et al.*, 2011; Behrens *et al.*, 2012). However, microwave TDSs have not yet been applied to LWFA beams.

The problem of characterizing few-fs LWFA bunches has spurred the proposal (Xiang and Huang, 2007; Bettoni *et al.*, 2016; Dornmair *et al.*, 2016) and laboratory demonstration (Bettoni *et al.*, 2016; C. Zhang *et al.*, 2016) of new TDS configurations that use near-IR light fields (Xiang and Huang, 2007; C. Zhang *et al.*, 2016) or wakefields (Bettoni *et al.*, 2016; Dornmair *et al.*, 2016) with few-fs periods to deflect electrons, instead of microwaves with ns periods. Bettoni *et al.* (2016) proposed and demonstrated a *passive* deflector based on the self-transverse wakefield interaction of the bunch passing off axis through a dielectric-lined or corrugated waveguide. Dornmair *et al.* (2016) proposed to propagate the subject electron bunch obliquely through the zero crossing between focusing and defocusing fields in a linear LWFA, where fields vary rapidly enough to deflect different longitudinal slices of a few-fs bunch in substantially different directions. Xiang and Huang (2007) proposed to propagate the subject bunch through a small aperture in a CTR foil oriented at 45° to its propagation direction. Radiation recoil from backreflected near-IR CTR [see Fig. 10(a)] deflects electrons in proportion to the product of bunch charge and form factor (33e), from which bunch length can be estimated.

C. Zhang *et al.* (2016) used electric fields in the trailing edge of a near-IR LWFA drive pulse to transversely deflect electrons in an energy-chirped bunch accelerating inside a LWFA, thereby locally enhancing their betatron motion in opposite directions every half cycle [see Fig. 17(a)]. The technique could equally well be implemented with a separate

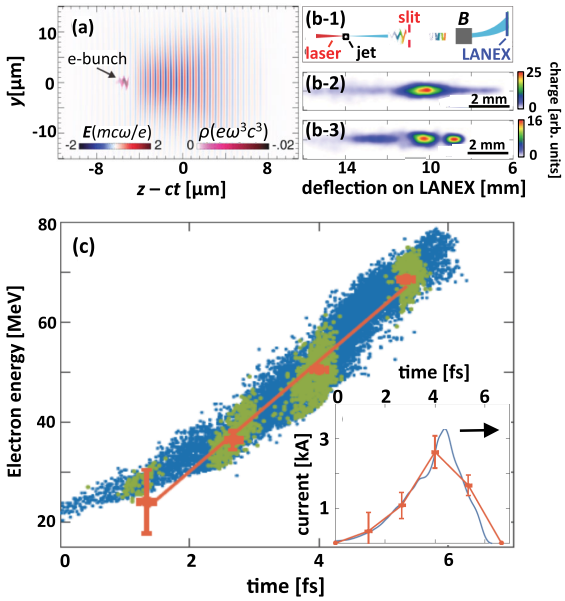

FIG. 17. Time-domain longitudinal profiling of a few-fs LWFA electron bunch. (a) Simulation snapshot showing a chirped, accelerating LWFA e bunch (charge density ρ) with periodic transverse deflections driven by a trailing edge of right-propagating $\lambda = 0.8$ μm drive pulse (field strength E). (b) Measurement of transverse deflections: (b-1) slit after laser-driven jet blocks most deflected parts of bunch, imprinting periodic energy modulation (b-3) on electron spectra recorded at the detector (LANEX screen) of a magnetic spectrometer; (b-2) unmodulated reference electron spectrum with slit removed. (c) Reconstructed energy-time phase profile of a bunch. Inset: energy-integrated longitudinal bunch profile. The arrow indicates the propagation direction. Adapted from C. Zhang *et al.*, 2016.

probe pulse overlapping and copropagating with the accelerating bunch. C. Zhang *et al.* (2016) relied on *energy chirp* within the accelerating bunch to map longitudinal position within the bunch onto energy. Thus when the modulated bunch exited the accelerator, and passed through a slit that blocked its most deflected parts [Fig. 17(b-1)], a periodic series of minima appeared in the energy distribution observed at the detection plane of a magnetic spectrometer [Fig. 17(b-3)]. Simply counting these minima yielded the bunch duration in units of optical half cycles. By analyzing energy-dependent modulation amplitudes, C. Zhang *et al.* (2016) reconstructed the longitudinal shape of the ∼4 fs bunch [Fig. 17(c)]. Although invasive and reliant on energy chirp in its current form, the method of C. Zhang *et al.* (2016) is an important first demonstration of the promise of advanced TDS methods for characterizing few-fs bunches.

b. Electro-optic methods

EO methods convert either the Lorentz-contracted Coulomb field of the electron bunch itself (Casalbuoni *et al.*, 2005) or a subcycle, THz-frequency CTR pulse that the bunch generated (Wilke *et al.*, 2002; Jamison *et al.*, 2003; Berden *et al.*, 2004; Schmidt, 2006; Berden *et al.*, 2007; Steffen *et al.*, 2009) into an optical signal of similar duration. The temporal envelope $|\vec{\mathcal{E}}(t)|$ of the bunch or CTR field approximates the bunch's longitudinal profile. The quasistatic $|\vec{\mathcal{E}}(t)|$ overlaps a time-synchronized, copropagating optical probe pulse in a transparent EO crystal (e.g., ZnTe, GaP), and modulates the probe's polarization via the Pockels effect. A polarization analyzer filters out this modulated portion of the probe [see Fig. 18(a)], which carries information about the duration $\tau_{\mathcal{E}}$ and profile of the $|\vec{\mathcal{E}}(t)|$ impulse. Direct EO detection of the fields of LWFA bunches near the LWFA exit (where they are shortest) is challenging because of strong background signals from the drive laser and irradiated plasma. The CTR approach avoids this background by propagating a CTR THz pulse generated near the accelerator to remote detectors, and has been used for most EO measurements of LWFA bunch length.

Time resolution of EO measurements has been discussed extensively in the literature. A conceptually simple EO measurement of $|\vec{\mathcal{E}}(t)|$ would use a transform-limited probe pulse with duration $\tau_{\mathrm{pr}}^{(0)} \lesssim \tau_{\mathcal{E}}$, then record the intensity of the EO-modulated probe versus the probe-CTR delay Δt. This procedure maps $|\vec{\mathcal{E}}(t)|$ with resolution $\tau_{\mathrm{pr}}^{(0)}$, but requires multiple shots. For single-shot EO measurements, Sun, Jiang, and Zhang (1998) *chirped* the probe to duration $\tau_{\mathrm{pr}}(\mathrm{ch}) > \tau_{\mathcal{E}}$, so that it overlapped the entire $|\vec{\mathcal{E}}(t)|$ profile. The THz field then encoded its waveform onto the probe spectrum [see Fig. 18(a)]. Measurement of the modulated probe spectrum then decoded this waveform, but degraded resolution to $[\tau_{\mathrm{pr}}^{(0)}\tau_{\mathrm{pr}}^{(\mathrm{ch})}]^{1/2}$, because the THz pulse modulated only a portion of the probe spectrum (Sun, Jiang, and Zhang, 1998). However, Berden *et al.* (2004) showed that by instead reconstructing the time-domain *field* of the EO-modulated probe using standard single-shot cross correlation (Salin *et al.*, 1987), one could recover resolution $\sim\tau_{\mathrm{pr}}^{(0)}$ in single-shot bunch

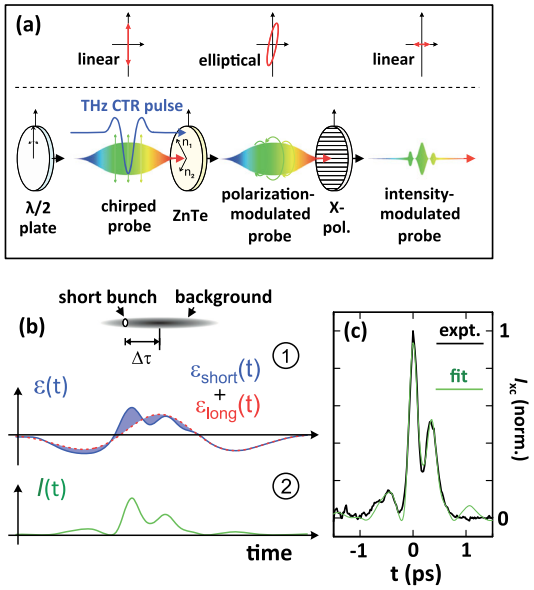

FIG. 18. Electro-optic (EO) bunch length measurement. (a) Schematic procedure. Below dashed line: THz CTR pulse $\vec{\mathcal{E}}(t)$ (solid curve) generated by, and approximating longitudinal profile of, subject electron bunch, copropagates with time-synchronized, linearly polarized, chirped optical probe pulse ($\lambda/2$ = half-wave plate). Via the Pockels effect, $\vec{\mathcal{E}}(t)$ modulates probe polarization in zinc telluride (ZnTe) crystal. The crossed polarization analyzer (X-pol) selects a modulated component, which a photodetector, spectrometer, or cross correlator then characterizes. Above dashed line: probe polarization at each stage of measurement. (b) Schematic depiction of (1) the total CTR field profile $\mathcal{E}(t)$, and (2) corresponding intensity $I(t)$, from time-domain interference of CTR fields $\mathcal{E}_{\mathrm{short}}(t)$, $\mathcal{E}_{\mathrm{long}}(t)$ generated, respectively, by a short 40 MeV bunch and trailing background electrons from LWFA, depicted left-propagating at top. (c) Experimental (thick black solid curve) and fitted (thin solid green curve) $I(t)$ profiles, measured by a cross correlator (xc). (b), (c) Adapted from Debus *et al.*, 2010.

profile measurements. They thereby recovered the profiles of ∼275 fs rms (650 fs FWHM), 50 MeV bunches from a radio-frequency accelerator with ∼50 fs resolution. EO measurements of shorter LWFA bunches, however, encounter further limits from THz transverse optical phonon resonances of common EO crystals (e.g., 5.3 THz for ZnTe, 11 THz for GaP), which absorb THz light and cause group-velocity walk-off of the THz signal from the optical probe. These effects can severely distort fs-duration profiles (Gallot *et al.*, 1999; Casalbuoni *et al.*, 2005). By using thin (100–300 μm) ZnTe crystals, van Tilborg *et al.* (2006) minimized these distortions and obtained an upper limit of ∼50 fs rms (120 fs FWHM) on LWFA bunch duration from a multishot EO measurement.

Debus *et al.* (2010) reduced this upper limit further to 13 fs rms (32 fs FWHM) in a single-shot EO measurement that took advantage of the CTR signal from a relatively long (0.71 ps) low-energy background electron bunch with thermal energy distribution ($kT_e = 6$ MeV) that emerged from a LWFA (45 fs, 0.5 J drive pulse, $\bar{n}_e = 1.5 \times 10^{19}$ cm^{-3} plasma) along with the main quasimonoenergetic [40 ± 7 (rms) MeV, ∼30 pC] bunch. At a CTR foil 5 mm downstream of the

accelerator, the centroid of the background bunch trailed the main bunch by 0.36 ps, with its leading edge overlapping [see Fig. 18(b), top]. Consequently the two contributions to the CTR signal formed a time-domain interference pattern [Fig. 18(b), bottom] that encoded the duration and phase of the ultrashort portion of the signal, and that a cross correlator measured. Debus *et al.* (2010) exploited the strong THz dispersion of the ZnTe crystal to reshape the ultrashort CTR component in a way that enhanced visibility of the interference fringes. A theoretical fit [Fig. 18(c), green curve] of the measured time-domain interference pattern [Fig. 18(c), bold black curve] yielded the reported 32 fs FWHM bunch duration. This milestone notwithstanding, EO measurements remain limited by probe pulse bandwidth and by the accuracy with which EO crystal dispersion can be modeled. Thus they have provided only an upper limit on LWFA bunch duration.

c. Magneto-optic methods

MO methods convert the Lorentz-contracted magnetic field of a relativistic bunch into an optical signal via Faraday rotation. They differ from EO techniques in two key ways. First, since $\vec{B}$ of a bunch is azimuthal (rather than radial), it is probed most effectively with a *transverse* (rather than copropagating) probe. This is because Faraday rotation occurs when $\vec{k}_{\rm pr} \| \vec{B}$ (Kaluza *et al.*, 2010). The transverse geometry, however, places stringent limits on probe pulse duration $\tau_{\rm pr}$, which must be $\lesssim \tau_b$ to avoid transit time broadening. Thus Buck *et al.* (2011) required ~6 fs probe pulses to resolve ~6 fs LWFA bunches. Second, Faraday rotation, unlike the Pockels effect, does not require a noncentrosymmetric crystal such as ZnTe. Faraday rotation can be observed in any transparent magnetized medium, including the plasma in which the wake propagates. Thus phonon resonances do not limit the time resolution of MO methods. Moreover, τ_b can be measured inside the plasma accelerator (Buck *et al.*, 2011). There, since polarization rotation angle $\Delta\phi_{rot} \propto Bn_e$, the largest rotation occurs in the bubble wall, the densest structure in the plasma, and, because of its proximity to the accelerating bunch, the most strongly magnetized. Changes in τ_b during acceleration can be tracked by changing probe delay over multiple shots (Buck *et al.*, 2011). In principle, MO methods could continue to track τ_b outside an LWFA, or to characterize the evolving structure of the bubble wall inside an LWFA. Since MO methods also serve as diagnostics of plasma accelerator structures, we discuss them in detail in Sec. IV.C.3 in conjunction with other transverse probes of such structures.

2. Frequency-domain methods

Spectral bunch length measurements are based on analyzing TR over a bandwidth that can extend from far infrared ($\lambda \sim 30$ μm) to ultraviolet ($\lambda \sim 0.3$ μm), including both coherent and incoherent emission (see Fig. 19). In principle, spectral methods can measure bunch length practically anywhere along an electron beam line with sub-fs resolution in a single shot, while disturbing the beam minimally. The principal challenges lie in calibrating TR spectral intensity accurately and with high spectral resolution over a wide

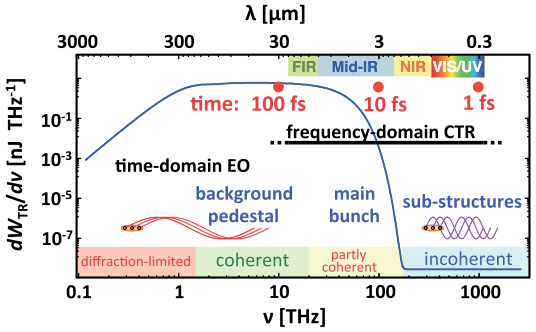

FIG. 19. Overview of time and spectral scales for single-shot profiling of a longitudinal LWFA bunch profile, including (right to left) substructures, main bunch profile, and background pedestal. Solid blue curve: TR spectrum of 200 MeV, 20 pC (Gaussian) bunch with $\tau_b = 10$ fs (FWHM). Horizontal black lines: ranges best suited for time-domain EO (left) and frequency-domain CTR (right) techniques.

wavelength and dynamic range, and in solving the difficult inverse problem of retrieving a sometimes complicated bunch profile uniquely from spectral intensity measurements. Bunches whose shortest features are of duration $\tau_b \gtrsim 100$ fs generate TR predominantly at far-IR wavelengths ($\lambda \gtrsim c\tau_b \sim 30$ μm), a range where sensitive detectors with high spectral resolution are lacking. Time-domain EO methods are thus superior in this τ_b range (see Fig. 19). On the other hand, bunches with $\tau_b \lesssim 10$ fs, i.e., those from strongly nonlinear LWFAs, can be accurately characterized via their mid-IR to UV TR, a range that is amenable to broadband, high-resolution spectral detection.

Leemans *et al.* (2003) first observed THz CTR from LWFA bunches. Ohkubo *et al.* (2007) first attempted to deduce the duration of these bunches from CTR spectra. Bolometer measurements at five discrete far-IR wavelengths on separate shots indicated a cutoff corresponding to $\tau_b \sim 130$ fs. However, the CTR foil was 180 mm downstream of the LWFA, far enough that the bunch not only elongated, but diverged sufficiently during transport to degrade transverse TR coherence. Hence the result may not have accurately reflected τ_b near the LWFA exit. Subsequent experiments have placed the CTR foil closer, often employing movable tape to remove foil damaged by the LWFA drive pulse after each shot.

Glinec *et al.* (2007) used a foil placed only 1.5 mm beyond a quasimonoenergetic LWFA and spectrally analyzed CTR in a single shot over a range $400 < \lambda < 850$ nm [see Fig. 20(a)]. This ~1-octave bandwidth was too narrow to resolve τ_b or the internal bunch structure. However, Glinec *et al.* (2007) observed strong frequency-domain interference fringes (discussed further in Sec. IV.B.2) with period $\Delta\omega = (\Delta t)^{-1}$, consistent with CTR from two sources separated longitudinally by $\Delta t = 74$ fs. A model of the CTR spectra suggested that these sources were a ~10 fs bunch in the first wakefield bucket, followed by a few-fs bunch, or one with a substructure on this scale, in the second [see Fig. 20(a), inset]. Later Lundh *et al.* (2013) used similar spectral interference fringes to diagnose bunch distribution among multiple buckets.

Lundh *et al.* (2011) analyzed CTR and ITR spectra from a foil 15 mm downstream of a quasimonoenergetic (85 MeV) LWFA

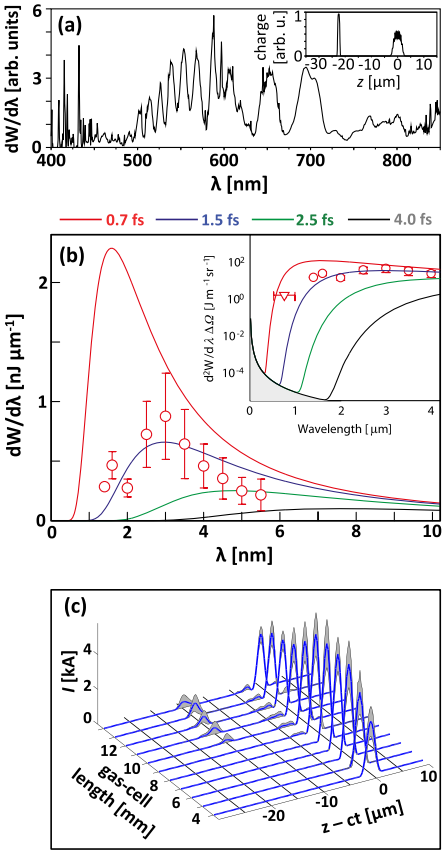

FIG. 20. CTR spectra of electron bunches from strongly nonlinear LWFAs and longitudinal bunch profile reconstruction. (a) Single-octave CTR power spectrum with periodic modulations, originating from electron bunches separated longitudinally by $\sim\lambda_p$, as shown in the inset. Adapted from Glinec *et al.*, 2007. (b) Three-octave CTR spectrum of electron bunches injected into a strongly nonlinear LWFA by colliding laser pulses, recorded by an IR monochromator (circles) and a visible spectrometer (triangle). Solid curves: calculated CTR spectra for indicated bunch durations, assuming Gaussian profiles. Inset: data divided by a solid angle of a solid collection angle of detection instrument. Gray area: ITR intensity. Adapted from Lundh *et al.*, 2011. (c) Longitudinal profiles (solid blue curves) of bunches from LWFA driven in a gas cell of adjustable length (3–14 mm), reconstructed from four-octave single-shot CTR spectra. The gray band around each curve indicates variance over a 30-shot data set. (c) Adapted from Heigoldt *et al.*, 2015.

over a 3.3-octave range extending from mid-IR ($\lambda = 5.5$ μm) to visible ($\lambda = 0.55$ μm) wavelengths [see Fig. 20(b)]. They combined an optical spectrometer with an infrared monochromator that could acquire only the IR portion of the spectra over multiple shots. Nevertheless, a fit based on Eq. (39) to the measured TR spectra, which exhibited a coherent threshold at $\lambda \approx 1$ μm, yielded a most probable ensemble duration 1.4–1.8 fs (rms). The researchers could not determine whether this was the duration of the entire bunch or the shortest feature in a longer bunch, nor whether their use of colliding optical pulse injection influenced the bunch duration. Nevertheless, this remains the shortest τ_b reported from a LWFA.

Bajlekov *et al.* (2013) and Heigoldt *et al.* (2015) demonstrated the first single-shot high-resolution spectroscopic bunch length measurements by distributing > 4 octaves of CTR bandwidth among visible (0.4–1.1 μm), near-IR (1.1–1.8 μm), and mid-IR (1.7–7.1 μm) spectrometers. In these experiments, a ~50 TW laser pulse drove a nonlinear LWFA in $\bar{n}_e = 3.9 \times 10^{19}$ cm^{-3} plasma in a cell that tuned in length L from 3 to 14 mm in 1 mm increments. As L increased from 3 mm, Heigoldt *et al.* (2015) observed the electron energy increased to a maximum ~650 MeV at $L = 9$ mm, consistent with the pump depletion length $L_{\rm pd}$. For $L < 9$ mm, they observed smooth CTR spectral profiles and correspondingly reconstructed longitudinal charge profiles $\rho_{\parallel}(t)$ consisting of single bunches of duration 5 fs (FWHM) [see Fig. 20(c)]. For $L > 9$ mm, on the other hand, they observed CTR spectra that were modulated at a single dominant frequency [as in Fig. 20(a)]. Correspondingly, the reconstructed $\rho_{\parallel}(t)$ included an additional bunch trailing by $\Delta t \approx 50$ fs [Fig. 20(c)], slightly less than a plasma period ($2\pi/\omega_p = 56$ fs). As $\bar{n}_e$ changed, Δt tracked, but remained less than $2\pi/\omega_p$. They conjectured that the trailing bunch was injected within the first LWFA cavity in response to a transition from LWFA to beam-driven PWFA starting at $L \approx L_{\rm pd}$. Indeed, such tunable bunch pairs are of interest as drive-witness pairs for tabletop PWFAs of interest in turn for compact electron acceleration free of dephasing. These results demonstrate the ability of multioctave-bandwidth CTR to reconstruct $\rho_{\parallel}(t)$ simultaneously on the few-fs scale of a single bunch and the tens-of-fs scale of separated bunches. They also demonstrate a quantitative diagnosis of bunch evolution with propagation through a LWFA.

CTR spectral intensity measurements diagnose electron bunch profiles indirectly. As discussed in Sec. III.A.4, these yield the *magnitude* $|F_{\parallel}(\omega,\theta)|$ of the form factor via Eq. (35), but not its spectral *phase*, which is required to extract $\rho_{\parallel}(z)$ directly via Eq. (34). In principle, the spectral phase of $F_{\parallel}$ could be determined from the spectral phase of the CTR field [via Eq. (39)], measured by CTR interferometry. However, this has so far proven impractical to do with high resolution over a multioctave bandwidth. Hence the inverse problem of reconstructing $\rho_{\parallel}(z)$ from CTR spectra is ill posed, analogous to determining the structure of a molecule from a diffraction pattern generated by coherent x rays. Iterative algorithms (Bajlekov *et al.*, 2013; Heigoldt *et al.*, 2015; Bakkali Taheri *et al.*, 2016) are used to reconstruct $\rho_{\parallel}(z)$, subject to physical constraints, from spectral intensity measurements alone. Briefly, most reconstruction algorithms are variants of the following approach: one starts with an initial guess $\rho_{\parallel}^{(0)}(z)$, calculates its complex Fourier transform $|G(k)|\exp[i\psi(k)]$, then replaces the amplitude $|G(k)|$ with the experimental $|F_{\parallel}(k)|$. An inverse Fourier transform then yields a revised estimate $\tilde{\rho}_{\parallel}^{(0)}(z)$. Finally, one forcibly adjusts $\tilde{\rho}_{\parallel}^{(0)}(z)$ to satisfy physical constraints: e.g., it must be real, positive definite, and nonzero only within a realistic temporal range, yielding $\rho_{\parallel}^{(1)}(z)$ to complete the first iteration. One then reiterates until, hopefully, the solution converges. Challenges include ensuring convergence, demonstrating uniqueness, and quantifying uncertainty of the result based on uncertainties of measured inputs. As with many inverse problems, simply

searching for one "needle," i.e., a best fit to available data, in a figurative haystack of possibilities is not enough. One must exhaust a sizable portion of the haystack to ensure there is only one, or no, needle left (Tarantola, 2006).

Current bunch profile reconstruction algorithms solve a 1D problem of reconstructing $\rho_{\parallel}(z)$ from Ω-integrated CTR power spectra. Expanding retrieval algorithms and CTR spectral data to two and three dimensions, analogous to x-ray scattering from molecules, will be an important future direction. Adding an angular dimension to spectral data not only enables simultaneous access to $\rho_{\perp}(\vec{r}_{\perp})$, but can reduce ambiguities in reconstructed $\rho_{\parallel}(\vec{r}_{\parallel})$ that are fundamental in the corresponding 1D problem. Diffraction radiation from bunches passing through noninterceptive slits and apertures adds such a dimension (Karlovets and Potylitsyn, 2008) and has led to reconstructions of transverse and longitudinal profiles of ∼ps bunches that benchmark successfully with independent diagnostics (Castellano *et al.*, 2001; Fiorito, 2001). Its noninvasiveness is especially attractive for ∼μm-scale LWFA bunches. DR thus appears ripe for an extension to a few-fs LWFA bunches, but will require small apertures to avoid short-wavelength and short-time-scale cutoffs and hence good pointing stability. Similar remarks apply to the Smith-Purcell radiation, emitted when a relativistic beam passes over a grating, i.e., a regular array of diffractive radiators placed within a vacuum formation length (Smith and Purcell, 1953; Brownell, Walsh, and Doucas, 1998; Karlovets and Potylitsyn, 2006; Kesar, 2010). The freedom to tailor grating dimension, spacing, blazing angle, groove shape, and material to a specific wavelength or time-scale range makes the Smith-Purcell radiation a versatile bunch length diagnostic. Indeed, the rf accelerator community has demonstrated the Smith-Purcell bunch length measurement down to sub-ps (Korbly *et al.*, 2006; Blackmore *et al.*, 2009; Andrews *et al.*, 2014a, 2014b), even a few-fs (Bartolini *et al.*, 2012) resolution. Extending these methods to plasma-accelerated beams should have high priority in future research.

IV. DIAGNOSTICS OF PLASMA ACCELERATOR STRUCTURES

Diagnostics of electron and positron beams only indirectly characterize the plasma structure that captured and accelerated them. Beam diagnostics alone rarely pinpoint the cause of suboptimal performance, or provide clear guidance on corrective action. Direct observation of the plasma structure in the laboratory, and comparison of laboratory images with simulations, then become essential. This is challenging for four reasons:

(i) The structures are microscopic. For the $\bar{n}_e$ range of interest for particle acceleration (see Sec. II.A.4) accelerator cavities have overall dimension $100 \gtrsim \lambda_p \gtrsim 10$ μm. Moreover, nonlinear wakes possess sharp micron-scale substructures (see Fig. 1). Diagnostic probes must resolve these spatial scales.

(ii) The structures have low optical contrast, for wavelengths $\lambda \ll \lambda_p$ that resolve structural details. For example, for a $\lambda = 1$ μm optical probe, an evacuated bubble in $\bar{n}_e = 10^{18}$ cm^{-3} plasma differs in refractive index by only $\Delta\eta \approx n_e/2n_{\rm cr} = 0.0005$ from the surrounding plasma.

(iii) The structures propagate at $\sim c$ over mm to meter distances. To minimize image blurring, a probe should copropagate with the structure. However, even if temporal slip between probe and wake is negligible, wakes can evolve on a ps time scale in ways that are important to diagnose. A copropagating probe integrates over this evolution. Thus diagnostics must combine longitudinal and transverse probing.

(iv) The structures are transient and prone to shot-to-shot variation. Single-shot probes are desirable.

These challenges have no counterpart in conventional rf acceleration, which uses macroscopic, stationary, permanent structures. This section reviews plasma wake diagnostics and results that have emerged uniquely with development of plasma-based electron accelerators. Table II lists five categories of plasma wake properties (first column) and new methods that have emerged to diagnose them (second column) that we review later in Sec. IV (fourth column). These new methods address challenges (i)–(iv) using wide-bandwidth optical probe pulses or ultrashort electron witness bunches (see Table II, third column) that are temporally synchronized with the wake structure. The earliest diagnostics detected wakes globally, without resolving internal structure (Sec. IV.A). Sub-λ_p resolution initially came at the cost of multishot probing and integrating over wake evolution (Sec. IV.B). Development of holistic, single-shot probes that resolve internal wake structure and dynamics is a more recent, and ongoing, field of research (Secs. IV.C and IV.D). Examples of quantitative comparison of diagnostic measurements with simulation results are described throughout. Clayton (2009) previously reviewed several early LWFA structure diagnostics. Here we complement that review and emphasize new developments since then.

A. Light emission and scattering from plasma waves

1. Plasma self-emission

Just as electromagnetic radiation from plasma-accelerated electrons (Sec. III.A) underlies multifarious beam diagnostics (Secs. III.B.3, III.C.2, III.C.3, and III.D), electromagnetic emission from the plasma wave itself helps to diagnose wake structure and dynamics. Hamster *et al.* (1993, 1994) first detected laser wakefields by observing far-infrared radiation (FIR) that they emit, using a liquid-helium-cooled bolometer in conjunction with a Fourier transform spectrometer. As $\bar{n}_e$ changed from $\sim 10^{15}$ to $\sim 10^{19}$ cm^{-3}, FIR frequency closely tracked ω_p in the few-THz range where it was measurable, while FIR intensity peaked at the resonant condition, which they defined as $\omega_p\tau = 2$, corresponding to $\bar{n}_e \approx 7\times 10^{16}$ cm^{-3} and laser pulse duration $\tau = 120$ fs. This showed that the FIR originated from collective charge density oscillations of a standard LWFA (see Sec. II.B.1). The observed time duration and angular distribution of FIR qualitatively diagnosed the wake's lifetime and 3D structure, respectively.

TABLE II. Properties of plasma wakes and methods developed to diagnose them. Key to wake properties: Plasma frequency (ω_p), wave vector ($\vec{k}_p$), wavelength (λ_p); $\delta n_e(z,\zeta,r)$ = wake electron density profile as a function of driver propagation distance (z), distance behind driver (ζ), and distance r from propagation axis; $\vec{E}(\zeta,r)$ = wake electric field profile. In column 3, the probe is described as optical (o) or electron (e); propagating longitudinally (L), transversely (T), or obliquely (O) to $\vec{k}_p$; having duration much less than ($\ll$), less than ($<$), similar to ($\approx$), or greater than ($>$) a plasma period τ_p; and diagnosing the wake in single (s) or multi (m) shot.

Wake property	Diagnostic method	Probe properties	Section
Wave-breaking, sheath dynamics	Light emission[a]	No probe	IV.A.1
Global ω_p, $\vec{k}_p$, $\delta n_e(\zeta)$	CTS[b]	o, L, or T; >, s, or m	IV.A.2
Quasistatic	FDI[c]	o, L, <, m	IV.B.2
sub-λ_p	FDH[d], FDS[e]	o, L, >, s	IV.C.1 and IV.C.2
$\delta n_e(\zeta,r)$	Faraday rotation[f]	o, T, $\ll$, s	IV.C.3.a
Structures	Transverse shadowgraphy[g]	o, T, $\ll$, s	IV.C.3.b
Evolving sub-λ_p	Shadowgraphic movies[h]	o, T, $\ll$, m	IV.D.1
$\delta n_e(z,\zeta,r)$	FDSC,[i] FDT[j]	o, O, >, s	IV.D.2
Structures	MOPI[k]	o, O, <, m	IV.D.3
Quasistatic	Delayed witness bunch[l]	e, L, <, m	IV.B.1
Sub-λ_p $\vec{E}(\zeta,r)$	Transverse radiography[m]	e, T, $\ll$, s	IV.C.4
Profiles	Longitudinal radiography[n]	e, L, $\approx$, s	IV.C.4

[a](Hamster *et al.*, 1994;Thomas *et al.*, 2007; Helle *et al.*, 2010).
[b]Collective Thomson scattering (Clayton, 2009).
[c]Frequency-domain interferometry (Siders, LeBlanc, Fisher *et al.*, 1996; Marquès *et al.*, 1997).
[d]Frequency-domain holography (Matlis *et al.*, 2006).
[e]Frequency-domain shadowgraphy (Dong *et al.*, 2010b).
[f](Kaluza *et al.*, 2010).
[g](Buck *et al.*, 2011).
[h](Sävert *et al.*, 2015).
[i]Frequency-domain streak camera (Li, Tsai *et al.*, 2014).
[j]Frequency-domain tomography (Li, Zgadzaj *et al.*, 2014).
[k]Multiobject-plane imaging (Z. Li *et al.*, 2013).
[l]Applied to PWFA (Rosenzweig *et al.*, 1989; Kallos *et al.*, 2008).
[m](Zhang *et al.*, 2017).
[n]Applied to PWFA (Clayton *et al.*, 2016).

In strongly nonlinear wakes, light emission is useful for diagnosing ultrafast, small-scale phenomena beyond the resolution of impinging probe pulses. One example is "wave-breaking" radiation (Thomas *et al.*, 2007; Thomas, 2010), a broadband light flash accompanying electron injection into a plasma bubble. Used in conjunction with transverse optical probes, it can pinpoint injection spatially and temporally within the larger wake formation and acceleration process. Figure 35 and accompanying text (Sec. IV.D.1) show an example. A second example is radiation emitted at the second harmonic of the drive pulse frequency from the ultrathin electron sheath surrounding a plasma bubble [see Figs. 1(b)–1(d)]. Here the source current is contained within a region smaller than the emitted wavelength, while fulfilling a Cherenkov-angle condition for the laser second harmonic (Gordon *et al.*, 2008). The resulting electro-optic shock is emitted in a characteristic ring pattern (Helle *et al.*, 2010).

The distinctive spectral, angular, and temporal features of wake self-emission have the potential to become quantitative diagnostics with advances in simulation capabilities. Recent work aims to calculate quantitative features of observed emission, such as angle- and time-resolved spectra, within particle-in-cell (PIC) simulations, taking into account all simulated particles (Pausch *et al.*, 2014; Pausch, Debus *et al.*, 2014).

2. Light scattering

Among the earliest diagnostics of plasma accelerator structures were experiments that scattered probe pulses of duration $\tau_{\rm pr} \gg \omega_p^{-1}$ from laser-driven electron plasma waves (EPWs). The theory (Froula *et al.*, 2011) and experimental approach (Villeneuve *et al.*, 1991; Clayton, 2009) resemble those for light scattering from ultrasonic waves in transparent media (Born and Wolf, 1980). In these experiments, a probe pulse of frequency $\omega_{\rm pr} \gg \omega_p$ and wave vector of magnitude $|\vec{k}_{\rm pr}| \gg |\vec{k}_p|$ impinged on a plasma wave (frequency ω_p, wave vector $\vec{k}_p$) either collinearly ($\vec{k}_{\rm pr} || \vec{k}_p$), transversely ($\vec{k}_{\rm pr} \perp \vec{k}_p$), or obliquely. Uncorrelated individual plasma electrons scatter probe light at frequency $\omega_{\rm pr}$ in a dipole pattern, due to their individual light-driven oscillatory motion, a process known as linear Thomson scattering (Jackson, 1999). However, a collective electron density oscillation $\delta n_e(\vec{x},t)$ driven above the level of thermal fluctuations, i.e., $k_p\lambda_D < 1$, where λ_D is the plasma Debye length (Froula *et al.*, 2011), appears to the probe as a refractive index grating

$$\eta(\vec{x},t)-\eta_0=\{1-[\bar{n}_e+\delta n_e(\vec{x},t)]/n_{\rm cr}\}^{1/2}-\eta_0 \approx \delta n_e(\vec{x},t)/2n_{\rm cr} \quad (43)$$

moving at phase velocity $\omega_p/|\vec{k}_p|$. Here $\eta_0=[1-\bar{n}_e/n_{\rm cr}]^{1/2}$ is the refractive index of unperturbed plasma, and the second line is valid for $\omega_{\rm pr}\gg\omega_p$. This grating imprints a moving sinusoidal phase modulation on the probe, resulting in scattered light at frequency $\omega_{\rm pr}\pm\omega_p$ and wave vectors $\vec{k}_{\rm pr}\pm\vec{k}_p$, over and above the linear Thomson-scattering background. This is known as linear *collective* Thomson scatter (CTS) (Slusher and Surko, 1980; Villeneuve *et al.*, 1991). For $\tau_{\rm pr}\gg\omega_p^{-1}$, the probe bandwidth can be much less than ω_p. If so, the CTS spectrum consists of discrete Stokes and anti-Stokes sidebands well outside the incident probe bandwidth, making it easily distinguishable in a spectrometer from background Thomson-scattered probe light. Moreover in the same limit, a *collimated* probe has wave-vector spread much smaller than $|\vec{k}_p|$. When such a probe interacts transversely with an EPW, CTS light scatters at discrete angles $\theta\approx|\vec{k}_p|/|\vec{k}_{\rm pr}|$ (typically a few degrees) from $\hat{k}_{\rm pr}$, well outside the transmitted probe diffraction cone, providing additional spatial discrimination. Thus frequencies $\omega_{\rm pr}\pm\omega_p$ and wave vectors $\vec{k}_{\rm pr}\pm\vec{k}_p$ of CTS light are the main observables. Analysis yields the frequency ω_p, wave vector $\vec{k}_p$, and local amplitude δn_e of the EPW. When $\tau_{\rm pr}$ is less than the EPW lifetime, the time evolution of δn_e behind the driver can also be measured by varying pump-probe delay Δt (Le Blanc *et al.*, 1996; Ting *et al.*, 1996). Nonlinear EPWs generate harmonics $\pm m\omega_p$ $(\pm m\vec{k}_p)$, where $m=1,2,3,\ldots$ of the frequency (wave-vector) shift of scattered light as an additional diagnostic (Everett *et al.*, 1995). When one or more harmonics is (are) present, analysis of harmonic *ratios* (Lal *et al.*, 1997) enables more accurate estimates of absolute δn_e than estimates based on $m=\pm1$ sidebands alone, which are subject to uncertainties in estimating propagation distance and transverse dimension of the EPW. Light scattering experiments, however, do not resolve internal sub-λ_p structure of the EPW. Clayton (2009) reviewed light scattering from plasma accelerator structures in detail. Thus here we discuss only two examples.

Figure 21(a) (left) schematically illustrates experiments by Le Blanc *et al.* (1996) and Ting *et al.* (1996) in which a sub-ps probe pulse ($\lambda_{\rm pr}=0.53$ μm, green rectangle) *copropagated* at delay Δt behind a drive pulse (peak power $P=1$–2 TW, $\tau=0.4$ ps, $\lambda_{\rm pu}=1.053$ μm, red rectangle) in a gas jet (gray) that the drive pulse ionized to density $0.75\times10^{18}<\bar{n}_e<3\times10^{18}$ cm^{-3} (Le Blanc *et al.*, 1996) or $\bar{n}_e\approx10^{19}$ cm^{-3} (Ting *et al.*, 1996). When P exceeded the critical power $P_{\rm cr}=17(\omega^2/\omega_p^2)$ GW for relativistic self-focusing, the drive pulse efficiently drove a SM LWFA (blue rectangle, see Sec. II.B.2). Under conditions of Le Blanc *et al.* (1996), the wake produced a strong collimated ~2 MeV electron beam (Umstadter *et al.*, 1996). In both experiments, the probe pulse overlapped 10–20 periods of this wake. A spectrometer, aided by a notch filter, isolated and recorded spectra of the transmitted wake-modulated probe as Δt varied over multiple shots. Results showed

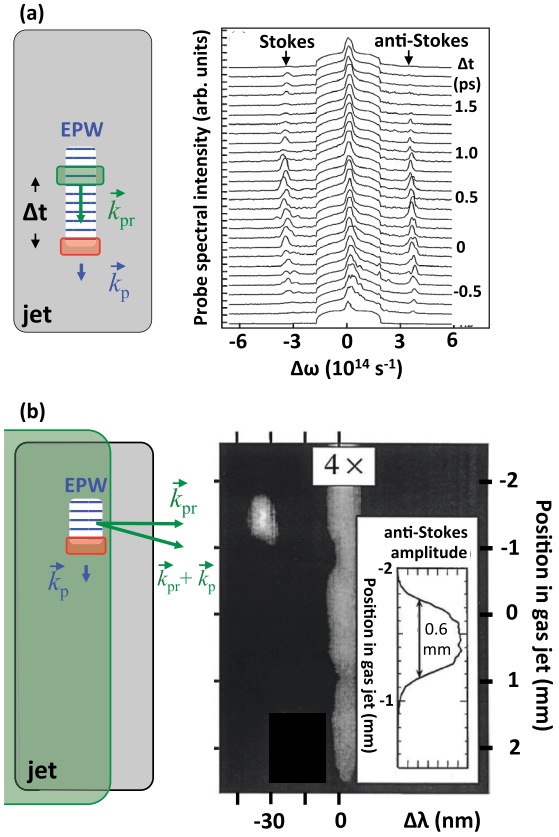

FIG. 21. Collective Thomson scatter from self-modulated LWFAs. (a) Left: schematic of EPW (blue rectangle with horizontal lines denoting wave peaks, wave vector $\vec{k}_p$) in He jet (large gray rectangle, ionized to $\bar{n}_e=3\times10^{19}$ cm^{-3}), with probe pulse (green rectangle, wave vector $\vec{k}_{\rm pr}$, $\tau_{\rm pr}=0.4$ ps) *copropagating* top to bottom at delay Δt behind drive pulse (red rectangle at front of EPW). Right: probe pulse spectra for $-1<\Delta t<2$ ps showing growth and decay of Stokes and anti-Stokes sidebands at $\Delta\omega=\mp\omega_p$, acquired over multiple shots. Adapted from Le Blanc *et al.*, 1996. (b) Left: same as (a), but with 20 ps, loosely focused ($w_0\approx5$ mm) probe pulse (large green rectangle) illuminating the entire length of the jet, propagating *transversely* to drive pulse. Right: space-resolved spectrum of anti-Stokes ($\Delta\lambda=-35$ nm) light scattered in direction $\vec{k}_{\rm pr}+\vec{k}_p$ ($3.4°\pm1.9°$ from $\vec{k}_{\rm pr}$) from EPW localized at $-2<z<-1$ mm, acquired in one shot along with background unshifted probe light ($\Delta\lambda=0$, attenuated 4 times). Inset: z lineout of anti-Stokes scattered light and thus of EPW amplitude. (b) Adapted from Gordon *et al.*, 1998.

Δt-dependent Stokes and anti-Stokes sidebands [Fig. 21(a), right] with amplitudes proportional to $\delta n_e(\Delta t)$. Using these data, Le Blanc *et al.* (1996) measured the EPW growth rate: sidebands appeared at $\Delta t\approx-0.5$ ps, then grew to a maximum corresponding to $\delta n_e/\bar{n}_e\sim0.1$ at $\Delta t\approx0.3$ ps. This wake, however, started earlier, and grew more slowly than a 2D theory of forward Raman scattering instability in uniform preformed plasma predicted (Decker *et al.*, 1996; Tzeng, Mori, and Decker, 1996). Le Blanc *et al.* (1996) thus concluded that plasma noise generated at the ionization front ($\Delta t\approx-0.7$ ps) seeded the instability earlier than expected,

and that a 3D theory (Esarey, Krall, and Sprangle, 1994; Andreev, Kirsanov, and Gorbunov, 1995) was required to explain its growth.

Both Le Blanc *et al.* (1996) and Ting *et al.* (1996) measured the EPW decay rate with different results. Le Blanc *et al.* (1996) found that sidebands (and thus δn_e) decayed to undetectable levels within 1.5 ps [Fig. 21(a), right]. They attributed the rapid decay to efficient conversion of collective EPW energy into electron beam energy. Ting *et al.* (1996), on the other hand, working at higher $\bar{n}_e$ with less efficient electron beam production, found that probe sidebands persisted out to $\Delta t \approx 5$–7 ps. They explained the slower decay rate via conversion of the EPW into ion acoustic waves (IAWs), a subject of considerable prior theoretical work (Zakharov, 1972; Mora *et al.*, 1988). They confirmed this by observing a sharp increase in scatter of the central probe spectral peak at angle ~30° from the pump-probe propagation axis over time interval $5 \lesssim \Delta t \lesssim 30$ ps, correlated with decay of the Stokes or anti-Stokes sidebands. They attributed this rising signal to CTS from growing EPW-fed, slow IAWs, which they observed to decay subsequently over $30 \lesssim \Delta t \lesssim 100$ ps. The physics of converting EPWs to IAWs, and to ion motion generally, is resurfacing in recent theoretical (Vieira *et al.*, 2012; Lotov, Sosedkin, and Petrenko, 2014; Sahai *et al.*, 2016; Sahai, 2017) and experimental (Zgadzaj *et al.*, 2016) wake diagnostic work because it is a strong plasma heating mechanism (see Sec. IV.D.3).

Filip *et al.* (2004) collinearly probed PBWAs (see Sec. II.B.3) driven by a two-color CO_2 laser in plasma of density $10^{16} \lesssim \bar{n}_e \lesssim 10^{17}$ cm^{-3}. At such low $\bar{n}_e$, special techniques were required to distinguish Stokes and anti-Stokes sidebands from the unshifted probe spectrum (Filip *et al.*, 2003). CTS showed that high δn_e wakes were achievable even when the beat frequency was far from ω_p. With the emergence of TW, ps CO_2 lasers (Polyanskiy, Babzien, and Pogorelsky, 2015), researchers are now also beginning to probe CO_2-laser-driven SM LWFAs, first studied theoretically by Andreev *et al.* (2003), using collinear CTS.

Figure 21(b) (left) schematically illustrates a complementary "transverse" CTS geometry in which a probe pulse crossed the path of a EPW of transverse width $\lesssim \lambda_p$ at ~90° (i.e., $\vec{k}_{\rm pr} \perp \vec{k}_p$). This geometry has characterized PBWAs (Clayton *et al.*, 1993) and the decay of laser-driven EPWs into a manifold of daughter waves (Everett *et al.*, 1995). Figure 21(b) (right) shows an example of transverse CTS data (Gordon *et al.*, 1998) from a SM LWFA that produced copious collimated electrons up to 94 MeV energy when driven in $\bar{n}_e = 1.4 \times 10^{19}$ cm^{-3} plasma by tightly focused drive pulses of similar wavelength and duration ($\lambda = 1.053$ μm, $\tau = 1$ ps), but higher power ($P \approx 20$ TW) than those used in the experiments of Le Blanc *et al.* (1996) and Ting *et al.* (1996). The duration ($\tau_{\rm pr} \approx 20$ ps) and radius ($w_0 \approx 0.5$ cm) of the transverse probe pulse ($\lambda_{\rm pr} = 0.53$ μm) were adjusted so that it illuminated the wake during its entire transit through the ~0.1 cm long gas jet. Gordon *et al.* (1998) used anti-Stokes ($\Delta\lambda \approx -35$ nm) light scattered at $\vec{k}_{\rm pr} + \vec{k}_p$ (~3.4° from $\vec{k}_{\rm pr}$) to image the EPW propagation path onto the slit of an imaging spectrometer. In Fig. 21(b) (right), this anti-Stokes image is visible at $\Delta\lambda \approx -35$ nm, from only a ~1 mm section ($-2 < z < -1$ mm) of the gas jet, along with background unshifted probe light ($\Delta\lambda = 0$) that scattered from the jet's entire length. This showed that the wake had significant amplitude only in this 1 mm section, because of tight pump focus there. For looser pump foci, on the other hand, wakes persisted for longer distances (up to the entire jet), but yielded lower-energy electrons. Transverse CTS provides this information about the wake's trajectory in a single shot, information unavailable from copropagating CTS because it integrates over the main pulse's propagation direction. The complementarity of diagnostic information available from copropagating (Secs. IV.B, IV.C.1, and IV.C.2) versus transverse (or oblique) probes (Secs. IV.C.3, IV.C.4, IV.D, and IV.E) is a recurring theme throughout the remainder of this section.

B. Multishot sub-λ_p probes

Optical diagnosis of sub-λ_p structure of plasma accelerators requires probes of bandwidth $\Delta\omega_{\rm pr} > \omega_p$. This precludes CTS, since Stokes and anti-Stokes shifts would be less than $\Delta\omega_{\rm pr}$. In this section, we describe experiments in which optical or electron probes of duration $\tau_{\rm pr} < \omega_p^{-1}$ copropagate behind the wake driver with controlled time delay Δt. The probe overlaps a sub-λ_p longitudinal slice of the structure, which modifies the probe. Photon frequency, electron energy analysis, or optical interferometry detects these modifications. In addition, the wake's transverse fields or density gradients deflect probe electrons or photons sideways. These transverse probe profile modifications are also detected downstream of the accelerator. Thus by varying Δt over multiple shots, these methods can map out both longitudinal and transverse wake structures with sub-λ_p resolution, if the structure is stable from shot to shot. The copropagating geometry also maximizes the probe's interaction length with the slice of the structure that it overlaps, thus optimizing sensitivity to low-contrast substructures.

1. Electron witness bunches

Beam-driven PWFAs (Chen *et al.*, 1985) were not only the first plasma-based electron accelerators to be demonstrated in the laboratory, but the first to be spatially and temporally diagnosed. The Advanced Accelerator Test Facility at Argonne National Laboratory (ANL) measured wakefields of an electron drive bunch ($E_e = 21$ MeV, $2 \le Q \le 4$ nC, $\tau_b = 16$ ps) through their effect on a 15 MeV witness bunch created by degrading the energy of part of the drive bunches with a carbon target and splitting them away with a dipole magnet. Separate beam transport lines delivered the two synchronized bunches collinearly to the plasma, the witness leg containing an adjustable "trombone" section that varied witness delay Δt [see Fig. 22(a)]. A dipole magnet spectrometer after the plasma measured witness bunch energy with ~0.01 MeV resolution, and transverse witness bunch deflection perpendicular to the spectrometer dispersion plane, as Δt varied. Rosenzweig *et al.* (1988, 1989) used this facility to drive and probe wakes in ~30-cm-long plasma of density $\bar{n}_e \approx 10^{13}$ cm^{-3}. Available bunch duration $\tau_b \sim 16$ ps (FWHM) dictated this choice of $\bar{n}_e$, which enabled these

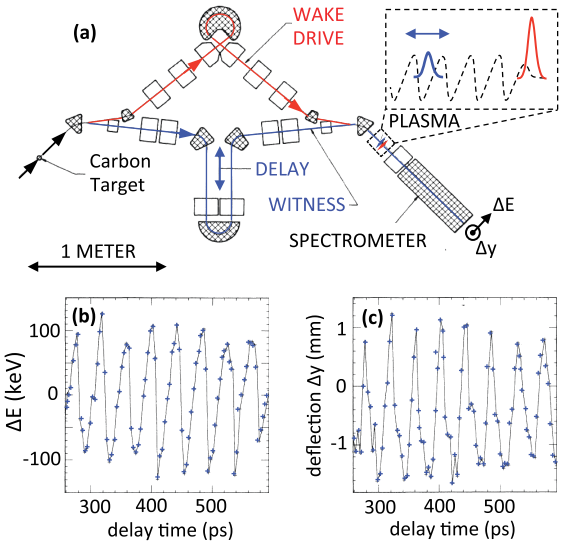

FIG. 22. Measurements of local electric field $\vec{E}(r, z-ct)$ of e-bunch-generated nonlinear plasma waves in $\bar{n}_e = 0.7\times10^{13}$ cm^{-3} plasma. (a) Schematic experimental setup. Carbon target decreased energy of part of incoming 21 MeV electron drive bunches (left) to create 15 MeV witness bunch, which dipole magnets (cross-hatched boxes) separated, guided through paths of variable relative length, and recombined collinearly with controlled time delay Δt. Upper right inset: schematic of plasma wave potential (dashed curve) and right-propagating drive (solid red, right) and witness (solid blue, left) bunches. Adapted from Rosenzweig *et al.*, 1988. (b) Energy change ΔE and (c) transverse deflection Δy perpendicular to energy dispersion plane of witness bunch vs Δt. (b), (c) Adapted from Rosenzweig *et al.*, 1989.

bunches to resonantly drive and resolve individual plasma oscillations of period $\omega_p^{-1} \sim 30$ ps [see Figs. 22(b) and 22(c)].

Initial experiments drove the plasma with 2 nC bunches of longitudinal (s) and radial (r) half-widths $\sigma_s \approx \sigma_r \approx 2.1$ mm, yielding bunch density $n_b \approx 0.015\bar{n}_e$ (Rosenzweig *et al.*, 1988). Since $n_b \ll \bar{n}_e$, these excited linear wakes with accelerating field $E_z^{(\max)} \ll E_0 \sim 300$ MV/m [see Eq. (4a)] and density perturbation $\delta n_e \ll \bar{n}_e$ (Lu *et al.*, 2005). These wakes modulated witness bunch centroid energy E_e sinusoidally as a function of Δt, with amplitude $\Delta E_e^{(\max)} \approx \pm 0.05$ MeV. The quotient of $\Delta E_e^{(\max)}$ and acceleration length yielded an effective gradient $E_z^{(\mathrm{eff})} \sim 0.05$ MeV/0.3 m $\approx$ 0.16 MV/m. However, fits of the data to a 2D linear theory of plasma wakes (Chen, 1985) showed that fields as high as $E_z^{(\max)} \approx 1$ MV/m $\approx 0.03E_0$ were generated. Radial averaging over wake and witness bunch profiles accounted for the discrepancy.

In follow-up experiments, Rosenzweig *et al.* (1989) delivered fivefold denser bunches (4 nC, $\sigma_r \approx 1.4$ mm) to the plasma. These self-pinched, increasing the peak current further. They excited nonlinear wakes in which $E_z(z-ct)$ oscillated in a sawtooth waveform [see Fig. 22(b)]. Fourier analysis showed that the waveform contained harmonics of ω_p, as expected for a nonlinear wake. Transverse deflections of the witness bunch also oscillated with Δt in phase with E_z [see Fig. 22(c)], simultaneously profiling radial fields $E_r(z-ct)$. 2D modeling suggested peak E_z up to 5 MV/m was achieved, with $E_z^{(\mathrm{eff})}$ smaller as before. Two features of these results were surprising. First, wake oscillations, despite their distinct nonlinearity, were observed out to 18 periods behind the driver with little degradation in form or amplitude. Second, the relativistic increase in plasma period $\sqrt{\gamma}\omega_p^{-1}$ expected (Rosenzweig, 1987) for such steepened plasma waves was not observed. Instead a slight decrease in period was observed as wake amplitude increased. Later, Marquès *et al.* (1997) revisited, and partially explained, similar features of nonlinear laser-driven plasma wakes (see Sec. IV.B.2). Still later, Matlis *et al.* (2006), in a study of high-amplitude laser-driven wakes (see Sec. IV.C.1), finally observed the expected relativistic increase in ω_p^{-1}.

Continuing experiments (Barov *et al.*, 2000) scaled bunch density into the strongly nonlinear blowout regime ($n_b \gg \bar{n}_e$), discussed in Secs. II.A.2 and II.A.3. This work produced drive and witness bunches more compactly by exciting a photocathode with tandem laser pulses. However, they were higher in emittance, longer, and less reproducible than expected. Thus, although this work observed $E_z^{(\mathrm{eff})} \sim 25$ MV/m, and inferred $E_z \sim 60$ MV/m, among its major conclusions was the need for improved methods of generating drive and witness bunches. Simulations by Serafini (1996) analyzed the challenges of producing high-quality, $\gtrsim$0.1 nC, 30–150 fs bunches suitable for high-density ($\bar{n}_e \sim 10^{18}$ cm^{-3}) PWFA experiments both by ultrafast photocathode illumination and by compression of ps-duration bunches.

The work of Kallos *et al.* (2008) and Muggli *et al.* (2008a, 2011) delivered these improvements. A photocathode rf gun and S-band linac at Brookhaven National Laboratory's (BNL's) Accelerator Test Facility (ATF) (Catravas *et al.*, 1999) provided 1.5 ps, 500 pC, 60 MeV bunches. Using a chicane compressor and "dog-leg" magnetic dipole configuration (Kimura, 2006), Kallos *et al.* (2008) compressed and split these bunches into drive (witness) bunches of 150 (90) fs duration, 300 (180) pC charge, and 60 (58) MeV energy, with fixed delay $\Delta t = 500$ fs [see the inset of Fig. 23(a)]. The resulting drive bunches ($n_b \approx 10^{14}$ cm^{-3}) drove standard linear ($n_b < \bar{n}_e$) wakes in a 6-mm-long ablative capillary discharge hydrogen plasma (Kaganovich *et al.*, 1999) with $\bar{n}_e$ ranging from 10^{14} to 4×10^{17} cm^{-3}, orders of magnitude denser than plasmas studied at ANL. Restricted to fixed Δt, Kallos *et al.* (2008) tuned $\bar{n}_e$, and observed maximum witness bunch energy gain $\Delta W_e \approx 0.9$ MeV at $\bar{n}_e \approx 10^{16}$ cm^{-3} [see Figs. 23(a)–23(c)], corresponding to $\Delta t = 1.5\lambda_p/c$. This corresponded to $E_z^{(\mathrm{eff})} = 0.9\,\mathrm{MeV}/0.06\,\mathrm{m} = 150\,\mathrm{MV/m}$, which matched the peak simulated E_z. Thus the witness bunch was sufficiently compressed and focused to observe the maximum E_z directly, without mathematical deconvolution of radial averaging.

Muggli *et al.* (2008a) refined the bunch-splitting technique by inserting a mask at a position in the dog leg where the beam's energy was transversely chirped. The incident bunch could then be split into a train of sub-ps microbunches of controllable number, length, and spacing by adjusting beam and mask parameters. An analogous technique generates controlled trains of ultrashort optical pulses (Weiner, 2000).

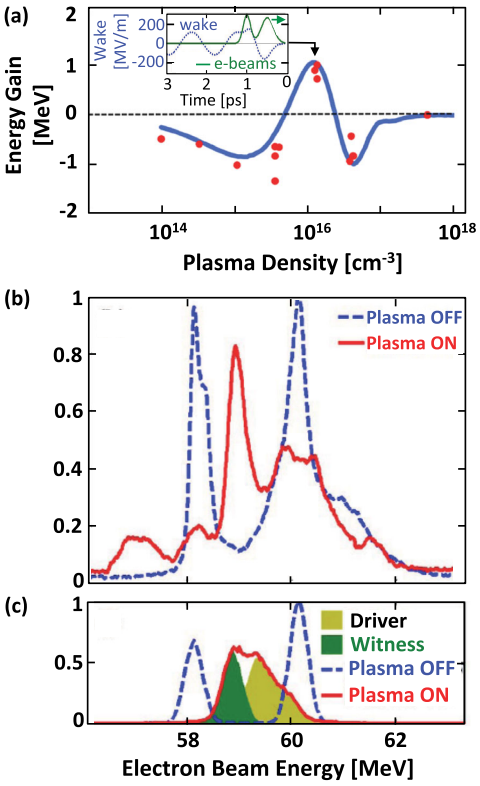

FIG. 23. Measurements of peak longitudinal electric field E_z of an e-bunch-generated linear plasma wave in $\bar{n}_e = 10^{16}$ cm^{-3} plasma. (a) Energy gain of witness bunch at fixed $\Delta t = 500$ fs behind a drive bunch as $\bar{n}_e$ changes. Inset: simulated plasma wave potential (dashed blue) and right-propagating drive and witness bunches (solid green). (b) Measured and (c) simulated energy spectra of witness and drive bunches without (dashed blue) and with (solid red) plasma of density $\bar{n}_e = 10^{16}$ cm^{-3}. Adapted from Kallos *et al.*, 2008.

This enabled production not only of a witness bunch, but of a train of drive bunches. Strategic adjustment of their spacing, shape, and charge can increase transformer ratio (Laziev, Tsakanov, and Vahanyan, 1988) and energy extraction efficiency (Maeda *et al.*, 2004) of a PWFA, in theory, by more than an order of magnitude (Nakajima, 1989; Farmer, Martorelli, and Pukhov, 2015) compared to a single-bunch driver (Ruth *et al.*, 1984; Lotov, 2013). Muggli *et al.* (2011) demonstrated acceleration of a witness bunch in a wake driven by two mask-generated drive bunches. However, experiments have not yet realized full predicted capabilities of the multibunch PWFA. Direct 2D mapping of a multibunch PWFA with an electron or optical witness bunch as drive parameters change is a promising future diagnostic experiment.

Recent experiments at SLAC's FACET (Hogan *et al.*, 2010) used copropagating electrons to diagnose internal fields of strongly blown out PWFAs in $\bar{n}_e \sim 2 \times 10^{17}$ cm^{-3} plasma. Clayton *et al.* (2016) mapped these fields in one shot, using electrons in the trailing portion of a drive bunch itself as witnesses. This is discussed with other single-shot experiments in Sec. IV.C.4. When the charge of a separate witness bunch becomes large enough to perturb the wake in which it is accelerating, it ceases to act purely as a diagnostic witness bunch. Such "beam loading" becomes beneficial when the accelerating bunch flattens local gradients in the wakefield, helping the bunch to accelerate monoenergetically (Lu *et al.*, 2006; Tzoufras *et al.*, 2008). Recent PWFA experiments realized this beam-loaded regime and imparted energy gains of several GeV to high-charge electron (Litos *et al.*, 2014) and positron (Corde *et al.*, 2015) bunches. 2D optical profiling of beam-loaded PWFAs is a promising future diagnostic experiment (Zgadzaj *et al.*, 2016).

2. Laser probe pulses

Delayed, copropagating electromagnetic probe pulses of duration $\tau_{\rm pr} < \omega_p^{-1}$ have also diagnosed plasma wake structure. For laser-driven wakes, inexpensive beam splitters trivially separate perfectly synchronized probe(s) from the driver while preserving durations $\tau \lesssim 30$ fs. For beam-driven wakes, state-of-the-art electronic techniques can synchronize an e beam and independent laser probe with < 1 fs jitter (Xin *et al.*, 2017).

The direct optical analog of e-beam diagnostics described in Sec. IV.B.1 is "photon acceleration" (Wilks *et al.*, 1989; Esarey, Ting, and Sprangle, 1990; Bulanov *et al.*, 1993), i.e., blueshifts or redshifts $\Delta\omega_{\rm pr}$ of probe pulses that copropagated with a longitudinal slice of the wake at which n_e locally increases ($dn_e/d\Delta t > 0$) or decreases ($dn_e/d\Delta t < 0$), respectively, with increasing Δt. From Poisson's equation, maximum $|dn_e/d\Delta t|$ correspond to strongest $|E_z|$. For copropagation distance L,

$$\Delta\omega_{\rm pr}(r,\Delta t) = -(\omega_{\rm pr}/c)\int_0^L (d\eta/d\Delta t)dz \tag{44a}$$

$$\approx(\omega_{\rm pr}L/2n_{\rm cr}c)dn_e/d\Delta t. \tag{44b}$$

Here η denotes local refractive index $\eta(r,\Delta t;z) = [1 - n_e(r,\Delta t;z)/n_{\rm cr}]^{1/2}$, and Eq. (44b) holds when $dn_e/d\Delta t$ is z independent and $n_e \ll n_{\rm cr}$. Both expressions assume L is short enough that the probe remains collimated. Thus a longitudinal wake slice that maximally accelerates an electron also maximally blueshifts a probe pulse. Multishot pump-probe blueshift experiments have diagnosed ionization front structure in atmospheric density gases (Wood, Siders, and Downer, 1991). However, despite in-depth theoretical analyses (Dias, e Silva, and Mendonca, 1998; Kasim *et al.*, 2015) and initial experiments (Trines *et al.*, 2009), photon acceleration has not yet probed detailed plasma wake structure $n_e(r,\Delta t)$. This can be attributed to the small magnitude of $|dn_e/d\Delta t|$ in linear wakes in subatmospheric density gases, and to the wide bandwidth of probe pulses capable of resolving sub-λ_p features, making subtle spectral centroid shifts difficult to observe. Photon deceleration (redshift) of wakefield drive pulses, which characterized their energy transfer to plasma waves, was observed (Murphy *et al.*, 2006; Shiraishi *et al.*, 2013), but does not measure detailed wake structure.

Researchers have had greater success diagnosing wake structure by analyzing the phase shift $\Delta\phi_{\rm pr}(r,\Delta t)$ that a wake imprints on a copropagating probe. Unlike $\Delta\omega_{\rm pr}$, $\Delta\phi_{\rm pr}$ can be measured *interferometrically* with high accuracy even for a wide-bandwidth probe. A collimated probe of duration $\tau_{\rm pr} < \omega_p^{-1}$ experiences a phase shift

$$\Delta\phi_{\rm pr}(r,\Delta t) = (\omega_{\rm pr}/c)\int_0^L \eta(r,\Delta t;z)dz \tag{45a}$$

$$\approx(\omega_{\rm pr}L/2n_{\rm cr}c)n_e(r,\Delta t), \tag{45b}$$

uniformly over its longitudinal profile. Here Eq. (45b) holds in the same limit as Eq. (44b). Thus $\Delta\phi_{\rm pr}(r,\Delta t)$ is proportional to the local density $n_e(r,\Delta t)$, rather than the local field $E_z(r,\Delta t)$, at which the probe propagates. By varying Δt and imaging the transverse probe profile, $n_e(r,\Delta t)$ can be mapped over multiple shots.

Frequency-domain interferometry (FDI) has mapped $\Delta\phi_{\rm pr}(r,\Delta t)$ in a variety of multishot pump-probe experiments (Reynaud, Salin, and Barthelemy, 1989; Tokunaga, Terasaki, and Kobayashi, 1992; Geindre *et al.*, 1994). Figure 24(a) shows a schematic FDI setup. A diagnostic pulse is split from the drive pulse, then shifted in frequency, rotated in polarization, or both to help discriminate it from scattered pump light after the interaction. The diagnostic pulse is subdivided into a reference pulse $E_{\rm ref}^{(0)}(t)$, and a probe pulse $E_{\rm pr}^{(0)}(t-T)$ that trails the reference by time T (e.g., by a Michelson interferometer with unequal arm lengths). These recombine with the pump (e.g., at a dichroic or polarizing mirror), and all three pulses copropagate through the interaction region without overlap.

Different 3-pulse sequences can be used. In standard FDI, $E_{\rm ref}^{(0)}(t)$ leads, and $E_{\rm pr}^{(0)}(t-T)$ trails, the pump with T fixed [see Fig. 24(a), center inset]. The pump-induced index change $\eta(r,\Delta t)$ then affects only the probe, phase shifting it to $E_{\rm pr}(t-T) = E_{\rm pr}^{(0)}(t-T)e^{i\Delta\phi_{\rm pr}(r,\Delta t)}$. This configuration has two limits. First, the requirement that the reference lead the pump limits pump-probe delay to $0 < \Delta t < T$. Second, if the pump ionizes neutral gas before generating a wake, both static plasma (density $\bar{n}_e$) and wake oscillations (amplitude δn_e) contribute to $\eta(r,\Delta t)$. But if $\delta n_e \ll \bar{n}_e$, and $\bar{n}_e L$ fluctuates from shot to shot, the fluctuations can mask the wake. "Differential" FDI, in which reference and probe both trail the pump, separated by a half-integer number of plasma periods, can then extend the Δt range and discriminate small wake oscillations more effectively (Marquès *et al.*, 1996, 1997; Siders, LeBlanc, Fisher *et al.*, 1996). In this configuration, the reference pulse shifts to $E_{\rm ref}(t) = E_{\rm ref}^{(0)}(t)e^{i\Delta\phi_{\rm ref}(r,\Delta t)}$, and the relative phase shift $\Delta\phi \equiv \Delta\phi_{\rm pr} - \Delta\phi_{\rm ref}$ is measured. The static contribution to $\Delta\phi$ cancels, while the oscillatory component doubles in amplitude compared to $\Delta\phi_{\rm pr}$ in the standard configuration. In both configurations, lens $L2$ [see Fig. 24(a)] images $E_{\rm ref}(r,t)$ and $E_{\rm pr}(r,t-T)$ to the entrance slit of an imaging spectrometer. The slit selects a slice along a direction hereafter called "y." Spectral dispersion temporally broadens both pulses, causing them to overlap at the spectrometer's array detector, which records their combined spectral intensity

$$I(y,\omega) = |F[E_{\rm ref}(y,t) + E_{\rm pr}(y,t-T)]|^2$$
$$= |E_{\rm ref}(y,\omega) + E_{\rm pr}(y,\omega)e^{-i\omega T}|^2 \tag{46a}$$

$$= S(y,\omega) + E_{\rm ref}(y,\omega)E_{\rm pr}^*(y,\omega)e^{i\omega T}$$
$$+ E_{\rm ref}^*(y,\omega)E_{\rm pr}(y,\omega)e^{-i\omega T}. \tag{46b}$$

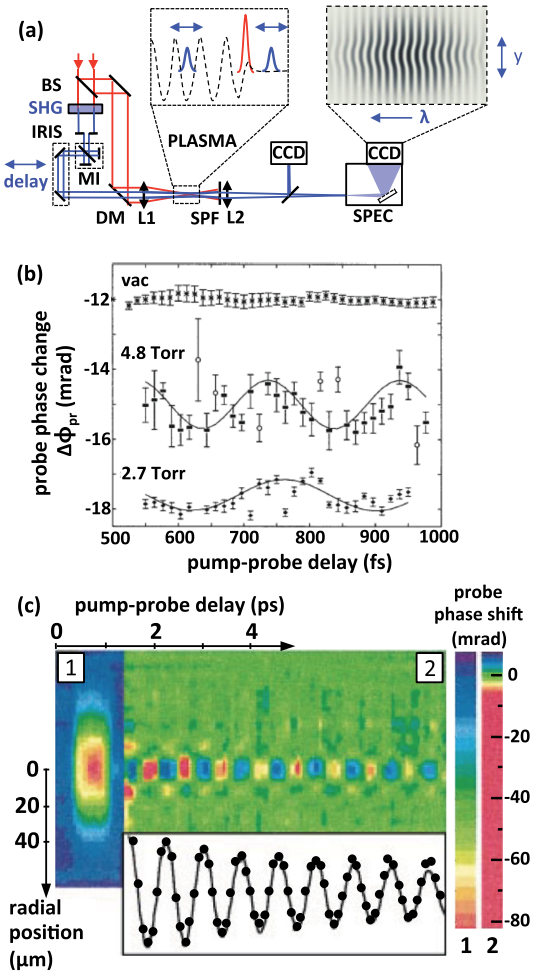

FIG. 24. Measurements of laser-generated electron density waves $n_e(r,z-ct)$ in $0.25 < \bar{n}_e < 3\times10^{17}$ cm^{-3} plasma. (a) Schematic frequency-domain interferometry (FDI) setup: BS = beam splitter, SHG = second-harmonic generation, MI = Michelson interferometer, DM = dichroic mirror, L = lens, SPEC = spectrometer, and CCD = charge-coupled device. Top-center inset: schematic of plasma wave density (dashed curve) created by right-propagating drive laser pulse (tall, red), with probe (trailing) and reference (leading) diagnostic pulses (short, blue). Top-right inset: schematic frequency-domain (FD) interferogram. Adapted from Marquès *et al.*, 1996. (b) Optical probe phase change $\Delta\phi_{\rm pr}(\Delta t)$ vs pump-probe delay Δt for fully ionized $\bar{n}_e = 0$ (top), 1.7 (middle), and 3 (bottom) $\times10^{17}$ cm^{-3} He plasmas excited by 100 fs, 0.8 μm, 10 mJ laser pulses focused with $f/4$. Adapted from Siders, LeBlanc, Fisher *et al.*, 1996. 4.8 (2.7) Torr data were acquired with standard (differential) FDI. (c) 2D map $\Delta\phi_{\rm pr}(r,\Delta t)$ of left-propagating nonlinear plasma wave for $\bar{n}_e = 0.25\times10^{17}$ cm^{-3}. (c) Adapted from Marquès *et al.*, 1997.

Here F denotes Fourier transform, $S(y,\omega) \equiv |E_{\rm ref}(y,\omega)|^2 + |E_{\rm pr}(y,\omega)|^2$, and $E_j(y,\omega) = E_j^{(0)}(y,\omega)e^{i\Delta\phi_i(y,\omega)}$ $(j = {\rm ref}, {\rm pr})$ are perturbed FD fields expressed in terms of unperturbed fields $E_j^{(0)}(y,\omega)$. For $E_{\rm ref}^{(0)} = E_{\rm pr}^{(0)} = E$ with no losses, refraction, or diffraction in the plasma, Eq. (46) becomes (Tokunaga, Terasaki, and Kobayashi, 1992)

$$I(y,\omega) = 2|E(y,\omega)|^2\{1+\cos[\omega T - \Delta\phi(y,\omega)]\}. \tag{46c}$$

Equation (46c), an oscillating function of frequency with period $2\pi/T$, is the "frequency-domain interferogram" that encodes probe-reference phase shifts (Reynaud, Salin, and Barthelemy, 1989). In the absence of an interaction ($\Delta\phi = 0$), straight (y-independent) fringes appear on the detector. In the presence of a y-dependent interaction, fringes distort in pump-excited y regions [see Fig. 24(a), right inset]. Straight fringes in unexcited y regions then serve as the reference null interferogram, from which the fringe *shift* $\Delta\phi(y,\omega)$ in excited y regions is extracted for each Δt. If $\tau_{\rm pr} \ll \omega_p^{-1}$, then $n_e(y,\Delta t)$, $\eta(y,\Delta t)$, and $\Delta\phi(y,\Delta t)$ are constant in time at each y over the probe longitudinal profile. If, in addition, the probe bandwidth $\delta\omega_{\rm pr} \ll \omega_{\rm pr}$, then $\eta(y,\Delta t)$ and $\Delta\phi(y,\Delta t)$ are also constant in frequency over the probe bandwidth. In this "FDI approximation," $\Delta\phi(y,\omega) = \Delta\phi(y,\Delta t)$, both quantities being frequency independent at each y and Δt. All fringes at each y and Δt then shift by the same amount, and the distinction between spectral and temporal phase disappears. Equation (46c) then becomes

$$I(y,\omega) = 2|E(y,\omega)|^2\{1+\cos[\omega T - \Delta\phi(y,\Delta t)]\}. \quad (46d)$$

$\Delta\phi(y,\Delta t)$ can now be extracted directly from the measured fringe shift between "signal" and null interferograms. Accurate extraction requires only that the pixel density of the spectrometer's 2D array detector be high enough for a given T (typically $\gtrsim$10 pixels per fringe) to resolve the fringe shift. The FDI approximation remains valid even when the Taylor expansion $\Delta\phi(y,t) \approx \Delta\phi(y,\Delta t) + \partial_t\Delta\phi(y,t)|_{t=\Delta t}(t-\Delta t)$ includes linear temporal variations within the probe longitudinal profile, since $\partial_t\Delta\phi(y,t)|_{t=\Delta t}$ is simply an overall probe centroid frequency shift (photon acceleration) (Siders, LeBlanc, Babine *et al.*, 1996). Only when quadratic and higher-order temporal variations within the probe become significant is the equivalence of $\Delta\phi(y,\omega)$ and $\Delta\phi(y,\Delta t)$ lost, necessitating more sophisticated Fourier analysis of the interferograms. They then become FD "holograms" (see Sec. IV.C).

The first FDI experiments to characterize plasma wakes (Marquès *et al.*, 1996; Siders, LeBlanc, Fisher *et al.*, 1996) used first-generation sub-TW Ti:S ($\lambda = 0.8$ μm) chirped-pulse amplified (CPA) laser technology (Backus *et al.*, 1998), for which pulse duration was limited to $\tau \sim 100$ fs and pump energy to $10 \lesssim \mathcal{E} \lesssim 30$ mJ. This τ limited $\bar{n}_e$ to $\leq 3\times10^{17}$ cm^{-3} (λ_p to ≥ 60 μm), in order to excite wakes resonantly and resolve sub-λ_p features, while this $\mathcal{E}$ necessitated focusing to strongly sub-λ_p spot sizes ($3.5 < w_0 < 6$ μm) to reach field strengths ($0.35 < a_0 < 0.5$) sufficient to excite observable wakes. An advantage of such tight focus was that the drive pulse's radial ponderomotive force dominated wake excitation, producing larger $\delta n_e/\bar{n}_e$ (up to ~1) and $\Delta\phi_{\rm pr}$ (up to ~30 mrad) than its longitudinal ponderomotive force alone would have produced. Equation (3b) quantifies this advantage. On axis ($r = 0$), the ratio $\delta n_r/\delta n_z = (\lambda_p/\pi w_0)^2$ of radial to longitudinal wake contributions ranged from 30 to 300 in the experiments of Marquès *et al.* (1996) and Siders, LeBlanc, Fisher *et al.* (1996). Moreover, the contribution of the longitudinal (radial) component of δn_e to $\Delta\phi_{\rm pr}$ is proportional to $\delta n_z z_R$ ($\delta n_r z_R$). From Eq. (3b), $\delta n_z z_R$ is independent of pump focus, whereas $\delta n_r z_R$ increases in proportion to $1/z_R$ as focus tightens. Thus with available lasers, tight focus was critical to initial FDI wake observation.

A disadvantage of tight pump focus was that the probe pulse averaged over radial wake profiles as it transited the interaction region. For example, the data in Fig. 24(b) correctly show $\Delta\phi_{\rm pr}(\Delta t)$ oscillating longitudinally at ω_p for each of two $\bar{n}_e$, but does not directly convey radial wake structure (Siders, LeBlanc, Fisher *et al.*, 1996). Instead these researchers inferred radial structure indirectly by calculating it via Eq. (3b), computing $\Delta\phi_{\rm pr}(\Delta t)$ induced on a focused (Siders, LeBlanc, Fisher *et al.*, 1996) or collimated (Marquès *et al.*, 1996) probe, and confirming that the computed $\Delta\phi_{\rm pr}(\Delta t)$ oscillation amplitude agreed with the measured value. The relationship between $\Delta\phi_{\rm pr}(\Delta t)$ and δn_e was thus more complicated than Eq. (45b), which assumed longitudinally invariant wake structure and collimated probe. Limited direct radial information was obtained by imaging the transverse profile of $\Delta\phi_{\rm pr}(y,\Delta t)$ with the probe at a wake peak or valley (Marquès *et al.*, 1996), or by observing increased $\Delta\phi_{\rm pr}(\Delta t)$ as the spectrometer slit narrowed (Siders, LeBlanc, Fisher *et al.*, 1996).

In a follow-up study, Marquès *et al.* (1997, 1998) mapped $\Delta\phi_{\rm pr}(y,\Delta t)$ behind a tightly focused drive pulse in greater detail. Figure 24(c) illustrates these expanded results. The left part ("1") of the image, acquired with standard FDI, shows $\Delta\phi_{\rm pr}(y,\Delta t)$ primarily from plasma formation. Regions of doubly (red) and singly ionized (green) He, integrated along the laser axis, can be seen. The right part ("2") of the image, acquired with differential FDI, shows only wake oscillations, which are localized within the doubly ionized region. The axial lineout below this image shows damped oscillation of the form $\Delta\phi_{\rm max}\exp(-\gamma\Delta t)\sin(\omega_p\Delta t)$ behind the pump.

Analysis led to two new discoveries. First, ω_p of the first few oscillations was ~5% higher than later oscillations, the frequency of which matched ω_p for doubly ionized helium. This finding resembled the temporary increase in ω_p that Rosenzweig *et al.* (1989) reported for a nonlinear PWFA (Sec. IV.B.1). Plasma heating, which increases electron thermal velocity v_{th} and thus plasma frequency via $[\omega_p(k)]^2 = \omega_p^2 + 3k_p^2v_{th}^2$, could account for $< 1\%$ increase in ω_p and would not relax within a few oscillation periods. Relativistic electron mass increase in high-amplitude electron oscillations, if present, would decrease rather than increase ω_p (Rosenbluth and Liu, 1972). Instead a simple electrostatic mechanism unique to high-amplitude radial wakes appeared to dominate: the radial displacement δr of an electron away from its initial position r_0 produced greater charge density at the center of symmetry, and thus a stronger restoring force, than in a planar wake, resulting in fractional increase $\Delta\omega_p/\omega_p \approx (\delta r/r_0)^2/12$ in ω_p (Dawson, 1959). Computer simulations reproduced the observed increase, as well as its temporal relaxation. Second, the damping rate γ was faster than expected from mechanisms expected in a uniform plasma, e.g., fine-scale mixing of orbits of electrons with amplitude-dependent oscillation frequencies (Dawson, 1959) or thermal convection. Instead radial electron excursions that cross the He^{2+}/He^{+} boundary and dephase from the wake provided the best quantitative explanation. These discoveries

illustrate how high-resolution wake structure diagnostics, in concert with simulations, advance plasma wakefield physics.

C. "Snapshots" of wake structures

Multishot techniques diagnose wakefield structure in microscopic detail, but require lengthy data acquisition and thus cannot provide rapid feedback. Moreover, the data are subject to shot-to-shot fluctuations, especially when wakes are excited nonlinearly. These considerations motivated development of diagnostics that recover plasma wake structure with equivalent detail in a single shot. Single-shot diagnostics developed most rapidly with optical, rather than electron, probes because of the relative ease with which optical pulses can be stretched, compressed, expanded, and imaged and with which their internal phase and amplitude structure can be measured. Nevertheless, single-shot, high-resolution electron radiography of internal fields of plasma-based electron accelerators was recently demonstrated (see Sec. IV.C.4).

The development of optical single-shot plasma wake diagnostics drew upon three established optical technologies, which have no counterpart in particle-beam technology. The first of these was holography. Holographic wake diagnostics drew from conventional holography the concepts of a coherent "object" (or probe) pulse that illuminates the entire object of interest simultaneously, and of a mutually coherent "reference" pulse with which the object pulse interferes on a recording medium. New challenges for holographic wake diagnostics included adapting these concepts to a near light-speed object, and developing methods for "reading" the "hologram" quickly and accurately (Sec. IV.C.1). The second underlying technology was ultrafast optics. By the year 2000, CPA lasers producing terawatt pulses of tens-of-fs duration were widely available, and techniques for stretching, manipulating, and recompressing such pulses while maintaining their coherence had matured (Backus *et al.*, 1998). Moreover, pulse retrieval algorithms such as frequency-resolved optical gating (Trebino *et al.*, 1997) and spectral shearing interferometry (Iaconis and Walmsley, 1998) for characterizing the internal amplitude and phase structure of individual laser pulses had been developed and advanced to single-shot implementation (Dorrer *et al.*, 1999; O'Shea *et al.*, 2001). Single-shot optical wake diagnostics developed naturally from these techniques. A third underlying technology was computerized tomography (CT), developed as an x-ray-based internal medical diagnostic in the 1970s (Kak and Slaney, 1998). Tomographic wake diagnostic methods are just beginning to emerge (Li, Zgadzaj *et al.*, 2014). They draw from established CT the concept of reconstructing multidimensional images of difficult-to-access objects from multiple projections. They also utilize elements of established reconstruction algorithms. New challenges include adapting these concepts to an evolving light-speed object, recovering its picosecond evolution, and achieving high spatial and temporal resolution simultaneously.

1. Frequency-domain holography

Siders, LeBlanc, Babine *et al.* (1996) first proposed extending FDI to a single-shot plasma wake diagnostic. One way of doing this is simply to time N probe pulses at different delays $\tau_{\mathrm{pr}}^{(i)}$ $(i = 1, 2, \ldots, N)$ behind the pump [see Fig. 25(a)]. A multiarmed Michelson interferometer, for example, has produced 16-pulse trains with high throughput (Siders *et al.*, 1998). Since each probe-reference delay $T^{(i)} = \tau_{\mathrm{ref}} - \tau_{\mathrm{pr}}^{(i)}$ corresponds to a different oscillation period of the resulting multiperiod FD interferogram [Fig. 25(a), inset], Fourier analysis (Takeda, Ina, and Kobayashi, 1982) then yields the time-domain phase shift $\Delta\phi(\tau_{\mathrm{pr}}^{(i)})$ on each probe in one shot. More simply, one can replace this multiplexed probe pulse train with a single continuous long pulse [see Fig. 25(b)]. Siders, LeBlanc, Babine *et al.* (1996) called the latter configuration "frequency-domain holography" (FDH) and envisioned creating the long probe pulse by inserting a flat-phase bandpass filter in the probe arm of a two-armed Michelson interferometer. This broadens the probe

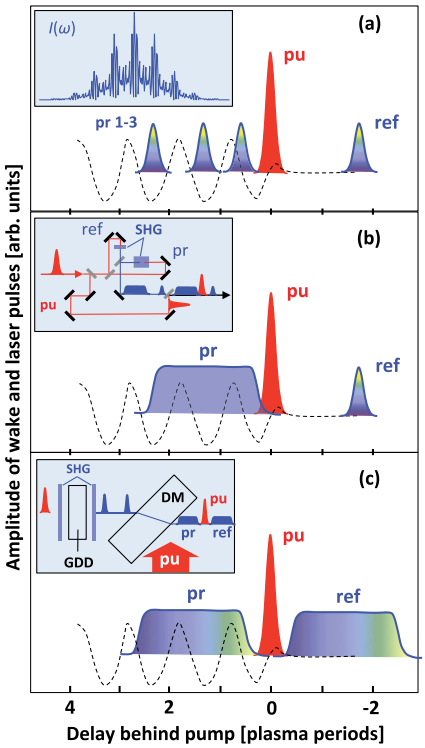

FIG. 25. Early development of the frequency-domain holography (FDH) concept based on the right-propagating pump (pu), probe (pr), and reference (ref) pulses, and wake (dashed curve). (a) Multiplexed FDI with several temporally short probe pulses (Siders, LeBlanc, Babine *et al.*, 1996). Inset: Spectral intensity $I(\omega)$ of three probes and one reference pulse at detector. (b) FDH with single temporally long, transform-limited probe and temporally short, transform-limited reference (Siders, LeBlanc, Babine *et al.*, 1996). Inset: laboratory implementation (LeBlanc *et al.*, 2000). (c) FDH with equivalent chirped, wide-bandwidth probe, and reference pulses (Chien *et al.*, 2000; Geindre *et al.*, 2001; Kim, Alexeev, and Milchberg, 2002b). Inset: laboratory implementation (Matlis *et al.*, 2006): incident 800 nm diagnostic pulse split from pump upconverts to 400 nm via second-harmonic generation (SHG) in a thin crystal, creating probe; glass plate group-delays (GDs) probe by ~2 ps from transmitted fundamental, which upconverts in the second thin SHG crystal, creating reference; both chirp to ~1 ps duration in a thick dichroic mirror (DM), which recombines them collinearly with pump.

temporally, but maintains its phase coherence with the still short reference pulse. LeBlanc *et al.* (2000) realized this goal in the laboratory by inserting phase-matched frequency-doubling crystals of different thickness into each arm of the interferometer [see Fig. 25(b), inset]. The thicker crystal (2 mm $LiIO_3$) had a narrow phase-matching bandwidth that generated a temporally long (1 ps) probe pulse, while the thinner crystal (150 μm potassium dihydrogen phosphate) generated a temporally short (70 fs) reference pulse. The unperturbed probe and reference pulses formed FD fringes only within the narrower bandwidth of the probe pulse. However, after interacting with the ultrafast pump-induced index transient, the probe acquired new frequency components that interfered with the broader reference spectrum. The latter bandwidth determined the temporal resolution of the phase reconstruction. LeBlanc *et al.* (2000) recovered laser-induced Kerr index transients in fused silica and ionization fronts in air over ~1 ps range with 70 fs time resolution, and 1D transverse spatial profiling, in a single shot.

Chien *et al.* (2000) and Geindre *et al.* (2001) implemented FDH using probe and reference pulses that were both broad bandwidth and temporally broadened simply by linearly chirping them, without narrowing their spectra [see Fig. 25(c)]. In a chirped pulse, frequency components are distributed in a monotonic time sequence $\omega(t)$ within the stretched pulse. Chien *et al.* (2000) and Geindre *et al.* (2001) introduced chirp by passing the diagnostic pulse through a transparent, linear dispersive material before a Michelson interferometer split it into probe and reference pulses. This simplified FDH by eliminating alignment-sensitive transmissive optics inside the interferometer. They demonstrated single-shot recovery of the dynamics of laser-induced air ionization (Chien *et al.*, 2000) and plastic target breakdown (Geindre *et al.*, 2001), also with 1D transverse spatial profiling.

Chirped-pulse FDH had the additional advantage of lending itself to wide-bandwidth supercontinuum probe and reference pulses (Kim, Alexeev, and Milchberg, 2002b), which provide high longitudinal time resolution, wide temporal range, and when generated in a frequency band near the pump smaller group-velocity walk-off from the pump than frequency-doubled pulses. This approach yielded high-resolution measurements of double ionization in He (Kim, Alexeev, and Milchberg, 2002a) and Kerr effect and plasma generation in various gases (Chen *et al.*, 2007; Wahlstrand *et al.*, 2011). However, nonlinear laser-wakefield excitation itself produces copious forward-directed chirped supercontinuum (Ralph *et al.*, 2009), which interferes with copropagating diagnostic pulses close to the drive pulse frequency, complicating image recovery. To avoid this, Matlis *et al.* (2006) returned to frequency-doubled diagnostic pulses to obtain the first FDH snapshots of laser wakefields. The inset of Fig. 25(c) shows the compact probe-reference generator, based on a linear Fabry-Perot interferometer configuration, that Matlis *et al.* (2006) introduced. This configuration proved more robust against vibrations and alignment errors than Michelson interferometers, while avoiding phase noise from background pump-generated supercontinuum. Visible supercontinuum pulses may nevertheless prove useful in imaging plasma wakes driven by particle beams or mid-wavelength to long-wavelength-infrared laser pulses, for which this background is absent or at much longer wavelengths.

Using chirped pulses offers the intuitively attractive possibility of mapping the evolving pump-induced index transient $\eta(t)$ directly onto the probe spectrum $\omega(t)$ (Chien *et al.*, 2000). In a simplified analysis, one divides the FD interferogram into N frequency bands $\Delta\omega^{(i)}(t^{(i)})$ $(i = 1, 2, \ldots, N)$, then measures the fringe shift within each band to find the corresponding instantaneous index $\eta(t^{(i)})$. However, Geindre *et al.* (2001) and Kim, Alexeev, and Milchberg (2002b) pointed out that the narrow bandwidth of each bin limits $\eta(t)$ recovery to slowly varying index transients that satisfy $\partial\eta/\partial t|_{t^{(i)}} < \Delta\omega^{(i)}$. More rapidly varying index transients shift spectral content out of bin $\Delta\omega^{(i)}$ into neighboring bins, causing inaccurate recovery of $\eta(t)$. Research on THz pulse modulation of chirped optical pulses has resulted in various strategies for addressing the distorted frequency-time relationship that the imprinting process causes (Fletcher, 2002; Yellampalle *et al.*, 2005; Peng *et al.*, 2008).

To recover rapidly varying $\eta(\Delta t)$ by FDH, limited only by the bandwidth $\Delta\omega$ of the entire reference pulse, LeBlanc *et al.* (2000), Geindre *et al.* (2001), and Kim, Alexeev, and Milchberg (2002b) introduced a holistic FDH signal reconstruction procedure valid for either transform-limited [Fig. 25(b)] or chirped [Fig. 25(c)] probes. Figures 26 and 27

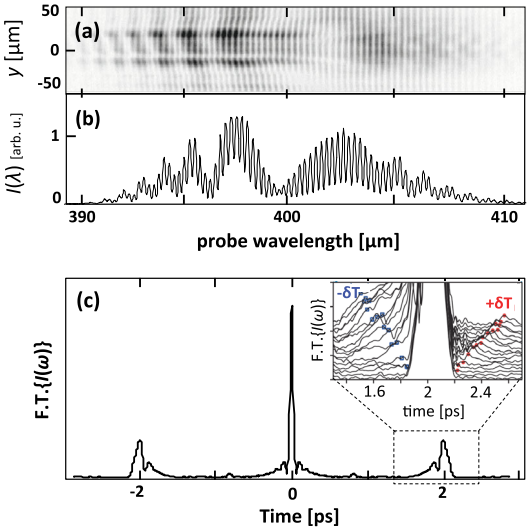

FIG. 26. FDH signal reconstruction procedure. (a) Raw FD hologram showing interference of chirped 400 nm probe and reference pulses at the detection plane of an imaging spectrometer, after copropagating through the He gas jet with 0.3 J, 30 fs, 800 nm pump pulse focused to $w_0 = 50$ μm, and imaging from the jet exit to the spectrometer slit through a 400 nm bandpass filter. Variations along the y axis, parallel to the spectrometer slit, reflect transverse spatial structure of pump-induced plasma. Adapted from Matlis *et al.*, 2006. (b) Lineout of a hologram at one y position. (c) Fourier transform of the lineout in (b). Dashed rectangle: the cross-correlation peak at $T = 2$ ps is isolated, then Fourier transformed for further processing. (b), (c) Adapted from Dong *et al.*, 2010a. Inset: detailed substructure of $T = 2$ ps peak for $\bar{n}_e$ from 0.95 to 6×10^{18} cm^{-3} (bottom to top). Adapted from Matlis *et al.*, 2016.

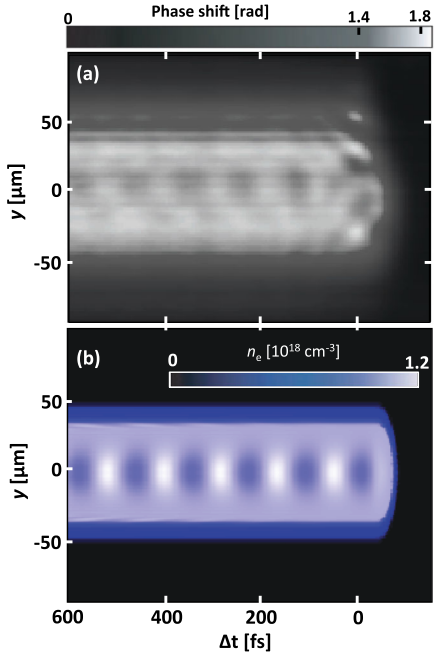

FIG. 27. (a) Composite "snapshot" of right-propagating wake formed by stacking temporal pump-induced phase structure $\Delta\phi_{\rm pr}(y,\Delta t)$ extracted from cross-correlation peaks at each y. (b) Simulated wake density profile $n_e(y,\Delta t)$ near center of gas jet for conditions matching the experimental data. Adapted from Matlis *et al.*, 2006.

illustrate the main steps, using data from Matlis *et al.* (2006) as an example. For the data shown, a 0.3 J, 30 fs (10 TW) Ti:S pump pulse focused to beam waist $w_0 \approx 50$ μm in a 2-mm-long He gas jet created plasma of average density $\bar{n}_e \sim 10^{18}$ cm^{-3} and a wake of wavelength $\lambda_p \sim 25$ μm in the doubly ionized region. Figure 26(a) shows a raw FD hologram, acquired using the standard chirped-pulse FDH configuration shown in Fig. 25(c). Both ionization front [not shown in Fig. 25(c)] and wake oscillations contributed to the fringe distortions in Fig. 26(a). Figure 26(b) shows a lineout of the hologram $I(y_0,\omega)$ at $y = y_0$. Formally, $I(y_0,\omega)$ is given by Eq. (46), and for identical unperturbed probe and reference pulses, by Eq. (46c). However, Eq. (46d) does not apply, since the FD phase $\Delta\phi_{\rm pr}(y,\omega)$ is no longer equivalent to, nor simply related to, the desired pump-induced TD phase shift $\Delta\phi(y,\Delta t)$ as in FDI.

To recover $\Delta\phi(y,\Delta t)$, LeBlanc *et al.* (2000), Geindre *et al.* (2001), and Kim, Alexeev, and Milchberg (2002b) began by isolating the complete frequency-domain probe electric field

$$E_{\rm pr}(y,\omega) = |E_{\rm pr}(y,\omega)|e^{i[\Delta\phi_{\rm pr}(y,\omega)+\phi_{\rm ch}(\omega)]} \tag{47}$$

from the FD hologram, using a computer-based fringe-pattern analysis method introduced by Takeda, Ina, and Kobayashi (1982). Here $\phi_{\rm ch}(\omega)$ is the FD phase due to the probe chirp. We now suppress the argument y for brevity. To isolate $E_{\rm pr}(\omega)$, they first inverse Fourier transformed the recorded FD hologram $I(\omega)$, given by Eq. (46b) or Fig. 26(b), at each y:

$$S(t) = \tilde{F}[I(\omega)]. \tag{48}$$

This operation electronically "reads" the recorded hologram with a plane wave, analogous to physically reading a conventional film-recorded hologram with the reference wave (Siders, LeBlanc, Babine *et al.*, 1996). The resulting complex time-domain function $S(t)$, of which Fig. 26(c) shows the amplitude, has the form $S(t) = 2h(t) + h(t+T) + h(t-T)$ with peaks at $t = 0$, $-T$, and T. These peaks correspond, respectively, to $\tilde{F}$ of the three terms in Eq. (46b). The central ($t = 0$) peak is the intensity autocorrelation of the reference and probe pulses, but lacks phase information. Only the side cross-correlation peaks at $t = \pm T$ encode the desired phase of $E_{\rm pr}$. Siders, LeBlanc, Babine *et al.* (1996) gave complete expressions for all three peaks. The side peak at $t = T$ has the general form

$$h(t-T) = \tilde{F}[E^*_{\rm ref}(y,\omega)E_{\rm pr}(y,\omega)e^{-i\omega T}]. \tag{49a}$$

For unperturbed linearly chirped, Gaussian pulses $E_{\rm pr}(\omega) = E_{\rm ref}(\omega) = E_0\exp\{-(1/2)(1+i\sigma)[(\omega-\omega_0)/\Delta\omega]^2\}$, where σ represents the FD chirp, it has the specific form (Matlis *et al.*, 2016)

$$h(t-T) = \Delta\omega(E_0^2/\sqrt{2})e^{-i\omega_0(t-T)}e^{-(1/4)(t/\delta t)^2}, \tag{49b}$$

where $\delta t \equiv 1/\Delta\omega$ is the coherence time of the probe and reference pulses. When a temporal phase shift $\Delta\phi_{\rm pr}(\Delta t)$ modulates the probe, $h(t-T)$ develops an informative substructure, shown for $0.95\times10^{18} < \bar{n}_e < 6\times10^{18}$ cm^{-3} in the magnified view of the base of the $t = T$ peak in the inset of Fig. 26(c). The step-function-like ionization front, which in the FD blueshifts frequency components that it overlaps, appears as a shoulder on the $t < T$ side of $h(t-T)$. This shoulder becomes more prominent at higher $\bar{n}_e$. A sinusoidal wake oscillation, which in the FD creates Stokes and anti-Stokes sidebands at $\pm\omega_p$, appears in the TD as sidebands at $T \pm \delta T$. Here δT, which is $\sigma\omega_p/\delta\omega^2$ for linearly chirped probe and reference pulses (Matlis *et al.*, 2016), increases as $\sqrt{\bar{n}_e}$, and exceeds δt throughout the $\bar{n}_e$ range shown. A nonlinear wake, which contains harmonics of ω_p, creates additional higher-order TD sidebands at $T \pm m\delta T$, where $m = 2, 3, \ldots$ [not shown in the inset of Fig. 26(c)]. For cases of interest, these ionization- and wake-induced spectral shifts are smaller than $\Delta\omega$ and thus are not visible directly in the FD. Chirped-pulse FDH, however, encodes them in the TD, and by Fourier transforming $I(\omega)$, converts them to temporal shifts δT greater than the temporal width δt of the reconstructed $h(t-T)$ peak. Matlis *et al.* (2016) called this process temporally encoded spectral shifting (TESS). TESS analysis enables subtle wake-induced phase modulations to be separated from the often much larger phase modulations that ionization fronts imprint, e.g., by analyzing the wake-induced sideband on the $t > T$ side of $h(t-T)$. This gives FDH a capability analogous to a differential FDI mode (see Sec. IV.B.2). Recently Cowley *et al.* (2017) used TESS to characterize plasma wakes driven by optimized trains of laser pulses.

To complete the extraction of $E_{\rm pr}(\omega)$, LeBlanc *et al.* (2000), Geindre *et al.* (2001), and Kim, Alexeev, and Milchberg (2002b) multiplied $h(t-T)$ by a soft-edged apodizing window centered at $t = T$ to isolate this peak [indicated by the

dashed rectangle in Fig. 26(c)]. The window must be wide enough to include all substructure that the interaction introduced. Fourier transformation back to the FD yields

$$|E_{\mathrm{ref}}(\omega)||E_{\mathrm{pr}}(y,\omega)|e^{i\Delta\phi_{\mathrm{pr}}(y,\omega)} \tag{50}$$

for the $t = T$ peak. Finally, one divides Eq. (50) by the independently measured reference pulse power spectrum $|E_{\mathrm{ref}}(\omega)|$ and augmented it with the FD chirp phase $\phi_{\mathrm{ch}}(\omega)$, measured by standard single-shot pulse characterization methods (Dorrer *et al.*, 1999; O'Shea *et al.*, 2001), to complete reconstruction of the field equation (47).

The final step in recovering $\Delta\phi(y,\Delta t)$ is inverse Fourier transformation of $E_{\mathrm{pr}}(y,\omega)$ to get the complete time-domain probe electric field

$$\begin{aligned} E_{\mathrm{pr}}(y,\Delta t) &= \tilde{F}[E_{\mathrm{pr}}(y,\omega)] \\ &= |E_{\mathrm{pr}}(y,\Delta t)|e^{i[\Delta\phi_{\mathrm{pr}}(y,\Delta t)+\phi_{\mathrm{ch}}(y,\Delta t)]}. \end{aligned} \tag{51}$$

After subtracting the independently characterized time-domain chirp $\phi_{\mathrm{ch}}(y,\Delta t)$ from its phase, we recover $\Delta\phi(y,\Delta t)$ at one y. Repeating this analysis for each y yields the 2D phase map shown in Fig. 27(a).

Figure 27(b) compares this phase map with simulated plasma density perturbations $\delta n_e(y,\Delta t)$ near the center of the gas jet ($z = 1$ mm) for the same conditions. The overall structures of $\delta n_e(y,\Delta t)$ and $\Delta\phi_{\mathrm{pr}}(y,\Delta t)$ match closely: boundaries of He^{2+} and He^{+} regions in Fig. 27(b) appear at y values similar to those of sharp $\Delta\phi_{\mathrm{pr}}$ boundaries in Fig. 27(a); plasma density oscillations in the He^{2+} region in Fig. 27(b) have the same wavelength and radial structure as corresponding $\Delta\phi_{\mathrm{pr}}$ oscillations in Fig. 27(a). Matlis *et al.* (2006) found similar correspondence for shots over a wide $\bar{n}_e$ range, showing that the approximation of a collimated probe pulse, discussed in connection with FDI in Sec. IV.B.2, remained valid here. Nevertheless, Matlis *et al.* (2006) found the amplitude of phase oscillations in Fig. 27(a) was significantly smaller than expected from probing the density perturbations in Fig. 27(b) over a uniform jet. Group-velocity walk-off of a 400 nm probe from a 800 nm pump did not explain the discrepancy. Instead it arose from longitudinal density nonuniformity of the gas jet, which caused the pump to generate, and probe to sample, wakes of different frequencies as they copropagated through the 2 mm jet. Remarkably, despite this averaging, the recovered hologram of Fig. 27(b) preserved the main features of the wake near the center of the jet. Longitudinally uniform gas targets are thus preferred to obtain accurate wake amplitudes from FDH.

Matlis *et al.* (2006) and Dong *et al.* (2010a) found that imaging of nonlinear wakes generated by 1 J, 30 fs (30 TW) pump pulses enabled independent *in situ* calibration of absolute wake oscillation amplitude. FDH images of wakes excited under these conditions had curved wave fronts [Fig. 28(a)], a signature of strongly driven, nonlinear laser-plasma interaction (Decker, Mori, and Katsouleas, 1994; Andreev, Gorbunov, and Ramazashvili, 1997). Wave fronts that were flat immediately behind the pump evolved into curved "horse-shoe" profiles after several periods. Simultaneously, the amplitude of the phase-shift oscillations

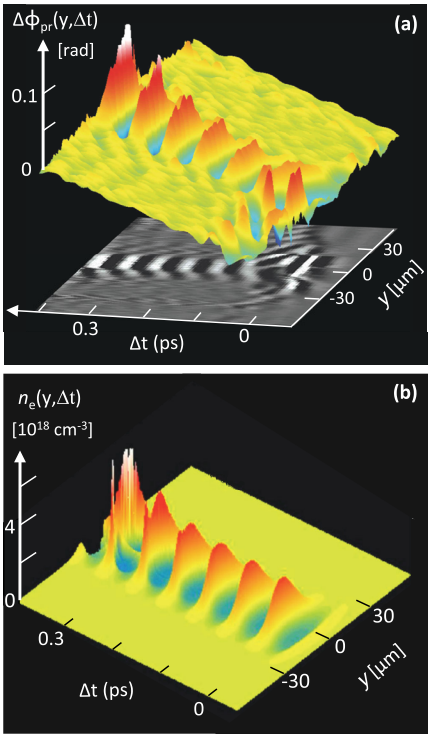

FIG. 28. Strongly driven right-propagating wake with curved wavefronts. (a) FDH phase profile $\Delta\phi_{\mathrm{pr}}(y,\Delta t)$ of wake (colored surface) that a 30 TW pump pulse generated in He^{2+} plasma with $\bar{n}_e = 2.2\times10^{18}$ cm^{-3}. The gray-scale image is a projection onto a plane. dc phase shift from surrounding plasma profile has been subtracted to highlight wake oscillations. (b) Simulated wake density profile $n_e(y,\Delta t)$ near the gas jet center, showing growth of wavefront curvature and amplitude with increasing Δt as in (a). Adapted from Dong *et al.*, 2010a.

increased over the same interval. A particle-in-cell simulation of the wake [Fig. 28(b)] showed that plasma density oscillations $\delta n_e(y,\Delta t)/\bar{n}_e$ near the center of the gas jet also exhibited both of these features. Both are relativistic in origin. The wave fronts curve because as $|\delta n_e(r=0,\Delta t)|$ approaches unity on axis ($r = 0$), electrons making up the wave oscillate relativistically ($\gamma > 1$), causing $\omega_p(r=0)$ to decrease by $\sqrt{\gamma}$ relative to its off-axis value (Decker, Mori, and Katsouleas, 1994; Andreev, Gorbunov, and Ramazashvili, 1997). Simulations showed that the reciprocal radius of curvature $\rho^{-1} = g\Delta t$ grows linearly with Δt, where the growth rate g depends sensitively on $|\delta n_e(r=0,\Delta t)/\bar{n}_e|$. Analysis of ρ^{-1} in the FDH image in Fig. 28(a) showed $|\delta n_e(r=0,\Delta t)/\bar{n}_e|$ was ~0.5 immediately behind the pump, then grew steadily over six cycles. Dong *et al.* (2010a) explained this growth by analogy with amplitude growth observed in simulations of wakes generated in plasma channels with parabolic radial density profiles (Andreev *et al.*, 1997; Shvets and Li, 1999). Here the radial relativistic $\gamma(r)\omega_p$ profile played the role of the channel density profile. With increasing Δt, trajectories of radially neighboring electron fluid elements, oscillating at slightly different frequencies, approach. In a process akin to optical pulse compression, interaction among fluid elements spanning the $\gamma(r)\omega_p$ bandwidth steepen and narrow the plasma wave fronts, causing the observed amplitude growth.

As trajectories cross, the waves can eventually break, although the image and simulation in Fig. 28 stop before this happens. Correlated growth of wave curvature and amplitude, effects never previously observed in the laboratory, are thus precursors of wave breaking and electron injection. The example illustrates the new wakefield physics that is accessible from dialog between *in situ* plasma structure diagnostics and simulations.

2. Longitudinal optical shadowgraphy

The images in Figs. 27(a) and 28(a) were reconstructed entirely from accumulated phase shift $\Delta\phi_{\rm pr}(r,\Delta t,z_{\rm exit})$ on the wake-modulated probe pulse at the exit plane of the accelerator. Corresponding changes in the probe amplitude $|E_{\rm pr}(r,\Delta t,z_{\rm exit})|$ were negligible under these conditions. As $\bar{n}_e L$ increases, plasma structures with high index contrast not only reshape the drive pulse (Decker *et al.*, 1996), but refract a copropagating FDH probe as well. As an example, the top row of Fig. 29 shows a PIC simulation using the code WAKE (Mora and Antonsen, 1997) of guiding and compression of an initially 30 fs, 30 TW drive pulse (outlined in red) as it generates nonlinear wake profile $n_e(r,\Delta t,z)$ (gray scale) upon propagating from $z=0.1$ mm (left) to its depletion distance $z=L_d=1.8$ mm (right) in plasma of average density $\bar{n}_e=8\times10^{18}$ cm^{-3}. The second row of Fig. 29 shows corresponding changes in the amplitude envelope $|E_{\rm pr}(r,\Delta t,z)|$ of a copropagating 400 nm FDH probe pulse. By $z=0.5$ mm, the pump compresses to 20 fs (top middle) as it blows out electrons from the first wake bucket. This high-index ($\eta=1$) plasma bubble also focuses probe light inside it (bottom middle), and, by $z=1.8$ mm, compresses it near the front of the bubble to dimensions $\lambda_p^3\sim(10\ \mu\text{m})^3$. Formation of such 3D-confined light packets correlates closely with, and noninvasively diagnoses, bubble formation.

Dong *et al.* (2010b) observed bubble-formed light packets, which they called "optical bullets," in the laboratory by recovering the amplitude profile $|E_{\rm pr}(r,\zeta,z_{\rm exit})|$ of an FDH probe pulse copropagating with a laser-generated bubble. Figure 30 shows sample results using a ~2-mm-long He gas jet and laser parameters as in the simulations. Figure 30(a) shows a reference reconstruction of the unaltered incident probe profile, acquired with the gas jet turned off. For Fig. 30(b), the pump created plasma of density $\bar{n}_e=1.2\times10^{19}$ cm^{-3}, and an optical bullet (highlighted by the vertical arrow), signifying bubble formation, appeared near the probe leading edge. Yet no electrons were produced in this case, showing that bubbles can form below the threshold for spontaneous electron injection. With further increase of density ($\bar{n}_e=3.2\times10^{19}$ cm^{-3}), a smaller, brighter optical bullet formed [Fig. 30(c-1)] and nearly monoenergetic electrons were produced [Fig. 30(c-2)]. Supporting simulations confirmed the observed bubble formation and injection thresholds (Dong *et al.*, 2010a, 2010b).

The FDH analysis procedure also outputs probe phase profiles $\Delta\phi_{\rm pr}(r,\zeta,z_{\rm exit})$ in the bullet formation regime. However, they are no longer as simply related to plasma structure as in the quasilinear regime of Matlis *et al.* (2006). This is in part because $\Delta\phi_{\rm pr}$ often exceeds 2π, creating phase jumps that are difficult to unwrap (Ghiglia and Romero, 1994), and in part because refraction distorts the radial distribution of $\Delta\phi_{\rm pr}(r,\zeta,z_{\rm exit})$. $|E_{\rm pr}(r,\zeta,z_{\rm exit})|$ profiles alone lend themselves to clear physical interpretation in highly refractive plasmas. Since they resemble shadowgraphs projected on a virtual screen at $z_{\rm exit}$, FDH can be called "FD shadowgraphy" (FDS) in this regime.

3. Transverse optical probing

In discussing scattering of long ($\tau_{\rm pr}>\omega_p^{-1}$) probe pulses from plasma waves (Sec. IV.A), we noted that copropagating and transverse probes yielded complementary diagnostic information. The same is true of ultrashort ($\tau_{\rm pr}<\omega_p^{-1}$) probe pulses. Copropagating CTS (Sec. IV.A), FDI (Sec. IV.B.2), FDH (Sec. IV.C.1), and FDS (Sec. IV.C.2) probes integrate

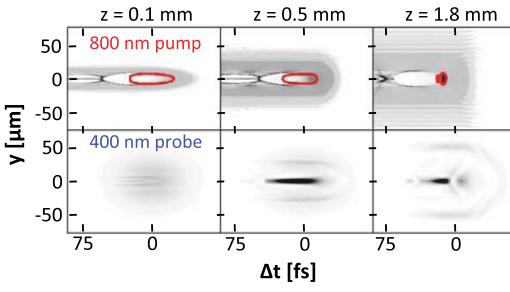

FIG. 29. WAKE simulations for $\bar{n}_e=8\times10^{18}$ cm^{-3} showing the formation of a plasma wake (top row), with pump e^{-2} isointensity contours outlined by solid red curves, and refraction of 400 nm FDH probe to form an optical bullet inside the bubble (bottom row). Pump and probe pulses propagate from gas jet entrance (left column) to $z=0.5$ mm (middle column) to the pump depletion and bullet formation length $z_{\rm exit}$ (right column) near the jet exit. The gray scale indicates electron density (top) or probe intensity (bottom). Adapted from Dong *et al.*, 2010a.

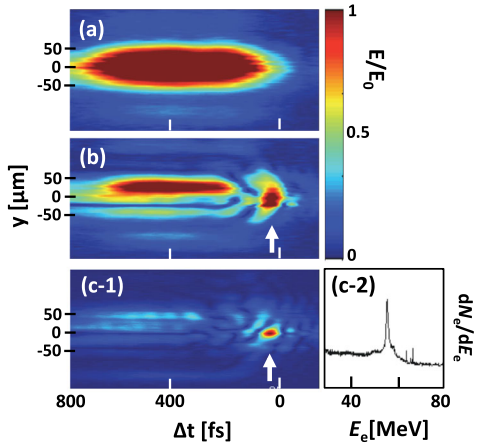

FIG. 30. Longitudinal shadowgraphy of strongly nonlinear LWFA. Probe amplitude profile $|E_{\rm pr}(r,\Delta t,z_{\rm exit})|$ is reconstructed using FDH methods (a) with no gas jet (undistorted profile), and after copropagating left to right with wake in a doubly ionized He plasma of density $\bar{n}_e[10^{19}\ \text{cm}^{-3}]=1.2$ (b) or 3.2 (c-2), showing optical bullets (highlighted with vertical arrows) trapped inside a bubble. (c-2) Electron energy spectrum. Adapted from Dong *et al.*, 2010a.

longitudinally over the wake's *evolution* as it propagates. Yet such evolution is an essential part of nonlinear wakefield acceleration. Its diagnosis requires a probe with a velocity component *transverse* to $\vec{k}_p$. Wake-induced alteration of an *ultrashort* transverse probe pulse can yield a snapshot related to the wake's internal plasma density (Sävert *et al.*, 2015) or magnetic field (Kaluza *et al.*, 2010) profile, or both (Buck *et al.*, 2011), with sub-λ_p resolution at time Δt. When shot-to-shot-fluctuations are small, a Δt sequence of such images from successive shots forms a *movie* of the evolving wake (see Sec. IV.D). Figure 31 shows a transversely probed plasma accelerator schematically.

a. Magnetic field measurements

Inside plasma electron accelerators, the current density $\vec{j}(\vec{r},t)$ of accelerating electrons and the displacement current density $\varepsilon_0 \partial \vec{E}(\vec{r},t)/\partial t$ of time-varying plasma-wave electric fields produce azimuthal magnetic fields

$$\nabla \times \vec{B}(\vec{r},t) = \mu_0 \left(\vec{j}(\vec{r},t) + \varepsilon_0 \frac{\partial \vec{E}(\vec{r},t)}{\partial t} \right) \tag{52}$$

that reach kilo-Tesla strength in plasma surrounding a bubble. A transverse linearly polarized probe impinging on the wake thus "sees" $\vec{B}$ components that are both parallel and perpendicular to $\vec{k}_{\rm pr}$ (see Fig. 31, lower left inset) that alter its polarization by the Faraday or Cotton-Mouton effects, respectively. The Faraday effect $[\vec{k}_{\rm pr} || \vec{B}(\vec{r},t)]$ locally rotates probe polarization, which remains linear. The Cotton-Mouton effect $[\vec{k}_{\rm pr} \perp \vec{B}(\vec{r},t)]$ locally induces polarization ellipticity. However, a transverse probe experiences equivalent components $\vec{B} \perp \vec{k}_{\rm pr}$ of opposite sign on the entrance and exit sides of the azimuthal field profile. Thus, the Cotton-Mouton effect approximately cancels out. In contrast, probe rays propagating above or below the central axis of the plasma-wave experience components $\vec{B} || \pm \vec{k}_{\rm pr}$ that retain their direction along each ray's entire path. Consequently, Faraday polarization rotation accumulates up to an angle

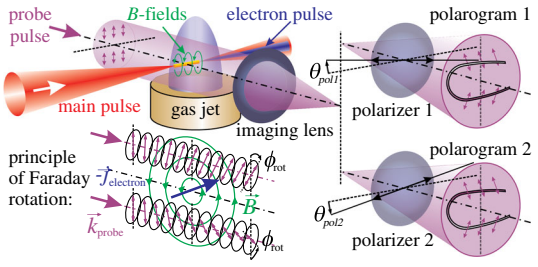

FIG. 31. Schematic experimental setup for transverse optical probing of a wakefield accelerator. A main laser pulse or particle bunch excites a gas jet, driving a plasma wake that captures and accelerates electrons. A transverse probe pulse backlights the interaction region. High-resolution optics (here represented by a simple lens) image probe light from the interaction region to CCD cameras. In the example shown, two CCDs, each equipped with a polarizer, locally detect B-field induced rotation of the probe pulse's polarization. Lower left inset: principle of polarization rotation induced by the Faraday effect. From Kaluza *et al.*, 2010.

$$\phi_{\rm rot} = \frac{e}{2 m_e c} \int_{\rm plasma} \frac{n_e(\vec{r})}{\langle \gamma \rangle n_{\rm cr}} \vec{B}(\vec{r}) \cdot d\vec{s}, \tag{53}$$

where the integration is along the path of each probe ray through the magnetized plasma, $n_{\rm cr}$ is the critical density at $\lambda_{\rm pr}$ [see Eq. (5)], and $\langle \gamma \rangle$ is the time-averaged Lorentz factor of streaming magnetized background plasma electrons (not of the accelerated electron bunch) that induce Faraday rotation. Kaluza *et al.* (2010) and Buck *et al.* (2011) observed typical Faraday rotations $\phi \sim 1°$.

The polarization of probe rays propagating above or below the plasma wave's axis rotates in opposite directions, since $\vec{B}(\vec{r}) \cdot d\vec{s}$ changes sign. A linear polarizer converts these local Faraday rotations into intensity modulations that a CCD camera detects. To distinguish subtle Faraday modulations from background probe intensity variations, Kaluza *et al.* (2010) and Buck *et al.* (2011) employed differential detection with two CCD cameras imaging the same region of plasma, as shown in Fig. 31. They detuned polarizers in front of each CCD in opposite directions from the blocking angle for the initial probe polarization. Consequently, when they divided the two raw images of Figs. 32(a) and 32(b), intensity variations unrelated to polarization rotation canceled out, whereas those induced by Faraday rotation doubled. Magnetized plasma regions then stood out clearly, as shown in Figs. 32(c)–32(e).

The transverse size ($\sim 55 \times 35\ \mu{\rm m}^2$) of the Faraday-rotated region in Fig. 32(c) (see dash-dotted ellipse) was determined mostly by imperfect imaging and by ~100 fs probe pulse duration (Kaluza *et al.*, 2010). With improved imaging resolution (~1 μm) and a shorter (8.5 fs) probe, the imaged signal shrank [see Fig. 32(f)] to a size limited by the transverse diameter of the plasma wave and the duration of the accelerating electron bunch, rather than the measurement system. Analysis of the horizontal extent of this improved Faraday signal yielded electron bunch duration $\tau_e = 5.8^{+1.9}_{-2.1}$ fs (see Sec. III.D). As Δt changed, this signal visualized formation and acceleration of the electron bunch (Buck *et al.*, 2011).

b. Transverse shadowgraphy of plasma wakes

Shadowgraphic images of the laser-driven plasma that Kaluza *et al.* (2010) recorded on each individual detector using $\tau_{\rm pr} \approx 100$ fs probe pulses [see Figs. 32(a) and 32(b)], despite clear intensity variations, showed no evidence of a wake structure oscillating with the period $\lambda_p \approx 5\ \mu$m expected in $\bar{n}_e = 4 \times 10^{19}\ {\rm cm}^{-3}$ plasma. This is because $c\tau_{\rm pr}/\lambda_p \approx 6$ cycles of the light-speed wake passed while the probe illuminated it transversely, washing out any signature of individual cycles in the shadowgraphic image. Buck *et al.* (2011) found that only by using probe pulses compressed to $c\tau_{\rm pr} \lesssim 0.5\lambda_p$ did a periodic wake appear in the shadowgraph, as shown in Fig. 32(f) for $c\tau_{\rm pr} \approx 0.43\lambda_p$ ($\tau_{\rm pr} = 8.5$ fs, $\lambda_p \approx 6\ \mu$m, $\bar{n}_e = 3.2 \times 10^{19}\ {\rm cm}^{-3}$). The period scaled with $\bar{n}_e^{-1/2}$, confirming that it originated from plasma waves. Superposition of Faraday rotation and shadowgraphic images derived from a common detection system [Fig. 32(f)] then localized the magnetized region surrounding the electron bunch with respect to the wake.

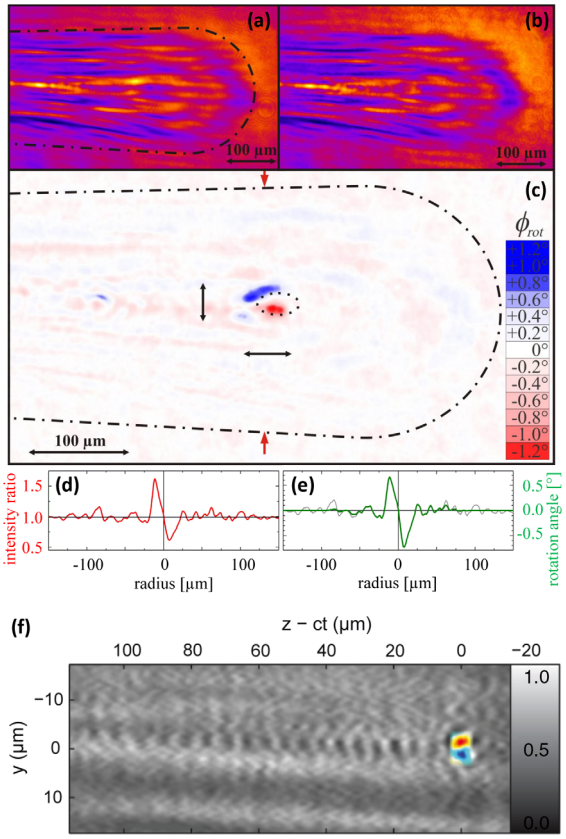

FIG. 32. Faraday-rotation measurements of quasilinear LWFA. (a), (b) Two CCD camera images of the same interaction region in $\bar{n}_e = 4 \times 10^{19}$ cm^{-3} plasma taken with 100 fs transverse probe light through polarization analyzers detuned in opposite directions from the blocking orientation. (c) Ratio of images (a)/(b), to highlight intensity variations caused by $+/-$ Faraday rotation (blue, upper and red, lower). (d) Lineout of intensity ratio along the vertical line connecting single red arrows at the top and bottom of (c); (e) deduced rotation angle. (a)–(e) From Kaluza *et al.*, 2010. (f) Similar result in $\bar{n}_e = 3.2 \times 10^{19}$ cm^{-3} plasma using 8.5 fs transverse probe and higher resolution imaging, showing the Faraday-rotation signal (color at $z - ct = y = 0$) induced by magnetic fields from laser-accelerated electron bunch of $5.8^{+1.9}_{-2.1}$ fs duration, superposed on a periodic structure (gray scale) observed in a single detector from probe refraction by a plasma wave. (f) Adapted from Buck *et al.*, 2011.

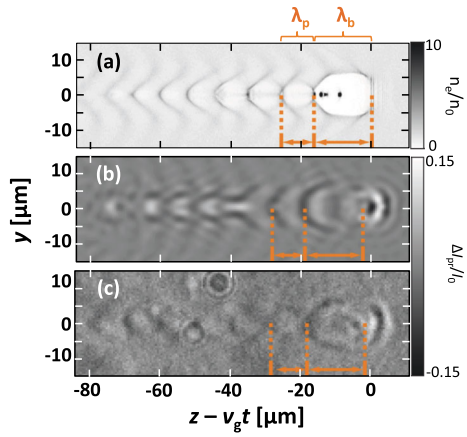

FIG. 33. Simulated and measured shadowgraphs of strongly nonlinear wake. (a) Simulated electron density relative to ambient $\bar{n}_e \equiv n_0 = 1.7 \times 10^{19}$ cm^{-3}, driven by 36 fs, 810 nm pulse focused to intensity 2.5×10^{18} W/cm^2, 18.8 μm spot (FWHM) after propagating $v_g t \approx 1.2$ mm. (b) Simulated shadowgraph for this distribution, and (c) corresponding experimental shadowgraph using $\lambda_{pr} = 0.75$ μm. Probe intensity change ΔI_{pr} relative to incident probe intensity I_0 is plotted. Brown dotted lines indicate lengths of first (λ_b) and second (λ_p) plasma wave periods. Adapted from Siminos *et al.*, 2016.

Buck *et al.* (2011) split 8.5 fs probe pulses from ~65 mJ (< 10 TW) pump pulses that were also compressed to 8.5 fs. Such short drive pulses had only enough energy to generate mildly nonlinear wakes and tens of MeV electrons. Later Schwab *et al.* (2013) spectrally broadened split-off probes in a gas-filled hollow core fiber before compressing them to the required few-cycle duration, thereby decoupling probe duration from drive pulse duration. This enabled transverse probing of strongly nonlinear wakes driven by more powerful (> 30 TW), albeit longer (~30 fs), pulses. Moreover, they generated diagnostic pulses as short as $\tau_{pr} = 5.9 \pm 0.4$ fs. A wider range of wakes could thereby be transversely imaged.

Figure 33(c) shows a shadowgraph of a right-propagating bubble-regime wake acquired with this versatile system (Sävert *et al.*, 2015). At the head of the wake, two dark, oppositely curved, arcs define an ellipse with major (minor) axis 10 (7) μm. This feature originates from the first, directly laser-driven period of the wake. Behind are several smaller (radius ~5 μm), lower-contrast dark circles that originate from subsequent periods of the wake. While it is tempting to correlate these features directly with electron density, in reality dark regions form when probe rays refract in density gradients. In addition, the wake moves distance λ_p during transit of even a δ-function probe pulse across the wake, causing temporal blurring. Optical aberrations and the finite light collection angle also influence the image.

To relate light intensity distribution in the shadowgraph to electron density distribution in the wake, Siminos *et al.* (2016) carried out 3D PIC simulations using the code EPOCH (Arber *et al.*, 2015) that included a transverse probe pulse. Figure 33(a) shows the simulated wake density distribution for conditions and propagation distance ($z = 1.2$ mm) corresponding to the shadowgraph in Fig. 33(c). Figure 33(b) shows the simulated shadowgraph, taking into account realistic imaging optics. The simulation showed that the probe refracted most strongly as it crossed the propagation axis, where longitudinal density gradients $\partial n_e/\partial z$ were strongest. This explained how sharp sub-λ_p features appeared in the shadowgraphs, even though the wake propagated ~λ_p during a probe transit. The length λ_b of the simulated, fully evacuated leading bubble [Fig. 33(a)] is ~20% smaller than the major axis of the simulated [Fig. 33(b)] and measured [Fig. 33(c)] leading shadowgraph ellipse. This is the result of transverse deflection of probe light at the dense front and back walls of the leading bubble. On the other hand, the diameters of near-circular trailing shadows closely match the length λ_p of trailing buckets of the simulated wake [Fig. 33(a)]. These trailing buckets are less fully evacuated and have less dense

walls than the leading bucket and thus deflect probe rays less. Sävert *et al.* (2015) and Siminos *et al.* (2016) attributed lengthening of the first bucket to a rapid increase of drive pulse intensity and of the associated relativistic mass of plasma electrons that immediately precedes, and prompts, self-injection of electrons into this bucket. Transverse shadowgraphy enabled direct visualization of this critical, and otherwise elusive, stage of wakefield physics.

4. Electron radiography

Transverse electron radiography complements transverse optical shadowgraphy by probing internal electromagnetic fields of a dynamic wake. Relativistic electron bunches probe wakes in the ray optics regime, limited by their energy bandwidth, transverse emittance, and duration rather than by refraction or diffraction. Hence they are subject to different resolution limits than optical probes. Moreover, as with longitudinal electron witness bunches (see Sec. IV.B.1), electron probes are sensitive to lower density plasma structures than optical probes, an advantage for diagnosing GeV plasma accelerators. Electron probes are also insensitive to quasineutral plasma and gas surrounding a wake, which can imprint unwanted background phase shift on a transverse optical probe.

Williams, Clayton, Joshi, and Katsouleas (1990), Williams, Clayton, Joshi, Katsouleas, and Mori (1990), and Williams (1995) simulated interaction of long ($\tau > \omega_p^{-1}$), transverse electron probes with wakes in $10^{16} \lesssim \bar{n}_e \lesssim 10^{17}$ cm^{-3} plasma. As for long optical probes (see Sec. IV.A), the simulations showed that scatter of low-emittance bunches could characterize global wake structure, but not sub-λ_p structure. Fainberg *et al.* (1996, 1998) proposed to resolve sub-λ_p structure of wakes in $\bar{n}_e \sim 10^{11}$ cm^{-3} plasma via picosecond transverse electron radiography. At such low $\bar{n}_e$, however, accelerating fields would be smaller than in conventional rf accelerators. Electron radiography of sub-λ_p structure of wakes in $\bar{n}_e \sim 10^{17}$ cm^{-3} plasma requires bunches of few femtosecond duration.

LWFAs themselves provide bunches of this duration (see Sec. III.D), and of very small ε_n (see Sec. III.C). Schumaker *et al.* (2013) exploited these properties to probe evolving magnetic fields in a laser-excited solid target with subpicosecond time and micrometer space resolution. C. J. Zhang *et al.* (2016) and Zhang *et al.* (2017) used ultrashort, low-ϵ_n, 60–80 MeV electron bunches from one LWFA to transversely probe the internal electromagnetic fields of a second LWFA ($\lambda_p \approx 65$ μm) driven by a split-off portion of the same laser pulse [see Fig. 34(a)]. The diverging probe, after expanding to ~800 μm diameter, irradiated a multi-λ_p section of the subject wake, which deflected probe electrons transversely. A scintillating screen at distance $L_{\rm scr}$ from the interaction recorded the 2D profile $I(x, y)$ of the transmitted electron bunch [see Fig. 34(a)]. The wide field of view enabled observation of variations in wake structure along its length. For example, a radiograph of a wake within a density ramp $n_e(z)$ [Figs. 34(b) and 34(c)] revealed changing λ_p along the ramp.

As with transverse optical shadowgraphs (see Sec. IV.C.3), the electron radiograph $I(x, y)$, although not a simple projection, is closely related to the wakefield that produced it. For best wake reconstruction, $L_{\rm scr}$ should be small enough to avoid electron trajectory crossing, which loses information. For the wakefield amplitude given by Eq. (4a), this condition leads to $L_{\rm scr} \lesssim M\gamma_{\rm pr}\lambda_p/10$, where M is a geometric magnification factor such that $M = 1$ (> 1) for a collimated (diverging) probe, and $\gamma_{\rm pr} = (1 - \beta_{\rm pr}^2)^{-1/2}$ is the probe Lorentz factor ($\beta_{\rm pr}$ is the probe velocity normalized to c). Optimal $L_{\rm scr}$ can range from a few to hundreds of millimeters. In the limit of an extremely short ($\tau_{\rm pr} \ll \omega_p^{-1}$) bunch probing a quasistatic linear wake that perturbs incident electron momentum $p_{\rm pr}$ only slightly, the effects of the radial $[E_r(r, z)]$ and longitudinal $[E_z(r, z)]$ wake electric fields on the probe decouple via the Panofsky-Wenzel theorem (Panofsky, 1956). $E_{r,z}(r, z)$ can then be recovered exactly by solving two Abel transforms

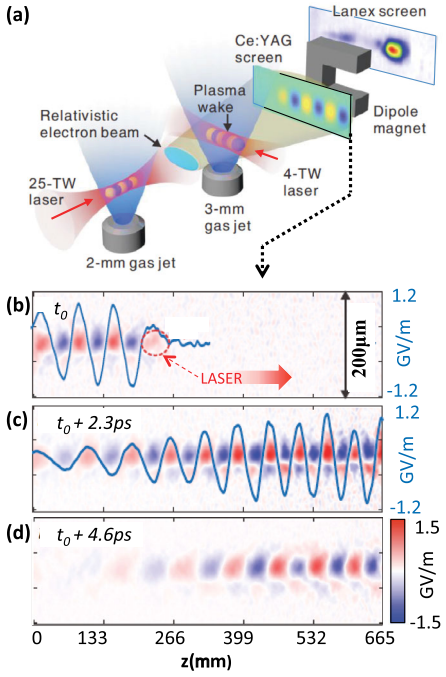

FIG. 34. Transverse electron radiography of laser wakefield. (a) Schematic experimental setup. The electron probe bunch (4 fs FWHM, 2–10 pC, 7 mrad FWHM divergence) from one plasma accelerator (2 mm gas jet, $\bar{n}_e = 8 \times 10^{18}$ cm^{-3}, 95% He, 5% N_2) driven by a 25 TW, 40 fs FWHM Ti:S laser pulse propagates transversely through the "subject" plasma accelerator (3 mm gas jet, with synchronized 4 TW, 100 fs FWHM Ti:S drive pulse) located 11 cm away, then exposes a Ce:YAG scintillator further downstream. A magnetic spectrometer can measure the probe bunch energy with scintillator removed. From Zhang *et al.*, 2017. Scintillator images at probe delays (b) t_0, (c) $t_0 + 2.3$ ps, and (d) $t_0 + 4.6$ ps of wake generated in a tapered density up ramp ($\bar{n}_e \approx 2.5 \times 10^{17}$ cm^{-3} at $z = 0$ to 3.5×10^{17} cm^{-3} at $z = 665$ μm), yielding a decreasing plasma period evident in (b) and (c). (b)–(d) From Zhang *et al.*, 2018.

$$\frac{\partial I}{\partial z} = \kappa K_m \nabla^2 \int_{-s}^{s} E_z'(r, z)dx, \tag{54a}$$

$$\frac{\partial I}{\partial y} = \kappa K_m \nabla^2 \int_{-s}^{s} E_r'(r, z)dx, \tag{54b}$$

where $\kappa = eL_m/(\beta_{\rm pr} c p_{\rm pr})$, $K_m = \exp[-(k_p\sigma_E)^2/2]$ is an averaging factor caused by wake motion that depends on wake width σ_E, and $E'_{r,z}$ denote static fields with the same form as $E_{r,z}$. Reconstruction becomes less accurate, but still possible, for strongly nonlinear wakes. The wake's magnetic field then contributes significantly to electron deflection. Unlike an optical probe, the electron probe senses the electric (as well as magnetic) field of the accelerating electron bunch inside the wake. This is because the bunch's electric field, unlike its refractive index, is not suppressed by a factor γ_e^{-1}, which makes a highly relativistic bunch practically invisible to an optical probe, except via Faraday rotation (see Sec. IV.C.3). Simultaneous sensitivity to the electric and magnetic fields of highly relativistic accelerating bunches and of tenuous plasma structures will make transverse electron radiography an attractive choice for characterizing multi-GeV laser- and beam-driven plasma accelerators.

Clayton *et al.* (2016), working at SLAC's FACET (Hogan *et al.*, 2010), mapped longitudinal variation of fields within a strongly blown out PWFA in one shot, using electrons in the trailing portion of the drive bunch itself (~20 GeV, $\sigma_z \sim 25$ μm) as witnesses. The energy spectrum of these electrons, imaged from the PWFA exit plane, exhibited a series of energy peaks and transverse bunch size modulations originating from their transverse oscillations in the bubble's radial E_r fields as they accelerated in its longitudinal E_z fields. Analysis of this structure enabled reconstruction of E_r along the bubble's length and showed that it was longitudinally uniform to within ±3%, as expected for a nearly fully blown out bubble. From the Panofsky-Wenzel theorem, they inferred comparable radial uniformity of E_z, a key requirement for emittance preservation. Such field maps can help to optimize placement and shape of separate, shorter, higher charge witness bunches.

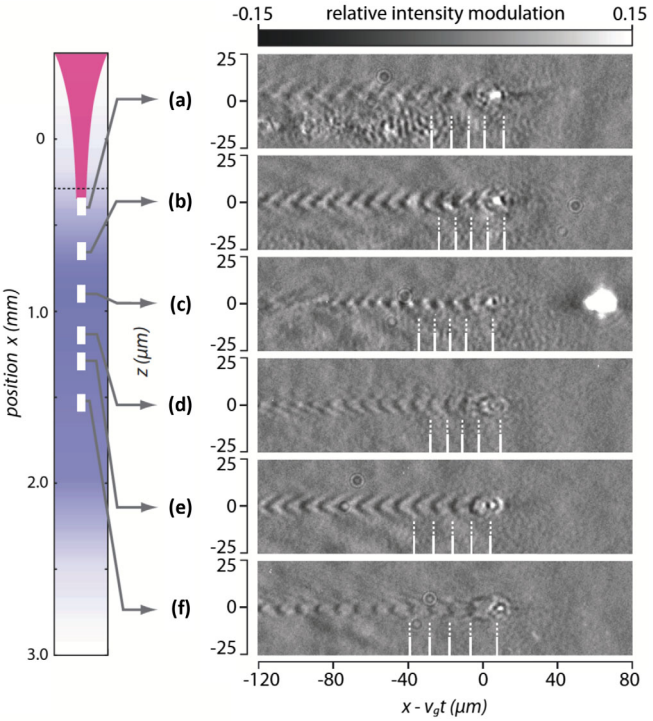

FIG. 35. Multishot shadowgraphic "movie" of strongly nonlinear wake propagating through a gas jet. Left: ionized gas density profile (deepest purple shading $\bar{n}_e = 1.65 \times 10^{19}$ cm^{-3}; white: $\bar{n}_e = 0$), intensity profile of focusing, downward-propagating laser (red funnel-shaped region, tightest focus at horizontal dashed line). (a)–(f) Experimental shadowgraphs (right) at six positions within a jet indicated by white rectangles (left), recorded with probes of wavelength $\lambda_{\rm pr} \approx 0.75$ μm and transform-limited duration 4.4 fs. White vertical lines (right): axial positions of plasma wave's peaks as deduced from simulated shadowgraphs (see Sec. IV.C.3). From Sävert *et al.*, 2015.

D. "Movies" of wake evolution

1. Multishot transverse probes

Transverse optical (Sec. IV.C.3) or electron (Sec. IV.C.4) probing records wake shadowgraphs or radiographs at fixed delay Δt between drive and probe pulses. If shot-to-shot variations can be neglected, a sequence of projections recorded over multiple shots with varying Δt yields a "movie" of the wake's evolution as it propagates through the plasma.

Figure 35 shows a Δt sequence of six optical shadowgraphs of a strongly nonlinear wake driven by 35 fs, 750 mJ pulses in $\bar{n}_e = 1.65 \times 10^{19}$ cm^{-3} plasma (Sävert *et al.*, 2015). They illustrate several stages of wake evolution. Early in the laser-plasma interaction [Fig. 35(a)], successive dark regions in the shadowgraph (positions highlighted by white vertical lines beneath) were spaced nearly equally, indicating a linear plasma wave. Subsequently, the contrast between dark and light regions increased [Fig. 35(b)], signifying increased wave amplitude. In Fig. 35(c), the first plasma period lengthened, signaling onset of strongly nonlinear laser-plasma interaction (see Sec. IV.C.3.b). Simultaneously, ~65 μm ahead of the wake, bright plasma emission, spectrally much broader (600–1000 nm) than the drive pulse, was observed, consistent with "wave-breaking" radiation (see Sec. IV.A), a signature of the onset of self-injection (Thomas *et al.*, 2007). Continuing increase in shadow contrast at the beginning of the wave train [Figs. 35(d)–35(f)] signifies increasing density gradient at the front of the bubble as the wave becomes highly nonlinear. In Fig. 35(f), the direction of curvature of the trailing shadowgraph wave periods even reverses. These features are closely linked to transverse wave breaking (Bulanov, Pegoraro *et al.*, 1997).

Two extensions of the results in Fig. 35 offer rich possibilities for future diagnostic development. First, the shadowgraphic movie of the evolving plasma structure can be coordinated with a Faraday rotation movie of the evolving electron bunch, as Buck *et al.* (2011) already did for single frames [see Fig. 32(f)]. The magnetic signature of injected electrons should appear with wave-breaking radiation as the primary bubble lengthens [Fig. 35(c)] and evolve in subsequent frames. Second, one could acquire the movie in one shot by multiplexing the probe pulse. The possibilities parallel those considered in developing single-shot FDH from multishot FDI (see Fig. 25). One is to split the probe into N replicas, each backlighting a different section of the interaction region and projecting its shadowgraph onto a separate detector. Another possibility (cf. FDH) is to chirp the probe pulse. This relieves the requirement of maintaining few-cycle pulse

duration and maps the probe arrival time at the wake onto the probe frequency (Siminos *et al.*, 2016). One could then distribute frequency bands $\Delta\omega_i$ $(i = 1, 2, \ldots, N)$ of the wake-diffracted probe to separate detectors, each recording a color-coded 2D shadowgraph of a different stage of wake evolution. However, as discussed in connection with a similar suggestion for chirped longitudinal probes (see Sec. IV.C.1), the wake diffracts the probe over the time scale $t \ll \Delta\omega_i^{-1}$, imprinting new frequency components on each band that cause them to contaminate neighboring bands. Instead, a holistic algorithm, analogous to FDH, is needed to deconvolve a time sequence of 2D images from the shadowgram of a chirped pulse. Nakagawa *et al.* (2014) recently demonstrated an all-optical "motion picture femtophotography" method that recovered images of propagating lattice vibration waves or expanding plasmas with few-μm spatial resolution and frame interval ~200 fs. The extension of such methods to transverse wake shadowgraphy is a promising direction for future research.

2. Single-shot frequency-domain streak camera

Li *et al.* (2010) and Li, Zgadzaj *et al.* (2014) introduced an alternative way to record single-shot movies using temporally broad, chirped probe pulses propagating *obliquely* to the pump pulse, as shown in Figs. 36(a) and 36(b). This approach generalized FDH and was insensitive to slight temporal broadening that occurred in manipulating the probe pulses.

In Figs. 36(a) and 36(b) a chirped probe pulse crosses the path of a pump-driven object (wake) at angle α inside a medium ("jet") of thickness L. In the probe frame, the evolving object sweeps across the probe pulse profile, imprinting a phase shift "streak" of length vector

$$\vec{L}_{\text{streak}} = L[(\cos\alpha - v_{\text{pr}}/v_{\text{ob}})\hat{z}_{\text{pr}} + \sin\alpha\hat{y}_{\text{pr}}], \tag{55}$$

that makes the projection angle

$$\phi = \tan^{-1}\frac{(v_{\text{pr}}v_{\text{ob}}/c)\sin\alpha}{v_{\text{ob}} - v_{\text{pr}}\cos\alpha} \tag{56}$$

with the object's propagation direction $\hat{z}_{\text{ob}}$. Here v_{ob} and v_{pr} denote lab frame group velocities of the object and the probe, respectively, in the medium. The streak is recovered by interfering the probe spectrally with a temporally advanced, equivalently chirped reference pulse [not shown in Figs. 36(a) and 36(b)], as in FDH (see Sec. IV.C.1). Figures 36(c)–36(e) show streaks of the nonlinear index of a pump transiting a glass Kerr medium, recorded simultaneously on probe pulses propagating at three different angles. A series of lineouts perpendicular to each streak axis $\hat{L}_{\text{streak}}$ constitutes a time sequence of the wake's projections at angle ϕ.

The streak resolves N stages of the object's evolution, where N is the number of separated objects that can be lined up sequentially along $\hat{L}_{\text{streak}}$ [e.g., $N = 5$ for the situation in Fig. 36(b)]. Phase streaks with $\phi = 0$ [Fig. 36(c)] obtained with copropagating pump and probe with $v_{\text{pr}} \neq v_{\text{ob}}$ reveal evolution of the object's transverse profile as it drifts longitudinally along the probe profile. This drift, a disadvantage in

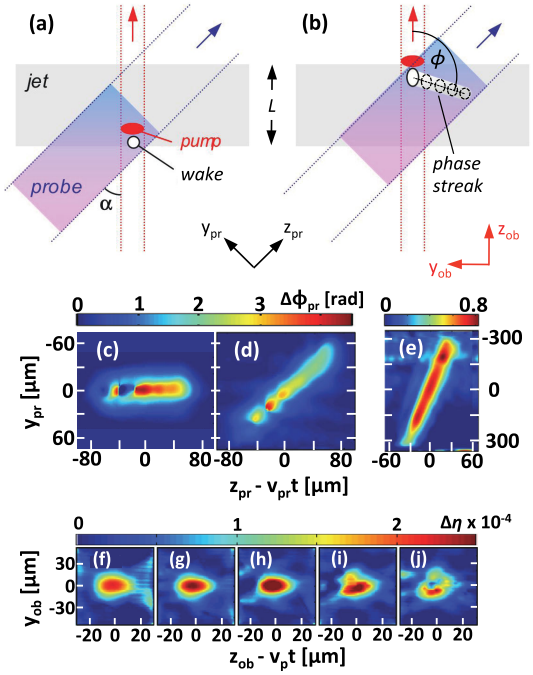

FIG. 36. Imprint of phase-shift streak on chirped probe pulse propagating obliquely to evolving laser-driven wake. (a) The beginning and (b) the end of the imprint, showing lab (α) and projection (ϕ) angles. Middle: three phase streaks from pump pulse transit through glass Kerr medium, recorded simultaneously for $\alpha(\phi) = 0.1°$ (c) (1°), (d) 1.4° (27°), and (e) 9.7° (68°). The pump entrance into the medium corresponds to the rightmost end of each streak. Bottom: Five-frame movie of pump-induced index change profile $\Delta\eta$ at normalized propagation distances (f) $z_{\text{ob}}/L = 0.17$, (g) 0.33, (h) 0.49, (i) 0.65, and (j) 0.81 into the Kerr medium, reconstructed tomographically from five streaks. Adapted from Li, Zgadzaj *et al.*, 2014.

FDH because it blurs the recovered image, provides valuable dynamic information. Streaks at $\phi = \pi/2$ [approximated by Fig. 36(e)] record evolution of the object's longitudinal profile as it drifts sideways across the probe profile. Streaks at intermediate ϕ [Fig. 36(d)] record evolution of a diagonal profile. Li *et al.* (2010) called this type of measurement a "frequency-domain streak camera" (FDSC).

By probing an evolving object simultaneously at several discrete angles, Li, Zgadzaj *et al.* (2014) reconstructed a time sequence of its entire 2D profile using tomographic algorithms. For example, Figs. 36(f)–36(j) show a five-frame movie of the nonlinear index profile of a 10 μJ, 30 fs laser pulse propagating through glass, reconstructed in one shot using five probes interfering with one reference pulse. Figures 36(f)–36(i) show a positive nonlinear index shift intensifying as the pump self-focuses, while in Fig. 36(j) a compensating negative shift appears in the center of the profile as a multiphoton-excited plasma appears. Li, Zgadzaj *et al.* (2014) called this extension of FDSC "frequency-domain tomography" (FDT). Matlis, Axley, and Leemans (2012) demonstrated a complementary spectrally multiplexed tomography (SMT) that probed an object at a continuous range of angles by angularly dispersing the frequency components of an ultrafast probe pulse. After measuring the object-induced phase shift of each component by FDI, they reconstructed the

position and cross-sectional structure of two quasistationary elliptical plasma filaments in one shot. Now that FDT and SMT have been demonstrated in such test experiments, their application to visualizing plasma wakes and plasma channels is a promising future direction.

Meanwhile, Li, Tsai *et al.* (2014) used single-probe FDSC to characterize formation, propagation, and lengthening of a laser-generated plasma bubble as it accelerated electrons quasimonoenergetically to ~100 MeV. Figure 37 summarizes results for two contrasting shots, one (left column) that produced a high-quality electron bunch (a-1), and the other (right) no relativistic electrons (b-1). During both shots, a loosely focused chirped probe pulse of bandwidth $\Delta\lambda_{\rm pr} \approx 10$ nm crossed the path of a tightly focused drive pulse in a He gas jet of length $L \approx 3$ mm at angle $\alpha = 8.6°$. At this α, plasma structures drifted across the probe profile at $\phi \approx 90°$. For both shots, the quasistatic, pump-ionized plasma column imprinted a wide uniform background phase shift $\Delta\phi_p \sim 10$ mrad (orange areas in Fig. 37, middle row). Uniquely on shot (a), a dynamic bubble of diameter $\lambda_p\sqrt{a_0}/\pi \sim 10$ μm (Lu *et al.*, 2007) in the pump's immediate wake generated a narrow phase-shift streak $\Delta\phi_b \sim -2$ mrad of opposite sign, due to the absence of free electrons inside the bubble and the dearth of electrons in the bubble's side (relative to its front and rear end) walls. Thus, after the pump blew out a fully formed bubble, which occurred at $z \approx 2L/3$ for the case shown in Fig. 37(a), $\Delta\phi_b$ carved a narrow dip [yellow streak in Fig. 37(a-2), highlighted by the arrow, lineouts in (a-3)] into the broader $\Delta\phi_p$ profile, exhibiting a time sequence of longitudinal projections of the plasma bubble. On Fig. 37(b),

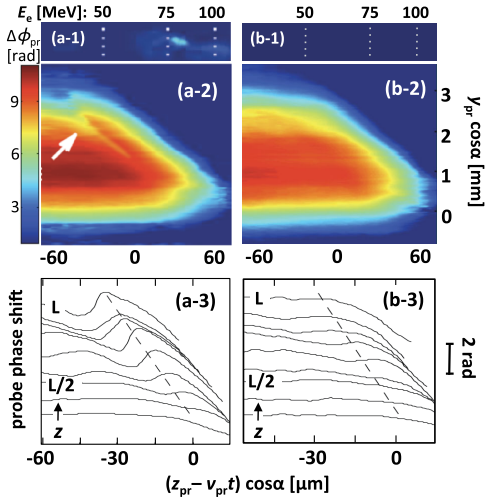

FIG. 37. FDSC study of nonlinear LWFA dynamics, showing data from (a) shot (left column) and (b) (right) at $\bar{n}_e = 2 \times 10^{19}$ cm^{-2}. Top row: electron spectra, showing (a-1) quasimonoenergetic 80 MeV electrons, and (b-1) no electrons. Middle, bottom rows: reconstructed probe phase shift $\Delta\phi_{\rm pr}$. Pump drifts from lower right to upper left as it transits a jet, imprinting nearly uniform background plasma-induced phase shift $\Delta\phi_p$ (yellow-orange area) as it ionizes gas. But only (a-2) shows narrow phase-shift dip $\Delta\phi_b$ [yellow streak, highlighted by white arrow in (a-2) and lineouts in (a-3)] imprinted by evolving bubble. Dashed lines in (a-3) and (b-3) show drift trajectories of the centers of pump pulses. Adapted from Li, Tsai *et al.*, 2014.

no $\Delta\phi_b$ phase dip was observed, i.e., no bubble formed, consistent with no relativistic electrons.

Li, Tsai *et al.* (2014) observed variations in the length, depth, and shape of the $\Delta\phi_b$ streak, and in corresponding electron spectra, as $\bar{n}_e$ and thus $P/P_{\rm cr}$ changed. For example, at 15% lower $\bar{n}_e$ than in Fig. 37(a), the bubble formed fully only near the end of the jet ($z \approx 5L/6 \approx 2.5$ mm) due to weaker self-focusing, leaving the acceleration length ($L/6 \approx 0.5$ mm) shorter than the dephasing length L_d. Consequently acceleration was incomplete, and broad low-energy electron spectra were observed. Conversely, at 10% higher $\bar{n}_e$ than in Fig. 37(a), the bubble formed at $z < L/2$, leaving acceleration length $> 4L_d$. This also yielded a broad electron energy spectrum and poor beam quality, due to strong dephasing. Stable, nearly monoenergetic electron beams were observed only in a narrow range $\bar{n}_e = (2.0 \pm 0.1) \times 10^{19}$ cm^{-3}, for which FDSC showed an acceleration length ~$1.5L_d$, assuming injection coincided with full bubble formation. Simulations confirmed this optimal acceleration length, somewhat greater than L_d. Evidently moderate dephasing helps to compress the electron spectrum by decelerating the fastest electrons just enough for the slowest electrons to catch up (Yi *et al.*, 2011). Among other LWFA physics, Li, Tsai *et al.* (2014) also observed that bubbles lengthened as they finished accelerating electrons, a signature of beam loading, and that bubbles were only partially evacuated at the injection threshold.

Simulations show that FDSC can access additional LWFA physics by using wider bandwidth probe and reference pulses. As an example, Fig. 38(a) shows the 3D wake electron density profile at $z = 2L/3 = 2$ mm for conditions corresponding to data in Fig. 37(a), simulated using the PIC code Virtual Laser Plasma Lab (VLPL) (Pukhov, 1999). The primary accelerating cavity, with injected electrons at its rear, and two trailing cavities separated by electron density sheaths of ~1 μm thickness, are visible. Figure 38(b) shows a $z = 2L/3$ lineout of the $\Delta\phi_b$ streak of a simulated FDSC experiment, using a 400 nm probe of unlimited bandwidth (dashed red curve) and with finite bandwidths $\Delta\lambda_{\rm pr} = 100$ nm (dashed blue) and 10 nm (solid blue). The last curve agrees well with the measured FDSC lineout (black curve) from Fig. 37(a). However, both average over sharp electron density spikes separating the three cavities. Direct observation of these sheaths is an important future diagnostic goal, since subtle sheath thickness variations govern electron injection (Yi *et al.*, 2011). On the other hand, a

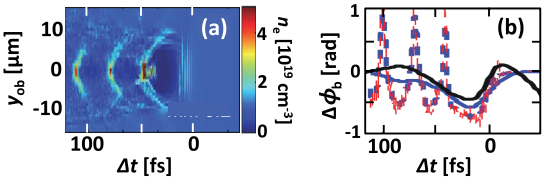

FIG. 38. Simulated FDSC experiment. (a) VLPL simulation of wake n_e profile at $z = 2L/3 = 2$ mm, for conditions of data in Fig. 37(a). (b) Lineout of the bubble phase shift $\Delta\phi_b$ for ideal FDSC probe (red dashed curve), and probes of 100 (thick blue dashed) and 10 nm (blue solid curve) bandwidth, compared with measured $\Delta\phi_b$ (black solid curve). Adapted from Li, Tsai *et al.*, 2014.

simulated $\Delta\lambda_{pr} = 100$ nm probe resolves these spikes well (dashed blue curve). Visible supercontinuum probe-reference pulses (Kim, Alexeev, and Milchberg, 2002a) provide the necessary bandwidth and should resolve μm-size structures in plasma accelerators that do not themselves produce strong background supercontinuum (Ralph *et al.*, 2009) at the probe angle α and probe wavelength range. Otherwise, ultraviolet supercontinuum probe-reference pulses and/or large α will be necessary for high-resolution FDSC.

3. Single-shot imaging of meter-long wakes

FDSC studies described in the previous section relied on the assumption that a phase modulation $\Delta\phi_{pr}(z_0)$ of width w_{ob} that an object imprinted locally on a probe pulse at position $0 < z_0 < L$ within a medium preserved its shape until it reached the medium's exit plane ($z = L$). An imaging system then relayed it to a detector. If, however, the distance $\Delta z \equiv L - z_0$ had exceeded diffraction length $\Delta z_{diff} \approx \pi w_{ob}^2/\lambda_{pr}$, then the imprinted phase modulation would have diffracted before reaching the exit. Thus a $\lambda_{pr} = 0.4$ μm probe can faithfully record the evolving shape of a plasma bubble of radius $w_{ob} = 10$ μm [see Fig. 38(a)] over propagation distance $\Delta z \sim 1$ mm, a limit that the experiment depicted in Fig. 37 barely satisfied, since the bubble formed ~1 mm from the jet exit. This places an additional limit on resolving bubble sheath structures over and above the limit set by probe bandwidth.

The depth of field Δz_{dof} of the imaging system that relays the wake-modulated probe(s) from $z = L$ to the detector must similarly be matched to Δz_{diff} of the smallest substructure one wants to resolve, otherwise portions of the imprinted streak will be out of focus at the detector. FDSC of plasma accelerators of length $\Delta z > \Delta z_{diff}$ encounters depth-of-field limits. Examples include multi-GeV laser plasma accelerators of multi-cm acceleration length (Wang *et al.*, 2013; Leemans *et al.*, 2014), meter-scale *e*-beam-driven PWFAs (Blumenfeld *et al.*, 2007), and proton-driven PWFAs hundreds of meters long (Caldwell *et al.*, 2009; Geschwendtner *et al.*, 2016).

Multiplexed transverse optical shadowgraphy (Sec. IV.C.3) or electron radiography (Sec. IV.C.4) provides one potential solution to single-shot imaging of plasma structures without depth-of-field limits, but will require maintaining a few-fs duration of multiple replicas of the incoming probe. Alternatively, Z. Li *et al.* (2013) introduced multi-object-plane imaging (MOPI) of a small-α probe, illustrated in Fig. 39. MOPI multiplexes detection of a single probe after, rather than before, it interacts with the plasma structure. Figure 39(a) (top) schematically depicts the setup. A collimated probe pulse (gray) crossed the path of a synchronized wake driver (red) at angle α, with beam waist w_0, illuminating wake structures over propagation distance $z \sim w_0/\alpha$. In contrast to FDSC, Z. Li *et al.* (2013) used a probe pulse compressed to ~100 fs. Thus it characterized only a ~100 fs longitudinal slice of the pump-generated structure. The illuminated slice swept transversely across the compressed probe profile, mapping its index profile at propagation distance z onto transverse position x on the probe profile via $x = z\alpha$. Tilting the probe intensity front by angle $\alpha/2$ with a prism prevented the phase streak from walking off of the compressed probe profile, extending the propagation distance

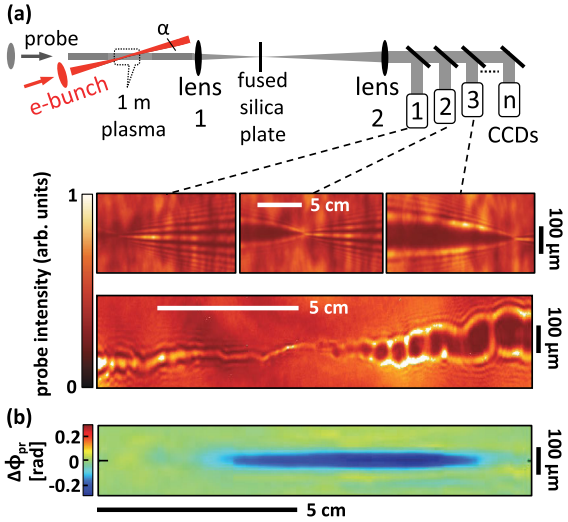

FIG. 39. Visualization of multi-cm plasma accelerator structures. (a) Top: schematic MOPI setup. Adapted from Z. Li *et al.*, 2013. Middle, triple panel: intensity modulation of 100 fs probe that propagated at an angle of 4°, delay $\Delta t \approx 100$ ps behind a 20 GeV, 2 nC, 100 fs electron bunch in hydrogen plasma of density $\bar{n}_e = 3 \times 10^{17}$ cm^{-3}, imaged from three object planes to each of three CCD cameras. Lower panel: image of unstable portion of electron trajectory captured by CCD1. (b) Continuous phase shift $\Delta\phi_{pr}(y, z)$ induced by $\bar{n}_e \approx 10^{16}$ cm^{-3} plasma over 10 cm path on 100 fs probe pulse that propagated at an angle of 1°, $\Delta t = 1.7$ ps behind a 3 mJ laser pulse in air, reconstructed from four CCD images using a Gerchberg-Saxton algorithm. (b) Adapted from Z. Li *et al.*, 2013.

that could be probed. After the interaction, copies of the phase-modulated probe created by beam splitters were imaged through a $4f$ system from multi-object planes (MOPs) along the pump path to corresponding image planes. Phase-contrast imaging (PCI), which Z. Li *et al.* (2013) implemented by placing a thin Kerr medium at the Fourier plane of the $4f$ system [see Fig. 39(a)], converted phase modulations to easily detectable amplitude modulations. CCD cameras recorded "bow-tie"-shaped images [Fig. 39(a), triple panel], in which "knots" corresponded to object planes, wider wings to nearby out-of-focus regions.

Transverse lineouts of the knots of recorded bow-tie intensity patterns straightforwardly yield phase shifts $\Delta\phi_{pr}(x_{ob}, z_i)$ that the plasma structure induced on the probe at selected object planes z_i. Z. Li *et al.* (2013) reconstructed phase shifts at intervening values of z by iteratively fitting the complete diffraction patterns of overlapping bow ties using a Gerchberg-Saxton algorithm (Fienup, 1982). Figure 39(b) shows an example of a continuous phase-shift streak $\Delta\phi_{pr}(x_{ob}, z)$ over a 10-cm propagation path, thus reconstructed from four MOPI bow-tie images of a probe that propagated at $\Delta t = 1.7$ ps behind a pump pulse propagating in air. The main feature in this reconstructed phase profile originates from plasma of density $\bar{n}_e \approx 10^{16}$ cm^{-3}, demonstrating high sensitivity of MOPI and PCI to tenuous plasma structures.

Zgadzaj *et al.* (2016) began to use MOPI to image plasma wake structures driven by 20 GeV, 2 nC electron bunches over

meter-scale propagation distances at SLAC's FACET. The bottom panel in Fig. 39(a) shows a bow-tie image of a 15-cm segment of the unstable propagation path of a 20 GeV e bunch through laser-ionized hydrogen plasma, observed at $\Delta t =$ 100 ps after passage of the bunch. At this late delay, the original electron wake had transferred most of its energy into an "ion wake" (Vieira *et al.*, 2012; Lotov, Sosedkin, and Petrenko, 2014; Sahai *et al.*, 2016; Sahai, 2017) that nevertheless preserved some features of the electron wake's propagation history. For example, transverse oscillations with periods of several cm evident in this image originated from the e-bunch's interaction with transverse density gradients in the laser-ionized plasma column (Adli *et al.*, 2016). Similarly, longitudinal oscillations of sub-cm period are a remnant of mismatched e-beam propagation with alternating focusing and defocusing. These MOPI studies are beginning to elucidate the largely unexplored relationship between short-lived electron and long-lived ion wakes, which in turn governs the repetition rate of PWFAs and LWFAs.

Diagnosis of meter-scale plasma accelerator structures via MOPI is at an early stage. Many opportunities remain for future research. Here we emphasize two. First, MOPI-PCI should be used to probe electron wakes directly at delays $0 < \Delta t < 1$ ps behind e-bunch or laser pulse drivers. Second, advanced MOPI methods that visualize an extended Δt range, rather than only a single Δt slice, of a meter-scale plasma accelerator in a single shot, should be developed, analogous to the extension of FDI (Sec. IV.B.2) to FDH (Sec. IV.C.1). Straightforward multiplexing using multiple MOPI probes at different Δt [analogous to Fig. 25(a)] is the first step. The possibility of combining MOPI with stretched-probe techniques (FDSC, FDT) should also be explored.

E. Scaling of wake probes with plasma density

Most single-shot optical wake diagnostics reviewed here were demonstrated on MeV plasma accelerators at $\bar{n}_e \sim 10^{19}$ cm^{-3}. However, future plasma accelerator research will focus on multi-GeV accelerators at $10^{17} < \bar{n}_e < 10^{18}$ cm^{-3}. Here we consider how these diagnostic methods scale as $\bar{n}_e$ decreases.

For transverse optical probes, signal strength is proportional to plasma structure width $L_\perp$, which scales as $\lambda_p \sim \bar{n}_e^{-1/2}$. For shadowgraphs, plasma structure visibility is proportional to local probe deflection angle

$$\Delta\theta_{\rm def} = \int_0^{L_\perp} \frac{d\eta}{dz} ds_\perp \approx \frac{d\eta}{dz} L_\perp \propto \frac{\bar{n}_e}{n_{\rm cr}}, \tag{57}$$

where $d\eta/dz$ is the local gradient of refractive index $\eta = (1 - n_e/n_{\rm cr})^{1/2} \approx 1 - n_e/2n_{\rm cr}$ along the wake propagation axis z, approximated as a constant over $L_\perp$ in the penultimate expression of Eq. (57). For local index change $\Delta\eta = \Delta n_e/2n_{\rm cr}$ over distance Δz, $\Delta n_e \propto \bar{n}_e$ and $\Delta z \propto \lambda_p \sim \bar{n}_e^{-1/2}$ as $\bar{n}_e$ changes. Taking $d\eta/dz \propto \Delta\eta/\Delta z$, we obtain the density scaling in the final expression of Eq. (57): equivalent shadowgraph contrast corresponds to constant $\bar{n}_e/n_{\rm cr}$. Since $n_{\rm cr} \propto \lambda_{\rm pr}^{-2}$, equivalent contrast is maintained by scaling $\lambda_{\rm pr} \sim \bar{n}_e^{-1/2}$ as $\bar{n}_e$ changes. Figure 40 presents simulated

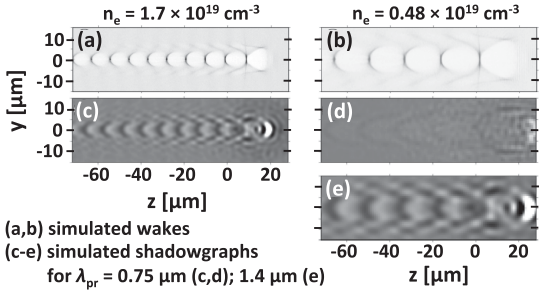

FIG. 40. 3D PIC simulations showing scaling of transverse optical shadowgraphy with plasma density $\bar{n}_e$. Top row: electron density profiles of plasma wakes driven by $\lambda_{\rm pu} = 0.8$ μm, ~0.7 J, 30 fs pulses in $\bar{n}_e =$ (a) 1.7 ($\lambda_p = 9\,\mu$m) and (b) 0.48×10^{19} cm^{-3} ($\lambda_p = 17$ μm) plasma. Second and third rows: simulated transverse shadowgraphs using (c), (d) $\lambda_{\rm pr} = 0.75$ μm and (e) 1.4 μm. From E. Siminos.

shadowgraphs of wakes in plasma of density $\bar{n}_e =$ (a) 1.7×10^{19} cm^{-3} and (b) 0.48×10^{19} cm^{-3} that confirm Eq. (57). The probe wavelength $\lambda_{\rm pr} = 0.75$ μm yields a high-contrast shadowgraph (c) at the higher $\bar{n}_e$, but low contrast at the lower $\bar{n}_e$ (d). Shifting to $\lambda_{\rm pr} = 1.4$ μm recovers high contrast at the lower (e) $\bar{n}_e$.

Equation (57) implies constant $\lambda_{\rm pr}/\lambda_p$. Thus spatial imaging resolution relative to feature size remains constant, even though absolute resolution scales with $\lambda_{\rm pr}$. Comparison of Figs. 40(c) and 40(e) confirms that constant $\bar{n}_e/n_{\rm cr}$ preserves feature resolution.

Similar arguments applied to Eq. (53) show that the sensitivity of Faraday rotation also depends on $\bar{n}_e/n_{\rm cr}$, although the strength of $\vec{B}$ remains an independent scaling parameter. For an interferometric probe propagating at angle α with respect to the wake (e.g., FDSC, MOPI), the signal strength is given by the local probe phase shift

$$\Delta\phi_{\rm pr} = \frac{2\pi}{\lambda_{\rm pr}} \int_0^{L_\perp/\sin\alpha} [\eta(s) - 1] ds \approx \frac{\pi}{\sin\alpha} \frac{L_\perp}{\lambda_{\rm pr}} \frac{\bar{n}_e}{n_{\rm cr}} \tag{58}$$

integrated over the probe's oblique path across the wake, along which the last expression in Eq. (58) assumes constant $n_e \propto \bar{n}_e$. The factor $L_\perp/\lambda_{\rm pr}$ now appears in addition to $\bar{n}_e/n_{\rm cr}$. However, constant $\bar{n}_e/n_{\rm cr}$ implies constant $L_\perp/\lambda_{\rm pr}$, and thus constant $\Delta\phi_{\rm pr}$. Resolution scales as for shadowgraphy. Thus $\bar{n}_e/n_{\rm cr}$ is a universal scaling factor for transverse optical probes.

For longitudinal optical interferometric probes (e.g., FDI, FDH), the phase shift is

$$\Delta\phi_{\rm pr} = \frac{2\pi}{\lambda_{\rm pr}} \int_0^{L_\parallel} [\eta(s) - 1] ds \approx \pi \frac{L_\parallel}{\lambda_{\rm pr}} \frac{n_e}{n_{\rm cr}}, \tag{59}$$

where again the last expression assumes constant $n_e \propto \bar{n}_e$ along the probed length $L_\parallel$. Here the limiting value of $L_\parallel$ determines $\bar{n}_e$ scaling. Several possibilities can arise. If the gas cell (or pump Rayleigh) length L limits the interaction and remains constant as $\bar{n}_e$ changes, then Eq. (59) yields $\Delta\phi_{\rm pr} \propto$

$\bar{n}_e$ for fixed $\lambda_{\rm pr}$, $\Delta\phi_{\rm pr} \propto \bar{n}_e^{1/2}$ for fixed $\bar{n}_e/n_{\rm cr}$, or $\Delta\phi_{\rm pr}$ constant for $\lambda_{\rm pr} \propto \bar{n}_e^{-1}$. If L can be adjusted as $\bar{n}_e$ changes, then often longitudinal drift of the probe-driver delay due to group-velocity mismatch $\Delta v_g = v_g^{(\rm pr)} - v_g^{(\rm dr)}$, which must be limited to a small fraction $f \ll 1$ of λ_p to avoid washing out longitudinal wake structure, determines $L_\parallel$. This limit is common for LWFAs, where $\lambda_{\rm pr}$ must differ significantly from $\lambda_{\rm pu}$ so that it can be spectrally filtered from forward-scattered pump light, but would also arise for PWFAs, where the velocity ($\approx c$) of a relativistic particle-bunch driver would always exceed $v_g^{(\rm pr)}$. In this case the allowable probe-driver drift occurs after propagation time $f\lambda_p/\Delta v_g$, yielding $L_\parallel = cf\lambda_p/\Delta v_g$. For LWFAs in which $\lambda_{\rm pr}$ and $\lambda_{\rm pu}$ remain fixed as $\bar{n}_e$ changes, $\Delta v_g \propto \bar{n}_e$ and $L_\parallel \propto \bar{n}_e^{-3/2}$, equivalent to the $\bar{n}_e$ scaling of electron dephasing length L_d [see Eq. (6)]. Then $\Delta\phi_{\rm pr} \propto \bar{n}_e^{-1/2}$, i.e., the signal strength increases with decreasing density. Dias, Oliveira e Silva, and Mendonca (1998) and Kasim *et al.* (2015) discussed other cases that can arise if $\lambda_{\rm pr}$ and/or $\lambda_{\rm dr}$ scale systematically with $\bar{n}_e$, or when L_d or $L_{\rm pd}$ [Eq. (7)] determine $L_\parallel$.

V. CONCLUSION

Approximately 10% of the budget of any accelerator is devoted to diagnostics. No accelerator can operate without them. The advent of plasma accelerators with cavities of dimensions $10 \lesssim \lambda_p \lesssim 100$ μm that accelerate lepton bunches of dimensions $\sigma \ll \lambda_p$ has posed unprecedented diagnostic challenges. Not only are these cavities and bunches much smaller than their conventional counterparts, but they evolve rapidly during acceleration. Moreover, plasma cavities are transient and light speed and thus extraordinarily difficult to visualize accurately in the laboratory. Theory and simulations have provided essential, yet incomplete, guidance in understanding plasma accelerators. Predictions of bunch size varied widely before accurate measurements were carried out, while the dynamics of 3D wave breaking, electron self-injection, and highly nonlinear wake evolution remained incompletely solved theoretical problems. Innovative laboratory diagnostics have filled many gaps in our understanding and helped transform plasma electron acceleration from a fringe empirical activity to a quantitative science at the center of international planning for next-generation light sources and colliders.

The coming transition from prototype acceleration experiments to operating accelerators will place new demands on stability, energy spread, and emittance of electron bunches, and thus on diagnostics. Early designs of plasma-accelerator-based light sources (Maier *et al.*, 2012) and colliders (Leemans and Esarey, 2009; Adli *et al.*, 2013) have already made clear that control of emittance growth and charge loss when transporting bunches from LWFA to undulator, or between collider stages, will be major challenges. Development of versatile, accurate, noninvasive bunch diagnostics in transport regions will be as important in future research as intrastage diagnostics in past research. For colliders, diagnostics will have to be replicated over hundreds of stages. This will favor those that are simple, reliable, and low cost while still achieving high spatial and temporal resolution. Moreover, integration of these diagnostics into machine learning systems and genetic algorithms (He *et al.*, 2015; Wu *et al.*, 2017) for feedback control and optimization of accelerator performance will become a focus of research.

The greatest bunch diagnostic challenges that plasma accelerators posed were measurements of ultrasmall transverse emittance ($\varepsilon_n < 1$ mm mrad) and ultrashort duration ($\tau_b \sim$ few fs) of electron bunches that strongly nonlinear LWFAs could uniquely produce (Secs. II.C.2 and II.C.3). Ultrasmall bunch dimensions were a source of numerical instabilities in simulations (Lehe *et al.*, 2013), requiring small grids and time steps as well as algorithmic advances for realistic results. Laboratory diagnostics therefore became the primary source of accurate information. Early efforts to measure ε_n of nonlinear LWFA bunches adapted the conventional pepper-pot method. However, it sampled phase space too sparsely, was limited in electron energy range, and was invasive (Sec. III.C.1.a). Similarly, early efforts to measure τ_b adapted EO methods in wide use for measuring compressed ps-duration bunches from conventional accelerators. However, strong THz dispersion of EO crystals limited even the most innovative measurements to > 10 fs rms resolution when applied to nonlinear LWFA bunches (Sec. III.D.1). Thus these conventional beam diagnostics, pushed to their limits, managed only to set upper bounds on ε_n and τ_b.

The most important breakthroughs in beam diagnostics that plasma accelerators spurred in the past decade were noninvasive methods for resolving ε_n and τ_b in one shot. Betatron x-ray spectroscopy first found evidence of bunch radii $\sigma_r \sim 0.1$ μm inside the LWFA. Full trace-space analysis methods reconstructed complete ε_n, including the correlation term, in one shot without invoking a downstream divergence measurement, and found values up to an order of magnitude smaller than pepper-pot methods had resolved (Sec. III.C.2). New spectrally resolved approaches to traditional quadrupole focus-scan methods avoided chromatic distortions, enabled single-shot measurements, and resolved ε_n values outside the accelerator as small as those that betatron spectroscopy measured inside (Sec. III.C.1.b).

Meanwhile, new methods for resolving few-fs τ_b emerged. MO measurements of Lorentz-contracted magnetic fields of relativistic bunches in plasma resolved τ_b down to ~5 fs (Buck *et al.*, 2011), free of phonon-dispersion limits of EO crystals. Combined with transverse optical shadowgraphy (Sec. IV.C.3.b), MO methods localize the accelerating bunch within an LWFA, but require probe pulses $\lesssim \tau_b$ in duration (Secs. III.D.1.c and IV.C.3.a). The use of copropagating infrared light pulses as transverse deflectors (TDs) of period $\lambda \sim 1$ μm has, in combination with a magnetic spectrometer, yielded single-shot measurements of internal energy-time structure of few-fs chirped LWFA bunches (C. Zhang *et al.*, 2016). Though technically challenging, such micro-TD experiments directly measure slice emittance and slice energy spread, key parameters for LWFA-driven FELs and colliders (Sec. III.D.1). Finally, researchers transformed TR, a beam diagnostic of long standing for conventional accelerators, into an effective diagnostic of few-fs LWFA bunches by developing multioctave, high-dynamic-range, single-shot spectrometers (Lundh *et al.*, 2011; Heigoldt *et al.*, 2015), and

new algorithms for recovering bunch temporal profiles from TR spectral intensity measurements (Bakkali Taheri *et al.*, 2016). TR spectroscopy complements time-domain MO and TD methods by characterizing τ_b outside the accelerator without probe pulses (Sec. III.D.2).

The biggest future challenge facing plasma accelerator beam diagnostics is to develop single-shot methods for recovering sub-μm transverse, as well as few-fs longitudinal, beam profiles simultaneously and with high resolution throughout beam transport lines, and over multiple accelerator stages. This challenge will increase as electron energies reach multi-GeV. CTR methods show the greatest promise for this task because of their demonstrated ability to profile bunches both longitudinally and transversely with high resolution outside the accelerator, and because of the relatively low cost of the components. Combinations of CDR and Smith-Purcell methods with multioctave spectroscopy appear promising for bringing about the required marriage of spatial and temporal diagnostics. In addition, all diagnostics must ultimately be applied to plasma-accelerated positron bunches.

The challenges that plasma accelerators posed for plasma structure diagnosis differed from those for beam diagnostics. Theory predicted the λ_p dimension of wake structural units with certainty from the beginning, and analytic 2D theories of the formation and internal morphology of linear and mildly nonlinear wakes were available early in the development of plasma electron accelerators (Chen, 1985; Gorbunov and Kirsanov, 1987; Esarey *et al.*, 1989). The main structural features of wakes that 3D simulations predicted even in the strongly nonlinear broken-wave regime (Pukhov and Meyer-ter-Vehn, 2002) were never in serious doubt, and most were large enough to be optically resolvable. The challenge lay rather in 4D visualization, i.e., 3D structure plus time evolution, a photography problem that Eadwaerd Muybridge solved for galloping horses in the 19th century (Clegg, 2007), but which remained unsolved for light-speed objects in the 21st century (Li, Zgadzaj *et al.*, 2014; Pleasants, 2014). Divergent spatial-temporal scales, i.e., internal wake structural dynamics measured in μm and fs, propagation in m and ns, together with low optical contrast and demand for single-shot visualization heightened the methodological challenge. The physics challenges were to observe difficult-to-simulate nonlinear features such as bubble formation and evolution, wave front curvature, wave breaking, self-injection, and beam-loading dynamics. A practical challenge was to monitor shot-to-shot variations in wake structure and dynamics arising from nonideal drivers or targets, which are often not fully included in idealized simulations.

Early wake diagnostic experiments drew upon established methods from other fields. Collective light scatter, a long-established diagnostic of holistic properties (ω_p, $\vec{k}_p$, $\delta n_e/\bar{n}_e$) of electron plasma waves (Froula *et al.*, 2011), helped early researchers discover laser-wakefield growth and decay processes that remain important today, but did not resolve sub-λ_p wake structure (Sec. IV.A). Likewise pump-probe experiments using fully compressed, copropagating optical or electron pulses, a staple of ultrafast science, first resolved sub-λ_p structure of plasma wakes, and observed variations in the length λ_p and amplitude $\delta n_e/\bar{n}_e$ of individual periods within a long wake, but required multiple shots and long, painstaking data acquisition (Sec. IV.B).

The singular new advances in wake diagnostics that plasma accelerators spurred were single-shot methods that resolved detailed sub-λ_p structure of plasma wakes. Frequency-domain holography, which recovers temporal phase $\phi_{\rm pr}(t)$ of long, but spectrally broad, copropagating probes pulses, captured snapshots of relativistic curvature (Matlis *et al.*, 2006) and amplitude spiking (Dong *et al.*, 2010a) of plasma wave fronts within mildly nonlinear wakes, and the variation of these effects from period to period (Sec. IV.C.1). Two generalizations of FDH expanded its diagnostic functionality: frequency-domain shadowgraphy, which recovers the probe's temporal amplitude $|E_{\rm pr}(t)|$, captured snapshots of strongly nonlinear plasma wakes (Dong *et al.*, 2010b) (Sec. IV.C.2); and frequency-domain streak camera, in which the probe propagates obliquely, captured movies of projections of a laser-driven bubble forming, deepening and expanding as it propagated (Li, Tsai *et al.*, 2014) (Sec. IV.D.2). Synchronized transversely propagating optical probes of few-fs duration projected shadowgraphs related to the wake's instantaneous density profile (Buck *et al.*, 2011) onto a camera (Sec. IV.C.3.b). A change of pump-probe delay over successive shots revealed structural changes during propagation and correlated these changes with injection of electrons (Sävert *et al.*, 2015), rendered visible by Faraday rotation (Kaluza *et al.*, 2010) (Sec. IV.D). Electron probes profiled the wake's instantaneous electric field profile (Clayton *et al.*, 2016; C. J. Zhang *et al.*, 2016; Zhang *et al.*, 2017) and proved sensitive at densities down to $\bar{n}_e \lesssim 10^{17}$ cm^{-3} (Sec. IV.C.4). Computer simulations benchmarked images obtained with this diverse and unprecedented suite of single-shot probes in detail, opening a rich new line of communication between experimental and theoretical plasma accelerator science.

Future challenges for plasma wake diagnostics lie in three main directions. One is full realization of the potential for single-shot 4D visualization, i.e., experimental output of a propagation (z) sequence of instantaneous wakefield density $n_e(x, y, z - v_g t, z)$ or field $E_e(x, y, z - v_g t, z)$ profiles. Such outputs are similar to snapshots from PIC simulations and thus might be called "PIC-tures." Frequency-domain tomography (Li, Zgadzaj *et al.*, 2014) and spectrally multiplexed tomography (Matlis, Axley, and Leemans, 2012) are promising approaches that have been demonstrated on test index objects, but must be extended to plasma wakes using wide-bandwidth probes (Sec. IV.D.2). Another promising path is multiplexing of transverse optical probes, enabling capture of a z sequence of transverse shadowgraphs and Faraday-rotation images in one shot. This approach uniquely observes the wake's shadow, the accelerated electron bunch, and wave-breaking radiation with a common apparatus, enabling correlation of diverse features of the plasma acceleration process (Sec. IV.C.3).

The second future direction is incorporating advanced diagnostics and their results directly into simulations. This is essential not only for data analysis, but for making testable predictions. One frontier is "synthetic diagnostics": simulating interactions of diagnostic probes with, or radiation from, the accelerator, not by postprocessing a subset of previously simulated results, but during a simulation, when all physics

quantities are accessible in memory. Another frontier is a computational solution of inverse problems. Already well advanced in photon science, astronomy, or geophysics, this approach uses diagnostic data from diverse sources to reconstruct quantities of interest, e.g., reconstructing electron bunch profiles using several diagnostics, even though part of the information (spectral phase) is not directly measurable (see Sec. III.D). This approach is especially powerful when analyzing diagnostics that are related by known physics, such as laser or electron beam profiles separated by propagation through vacuum.

The third future direction is expanding the application of single-shot wake diagnostics to a wider range of drivers, densities, and contexts. Even though beam-driven PWFAs were among the first to be diagnosed with sub-λ_p precision (Sec. IV.B.1), researchers are now only beginning to apply modern single-shot optical wake diagnostics to strongly nonlinear PWFAs (Zgadzaj *et al.*, 2016). This application brings the added methodological challenges of imaging sub-mm-wide wakes over multi-meter-long acceleration paths, synchronizing optical and electron probes with e-beam drivers, and probing wakes at lower density plasma ($\bar{n}_e < 10^{17}$ cm^{-3}) than in many past experiments (Sec. IV.D.3). New physics challenges include visualization of differences among electron-, positron-, and proton-driven wakes, characterization of beam-plasma instabilities, and probing of ion wakes on a ns time scale after excitation. Pulses from emerging TW-peak-power CO_2 lasers (Polyanskiy, Babzien, and Pogorelsky, 2015), because of the large ponderomotive force they exert on a plasma for given pulse energy, duration, and spot size [see Eq. (1)], will similarly be able to drive bubble-regime wakes of hundreds of microns diameter in $\bar{n}_e < 10^{17}$ cm^{-3} plasma. Such bubbles "writ large" offer the possibility not only of precisely injecting synchronized, low $\Delta E_e/E_e$, low-ε_n bunches from conventional linacs into plasma accelerators, but of probing their internal structures and evolution with higher resolution than in past experiments. Such challenges will continue to spur creativity and innovation in diagnostics for plasma electron accelerators for years to come.

ACKNOWLEDGMENTS

M. C. D. acknowledges support from the Alexander von Humboldt Foundation during preparation of this manuscript, as well as support from the U.S. Department of Energy (Grants No. DE-SC0011617, No. DE-SC0014043, and No. DE-SC0014043), the National Science Foundation (No. PHY-1734319), the Air Force Office of Scientific Research (Grants No. FA9550-16-1-0013 and No. FA9550-14-1-0045), and the Robert Welch Foundation (Grant No. F-1038). M. C. K. acknowledges support from the Bundesministerium für Bildung und Forschung (Grant No. 05K16SJC).

REFERENCES

Abuazoum, S., *et al.*, 2012, Appl. Phys. Lett. **100**, 014106.
Adli, E., J.-P. Delahaye, S. J. Gessner, M. J. Hogan, T. Raubenheimer, W. An, C. Joshi, and W. Mori, 2013, arXiv:1308.1145.
Adli, E., *et al.*, 2016, Nucl. Instrum. Methods Phys. Res., Sect. A **829**, 94.
Albert, F., R. Shah, K. Ta Phuoc, R. Fitour, F. Burgy, J. P. Rousseau, A. Tafzi, D. Douillet, T. Lefrou, and A. Rousse, 2008, Phys. Rev. E **77**, 056402.
Albert, F., *et al.*, 2013, Phys. Rev. Lett. **111**, 235004.
Amemiya, Y., and J. Miyahara, 1988, Nature (London) **336**, 89.
Amiranoff, F., *et al.*, 1995, Phys. Rev. Lett. **74**, 5220.
Amiranoff, F., *et al.*, 1998, Phys. Rev. Lett. **81**, 995.
Anania, M. P., *et al.*, 2014, Appl. Phys. Lett. **104**, 264102.
Andreev, N., 1992, JETP Lett. **55**, 571.
Andreev, N., L. Gorbunov, V. Kirsanov, K. Nakajima, and A. Ogata, 1997, Phys. Plasmas **4**, 1145.
Andreev, N., L. Gorbunov, and R. Ramazashvili, 1997, Plasma Phys. Rep. **23**, 277.
Andreev, N., V. Kirsanov, and L. Gorbunov, 1995, Phys. Plasmas **2**, 2573.
Andreev, N., S. Kuznetsov, A. Pogosova, L. Steinhauer, and W. Kimura, 2003, Phys. Rev. ST Accel. Beams **6**, 041301.
Andrews, H. L., *et al.*, 2014a, Nucl. Instrum. Methods Phys. Res., Sect. A **740**, 212.
Andrews, H. L., *et al.*, 2014b, Phys. Rev. ST Accel. Beams **17**, 052802.
Antici, P., *et al.*, 2012, J. Appl. Phys. **112**, 044902.
Antonsen, Jr., T., and P. Mora, 1992, Phys. Rev. Lett. **69**, 2204.
Arber, T., *et al.*, 2015, Plasma Phys. Controlled Fusion **57**, 113001.
Artru, X., M. Castellano, L. Catani, R. Chehab, D. Giove, K. Honkavaara, P. Patteri, M. Taurigna-Quere, A. Variola, and L. Wartski, 1998, Nucl. Instrum. Methods Phys. Res., Sect. A **410**, 148.
Artru, X., R. Chehab, K. Honkavaara, and A. Variola, 1998, Nucl. Instrum. Methods Phys. Res., Sect. B **145**, 160.
Artru, X., G. B. Yodh, and G. Mennessier, 1975, Phys. Rev. D **12**, 1289.
Arutyunyan, F., A. K. Mkhitaryan, R. Oganesyan, B. Rostomyan, and M. Sarinyan, 1979, Sov. Phys. JETP **50**, 895.
Attwood, D. T., *et al.*, 1999, IEEE J. Quantum Electron. **35**, 709.
Augst, S., D. D. Meyerhofer, D. Strickland, and S. L. Chin, 1991, J. Opt. Soc. Am. B **8**, 858.
Backus, S., C. G. Durfee, III, M. M. Murnane, and H. C. Kapteyn, 1998, Rev. Sci. Instrum. **69**, 1207.
Baghiyan, R. A., 2001, Phys. Rev. E **64**, 026610.
Baghiyan, R. A., 2004, Phys. Rev. E **69**, 026609.
Bajlekov, S., M. Heigoldt, A. Popp, J. Wenz, K. Khrennikov, S. Karsch, and S. Hooker, 2013, Phys. Rev. ST Accel. Beams **16**, 040701.
Bakkali Taheri, F., I. Konoplev, G. Doucas, P. Baddoo, R. Bartolini, J. Cowley, and S. Hooker, 2016, Phys. Rev. Accel. Beams **19**, 032801.
Barber, S. K., *et al.*, 2017, Phys. Rev. Lett. **119**, 104801.
Bardsley, J. N., B. M. Penetrante, and M. H. Mittleman, 1989, Phys. Rev. A **40**, 3823.
Barov, N., J. B. Rosenzweig, M. E. Conde, W. Gai, and J. G. Power, 2000, Phys. Rev. ST Accel. Beams **3**, 011301.
Bartolini, R., C. Clarke, N. Delerue, G. Doucas, and A. Reichold, 2012, J. Instrum. **7**, P01009.
Becker, S., *et al.*, 2009, Phys. Rev. ST Accel. Beams **12**, 102801.
Behnke, T., 2015, "The International Linear Collider Technical Design Report" (U.S. Department of Energy).
Behrens, C., C. Gerth, G. Kube, B. Schmidt, S. Wesch, and M. Yan, 2012, Phys. Rev. ST Accel. Beams **15**, 062801.
Behrens, C., *et al.*, 2014, Nat. Commun. **5**, 3762.
Berden, G., S. Jamison, A. MacLeod, W. Gillespie, B. Redlich, and A. van Der Meer, 2004, Phys. Rev. Lett. **93**, 114802.
Berden, G., *et al.*, 2007, Phys. Rev. Lett. **99**, 164801.

Berezhiani, V., and I. Murusidze, 1990, Phys. Lett. A **148**, 338.
Bergoz, J., *et al.*, 1991, Nucl. Phys. A **525**, 595.
Bernard, D., F. Amiranoff, W. P. Leemans, E. Esarey, and C. Joshi, 1999, Nucl. Instrum. Methods Phys. Res., Sect. A **432**, 227.
Bettoni, S., P. Craievich, A. Lutman, and M. Pedrozzi, 2016, Phys. Rev. Accel. Beams **19**, 021304.
Blackmore, V., G. Doucas, C. Perry, B. Ottewell, M. F. Kimmitt, M. Woods, S. Molloy, and R. Arnold, 2009, Phys. Rev. ST Accel. Beams **12**, 032803.
Blue, B. E., *et al.*, 2003, Phys. Rev. Lett. **90**, 214801.
Blumenfeld, I., *et al.*, 2007, Nature (London) **445**, 741.
Bolotovski, B. M., and G. V. Voskresenski, 1966, Sov. Phys. Usp. **9**, 73.
Bolotovskii, B. M., and A. V. Serov, 2009, Phys. Usp. **52**, 487.
Born, M., and E. Wolf, 1980, *Principles of Optics* (Pergamon Press, Oxford).
Bourgeois, N., M. Heigoldt, W. Rittershofer, A. Popp, K. Khrennikov, S. Bajlekov, S. Karsh, and S. Hooker, 2012, in *AIP Conference Proceedings* (AIP, New York), Vol. 1507, pp. 258–261.
Bret, A., L. Gremillet, and M. E. Dieckmann, 2010, Phys. Plasmas **17**, 120501.
Brown, G. L., 1975, "A First- and Second-order Matrix Theory for the Design of Beam Transport Systems and Charged Particle Spectrometers," Technical Report (SLAC).
Brown, L. S., and T. W. B. Kibble, 1964, Phys. Rev. **133**, A705.
Brown, W. J., and F. V. Hartemann, 2004, Phys. Rev. ST Accel. Beams **7**, 060703.
Brownell, J., J. Walsh, and G. Doucas, 1998, Phys. Rev. E **57**, 1075.
Brunetti, E., *et al.*, 2010, Phys. Rev. Lett. **105**, 215007.
Buck, A., M. Nicolai, K. Schmid, C. M. S. Sears, A. Saevert, J. M. Mikhailova, F. Krausz, M. C. Kaluza, and L. Veisz, 2011, Nat. Phys. **7**, 543.
Buck, A., *et al.*, 2010, Rev. Sci. Instrum. **81**, 033301.
Buck, A., *et al.*, 2013, Phys. Rev. Lett. **110**, 185006.
Bulanov, S., V. Kirsanov, and A. Sakharov, 1989, JETP Lett. **50**, 198.
Bulanov, S., N. Naumova, F. Pegoraro, and J. Sakai, 1998, Phys. Rev. E **58**, R5257.
Bulanov, S., F. Pegoraro, and A. Pukhov, 1995, Phys. Rev. Lett. **74**, 710.
Bulanov, S. V., V. I. irsanov, F. Pegoraro, and A. S. Sakharov, 1993, Laser Phys. **3**, 1078.
Bulanov, S. V., F. Pegoraro, A. M. Pukhov, and A. S. Sakharov, 1997, Phys. Rev. Lett. **78**, 4205.
Bulanov, S. V., V. A. Vshivkov, G. I. Dudnikova, N. M. Naumova, F. Pegoraro, and I. V. Pogorelksy, 1997, Plasma Phys. Rep. **23**, 259.
Caldwell, A., and K. Lotov, 2011, Phys. Plasmas **18**, 103101.
Caldwell, A., K. Lotov, A. Pukhov, and F. Simon, 2009, Nat. Phys. **5**, 363.
Caldwell, A., *et al.*, 2016, Nucl. Instrum. Methods Phys. Res., Sect. A **829**, 3.
Carron, N., 2000, Prog. Electromagn. Res. C **28**, 147.
Casalbuoni, S., H. Schlarb, B. Schmidt, P. Schmüser, B. Steffen, and A. Winter, 2008, Phys. Rev. ST Accel. Beams **11**, 072802.
Casalbuoni, S., H. Schlarb, B. Schmidt, B. Steffen, P. Schmuser, and A. Winter, 2005, "TESLA Report: Numerical Studies on the Electro-Optic Sampling of Relativistic Electron Bunches," Technical Report 2005-01 (DESY Hamburg).
Casalbuoni, S., B. Schmidt, and P. Schmuser, 2005, TESLA Report: Far-Infrared Transition and Diffraction Radiation, Technical Report 2005-15 (DESY Hamburg).
Castellano, M., V. Verzilov, L. Catani, a. Cianchi, G. Orlandi, and M. Geitz, 2001, Phys. Rev. E **63**, 056501.
Castellano, M., and V. A. Verzilov, 1998, Phys. Rev. ST Accel. Beams **1**, 062801.
Catravas, P., W. P. Leemans, J. S. Wurtele, M. S. Zolotorev, M. Babzien, I. Ben-Zvi, Z. Segalov, X.-J. Wang, and V. Yakimenko, 1999, Phys. Rev. Lett. **82**, 5261.
Cha, H. J., I. W. Choi, H. T. Kim, I. J. Kim, K. H. Nam, T. M. Jeong, and J. Lee, 2012, Rev. Sci. Instrum. **83**, 063301.
Chen, P., 1985, Part. Accel. **20**, 171.
Chen, P., J. M. Dawson, R. W. Huff, and T. Katsouleas, 1985, Phys. Rev. Lett. **54**, 693.
Chen, P., J. J. Su, J. M. Dawson, K. L. F. Bane, and P. B. Wilson, 1986, Phys. Rev. Lett. **56**, 1252.
Chen, Y. -H., S. Varma, I. Alexeev, and H. M. Milchberg, 2007, Opt. Express **15**, 7458.
Chien, C. Y., B. L. Fontaine, A. Despararois, Z. Jiang, T. W. Johnston, J. C. Kieffer, H. Pépin, F. Vidal, and H. P. Mercure, 2000, Opt. Lett. **25**, 578.
Chiou, T., and T. Katsouleas, 1998, Phys. Rev. Lett. **81**, 3411.
Chouffani, K., F. Harmon, D. Wells, J. Jones, and G. Lancaster, 2006, Phys. Rev. ST Accel. Beams **9**, 050701.
Cianchi, A., *et al.*, 2013, Nucl. Instrum. Methods Phys. Res., Sect. A **720**, 153.
Cipiccia, S., *et al.*, 2011, Nat. Phys. **7**, 867.
Clarke, J. A., 2004, *The Science and Technology of Undulators and Wigglers (Oxford Series on Synchrotron Radiation)* (Oxford University Press, New York).
Clayton, C., 2009, "An Experimentalist's Perspective on Plasma Accelerators," in *Laser-Plasma Interactions*, edited by D. A. Jaroszynski, R. Bingham, and R. A. Cairns (CRC Press—Taylor and Francis, Boca Raton), Chap. 2, pp. 19–78.
Clayton, C., M. Everett, A. Lal, D. Gordon, K. Marsh, and C. Joshi, 1994, Phys. Plasmas **1**, 1753.
Clayton, C., C. Joshi, C. Darrow, and D. Umstadter, 1985, Phys. Rev. Lett. **54**, 2343.
Clayton, C., *et al.*, 2010, Phys. Rev. Lett. **105**, 105003.
Clayton, C. E., K. A. Marsh, A. Dyson, M. Everett, A. Lal, W. P. Leemans, R. Williams, and C. Joshi, 1993, Phys. Rev. Lett. **70**, 37.
Clayton, C. E., K. A. Marsh, A. Dyson, M. Everett, A. Lal, W. P. Leemans, R. Williams, and C. Joshi, 1993, Phys. Rev. Lett. **70**, 37.
Clayton, C. E., *et al.*, 2016, Nat. Commun. **7**, 12483.
Clegg, B., 2007, *The Man Who Stopped Time: The Illuminating Story of Eadweard Muybridge—Pioneer Photographer, Father of the Motion Picture, Murderer* (Joseph Henry Press, Washington, DC).
Corde, S., K. Ta Phuoc, G. Lambert, R. Fitour, V. Malka, A. Rousse, A. Beck, and E. Lefebvre, 2013, Rev. Mod. Phys. **85**, 1.
Corde, S., *et al.*, 2015, Nature (London) **524**, 442.
Couperus, J., *et al.*, 2017, Nat. Commun., in press.
Coverdale, C., C. Darrow, C. Decker, W. Mori, K. Tzeng, K. Marsh, C. Clayton, and C. Joshi, 1995, Phys. Rev. Lett. **74**, 4659.
Cowley, J., *et al.*, 2017, Phys. Rev. Lett. **119**, 044802.
Curcio, A., D. Giulietti, G. Dattoli, and M. Ferrario, 2015, J. Plasma Phys. **81**, 495810513.
Curcio, A., *et al.*, 2017, Phys. Rev. Accel. Beams **20**, 012801.
Dawson, J. M., 1959, Phys. Rev. **113**, 383.
Debus, A., S. Bock, M. Bussmann, T. E. Cowan, A. Jochmann, T. Kluge, S. D. Kraft, R. Sauerbrey, K. Zeil, and U. Schramm, 2009, in *SPIE Proceedings*, edited by D. A. Jaroszynski and A. Rousse (SPIE–International Society for Optical Engineering, Bellingham, WA), p. 735908.
Debus, A., M. Bussmann, M. Siebold, A. Jochmann, U. Schramm, T. Cowan, and R. Sauerbrey, 2010, Appl. Phys. B **100**, 61.
Debus, A., *et al.*, 2010, Phys. Rev. Lett. **104**, 084802.

Decker, C., and W. Mori, 1994, Phys. Rev. Lett. **72**, 490.
Decker, C., W. Mori, and T. Katsouleas, 1994, Phys. Rev. E **50**, R3338.
Decker, C. D., W. B. Mori, K.-C. Tzeng, and T. Katsouleas, 1996, Phys. Plasmas **3**, 2047.
Delerue, N., 2011, Nucl. Instrum. Methods Phys. Res., Sect. A **644**, 1.
Deng, S., *et al.*, 2003, Phys. Rev. E **68**, 047401.
Deng, S., *et al.*, 2006, Phys. Rev. Lett. **96**, 045001.
Dewa, H., *et al.*, 1998, Nucl. Instrum. Methods Phys. Res., Sect. A **410**, 357.
Dias, J. M., L. Oliveira e Silva, and J. T. Mendonca, 1998, Phys. Rev. ST Accel. Beams **1**, 031301.
Ding, Y., C. Behrens, P. Emma, J. Frisch, Z. Huang, H. Loos, P. Krejcik, and M. H. Wang, 2011, Phys. Rev. ST Accel. Beams **14**, 120701.
Dodd, E. S., R. G. Hemker, C.-K. Huang, S. Wang, C. Ren, W. B. Mori, S. Lee, and T. Katsouleas, 2002, Phys. Rev. Lett. **88**, 125001.
Dohlus, M., T. Limberg, and P. Emma, 2005, ICFA Beam Dynamics Newsletter **38**, 15 [http://icfa-bd.kek.jp/news.html].
Dolgashev, V. A., G. Bowden, Y. Ding, P. Emma, P. Krejcik, J. Lewandowski, C. Limborg, M. Litos, J. Wang, and D. Xiang, 2014, Phys. Rev. ST Accel. Beams **17**, 102801.
Dolgoshein, B., 1993, Nucl. Instrum. Methods Phys. Res., Sect. A **326**, 434.
Dong, P., *et al.*, 2010a, New J. Phys. **12**, 045016.
Dong, P., *et al.*, 2010b, Phys. Rev. Lett. **104**, 134801.
Dornmair, I., K. Floettmann, and A. R. Maier, 2015, Phys. Rev. ST Accel. Beams **18**, 041302.
Dornmair, I., C. B. Schroeder, K. Floettmann, B. Marchetti, and A. R. Maier, 2016, Phys. Rev. Accel. Beams **19**, 062801.
Dorrer, C., B. de Beauvoir, C. L. Blanc, S. Ranc, J.-P. Rousseau, P. Rousseau, J.-P. Chambaret, and F. Salin, 1999, Opt. Lett. **24**, 1644.
Durfee III, C., J. Lynch, and H. Milchberg, 1995, Phys. Rev. E **51**, 2368.
Eichner, T., F. Grüner, S. Becker, M. Fuchs, D. Habs, R. Weingartner, U. Schramm, H. Backe, P. Kunz, and W. Lauth, 2007, Phys. Rev. ST Accel. Beams **10**, 082401.
Esarey, E., R. Hubbard, W. Leemans, A. Ting, and P. Sprangle, 1997, Phys. Rev. Lett. **79**, 2682.
Esarey, E., J. Krall, and P. Sprangle, 1994, Phys. Rev. Lett. **72**, 2887.
Esarey, E., S. K. Ride, and P. Sprangle, 1993, Phys. Rev. E **48**, 3003.
Esarey, E., C. B. Schroeder, and W. P. Leemans, 2009, Rev. Mod. Phys. **81**, 1229.
Esarey, E., B. A. Shadwick, P. Catravas, and W. P. Leemans, 2002, Phys. Rev. E **65**, 056505.
Esarey, E., A. Ting, and P. Sprangle, 1990, Phys. Rev. A **42**, 3526.
Esarey, E., A. Ting, P. Sprangle, and G. Joyce, 1989, Comments Plasma Phys. Control. Fusion **12**, 191.
Everett, M., A. Lal, C. Clayton, W. Mori, T. Johnston, and C. Joshi, 1995, Phys. Rev. Lett. **74**, 2236.
Fainberg, Y., V. Balakirev, A. Berezin, V. Karas, V. Kiselev, I. Onishchenko, and A. Tolstoluzhsky, 1996, in *Proceedings of the 17th International Symposium on Discharges and Electrical Insulation in Vacuum*, Vols. I and II (IEEE, New York), pp. 640–643.
Fainberg, Y., *et al.*, 1998, in *Proceedings of the 1997 Particle Accelerator Conference*, Vols. 1–3, edited by M. Comyn, M. Craddock, M. Reiser, and J. Thomson (CERN, Geneva, Switzerland), pp. 651–653.
Farmer, J., R. Martorelli, and A. Pukhov, 2015, Phys. Plasmas **22**, 123113.
Faure, J., 2017, CERN Yellow Reports Vol. **1**, p. 143.
Faure, J., Y. Glinec, A. Pukhov, S. Kiselev, S. Gordienko, E. Lefebvre, J.-P. Rousseau, F. Burgy, and V. Malka, 2004, Nature (London) **431**, 541.
Faure, J., C. Rechatin, A. Norlin, A. Lifschitz, Y. Glinec, and V. Malka, 2006, Nature (London) **444**, 737.
Fienup, J. R., 1982, Appl. Opt. **21**, 2758.
Filip, C., R. Narang, S. Y. Tochitsky, C. Clayton, P. Musumeci, R. Yoder, K. Marsh, J. Rosenzweig, C. Pellegrini, and C. Joshi, 2004, Phys. Rev. E **69**, 026404.
Filip, C. V., S. Y. Tochitsky, R. Narang, C. E. Clayton, K. A. Marsh, and C. J. Joshi, 2003, Rev. Sci. Instrum. **74**, 3576.
Fiorito, R., 2001, Nucl. Instrum. Methods Phys. Res., Sect. B **173**, 67.
Fiorito, R. B., and D. W. Rule, 1994, AIP Conf. Proc. **319**, 21.
Fiorito, R. B., A. G. Shkvarunets, T. Watanabe, V. Yakimenko, and D. Snyder, 2006, Phys. Rev. ST Accel. Beams **9**, 052802.
Fletcher, J., 2002, Opt. Express **10**, 1425.
Floettmann, K., 2014, Phys. Rev. ST Accel. Beams **17**, 054402.
Frank, I., 1966, Sov. Phys. Usp. **8**, 729.
Fritzler, S., E. Lefebvre, V. Malka, F. Burgy, A. E. Dangor, K. Krushelnick, S. P. D. Mangles, Z. Najmudin, J.-P. Rousseau, and B. Walton, 2004, Phys. Rev. Lett. **92**, 165006.
Froula, D., *et al.*, 2009, Phys. Rev. Lett. **103**, 215006.
Froula, D. H., S. H. Glenzer, N. C. Luhmann, Jr., and J. Sheffield, 2011, *Plasma Scattering of Electromagnetic Radiation*, (Academic Press, New York), 2nd ed.
Fubiani, G., E. Esarey, C. Schroeder, and W. Leemans, 2004, Phys. Rev. E **70**, 016402.
Fubiani, G., E. Esarey, C. Schroeder, and W. Leemans, 2006, Phys. Rev. E **73**, 026402.
Fuchs, M., *et al.*, 2009, Nat. Phys. **5**, 826.
Gahn, C., G. Pretzler, A. Saemann, G. D. Tsakiris, K. J. Witte, D. Gassmann, T. Schtz, U. Schramm, P. Thirolf, and D. Habs, 1998, Appl. Phys. Lett. **73**, 3662.
Gahn, C., G. Tsakiris, K. Witte, P. Thirolf, and D. Habs, 2000, Rev. Sci. Instrum. **71**, 1642.
Galimberti, M., A. Giulietti, D. Giulietti, and L. A. Gizzi, 2005, Rev. Sci. Instrum. **76**, 053303.
Gallacher, J. G., *et al.*, 2009, Phys. Plasmas **16**, 093102.
Gallot, G., J. Zhang, R. W. McGowan, T. Jeon, and D. Grischkowsky, 1999, Appl. Phys. Lett. **74**, 3450.
Geddes, C., K. Nakamura, G. Plateau, C. Toth, E. Cormier-Michel, E. Esarey, C. Schroeder, J. Cary, and W. Leemans, 2008, Phys. Rev. Lett. **100**, 215004.
Geddes, C., C. Toth, J. Van Tilborg, E. Esarey, C. Schroeder, D. Bruhwiler, C. Nieter, J. Cary, and W. Leemans, 2004, Nature (London) **431**, 538.
Geindre, J. P., P. Audebert, S. Rebibo, and J. C. Gauthier, 2001, Opt. Lett. **26**, 1612.
Geindre, J. P., P. Audebert, A. Rousse, F. Falliès, J. C. Gauthier, A. Mysyrowicz, A. D. Santos, G. Hamoniaux, and A. Antonetti, 1994, Opt. Lett. **19**, 1997.
Geschwendtner, E., E. Adli, L. Amorim, R. Apsimon, R. Assmann, A.-M. Bachmann, F. Batsch, J. Bauche, and V. K. B. Olsen, 2016, Nucl. Instrum. Methods Phys. Res., Sect. A **829**, 76.
Gessner, S., *et al.*, 2016, Nat. Commun. **7**, 11785.
Ghiglia, D. C., and L. A. Romero, 1994, J. Opt. Soc. Am. A **11**, 107.
Ginzburg, V., and I. Frank, 1946, Sov. Phys. JETP **16**, 15.
Ginzburg, V., and V. N. Tsytovich, 1979, Phys. Rep. **49**, 1.
Giulietti, D., *et al.*, 2002, Phys. Plasmas **9**, 3655.
Glinec, Y., J. Faure, A. Guemnie-Tafo, V. Malka, H. Monard, J. P. Larbre, V. D. Waele, J. L. Marignier, and M. Mostafavi, 2006, Rev. Sci. Instrum. **77**, 103301.

Glinec, Y., J. Faure, A. Norlin, A. Pukhov, and V. Malka, 2007, Phys. Rev. Lett. **98**, 194801.
Golovin, G., *et al.*, 2016, Sci. Rep. **6**, 24622.
Gonsalves, A., *et al.*, 2011, Nat. Phys. **7**, 862.
Gorbunov, L., and V. Kirsanov, 1987, Sov. Phys. JETP **66**, 290.
Gordon, D., B. Hafizi, D. Kaganovich, and A. Ting, 2008, Phys. Rev. Lett. **101**, 045004.
Gordon, D., *et al.*, 1998, Phys. Rev. Lett. **80**, 2133.
Green, S. Z., M. J. Hogan, N. Lipkowitz, B. O'Shea, G. White, V. Yakimenko, and G. Yocky, 2017, in Proceedings of the International Beam Instrument Conference (IBIC'17), SLAC-PUB-17134.
Green, S. Z., *et al.*, 2014, Plasma Phys. Controlled Fusion **56**, 084011.
Gruener, F., *et al.*, 2007, Appl. Phys. B **86**, 431.
Guillaume, E., *et al.*, 2015, Phys. Rev. Lett. **115**, 155002.
Günther, M. M., K. Sonnabend, E. Brambrink, K. Vogt, V. Bagnoud, K. Harres, and M. Roth, 2011, Phys. Plasmas **18**, 083102.
Hamster, H., A. Sullivan, S. Gordon, and R. W. Falcone, 1994, Phys. Rev. E **49**, 671.
Hamster, H., A. Sullivan, S. Gordon, W. White, and R. W. Falcone, 1993, Phys. Rev. Lett. **71**, 2725.
Harris, D. J., 2016, Proc. Natl. Acad. Sci. U.S.A. **113**, 1107.
Hartemann, F., W. Brown, D. Gibson, S. Anderson, A. Tremaine, P. Springer, A. Wootton, E. Hartouni, and C. Barty, 2005, Phys. Rev. ST Accel. Beams **8**, 100702.
Hartemann, F., D. Gibson, W. Brown, A. Rousse, K. Ta Phuoc, V. Mallka, J. Faure, and A. Pukhov, 2007, Phys. Rev. ST Accel. Beams **10**, 011301.
He, Z. -H., B. Hou, V. Lebailly, J. Nees, K. Krushelnick, and A. Thomas, 2015, Nat. Commun. **6**, 7156.
Heigoldt, M., A. Popp, K. Khrennikov, J. Wenz, S. W. Chou, S. Karsch, S. I. Bajlekov, S. M. Hooker, and B. Schmidt, 2015, Phys. Rev. ST Accel. Beams **18**, 121302.
Helle, M., D. Kaganovich, D. Gordon, and A. Ting, 2010, Phys. Rev. Lett. **105**, 105001.
HEPAP, 2015, "Accelerating Discovery: A Strategic Plan for Accelerator Research and Development in the U. S.," Technical Report (Accelerator Research and Development Subpanel of the High-Energy Physics Advisory Panel).
Hidding, B., G. Pretzler, J. Rosenzweig, T. Königstein, D. Schiller, and D. Bruhwiler, 2012, Phys. Rev. Lett. **108**, 035001.
Hidding, B., *et al.*, 2007, Rev. Sci. Instrum. **78**, 083301.
Hogan, M. J., *et al.*, 2003, Phys. Rev. Lett. **90**, 205002.
Hogan, M. J., *et al.*, 2010, New J. Phys. **12**, 055030.
Hooker, S. M., 2013, Nat. Photonics **7**, 775.
Hooker, S. M., R. Bartolini, S. P. D. Mangles, A. Tünnermann, L. Corner, J. Limpert, A. Seryi, and R. Walczak, 2014, J. Phys. B **47**, 234003.
Horst, F., G. Fehrenbacher, T. Radon, E. Kozlova, O. Rosmej, D. Czarnecki, O. Schrenk, J. Breckow, and K. Zink, 2015, Nucl. Instrum. Methods Phys. Res., Sect. A **782**, 69.
Huang, C., *et al.*, 2007, Phys. Rev. Lett. **99**, 255001.
Huang, Z., Y. Ding, and C. B. Schroeder, 2012, Phys. Rev. Lett. **109**, 204801.
Huang, Z., and K.-J. Kim, 2007, Phys. Rev. ST Accel. Beams **10**, 034801.
Iaconis, C., and I. A. Walmsley, 1998, Opt. Lett. **23**, 792.
Iwabuchi, Y., N. Mori, K. Takahashi, T. Matsuda, and S. Shionoya, 1994, Jpn. J. Appl. Phys. **33**, 178.
Jackson, J. D., 1999, *Classical Electrodynamics* (John Wiley & Sons Inc., New York, NY), 3rd ed.
Jamison, S. P., J. Shen, A. M. MacLeod, W. A. Gillespie, and D. A. Jaroszynski, 2003, Opt. Lett. **28**, 1710.
Jochmann, A., *et al.*, 2013, Phys. Rev. Lett. **111**, 114803.
Kaganovich, D., P. Sasorov, C. Cohen, and A. Zigler, 1999, Appl. Phys. Lett. **75**, 772.
Kak, A. C., and M. Slaney, 1998, *Principles of Computerized Tomographic Imaging* (IEEE Press, New York).
Kallos, E., T. Kaltsouleas, W. D. Kimura, K. Kusche, P. Muggli, I. Pavlishan, I. Pogorelsky, D. Stolyarov, and V. Yakimenko, 2008, Phys. Rev. Lett. **100**, 074802.
Kalmykov, S., S. A. Yi, and G. Shvets, 2009, Phys. Rev. Lett. **103**, 135004.
Kalmykov, S. Y., A. Beck, X. Davoine, E. Lefebvre, and B. A. Shadwick, 2012, New J. Phys. **14**, 033025.
Kaluza, M. C., H.-P. Schlenvoigt, S. P. D. Mangles, A. G. R. Thomas, A. E. Dangor, H. Schwoerer, W. B. Mori, Z. Najmudin, and K. M. Krushelnick, 2010, Phys. Rev. Lett. **105**, 115002.
Karataev, P., A. Aryshev, S. Boogert, D. Howell, N. Terunuma, and J. Urakawa, 2011, Phys. Rev. Lett. **107**, 174801.
Karlovets, D. V., and A. P. Potylitsyn, 2006, Phys. Rev. ST Accel. Beams **9**, 080701.
Karlovets, D. V., and A. P. Potylitsyn, 2008, J. Exp. Theor. Phys. **107**, 755.
Kasim, M. F., *et al.*, 2015, Phys. Rev. ST Accel. Beams **18**, 081302.
Katsouleas, T., 1986, Phys. Rev. A **33**, 2056.
Kesar, A. S., 2010, Phys. Rev. ST Accel. Beams **13**, 022804.
Khrennikov, K., J. Wenz, A. Buck, J. Xu, M. Heigoldt, L. Veisz, and S. Karsch, 2015, Phys. Rev. Lett. **114**, 195003.
Kim, H. T., K. Y. Pae, H. J. Cha, I. J. Kim, T. J. Yu, J. H. Sung, S. K. Lee, T. M. Jeong, and J. Lee, 2013, Phys. Rev. Lett. **111**, 165002.
Kim, K. Y., I. Alexeev, and H. M. Milchberg, 2002a, Opt. Express **10**, 1563.
Kim, K. Y., I. Alexeev, and H. M. Milchberg, 2002b, Appl. Phys. Lett. **81**, 4124.
Kim, M. S., D. G. Jan, T. H. Lee, I. H. Nam, I. W. Lee, and H. Suk, 2013, Appl. Phys. Lett. **102**, 204103.
Kimura, W., H. Milchberg, P. Muggli, X. Li, and W. Mori, 2011, Phys. Rev. ST Accel. Beams **14**, 041301.
Kimura, W. D., 2006, AIP Conf. Proc. **877**, 527.
Kitagawa, Y., *et al.*, 1992, Phys. Rev. Lett. **68**, 48.
Kitagawa, Y., *et al.*, 2004, Phys. Rev. Lett. **92**, 205002.
Kneip, S., *et al.*, 2008, Phys. Rev. Lett. **100**, 105006.
Kneip, S., *et al.*, 2009, Phys. Rev. Lett. **103**, 035002.
Kneip, S., *et al.*, 2010, Nat. Phys. **6**, 980.
Kneip, S., *et al.*, 2012, Phys. Rev. ST Accel. Beams **15**, 021302.
Köhler, A., J. Couperus, O. Zarini, A. Jochmann, A. Irman, and U. Schramm, 2016, Nucl. Instrum. Methods Phys. Res., Sect. A **829**, 265.
Korbly, S., A. Kesar, R. Temkin, and J. Brownell, 2006, Phys. Rev. ST Accel. Beams **9**, 022802.
Kostyukov, I., S. Kiselev, and A. Pukhov, 2003, Phys. Plasmas **10**, 4818.
Kostyukov, I., A. Pukhov, and S. Kiselev, 2004, Phys. Plasmas **11**, 5256.
Krall, J., and G. Joyce, 1995, Phys. Plasmas **2**, 1326.
Krämer, J., *et al.*, 2018, Sci. Rep. **8**, 1398.
Kruer, W. L., 1988, *The Physics of Laser-Plasma Interactions* (Addison-Wesley, Redwood City).
Kurz, T., J. Couperus, A.Irman, S. Karsch, and U. Schramm, 2018 (unpublished).
Lal, A., D. Gordon, K. Wharton, C. Clayton, K. Marsh, W. Mori, C. Joshi, M. Everett, and T. Johnston, 1997, Phys. Plasmas **4**, 1434.

Lambert, G., *et al.*, 2012, in *Proceedings of the FEL Conference* (CERN, Geneva, Switzerland), p. 2.

Laziev, E. M., E. V. Tsakanov, and S. Vahanyan, 1988, in *Proceedings of the European Particle Accelerator Conference* (CERN, Geneva, Switzerland), p. 523.

Le Blanc, S. P., M. C. Downer, R. Wagner, S.-Y. Chen, A. Maksimchuk, G. Mourou, and D. Umstadter, 1996, Phys. Rev. Lett. **77**, 5381.

LeBlanc, S. P., E. W. Gaul, N. H. Matlis, A. Rundquist, and M. C. Downer, 2000, Opt. Lett. **25**, 764.

Lee, S., T. Katsouleas, R. G. Hemker, E. S. Dodd, and W. B. Mori, 2001, Phys. Rev. E **64**, 045501.

Lee, S., *et al.*, 2002, Phys. Rev. ST Accel. Beams **5**, 011001.

Lee, S. -Y., 2004, *Accelerator Physics* (World Scientific, Singapore).

Leemans, W., B. Nagler, A. Gonsalves, C. Tóth, K. Nakamura, C. Geddes, E. Esarey, C. Schroeder, and S. Hooker, 2006, Nat. Phys. **2**, 696.

Leemans, W., D. Rodgers, P. Catravas, C. Geddes, G. Fubiani, E. Esarey, B. Shadwick, R. Donahue, and A. Smith, 2001, Phys. Plasmas **8**, 2510.

Leemans, W., *et al.*, 2003, Phys. Rev. Lett. **91**, 074802.

Leemans, W. P., and E. Esarey, 2009, Phys. Today **62**, 44.

Leemans, W. P., R. W. Schoenlein, P. Volfbeyn, A. H. Chin, T. E. Glover, P. Balling, M. Zolotorev, K. J. Kim, S. Chattopadhyay, and C. V. Shank, 1996, Phys. Rev. Lett. **77**, 4182.

Leemans, W. P., *et al.*, 2014, Phys. Rev. Lett. **113**, 245002.

Lehe, R., A. Lifschitz, C. Thaury, V. Malka, and X. Davoine, 2013, Phys. Rev. ST Accel. Beams **16**, 021301.

Lejeune, C., and J. Aubert, 1980, Appl. Charged Part. Opt. Suppl. **13A**, 159.

Li, F., Z.-M. Sheng, Y. Liu, J. Meyer-ter Vehn, W. Mori, W. Lu, and J. Zhang, 2013, Phys. Rev. Lett. **110**, 135002.

Li, F., *et al.*, 2016, Plasma Phys. Controlled Fusion **58**, 034004.

Li, S. Z., and M. J. Hogan, 2011, in Proceedings of the Particle Accelerator Conference (PAC'11), SLAC-PUB-14412 (IEEE, New York).

Li, Y., *et al.*, 2017, Phys. Plasmas **24**, 023108.

Li, Z., C.-H. Pai, Y. Y. Chang, R. Zgadzaj, X. Wang, and M. C. Downer, 2013, Opt. Lett. **38**, 5157.

Li, Z., H.-E. Tsai, X. Zhang, C.-H. Pai, Y.-Y. Chang, R. Zgadzaj, X. Wang, V. Khudik, G. Shvets, and M. C. Downer, 2014, Phys. Rev. Lett. **113**, 085001.

Li, Z., R. Zgadzaj, X. Wang, Y.-Y. Chang, and M. C. Downer, 2014, Nat. Commun. **5**, 3085.

Li, Z., R. Zgadzaj, X. Zhang, S. Reed, P. Dong, and M. C. Downer, 2010, Opt. Lett. **35**, 4087.

Lin, C., *et al.*, 2012, Phys. Rev. Lett. **108**, 094801.

Litos, M., and S. Corde, 2012, in *AIP Conf. Proc.* (AIP, New York), Vol. 1507, pp. 705–710.

Litos, M., *et al.*, 2014, Nature (London) **515**, 92.

Liu, J., *et al.*, 2011, Phys. Rev. Lett. **107**, 035001.

Lotov, K., 2010, Phys. Rev. ST Accel. Beams **13**, 041301.

Lotov, K., 2013, Phys. Plasmas **20**, 083119.

Lotov, K. V., A. P. Sosedkin, and A. V. Petrenko, 2014, Phys. Rev. Lett. **112**, 194801.

Lu, W., C. Huang, M. Zhou, W. Mori, and T. Katsouleas, 2005, Phys. Plasmas **12**, 063101.

Lu, W., C. Huang, M. Zhou, W. B. Mori, and T. Katsouleas, 2006, Phys. Rev. Lett. **96**, 165002.

Lu, W., M. Tzoufras, C. Joshi, F. S. Tsung, W. B. Mori, J. Vieira, R. A. Fonseca, and L. O. Silva, 2007, Phys. Rev. ST Accel. Beams **10**, 061301.

Lundh, O., C. Rechatin, J. Lim, V. Malka, and J. Faure, 2013, Phys. Rev. Lett. **110**, 065005.

Lundh, O., *et al.*, 2011, Nat. Phys. **7**, 219.

Maeda, R., T. Katsouleas, P. Muggli, C. Joshi, W. B. Mori, and W. Quillinan, 2004, Phys. Rev. ST Accel. Beams **7**, 111301.

Maier, A. R., A. Meseck, S. Reiche, C. B. Schroeder, T. Seggebrock, and F. Grüner, 2012, Phys. Rev. X **2**, 031019.

Malka, V., 2012, Phys. Plasmas **19**, 055501.

Malka, V., J. Faure, Y. A. Gauduel, E. Lefebvre, A. Rousse, and K. Ta Phuoc, 2008, Nat. Phys. **4**, 447.

Manahan, G. G., *et al.*, 2014, New J. Phys. **16**, 103006.

Mangles, S. P., *et al.*, 2004, Nature (London) **431**, 535.

Mangles, S. P. D., *et al.*, 2006, Phys. Rev. Lett. **96**, 215001.

Marquès, J., F. Dorchies, F. Amiranoff, P. Audebert, J. Gauthier, J. Geindre, A. Antonetti, T. Antonsen, Jr., P. Chessa, and P. Mora, 1998, Phys. Plasmas **5**, 1162.

Marquès, J. R., J. P. Geindre, F. Amiranoff, P. Audebert, J. C. Gauthier, A. Antonetti, and G. Grillon, 1996, Phys. Rev. Lett. **76**, 3566.

Marquès, J. R., *et al.*, 1997, Phys. Rev. Lett. **78**, 3463.

Matlis, N., A. Axley, and W. Leemans, 2012, Nat. Commun. **3**, 1111.

Matlis, N. H., A. Maksimchuk, V. Yanovsky, W. P. Leemans, and M. C. Downer, 2016, Opt. Lett. **41**, 5503.

Matlis, N. H., *et al.*, 2006, Nat. Phys. **2**, 749.

McGuffey, C., *et al.*, 2010, Phys. Rev. Lett. **104**, 025004.

Minty, M. G., and F. Zimmermann, 2013, *Measurement and control of charged particle beams* (Springer Science & Business Media, Berlin).

Mirzaie, M., *et al.*, 2015, Sci. Rep. **5**, 14659.

Miyahara, J., K. Takahashi, Y. Amemiya, N. Kamiya, and Y. Satow, 1986, Nucl. Instrum. Methods Phys. Res., Sect. A **246**, 572.

Modena, A., *et al.*, 1995, Nature (London) **377**, 606.

Mora, P., and T. M. Antonsen, Jr., 1997, Phys. Plasmas **4**, 217.

Mora, P., D. Pesme, A. Héron, G. Laval, and N. Silvestre, 1988, Phys. Rev. Lett. **61**, 1611.

Mostacci, A., A. Bacci, M. Boscolo, E. Chiadroni, A. Cianchi, D. Filippetto, M. Migliorati, P. Musumeci, C. Ronsivalle, and A. Rossi, 2008, Rev. Sci. Instrum. **79**, 013303.

Mostacci, A., M. Bellaveglia, E. Chiadroni, A. Cianchi, M. Ferrario, D. Filippetto, G. Gatti, and C. Ronsivalle, 2012, Phys. Rev. ST Accel. Beams **15**, 082802.

Muggli, P., 2016, arXiv:1705.10537v1.

Muggli, P., B. Allen, Y. Fang, V. Yakimenko, M. Fedurin, K. Kusche, M. Babzien, C. Swinson, and R. Malone, 2011, in *Proceedings of the Particle Accelerator Conference* (CERN, Geneva, Switzerland), pp. 712–714.

Muggli, P., and M. J. Hogan, 2009, C.R. Phys. **10**, 116.

Muggli, P., K. A. Marsh, S. Wang, C. E. Clayton, S. Lee, T. C. Katsouleas, and C. Joshi, 1999, IEEE Trans. Plasma Sci. **27**, 791.

Muggli, P., V. Yakimenko, M. Babzien, E. Kallos, and K. P. Kusche, 2008a, Phys. Rev. Lett. **101**, 054801.

Muggli, P., V. Yakimenko, M. Babzien, E. Kallos, and K. P. Kusche, 2008b, Phys. Rev. Lett. **101**, 055001.

Murphy, C. D., *et al.*, 2006, Phys. Plasmas **13**, 033108.

Nakagawa, K., *et al.*, 2014, Nat. Photonics **8**, 695.

Nakajima, K., 1989, Part. Accel. **32**, 209.

Nakajima, K., 2008, Nat. Phys. **4**, 92.

Nakajima, K., *et al.*, 1995, Phys. Rev. Lett. **74**, 4428.

Nakamura, K., A. Gonsalves, C. Lin, A. Smith, D. Rodgers, R. Donahue, W. Byrne, and W. Leemans, 2011, Phys. Rev. ST Accel. Beams **14**, 062801.

Nakamura, K., D. E. Mittelberger, A. J. Gonsalves, J. Daniels, H.-S. Mao, F. Stulle, J. Bergoz, and W. P. Leemans, 2016, Plasma Phys. Controlled Fusion **58**, 034010.
Nakamura, K., W. Wan, N. Ybarrolaza, D. Syversrud, J. Wallig, and W. P. Leemans, 2008, Rev. Sci. Instrum. **79**, 053301.
Németh, K., B. Shen, Y. Li, H. Shang, R. Crowell, K. Harkay, and J. Cary, 2008, Phys. Rev. Lett. **100**, 095002.
Norreys, P. A., 2009, Nat. Photonics **3**, 423.
O'Connell, C. L., *et al.*, 2006, Phys. Rev. ST Accel. Beams **9**, 101301.
Ohkubo, T., *et al.*, 2007, Phys. Rev. ST Accel. Beams **10**, 031301.
Onuki, H., and P. Elleaume, 2002, *Undulators, Wigglers and Their Applications* (CRC Press, Boca Raton, FL).
O'Shea, P., M. Kimmel, X. Gu, and R. Trebino, 2001, Opt. Lett. **26**, 932.
Osterhoff, J., *et al.*, 2008, Phys. Rev. Lett. **101**, 085002.
Pafomov, V. E., 1971, "Radiation of a Charged Particle in the Presence of a Separating Boundary," in *Nuclear Physics and Interaction of Particles with Matter*, edited by D. V. Skobel'tsyn (Springer, Boston, MA), pp. 25–157.
Pak, A., K. A. Marsh, S. F. Martins, W. Lu, W. B. Mori, and C. Joshi, 2010, Phys. Rev. Lett. **104**, 025003.
Panofsky, W. K. H., 1956, Rev. Sci. Instrum. **27**, 967.
Pausch, R., A. Debus, R. Widera, K. Steiniger, A. Huebl, H. Burau, M. Bussmann, and U. Schramm, 2014, Nucl. Instrum. Methods Phys. Res., Sect. A **740**, 250.
Pausch, R., *et al.*, 2014, in *Proceedings of IPAC2014* (CERN, Geneva, Switzerland), pp. 761–764.
Peng, X.-Y., O. Willi, M. Chen, and A. Pukhov, 2008, Opt. Express **16**, 12342.
Plateau, G. R., *et al.*, 2012, Phys. Rev. Lett. **109**, 064802.
Platt, B., and R. Shack, 2001, J. Refract. Surg. **17**, S573.
Pleasants, S., 2014, Nat. Photonics **8**, 271.
Pogorelsky, I., and I. Ben-Zvi, 2014, Plasma Phys. Controlled Fusion **56**, 084017.
Pollock, B. *et al.*, 2009, Two-screen method for determining electron beam energy and deflection from laser wakefield acceleration, Technical Report [Lawrence Livermore National Laboratory (LLNL), Livermore, CA].
Pollock, B., *et al.*, 2011, Phys. Rev. Lett. **107**, 045001.
Polyanskiy, M. N., M. Babzien, and I. V. Pogorelsky, 2015, Optica **2**, 675.
Powers, N. D., I. Ghebregziabher, G. Golovin, C. Liu, S. Chen, S. Banerjee, J. Zhang, and D. P. Umstadter, 2014, Nat. Photonics **8**, 28.
Protopapas, M., C. H. Keitel, and P. L. Knight, 1997, Rep. Prog. Phys. **60**, 389.
Pukhov, A., 1999, J. Plasma Phys. **61**, 425.
Pukhov, A., and J. Meyer-ter-Vehn, 2002, Appl. Phys. B **74**, 355.
Ralph, J. E., K. A. Marsh, A. E. Pak, W. Lu, C. E. Clayton, F. Fang, W. B. Mori, and C. Joshi, 2009, Phys. Rev. Lett. **102**, 175003.
Rechatin, C., J. Faure, A. Ben-Ismail, J. Lim, R. Fitour, A. Specka, H. Videau, A. Tafzi, F. Burgy, and V. Malka, 2009, Phys. Rev. Lett. **102**, 164801.
Reed, S., V. Chvykov, G. Kalintchenko, T. Matsuoka, V. Yanovsky, C. R. Vane, J. R. Beene, D. Stracener, D. R. Schultz, and A. Maksimchuk, 2007, J. Appl. Phys. **102**, 073103.
Rees, J., and L. Rivkin, 1984, Measuring emittances and sigma matrices, Technical Report (Stanford Linear Accelerator Center, CA).
Reiche, S., and J. Rosenzweig, 2001, PACS2001, *Proceedings of the 2001 Particle Accelerator Conference* (Cat. No. 01CH37268), 7.
Reiser, M., 2008, *Theory and design of charged particle beams* (Wiley-VCH, Weinheim).
Reynaud, F., F. Salin, and A. Barthelemy, 1989, Opt. Lett. **14**, 275.
Ride, S. K., E. Esarey, and M. Baine, 1995, Phys. Rev. E **52**, 5425.
Rittershofer, W., C. B. Schroeder, E. Esarey, F. J. Grüner, and W. P. Leemans, 2010, Phys. Plasmas **17**, 063104.
Ritz, S., 2014, Building for Discovery: Strategic Plan for U. S. Particle Physics in the Global Context, Technical Report [Particle Physics Project Prioritization Panel (P5)].
Röhrs, M., C. Gerth, H. Schlarb, B. Schmidt, and P. Schmüser, 2009, Phys. Rev. ST Accel. Beams **12**, 050704.
Rosenbluth, M., and C. Liu, 1972, Phys. Rev. Lett. **29**, 701.
Rosenzweig, J., N. Barov, A. Murokh, E. Colby, and P. Colestock, 1998, Nucl. Instrum. Methods Phys. Res., Sect. A **410**, 532.
Rosenzweig, J. B., 1987, Phys. Rev. Lett. **58**, 555.
Rosenzweig, J. B., B. Breizman, T. Katsouleas, and J. J. Su, 1991, Phys. Rev. A **44**, R6189.
Rosenzweig, J. B., D. B. Cline, B. Cole, H. Figureroa, W. Gai, R. Konecny, J. Norem, P. Schoessow, and J. Simpson, 1988, Phys. Rev. Lett. **61**, 98.
Rosenzweig, J. B., P. Schoessow, B. Cole, W. Gai, R. Konecny, J. Norem, and J. Simpson, 1989, Phys. Rev. A **39**, 1586.
Rousse, A., *et al.*, 2004, Phys. Rev. Lett. **93**, 135005.
Ruth, R. D., P. Morton, P. B. Wilson, and A. Chao, 1984, Part. Accel. **17**, 171.
Rykovanov, S., C. Geddes, J. Vay, C. Schroeder, E. Esarey, and W. Leemans, 2014, J. Phys. B **47**, 234013.
Sahai, A. A., 2017, Phys. Rev. Accel. Beams **20**, 081004.
Sahai, A. A., T. C. Katsouleas, F. S. Tsung, and W. B. Mori, 2016, arXiv:1405.4302.
Salin, F., P. Georges, G. Roger, and A. Brun, 1987, Appl. Opt. **26**, 4528.
Sannibale, F., G. V. Stupakov, M. S. Zolotorev, D. Filippetto, and L. Jägerhofer, 2009, Phys. Rev. ST Accel. Beams **12**, 032801.
Sarri, G., *et al.*, 2014, Phys. Rev. Lett. **113**, 224801.
Sävert, A., *et al.*, 2015, Phys. Rev. Lett. **115**, 055002.
Savran, D., *et al.*, 2010, Nucl. Instrum. Methods Phys. Res., Sect. A **613**, 232.
Schlenvoigt, H. P., *et al.*, 2008, Nat. Phys. **4**, 130.
Schmid, K., A. Buck, C. M. Sears, J. M. Mikhailova, R. Tautz, D. Herrmann, M. Geissler, F. Krausz, and L. Veisz, 2010, Phys. Rev. ST Accel. Beams **13**, 091301.
Schmidt, B., 2006, in *Proceedings of the 28th International Free Electron Laser Conference* (CERN, Geneva, Switzerland), p. 761.
Schnell, M., *et al.*, 2012, Phys. Rev. Lett. **108**, 075001.
Schnell, M., *et al.*, 2013, Nat. Commun. **4**, 2421.
Schramm, U., *et al.*, 2017, J. Phys. Conf. Ser. **874**, 012028.
Schroeder, C., E. Esarey, J. Van Tilborg, and W. Leemans, 2004, Phys. Rev. E **69**, 016501.
Schroeder, C., P. Lee, J. Wurtele, E. Esarey, and W. Leemans, 1999, Phys. Rev. E **59**, 6037.
Schroeder, C., D. Whittum, and J. Wurtele, 1999, Phys. Rev. Lett. **82**, 1177.
Schumaker, W., *et al.*, 2013, Phys. Rev. Lett. **110**, 015003.
Schwab, M. B., *et al.*, 2013, Appl. Phys. Lett. **103**, 191118.
Schwoerer, H., B. Liesfeld, H. Schlenvoigt, K. Amthor, and R. Sauerbrey, 2006, Phys. Rev. Lett. **96**, 014802.
Sears, C. M. S., A. Buck, K. Schmid, J. Mikhailova, F. Krausz, and L. Veisz, 2010, Phys. Rev. ST Accel. Beams **13**, 092803.
Sears, C. M. S., S. B. Cuevas, U. Schramm, K. Schmid, A. Buck, D. Habs, F. Krausz, and L. Veisz, 2010, Rev. Sci. Instrum. **81**, 073304.
Seggebrock, T., A. R. Maier, I. Dornmair, and F. Gruener, 2013, Phys. Rev. ST Accel. Beams **16**, 070703.

Serafini, L., 1996, IEEE Trans. Plasma Sci. **24**, 421.
Shah, R. C., F. Albert, K. Ta Phuoc, F. Burgy, J. P. Rousseau, O. Shevchenko, D. Boschetto, A. Rousse, A. Pukhov, and S. Kiselev, 2006, Phys. Rev. E **74**, 045401(R).
Shaw, B., *et al.*, 2012, in *AIP Conference Proceedings* (AIP, New York), Vol. 1507, pp. 310–314.
Shaw, J., *et al.*, 2017, arXiv:1705.08637.
Shiraishi, S., *et al.*, 2013, Phys. Plasmas **20**, 063103.
Shkvarunets, A. G., and R. B. Fiorito, 2008, Phys. Rev. ST Accel. Beams **11**, 012801.
Shvets, G., and X. Li, 1999, Phys. Plasmas **6**, 591.
Siders, C. W., S. P. LeBlanc, A. Babine, A. Stepanov, A. Sergeev, T. Tajima, and M. C. Downer, 1996, IEEE Trans. Plasma Sci. **24**, 301.
Siders, C. W., S. P. LeBlanc, D. Fisher, T. Tajima, M. C. Downer, A. Babine, A. Stepanov, and A. Sergeev, 1996, Phys. Rev. Lett. **76**, 3570.
Siders, C. W., J. L. Siders, A. J. Taylor, S.-G. Park, and A. M. Weiner, 1998, Appl. Opt. **37**, 5302.
Siminos, E., S. Skupin, A. Saevert, J. M. Cole, S. P. D. Mangles, and M. C. Kaluza, 2016, Plasma Phys. Controlled Fusion **58**, 065004.
Slusher, R., and C. M. Surko, 1980, Phys. Fluids **23**, 472.
Smith, S. J., and E. Purcell, 1953, Phys. Rev. **92**, 1069.
Sprangle, P., E. Esarey, J. Krall, and G. Joyce, 1992, Phys. Rev. Lett. **69**, 2200.
Sprangle, P., E. Esarey, and A. Ting, 1990a, Phys. Rev. A **41**, 4463.
Sprangle, P., E. Esarey, and A. Ting, 1990b, Phys. Rev. Lett. **64**, 2011.
Sprangle, P., B. Hafizi, J. R. Peano, R. F. Hubbard, A. Ting, C. I. Moore, D. F. Gordon, A. Zigler, D. Kaganovich, and J. T. M. Antonsen, 2001, Phys. Rev. E **63**, 056405.
Sprangle, P., C.-M. Tang, and E. Esarey, 1987, IEEE Trans. Plasma Sci. **15**, 145.
Steffen, B., *et al.*, 2009, Phys. Rev. ST Accel. Beams **12**, 032802.
Steinke, S., *et al.*, 2016, Nature (London) **530**, 190.
Suk, H., N. Barov, J. B. Rosenzweig, and E. Esarey, 2001, Phys. Rev. Lett. **86**, 1011.
Sun, F. G., Z. Jiang, and X.-C. Zhang, 1998, Appl. Phys. Lett. **73**, 2233.
Sütterlin, D., D. Erni, M. Dehler, H. Jäckel, H. Sigg, and V. Schlott, 2007, Nucl. Instrum. Methods Phys. Res., Sect. B **264**, 361.
Swanson, K., *et al.*, 2017, Phys. Rev. Accel. Beams **20**, 051301.
Tajima, T., and J. M. Dawson, 1979, Phys. Rev. Lett. **43**, 267.
Takeda, M., H. Ina, and S. Kobayashi, 1982, J. Opt. Soc. Am. **72**, 156.
Tanaka, K. A., T. Yabuuchi, T. Sato, R. Kodama, Y. Kitagawa, T. Takahashi, T. Ikeda, Y. Honda, and S. Okuda, 2005, Rev. Sci. Instrum. **76**, 013507.
Ta Phuoc, K., S. Corde, R. Shah, F. Albert, R. Fitour, J.-P. Rousseau, F. Burgy, B. Mercier, and A. Rousse, 2006, Phys. Rev. Lett. **97**, 225002.
Ta Phuoc, K., S. Corde, C. Thaury, V. Malka, A. Tafzi, J. P. Goddet, R. C. Shah, S. Sebban, and A. Rousse, 2012, Nat. Photonics **6**, 308.
Tarantola, A., 2006, Nat. Phys. **2**, 492.
Ter-Mikaelian, M. L., 1972, *New York* (Wiley, New York).
Thaury, C., E. Guillaume, S. Corde, R. Lehe, M. Le Bouteiller, K. Ta Phuoc, X. Davoine, J. M. Rax, A. Rousse, and V. Malka, 2013, Phys. Rev. Lett. **111**, 135002.
Thomas, A. G. R., 2010, Phys. Plasmas **17**, 056708.
Thomas, A. G. R., S. P. D. Mangles, Z. Najmudin, M. C. Kaluza, C. D. Murphy, and K. Krushelnick, 2007, Phys. Rev. Lett. **98**, 054802.
Thomas, C., N. Delerue, and R. Bartolini, 2013, Nucl. Instrum. Methods Phys. Res., Sect. A **729**, 554.
Ting, A., K. Krushelnick, C. Moore, H. Burris, E. Esarey, J. Krall, and P. Sprangle, 1996, Phys. Rev. Lett. **77**, 5377.
Tokunaga, E., A. Terasaki, and T. Kobayashi, 1992, Opt. Lett. **17**, 1131.
Trebino, R., K. W. DeLong, D. N. Fittinghoff, J. N. Sweetser, M. A. Krumbügel, B. A. Richman, and D. J. Kane, 1997, Rev. Sci. Instrum. **68**, 3277.
Trines, R. M. G. M., *et al.*, 2009, Plasma Phys. Controlled Fusion **51**, 024008.
Tsai, H. E., *et al.*, 2015, Phys. Plasmas **22**, 023106.
Tzeng, K., W. B. Mori, and C. Decker, 1996, Phys. Rev. Lett. **76**, 3332.
Tzoufras, M., W. Lu, F. S. Tsung, C. Huang, W. B. Mori, T. Katsouleas, J. Vieira, R. A. Fonseca, and L. O. Silva, 2008, Phys. Rev. Lett. **101**, 145002.
Umstadter, D., S.-Y. Chen, A. Maksimchuk, G. Mourou, and R. Wagner, 1996, Science **273**, 472.
Umstadter, D., E. Esarey, and J. Kim, 1994, Phys. Rev. Lett. **72**, 1224.
Umstadter, D., J. Kim, E. Esarey, E. Dodd, and T. Neubert, 1995, Phys. Rev. E **51**, 3484.
Umstadter, D. P., 2015, Contemp. Phys. **56**, 417.
Unser, K., 1989, in *Proceedings of the Particle Accelerator Conference* (IEEE, New York), pp. 71–73.
van Tilborg, J., C. Schroeder, C. Filip, C. Tóth, C. Geddes, G. Fubiani, R. Huber, R. Kaindl, E. Esarey, and W. Leemans, 2006, Phys. Rev. Lett. **96**, 014801.
van Tilborg, J., C. B. Schroeder, E. Esarey, and W. P. Leemans, 2004, Laser Part. Beams **22**, 415.
van Tilborg, J., *et al.*, 2015, Phys. Rev. Lett. **115**, 184802.
Vieira, J., R. Fonseca, W. Mori, and L. Silva, 2012, Phys. Rev. Lett. **109**, 145005.
Villeneuve, D., H. Baldis, J. Bernard, and R. Benesch, 1991, J. Opt. Soc. Am. B **8**, 895.
Wagner, R., S.-Y. Chen, A. Maksimchuk, and D. Umstadter, 1997, Phys. Rev. Lett. **78**, 3125.
Wahlstrand, J., Y.-H. Cheng, Y.-H. Chen, and H. Milchberg, 2011, Phys. Rev. Lett. **107**, 103901.
Wang, S., *et al.*, 2002, Phys. Rev. Lett. **88**, 135004.
Wang, W., *et al.*, 2016, Phys. Rev. Lett. **117**, 124801.
Wang, X., *et al.*, 2013, Nat. Commun. **4**, 1988.
Wartski, L., S. Roland, J. Lasalle, M. Bolore, and G. Filippi, 1975, J. Appl. Phys. **46**, 3644.
Weiner, A. M., 2000, Rev. Sci. Instrum. **71**, 1929.
Weingartner, R., *et al.*, 2011, Phys. Rev. ST Accel. Beams **14**, 052801.
Weingartner, R., *et al.*, 2012, Phys. Rev. ST Accel. Beams **15**, 111302.
Wickersheim, K., R. Alves, and R. Buchanan, 1970, IEEE Trans. Nucl. Sci. **17**, 57.
Wilke, I., A. M. MacLeod, W. A. Gillespie, G. Berden, G. M. H. Knippels, and A. F. G. van der Meer, 2002, Phys. Rev. Lett. **88**, 124801.
Wilks, S. C., J. M. Dawson, W. B. Mori, T. Katsouleas, and M. E. Jones, 1989, Phys. Rev. Lett. **62**, 2600.
Williams, R. L., 1995, Rev. Sci. Instrum. **66**, 468.
Williams, R. L., C. E. Clayton, C. Joshi, and T. Katsouleas, 1990, Rev. Sci. Instrum. **61**, 3037.
Williams, R. L., C. E. Clayton, C. Joshi, T. Katsouleas, and W. B. Mori, 1990, Laser Part. Beams **8**, 427.
Wittig, G., *et al.*, 2015, Phys. Rev. ST Accel. Beams **18**, 081304.
Wood, W. M., C. W. Siders, and M. C. Downer, 1991, Phys. Rev. Lett. **67**, 3523.
Wu, J., *et al.*, 2017, Nucl. Instrum. Methods Phys. Res., Sect. A **846**, 56.

Xiang, D., and W.-h. Huang, 2007, Phys. Rev. ST Accel. Beams **10**, 012801.
Xiang, D., *et al.*, 2011, Phys. Rev. ST Accel. Beams **14**, 112801.
Xin, M., K. Safak, M. Y. Peng, A. Kalaydzhyan, P. T. Callahan, W. Wang, O. D. Muecke, and F. X. Kaertner, 2017, IEEE J. Sel. Top. Quantum Electron. **23**, 97.
Xu, X. L., *et al.*, 2016, Phys. Rev. Lett. **116**, 124801.
Yan, W., *et al.*, 2017, Nat. Photonics **11**, 514.
Yellampalle, B., K. Y. Kim, G. Rodriguez, J. H. Glownia, and A. J. Taylor, 2005, Appl. Phys. Lett. **87**, 211109.
Yi, S., V. Khudik, S. Y. Kalmykov, and G. Shvets, 2011, Plasma Phys. Controlled Fusion **53**, 014012.
Zakharov, V. E., 1972, Sov. Phys. JETP **35**, 908.
Zeil, K., S. D. Kraft, A. Jochmann, F. Kroll, W. Jahr, U. Schramm, L. Karsch, J. Pawelke, B. Hidding, and G. Pretzler, 2010, Rev. Sci. Instrum. **81**, 013307.
Zgadzaj, R., *et al.*, 2016, in *AIP Conference Proceedings* (AIP, New York), Vol. 1777, p. 070014.
Zhang, C., *et al.*, 2016, Phys. Rev. Accel. Beams **19**, 062802.
Zhang, C., *et al.*, 2017, Phys. Rev. Lett. **119**, 064801.
Zhang, C., *et al.*, 2018, Plasma Phys. Controlled Fusion **60**, 044013.
Zhang, C. J., *et al.*, 2016, Sci. Rep. **6**, 29485.
Zhang, M., 1996, "Fermilab-tm-1988."